REPORT TITLE: MULTI-ATTRIBUTE SEISMIC/ROCK PHYSICS APPROACH TO CHARACTERIZING FRACTURED RESERVOIRS

TYPE OF REPORT: FINAL REPORT

REPORTING PERIOD: FOR THE PERIOD OF 10/01/1999 – 09/30/2004

PI: GARY MAVKO, PROFESSOR (RESEARCH)

REPORT ISSUED: FEBRUARY 2005

DOE AWARD #: DE-AC26-99FT40692

NAME & ADDRESS OF SUBMITTING ORGANIZATION: STANFORD UNIVERSITY, GEOPHYSICS DEPARTMENT/SRB PROGRAM, STANFORD, CA 94305-2215

DISCLAIMER

ABSTRACT

Most current seismic methods to seismically characterize fractures in tight reservoirs depend on a few anisotropic wave propagation signatures that can arise from aligned fractures. While seismic anisotropy can be a powerful fracture diagnostic, a number of situations can lessen its usefulness or introduce interpretation ambiguities. Fortunately, laboratory and theoretical work in rock physics indicates that a much broader spectrum of fracture seismic signatures can occur, including a decrease in P- and S-wave velocities, a change in Poisson's ratio, an increase in velocity dispersion and wave attenuation, as well as well as indirect images of structural features that can control fracture occurrence.

The goal of this project was to demonstrate a practical interpretation and integration strategy for detecting and characterizing natural fractures in rocks. The approach was to exploit as many sources of information as possible, and to use the principles of rock physics as the link among seismic, geologic, and log data. Since no single seismic attribute is a reliable fracture indicator in all situations, the focus was to develop a quantitative scheme for integrating the diverse sources of information. The integrated study incorporated three key elements:

The first element was establishing prior constraints on fracture occurrence, based on laboratory data, previous field observations, and geologic patterns of fracturing. The geologic aspects include analysis of the stratigraphic, structural, and tectonic environments of the field sites. Field observations and geomechanical analysis indicates that fractures tend to occur in the more brittle facies, for example, in tight sands and carbonates. In contrast, strain in shale is more likely to be accommodated by ductile flow. Hence, prior knowledge of bed thickness and facies architecture, calibrated to outcrops, are powerful constraints on the interpreted fracture distribution. Another important constraint is that fracturing is likely to be more intense near faults – sometimes referred to as the damaged zone. Yet another constraint, based on world-wide observations, is that the maximum likely fracture density increases with depth in a well-defined way. Defining these prior constrains has several benefits: they lead to a priori probability distributions of fractures, that are important for objective statistical integration; they limit the number of geologic hypotheses that need to be theoretically modeled; they provide plausible models for fracture distributions below the seismic resolution.

The second element was theoretical rock physics modeling of optimal seismic attributes, including offset and azimuth dependence of traveltime, amplitude, and impedance signatures of anisotropic fractured rocks. The suggested workflow is to begin

with an elastic earth model, based on well logs, theoretically add fractures to the likely facies as defined by the geologic prior information, and then compute synthetic seismic traces and attributes, including variations in P and S-wave velocities, Poisson's ratio, reflectivity, travel time, attenuation, and anisotropies of these parameters. This workflow is done in a Monte-Carlo fashion, yielding ranges of expected fracture signatures, and allowing realistic assessments of uncertainty to be honored.

The third element was statistical integration of the geophysical data and prior constraints to map fracture intensity and orientations, along with uncertainties. A Bayesian framework was developed that allowed systematic integration of the prior constraints, the theoretical relations between fractures and their seismic signatures, and the various observed seismic observations. The integration scheme was successfully applied on an East Texas field site.

The primary benefit from the study was the optimization and refinement of practical workflows for improved geophysical characterization of natural fractures and for quantifying the uncertainty of these interpretations. By presenting a methodology for integrating various types of information, the workflow will help to reduce the risk (and therefore the cost) of exploring for and recovering natural gas and oil reserves in fractured reservoirs.

FINAL REPORT

MULTI-ATTRIBUTE SEISMIC/ROCK PHYSICS APPROACH TO CHARACTERIZING FRACTURED RESERVOIRS

Prepared for

U. S. Department of Energy
Federal Energy Technology Center
DE-AC26-99FT40692

by

Gary Mavko, P.I.,
Tapan Mukerji, with Diana Sava & Juan Florez

Stanford Rock Physics Laboratory
Department of Geophysics
Stanford University

650 723 0839
mavko@stanford.edu

Feb. 1, 2005

TABLE OF CONTENTS

INTRODUCTION **3**
SUMMARY OF TECHNICAL RESULTS **4**
PRACTICAL RECOMMENDATIONS **29**

ATTACHMENTS
A GEOLOGIC MODEL OF FRACTURE OCCURRENCE IN THE JAMES LIME FIELD
B EVOLUTION OF CONJUGATE NORMAL FAULTS IN SEDIMENTARY SEQUENCES WITH HIGH BRITTLENESS/DUCTILITY CONTRAST
C PROBABILISTIC MODELING OF FRACTURE DENSITY CONSTRAINED BY OUTCROP DATA AND GEOMECHANICS
D FIELD DATA ON SHEAR-WAVE ANISOTROPY: PRACTICAL BOUNDS ON CRACK DENSITY
E ROCK PHYSICS AND FRACTURE MODELING OF THE JAMES LIME RESERVOIR
F ANALYSES OF VSP DATA
G 3D SEISMIC: ANALYSIS OF AZIMUTHAL VARIATION OF REFLECTIVITY
H QUANTITATIVE INTEGRATION FOR FRACTURE CHARACTERIZATION
I REFERENCES

INTRODUCTION

The key to successful development of many low permeability reservoirs lies in reliably detecting, characterizing, and mapping natural fractures. Fractures play a crucial role in controlling almost all of the fluid transport in tight reservoirs, and they can influence production even in reservoirs with moderate permeability.

Most current seismic methods to characterize fractures depend on a few anisotropic wave propagation signatures that can arise from aligned fractures. Common among these are seismic shear wave splitting, azimuthal variation of P-wave AVO, and azimuthal variation in P-wave normal moveout (NMO) velocity. While seismic anisotropy can be a powerful fracture diagnostic, a number of situations can lessen its usefulness or introduce interpretation ambiguities. These include (a) multiple fracture sets at different orientations that combine to lessen the anisotropy, (b) the presence of nonfracture rock anisotropy as might occur with large differences in horizontal principal stresses, (c) fracture occurrence in narrow bands or swarms that are not sampled well by azimuthal methods, and (d) seismic acquisition geometries that provide limited azimuthal coverage – actually quite typical in spite of the name "3D seismic."

Fortunately, laboratory and theoretical work in rock physics indicates that a much broader spectrum of fracture seismic signatures can occur, including a decrease in P- and S-wave velocities, a change in Poisson's ratio, an increase in velocity dispersion and wave attenuation, as well as well as indirect images of structural features that can control fracture occurrence. Many of these lead to "isotropic" fracture signatures that have the potential for complimenting or replacing some of the anisotropic methods.

In this project, we have pursued an integrated study with the *objective to demonstrate an interpretation and integration strategy* for detecting and characterizing natural fractures in rocks. Our approach has been to exploit as many sources of information as possible, and we use the principles of rock physics as the link among seismic, geologic, and log data. Experience has shown that no single attribute is a reliable fracture indicator in all situations. Hence, we have developed a quantitative scheme for integrating the diverse sources of information.

Although this work has involved developing and using powerful theoretical methods, our focus has been to demonstrate *practical* methodologies that can be applied in the field to reduce interpretation risk and improve gas recovery.

Our integrated study incorporates three key elements:

(1) Establishing **prior constraints** on fracture occurrence, based on laboratory data, previous field observations, and geologic patterns of fracturing.

(2) **Theoretical rock physics modeling of optimal seismic attributes**, including offset and azimuth dependence of traveltime, amplitude, and impedance signatures of anisotropic fractured rocks.

(3) **Integration and interpretation** of seismic, well log, laboratory and geologic data. This **includes estimates of the uncertainty** of the fracture interpretation.

The focal point for this project has been the development and demonstration of our fracture detection and characterization methodologies on data provided by Marathon Oil Company for the Neuville Field of East Texas.

This report summarizes the final results of the project, including technical developments, lessons learned, and recommended practices for use by the gas industry.

SUMMARY OF TECHNICAL RESULTS

In this section, we summarize the technical results of this project. They include theoretical developments, geologic field work, and integrated analysis of diverse data from a fractured reservoir site. Additional details are given in a series of attachments. Recommended practices and pitfalls will be summarized in the next section.

With the generous cooperation of Marathon Oil, we received well logs, lithologic descriptions, and geologic insights into two Texas sites: fractured carbonates in the San Andres formation of the West Texas Yates Field, and fractured carbonates in the James Lime formation in the East Texas Neuville field. Although we performed basic rock physics and fracture modeling in both fields, we ultimately focused on the Neuville field, largely because of better data availability, and Marathon's greater ability to cooperate there.

Our work involved several key steps:

(1) Analysis of the stratigraphic, structural, and tectonic environments of the field sites,

(2) Geomechanical modeling of candidate structural scenarios, to help identify mechanically likely distributions of fractures, as controlled by rock moduli, bed thickness, bed topology, and regional stress boundary conditions,

(3) Compilation of observable patterns of fracturing from nearby wells,

(4) Rock physics modeling calibrated to well logs, to explore the various seismic signatures of fractures, including variations in P and S-wave velocities, Poisson's ratio, reflectivity, travel time, attenuation, and anisotropies of these parameters.
(5) Analysis of VSP data to identify potential fractures and to compare their signatures with the rock physics modeling
(6) Development of a general methodology for integrating diverse fracture-related data, and demonstration of the methodology on the field site with 3D seismic.

During Phase II of this project, we acquired a small-scale multi-offset-multi-azimuth VSP (Vertical Seismic Profile) data set in the in the James Lime play. The goal was to develop and validate the feasibility of our interpretation schemes for detection and characterization of fracture systems, on a small-scale and controlled experiment. Marathon Oil provided log data and expertise as needed. They took the lead in managing the practical aspects of the field pilot VSP study, including design of the survey specifications, and performing basic processing of the data. Stanford and Marathon jointly participated in the analysis. We show below that we were successful in finding and understanding many of the fracture signatures in the VSP, quantifying them using rock physics models, and relating them to the wellbore data and to the geologic environment.

During Phase III, we analyzed 3-D seismic from the same field, using it to demonstrate our integration methodology. The 3-D data were also provided by Marathon. Marathon provided the basic seismic processing, and Stanford extracted relevant seismic attributes from the processed data. Stanford also developed and demonstrated a generalized statistical rock physics integration scheme, as described below.

We now summarize the key results in more detail.

Integrated Strategy for Fracture Characterization

Many types of information can be used to study fractures, and each one of them contributes in a different way to fracture characterization. For example, geological outcrop studies give us direct observations of the fracture orientation, spatial density, and sometimes even their length. Outcrops also lend insights into the geomechanical relations, such as how fractures are related to strain, bed thickness, and facies brittleness. However, the challenge is to extrapolate this information to the reservoir at depth. Seismic data, on the other hand, provide good coverage at depth, but the measurements

are indirectly related to fractures, and their resolution is lower than the scale of the features we are interested in. However, even though we cannot directly image the fractures from seismic measurements, we can use various seismic attributes, which give us information about fracture density, orientation, and sometimes the type of fluid saturating the fractures.

In this project, we demonstrated a methodology for integrating these various types of geologic, well log, and seismic information using rock physics theories, in the framework of an inverse problem, as defined by Tarantola (1982, 1987). A typical inverse problem has three different elements: 1) the *model parameters*, represented by the subsurface rock properties that we wish to detect and map, (in this case, the fracture characteristics), 2) the *data parameters* (e.g. seismic and log measurements), and 3) the *physical laws* that relate the model parameters to the data parameters, which are given by *rock physics theories*. In addition to the seismic and log data, we often have prior information about the subsurface rock properties (fracture parameters) from geologic interpretations and constraints. These various types of geological and geophysical information can be combined quantitatively if we translate them into the common language of probability theory.

A general way of expressing mathematically the prior geologic knowledge about the model parameters (fracture characteristics) is through *a priori* probability density functions (PDFs). We can think of the prior model as the geologist's best prediction of where the fractures are likely to be, before seeing the quantitative seismic information. This prior model is best expressed as a PDF, because a PDF allows us to express likely fracture hypotheses, while at the same time quantifying our confidence (or lack thereof) in the predictions. The seismic data, which are affected by measurement errors (from acquisition, processing, noise, etc), can also be described through PDFs. Furthermore, the theoretical relations between the model parameters (fracture characteristics) and the data parameters (seismic attributes), given by rock physics theories, are also uncertain. This uncertainty results from approximations in the rock physics models and from natural variability of the rock properties. Therefore, we also use PDFs to express mathematically the uncertainty in the physical correlations between the model and data parameters.

The language of probability theory allows us to integrate quantitatively the various types of information and, at the same time, *to estimate the uncertainty* in our predictions. The solution to the integration methodology formulated in this framework is represented by the *a posteriori* PDF for the model parameters (fracture characteristics), obtained by combining quantitatively the prior geological information, the seismic measurements, and the information from the rock physics theories. From this posterior PDF we can obtain

the expected values for fracture parameters, but we can also derive probability maps, as a general way of expressing the *uncertainty* in our estimations. The language of probability also allows us to estimate the impact of each type of information in reducing the uncertainty in our predictions (Shannon, 1948; Takahashi et al., 1999). Therefore, this method can have a significant impact on risk and decision analysis for reservoir management in various exploration and production stages.

We obtain several types of outputs from this integrated approach:

- A map with the most likely distribution of fracture density and orientation, based on the prior geological information and constrained by seismic data,
- Objective methodologies for updating the map when new information becomes available,
- Objective estimates of the uncertainty associated with the fracture maps, and
- Objective methods for assessing the relative value of each type of measurement. For example, in a given situation, what new measurement will be most valuable for reducing fracture uncertainty?

The workflow that we developed and recommend consists of the following steps, which are described in detail in the following sections:

1. Analysis of the geologic scenarios, including stratigraphic and structural controls on fracture occurrence. The end results of this step are a list of likely fracture scenarios to evaluate (e.g., Which intervals might be fractured? How many fracture sets might exist? What pore fluids should be considered?), constraints on fracture occurrence, and a prior fracture model, expressed as a PDF.
2. Rock physics fracture modeling, to explore the seismic signatures of the fracture distributions that are possible and likely at the site. These tasks are best calibrated with log data. The end results are physical insights into fracture signatures, and PDFs expressing the theoretical relations (with uncertainty) between the target fracture parameters and the data.
3. Analysis of field seismic data to ensure optimum processing, identify potential artifacts (such as acquisition footprint), and extract attributes that will be useful for the fracture interpretation, based on the rock physics modeling.
4. Finally, integration of the prior information, the theoretical relations, and the geophysical data to produce the final fracture interpretation, expressed probabilistically, as well as quantitative estimates of uncertainty.

Geologic Model of Fracture Occurrence in the James Lime Field

ATTACHMENT A summarizes the geologic setting of our site in the James Lime play of the Neuville Field in East Texas where the bulk of our field demonstration was focused.

In spite of the lack of reservoir exposures, which prevents a direct outcrop analogue study, we develop a conceptual model based on mechanical stratigraphy and the tectonic setting. The dominant structural style is normal faulting, and the current state of stress is also extensional. In the case of the James Limestone, the interposition of brittle and ductile layers at different scales and the development of the Sabine uplift at the Texas-Louisiana border during the Cretaceous are two factors with definite impact in the development and orientation of conjugate normal faults and the development of fracture swarms.

The lithologic composition of James Limestone, characterized by the interposition of meter-scale layers of limestone and calcareous shale, plays a significant role in the distribution of fractures. This lithologic composition is dominant in the Mesozoic sequence of the Gulf of Mexico, which basically consists of the interposition of ductile and brittle layers at different scales. In general, joints form within the limestone (brittle) lithologies and abut against the shale (ductile) layers. Propagation of small faults depends on the fault offset and shale thickness. In the same way that salt layers have played a significant role in the development of conjugate and listric normal faults in the Gulf of Mexico, shale intervals above, below, and within the James Lime may constitute gliding planes for shearing and localized faulting. The details of this faulting mechanism are explained in ATTACHMENT B. Conjugate normal faulting is considered as the main deformation mechanism within the James Limestone. Conjugate normal faults form narrow zones with high fracture density. Fracture swarms or clusters are therefore associated with subseismic faults, or faults that cannot be detected with conventional seismic methods. Between these fracture swarms, the background fracture density may correspond to regularly spaced joints.

The geologic interpretation based on the integration of the Multi-offset VSP (ATTACHMENT F) and the horizontal lateral sections of the Henderson-1 well, confirms the presence of subseismic faults and fracture swarms within the James Limestone. The presence of small faults is indicated by changes in the stratigraphy along the well trajectory, as well as by small displacements of the James-Lime reflection observed in the VSP data. These faults are also associated with reduction in the P-to-P

reflectivity, an indication of low bulk compressibility, most likely related to fracture swarms.

Fracture orientation, a critical uncertainty in fractured reservoirs, has been determined from the 3D seismic data. In the case of the well Henderson-1 we had three possible scenarios: (1) scenario A, fractures parallel to the Cretaceous depositional slope that basically means parallel to the adjacent normal faults; (2) scenario B, fractures approximately normal to the adjacent normal faults; and (3) scenario C, fractures parallel to the current depositional slope, which means oblique to the adjacent normal faults. A previous geomechanical model showed that fracture orientation at Henderson-1 depended exclusively on loading conditions, and we could not rule out any of these three probable scenarios. The AVOZ analysis from 3D seismic data (ATTACHMENT G) shows seismic anisotropy consistent with faults and fractures sub-parallel to the adjacent normal fault. The results from the AVOZ analysis not only rule out the possibility of scenarios B and C, but also show the spatial variability of fracture orientation, which in general ranges from parallel to slightly oblique to the large normal faults.

Regarding fault spacing, we combined a systematic analysis of the LWD gamma ray and the seismic attributes of the VSP data to obtain the distribution of faults along the path of Henderson-1. Even though this method has limitations in resolution, since it cannot identify faults with very small offset, it can be particularly useful in wells where wellbore-image logs are not possible or available.

Evolution Of Conjugate Normal Faults In Sedimentary Sequences With High Brittleness/Ductility Contrast

ATTACHMENT B describes a mechanical model for fracture occurrence in these types of formations. Conjugate normal faults are a common geometric fault configuration that occurs in different natural settings at different scales. The origin and evolution of these faults is poorly understood. Here we propose a model for evolution of conjugate normal faults in sedimentary sequences with high brittleness/ductility contrast. The model is based on both field observations and numerical modeling. It is shown that conjugate normal fault patterns are the result of sequential events of slip and hierarchical splay jointing. Basically, slip along ductile bedding surfaces or layers generates a stress perturbation that results in the formation of subvertical splay joints. Slip along these subvertical splay joints (sheared joints) generates a new stress perturbation that creates a new set of splay joints. The azimuth of the new set of splay joints is parallel to the

sheared joints, but they have opposite dip direction. The new splay joints constitute new low-friction planes that slip, forming a set of conjugate normal faults. Interaction between bed-confined, subparallel sheared joints (normal faults) is required in order to form larger normal faults.

This sequential evolution of conjugate normal faults results in a particular shape that we call *the tectonic bowtie*. The limits of the bowtie are defined by the parent (synthetic) normal fault and the main two opposite-dipping antithetic faults. With respect to the parent fault, the antithetic faults are located at the upper quadrant of the hanging wall and the lower quadrant of the footwall. The zones between the parent fault and the antithetic faults are characterized by high-density of fractures, or fracture swarms, which are parallel to the parent fault. The bowtie can be well-preserved or partially preserved depending upon the actual geometry of the parent fault.

The deformation documented in this paper is associated to faults with less than 1 m of vertical offset, and therefore corresponds to faults that are below the limit of seismic resolution. Nevertheless, these fracture swarms may have a significant impact on both rock impedance and rock permeability. Figure 1 shows examples in an outcrop.

Figure 1. Outcrop examples of tectonic bowties.

As we have been discussing, faults and fractures can have a range of seismic signatures. However, seismic analysis can never resolve individual fractures and many of their geometric details. Hence, we believe it is critical to have a geologically sound model for the subresolution details of the fracture zones that we can use as inputs to our rock physics models. We have adopted the bowtie model for fault and fracture occurrence in the James Lime play.

Quantitative Integration of Outcrop Studies to Reservoir Modeling

ATTACHMENT C presents a pioneer work in the use of outcrop descriptions to constrain the static model of fractured reservoirs. Outcrop analogue studies are commonly used to generate conceptual models of the reservoir. More quantitative studies look for statistical correlations between fracture density and kinematic, geometric or stratigraphic variables like shear, tilting, or bed thickness. These statistical correlations are somewhat deterministic, since they use the mean or the median as the main statistical parameter. In this paper we propose to take the whole population, reproducible using the type of distribution and their respective statistical parameters, and apply geostatistical methods to reproduce the spatial variability observed at the outcrop. We believe this method has the potential to become an alternative to the Discrete Fracture Network technique, however it requires further research.

Rock Physics Analysis and Fracture Modeling

As just discussed, the geological model for the James Limestone reservoir suggests the presence of fracture swarms or clusters associated with small faults. Also, between these fracture swarms, the reservoir may exhibit regularly spaced vertical joints. Therefore, the reservoir is modeled with distributions of fractures that may correspond to the bowtie fracture swarms (discussed in ATTACHMENT B), within which the distribution of fractures can be more or less random, as in a brecciated zone. We also consider a set of vertical joints that generates an azimuthally anisotropic medium with HTI symmetry (transversely isotropic with horizontal symmetry axis).

Another critical input to developing a prior fracture model is an understanding of what range of fracturing has been seen in other field situations, and what degree of seismic anisotropy would be considered significant and anomalous. ATTACHMENT D gives an analysis of previous field data on shear-wave anisotropy acquired by various authors in different types of environments and summarized by Crampin (1994). The results of this analysis are valuable *a priori* information, which can be used to constrain the fracture density in our modeling, as a function of depth. This helps us evaluate the feasibility of various seismic methods to detect fractures, depending on the depth of the reservoirs.

In ATTACHMENT E we present our general methodology for stochastic simulations of seismic properties of fractured media. Based on this methodology we model both the interval and interface seismic properties for the fractured James Lime reservoir, with the main objective of understanding how fractures impact the seismic response in different possible scenarios. The first part of this attachment focuses on the rock physics analysis of the well log data, and on the information about fracture occurrence available from the FMI data. The second part presents the results of our stochastic simulations for seismic properties of the fractured James Lime reservoir. The main objective is to understand how reservoir heterogeneities and especially fractures impact the seismic response, and to provide a framework for quantitative analysis of the VSP and 3D seismic data for estimating fracture orientation, fracture density and fluid type. Our approach also allows for estimating the uncertainty in fracture characterization due to natural variability in the fractures and background host rock.

The results of our rock physics analysis, together with the interpreted FMI information about fractures from well McCoy #1, show that fractures in the James Lime reservoir are associated with the cleaner limestones intervals that have higher velocities and lower porosities.

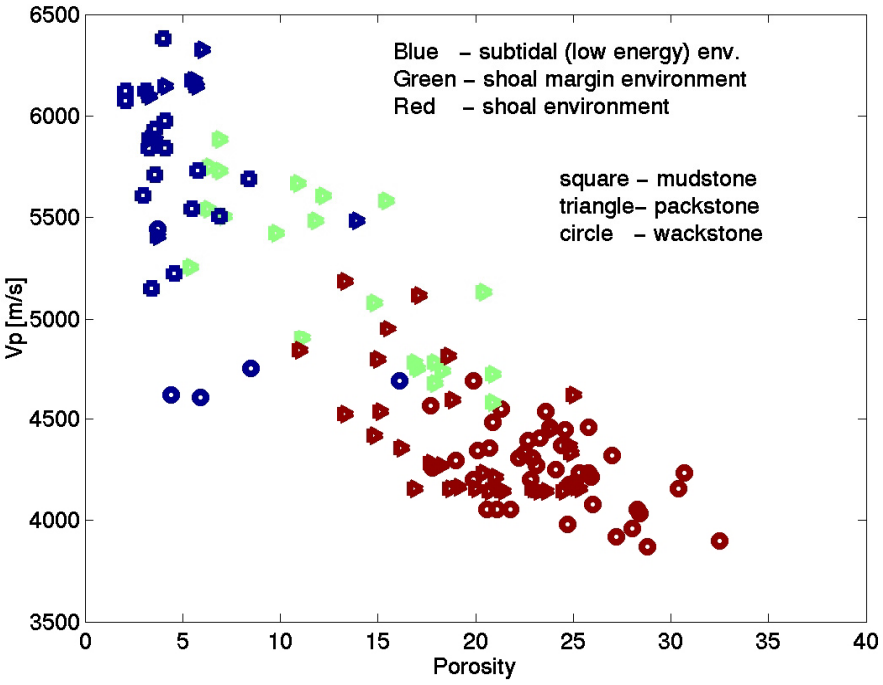

Figure 2: V_P-V_S scatter-plot for the San Andres reservoir, Yates field. The data are color-coded by depositional environment: low-energy, subtidal (blue), shoal-margin (green), shoal (red).

The preferential association of the fractures with a particular type of depositional environment with the corresponding facies was also observed for San Andres reservoir in Yates field. In that case, the fractures occur primarily in the low-energy, subtidal depositional environment, represented by dolomitic mudstones. Figure 2 presents a seismic V_P-V_S scatter-plot, derived from the well-log data corresponding to the San Andres reservoir. The data are color-coded by the type of the depositional environment: the low energy, subtidal environment (blue), the shoal-margin environment (green), and the shoal environment (red). We can see that the three different types of environments have different elastic signatures, so they may be seismically differentiable.

From the core analysis in the same well we observe that most of the fractures are associated with the low-energy, subtidal environment, characterized by higher velocities and lower porosities. On the left panel of Figure 3 we show the proportion of each depositional environment present in this well. On the right panel of Figure 3 we show the total number of fractures (from core analysis) that occurs in each of the three different types of environments encountered in the San Andres reservoir. We can see that 50% of the fractures occur in the low-energy depositional facies, even though that facies accounts for only 25% of the sections.

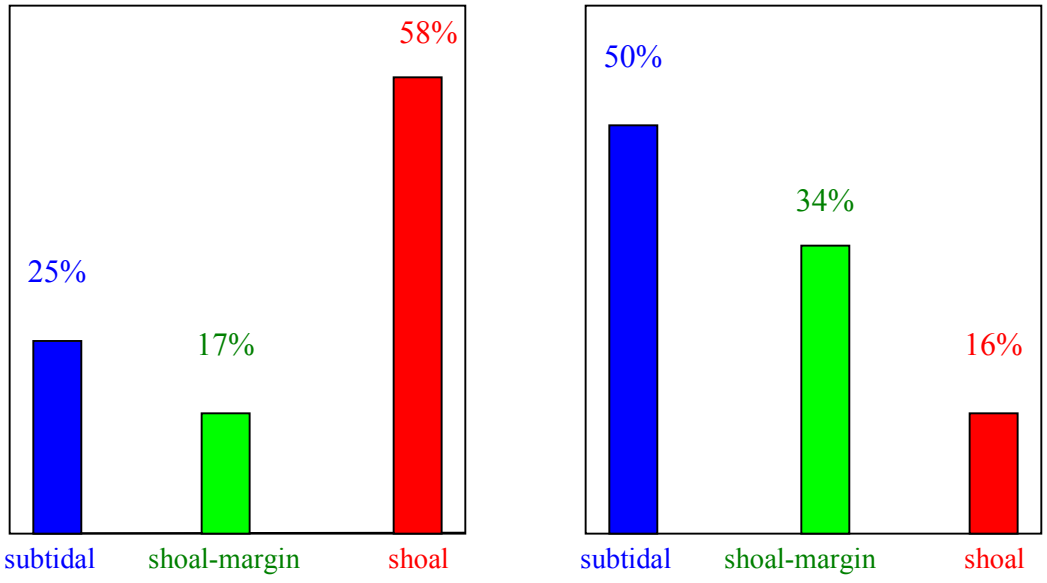

Figure 3: *Left panel:* Percentages for the different depositional environments corresponding to San Andres reservoir occurring in one of the wells. *Right panel*: Percentages from the total number of fractures that correspond to each of the three different depositional environments: low-energy, subtidal (blue), shoal-margin (green), shoal (red).

This association of the fractures with the higher velocity rocks, observed for both James Lime, as well as San Andres reservoirs, can have an impact on fracture delineation from seismic data. Even if the velocity will be drastically lowered for the most fractured zones, on average the velocities of the fractured regions may be larger than the velocities of the unfractured rocks, characterized by higher clay content. Therefore, an impedance inversion may help in delineating the zones with higher fracture probability. Inside each high impedance region, we can then do a more detailed analysis to determine the zones of the highest fracture density.

Based on the well-log analysis of the James Lime, we consider that the reservoir may exhibit three main types of facies: 1) unfractured, clean limestones, 2) shaly limestones, and 3) fractured, clean limestones, which we have modeled with different distributions of fractures. The goal is to find the optimal combination of seismic attributes for distinguishing the gas-filled fractured zones from the shaly and unfractured limestones in the reservoir.

For each of the hypotheses of isotropic and anisotropic fracture distribution we stochastically model seismic interval and interface properties such as interval velocities, Impedances, travel time, PP reflectivity as a function of angle of incidence and azimuth. The modeling shows that all of these properties may be influenced by the presence of the fractures. The gas filled fractures enhance the ability to detect fractured zones, as compared with the brine-filled fractures.

The **interval velocities** decrease with the fracture density. For gas filled fractures the P-wave velocity is more sensitive to the presence of the fractures than S-wave velocity. The largest decrease in V_P for fixed crack density is in the direction orthogonal to a set of vertical joints. V_P parallel to crack plane is the least sensitive to fractures, as expected. P-wave velocity for an isotropic distribution of fractures is also significantly lowered. For large crack densities, the V_P of the gas-filled fractured zones becomes comparable to the V_P of the shaly limestones in the reservoir, which are less susceptible to fracture. The *S*-wave velocity decreases less than V_P, and its expected value remains larger than the *S*-wave velocity of the shaly rocks. Therefore, V_S is a valuable piece of information to discriminate between the gas-filled fractured zones and the shaly limestones in the reservoir.

In the case of an isotropic distribution for the fracture orientation, the **P-wave Impedance - Poisson's ratio** domain is an optimal combination of interval properties for delineating the gas-filled fractured zones in the reservoir. However, if the fractures are saturated with brine, it is difficult to distinguish them from the unfractured, clean limestones.

The **travel time** can be also influenced by the presence of fractures. For the case of an HTI medium, the travel time in the direction orthogonal to fractures is larger than the travel time through an unfractured medium. However, for the James Lime reservoir modeled as an HTI medium, the travel time difference between fractured, slow direction, and unfractured is very small, even for a relatively high fracture density such as 0.07. In the hypothesis of a fractured reservoir modeled with randomly distributed fractures, the difference between travel time through fractured and unfractured zones is a little higher, approximately 5 milliseconds. However, since the sampling rate for VSP and seismic data is 2 to 4 milliseconds, the travel time is not an optimal attribute for fracture characterization in this case, due to the fact that the reservoir is too thin.

The interface properties such as **PP reflectivity** can be very useful to discriminate fractured zones from unfractured ones, and also to quantify the density of the fractures. The advantage of using this attribute is that it can provide localized information at the interface of interest, unlike the travel time methods. We consider again both the isotropic and anisotropic fracture distributions in the James Lime reservoir. The cap rock is the Bexar shale, whose elastic properties are very different from those of the reservoir. That is why at the top of James Lime we can notice a very strong reflection in the VSP and seismic data (ATTACHMENT F). However, our modeling suggests that the presence of randomly oriented cracks filled with gas decrease the amplitude of the reflected wave considerably. The higher the fracture density, the larger the decrease in Rpp amplitude. Therefore, even at normal incidence the expected Rpp can be a very efficient attribute to discriminate between fractured and unfractured zones, especially if the fractures are randomly orientated.

At normal incidence, the Rpp from a fractured zone with vertical joints filled with gas is smaller than the Rpp from the unfractaured zone. However, for the same crack density, the decrease in the normal incidence Rpp amplitude for vertical joints is smaller than for randomly distributed fractures, as expected.

For the interface properties, the **AVO Gradient - Intercept** domain is a potentially useful combination for discriminating gas-filled fractures in the reservoir. However, due to a large variability in the seismic properties of the cap rock, the uncertainty in differentiating fractured zones from interface properties is a little higher than from interval properties, such as *P-Impedance* and *Poisson's Ratio*. As the fracture density increases, the *PP reflectivity* from the fractured zones decreases, and becomes closer to the *PP reflectivity* from the shaly limestones in the reservoir. The *AVO gradient* can help resolve this ambiguity. Modeling shows that the shaliness moves the *AVO gradient* to smaller negative values as compared to the clean, unfractured limestones, while the

fractures filled with gas move the *AVO gradient* to larger negative values as compared to the clean, unfractured limestones (Figure 4). Therefore, the *AVO gradient* can help in better separating the gas-filled fractured zones from the shaly zones in the reservoir.

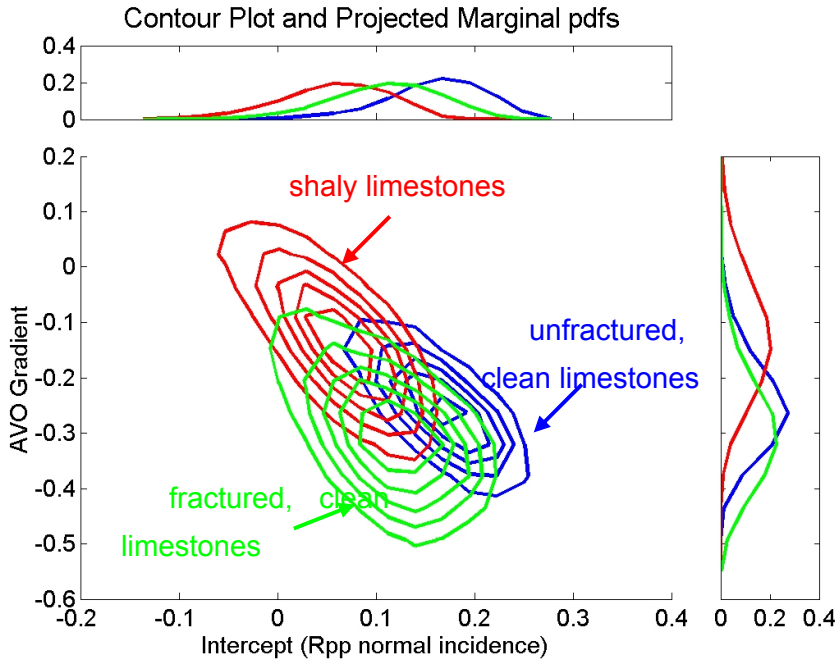

Figure 4: Joint probability distribution functions of the AVO Gradient and Intercept for the Monte Carlo simulations of the unfractured, clean limestones (blue), fractured limestones with **randomly oriented** cracks (green), and shaly rocks (red). Fractures are filled with **gas**.

Brine-saturated fractures are difficult to distinguish also in the *AVO Gradient - Intercept* domain.

In the hypothesis of a nearly vertical set of joints, we also consider the Rpp Amplitude Variation with Incidence Angle and Azimuth (**AVAZ**). The azimuthal variation depends on the fluid type. In the assumption of little fluid communication between fracture and matrix porosity during a seismic period, the gas filled fractures and brine filled fractures have opposite azimuthal polarity. For the brine filled fractures, the maximum Rpp value at a fixed angle of incidence is in the direction perpendicular to fractures, while for the gas saturated fractures the maximum Rpp value is in the direction parallel to fractures. This is an interesting result that can be used to differentiate between gas filled and brine filled fractures for a vertical set of joints. The orientation of fractures should be determined from geological information or other seismic attributes, such as travel time. Therefore, quantitative azimuthal analysis of Rpp from 3D seismic data can be used to determine also the fluid type.

In summary, our fracture modeling shows the possible changes in the seismic response due to fractures in James Lime reservoir for two different hypotheses: 1) random distribution of fractures corresponding to swarms of fractures in the vicinity of faults, and 2) parallel, vertical set of joints. Rock physics fracture modeling and stochastic simulations for seismic attributes of James Lime reservoir provide a framework for quantitative analysis of the seismic data, with the objective of estimating fracture orientation, fracture density and also fluid type.

The Integration Methodology

Figure 5 presents schematically the flow for the quantitative integration of geological, well-log, and seismic information using rock physics theories.

ATTACHMENT H describes the approach in detail.

In the following we give a summary with the practical steps for integrating the prior information about fracture distribution, obtained from the geological interpretation, with the well-log and seismic measurements, using stochastic rock physics modeling within a Bayesian framework:

1) Prior information about fracture parameters

We first need to evaluate the possible geological hypotheses for the fracture distribution, based on the site-specific outcrop observations, if available, or outcrop analogs, as well as on the well-log information. Another valuable source of information for fracture distribution can be derived from the geological structure of the reservoir, which can be obtained from the interpretation of seismic data. Some of the important parameters controlling fracture occurrence are: bed thickness, bed curvature, distance from the faults, local tectonic stresses, etc. We also need to quantify the uncertainty about the prior information, and the method we propose is using the MaxEnt principle, which is explained in ATTACHMENT H.

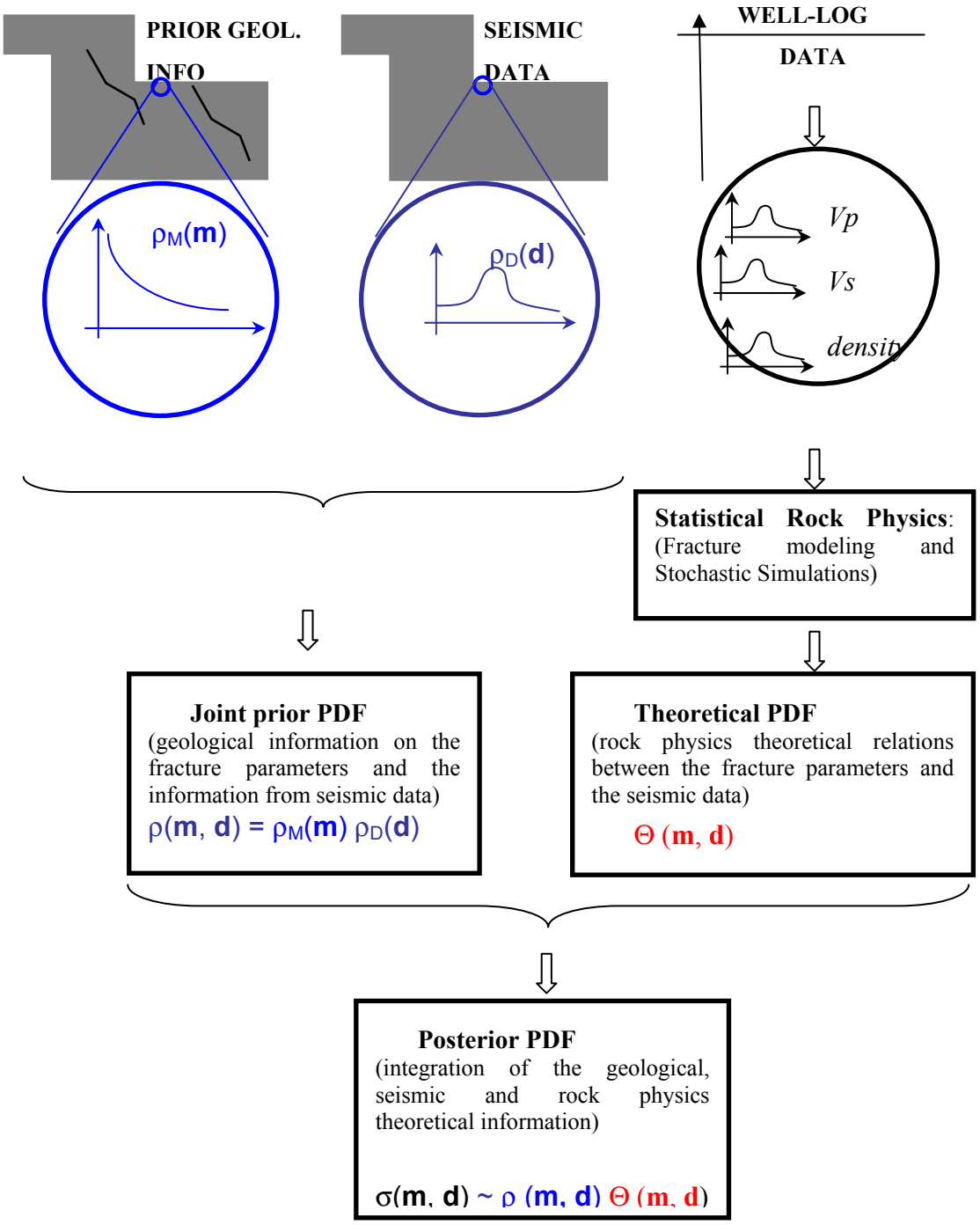

Figure 5. Workflow for statistically integrating log, seismic, and geologic information for fracture characterization using rock physics theories.

For James Limestone reservoir the fracture occurrence is controlled primarily by the existing faults. Rocks undergoing fracturing exhibit increased fracture density with increased strain (Nelson, 1985). Therefore, large fracture densities are usually associated with the presence of faults. Fracture density increases in the proximity of faults, and it decreases away from them.

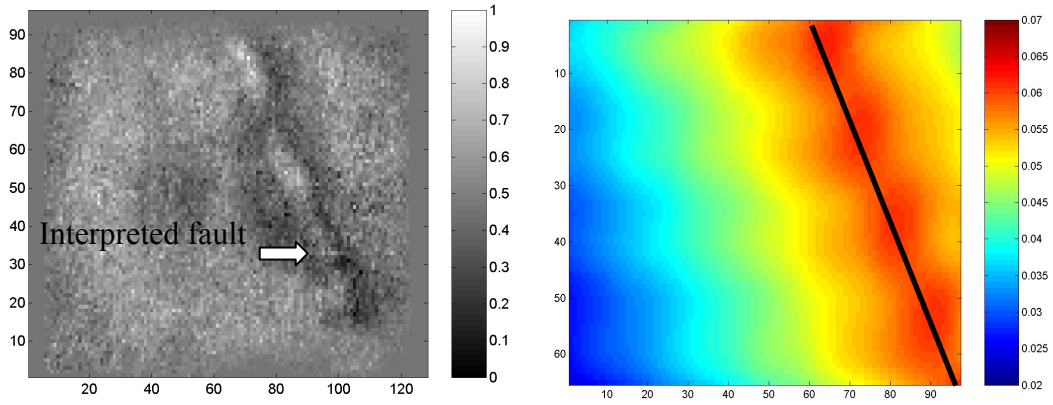

Figure 6: *Left panel*: Amplitude map at the top of a fractured carbonate reservoir, with the interpreted fault. Bin size is 200 ft. *Right panel*: Map with the interpolated *a priori* spatial distribution of the mean value of fracture density at the top of the reservoir, based on the geological interpretation of a fault, schematically represented in the figure.

Figure 6 presents in the right panel a map with the distribution of the mean values of fracture density at the top of the fractured reservoir. This spatial distribution is based on the geological interpretation of a fault from seismic data (Figure 6, left panel). In the proximity of the fault, the expected crack density is larger than away from the fault. Outcrop observations can help in calibrating the initial distribution of the mean values for fracture density in relation to the fault observed from seismic data. However, the fracture density values from outcrops should be transformed to the corresponding reservoir stresses. For the James Limestone reservoir, we assume a smooth exponential decay for the mean fracture density with increasing distance from the fault, as we show in Figure 6, right panel. The maximum expected fracture density in the proximity of the fault is assumed to be 0.07. This value corresponds to an upper value for the crack density for a reservoir at 2 km depth, based on the previous field data on shear-wave anisotropy collected by Crampin (1994), presented in ATTACHMENT D.

At each location we estimate the prior uncertainty about the fracture density using the MaxEnt principle, which predicts a prior exponential distribution, over the range of variability for fracture density considered (Figure 7). The prior PDF, symbolically denoted as $\rho_M(\mathbf{m})$, varies with location.

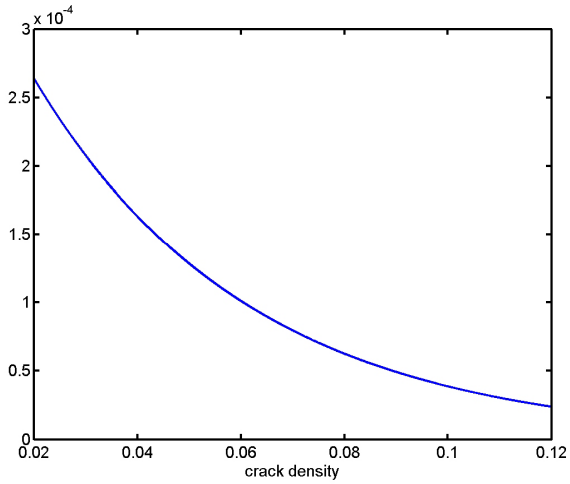

Figure 7: Example for a prior probability density function for fracture density. The PDF is an exponential distribution on the interval 0.02 to 0.12, with mean 0.04.

For James Limestone reservoir we consider two geological hypotheses: 1) of isotropic distribution of fractures, such as in brecciated zones, and 2) of a single set of vertical aligned fractures, as the FMI data from a nearby well suggests.

2) Rock-physics modeling and stochastic simulations: Theoretical PDF

Next, we perform rock-physics forward modeling and stochastic simulations based on the well-log data available, under the chosen geological hypotheses. The goals of this step are, first, to choose the most informative seismic attributes with respect to the fracture density (Takahashi, 2000), and second, to derive the physical relations between the fracture parameters and the chosen seismic attributes. We use rock-physics fracture modeling and stochastic simulations to incorporate the natural variability of the background rock properties. By using *Monte Carlo* simulations, we obtain many realizations of sets of fracture parameters and seismic attributes that span the intrinsic natural variability. Based on these realizations, we can estimate the theoretical joint PDF $\Theta(\mathbf{m}, \mathbf{d})$, which describes the physical relations between the fracture parameters (e.g. fracture density) and the seismic attributes. The theoretical PDF is assumed stationary and representative for the area of study. However, this theoretical joint PDF is site specific.

Figure 8 gives an example for the theoretical joint PDF between the fracture density (model parameter), and the azimuthal reflectivity anisotropy (data parameter), in the geological hypothesis of a single set of aligned vertical fractures. The physical law from which we generate the joint PDF in Figure 8 is given by Hudson's (1981) theory, which relates the fracture density to the elastic properties of the fractured media. Using the

elastic properties for the fractured rocks we estimate the seismic reflectivity anisotropy based on the Ruger's (1997) equations, in the hypothesis of a vertical set of fractures (more details in ATTACHMENT E). As expected, the rock physics theory predicts increasing azimuthal reflectivity anisotropy with increasing fracture density.

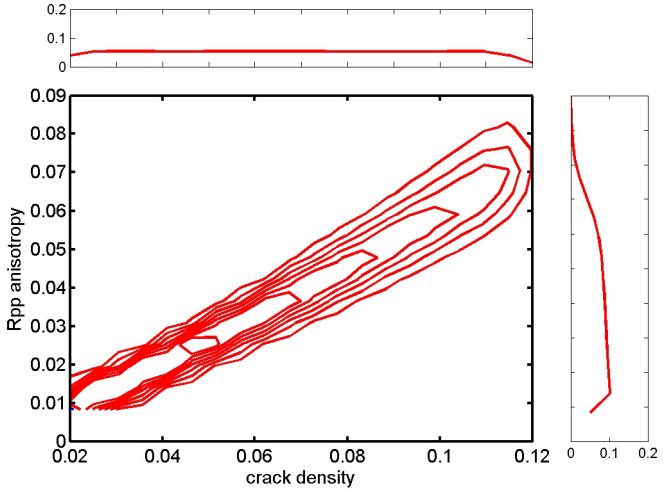

Figure 8: Theoretical joint PDF of crack density and azimuthal reflectivity anisotropy, derived based on the rock physics theories. The uncertainty is due to natural variability of the target rock properties.

3) Seismic data

For the James Limestone reservoir, the data parameters are represented by various reflectivity attributes from a 3D seismic dataset acquired over the reservoir, presented in ATTACHMENT G.

For example, in the hypothesis of a nearly vertical set of fractures, as the FMI data from a nearby well suggests, the reflectivity at far offsets varies with azimuth. Amplitude variation with azimuth (AVAZ) is a useful attribute to determine the fracture strike and the relative intensity of fracturing. Figure 9 presents the azimuthal reflectivity anisotropy at far offsets (left panel), with the associated standard deviations (right panel). The mean values as well as the standard deviations are derived using a bootstrap method to take into account the measurement errors associated with the reflectivity. The uncertainty due to measurement errors is assumed to be Gaussian.

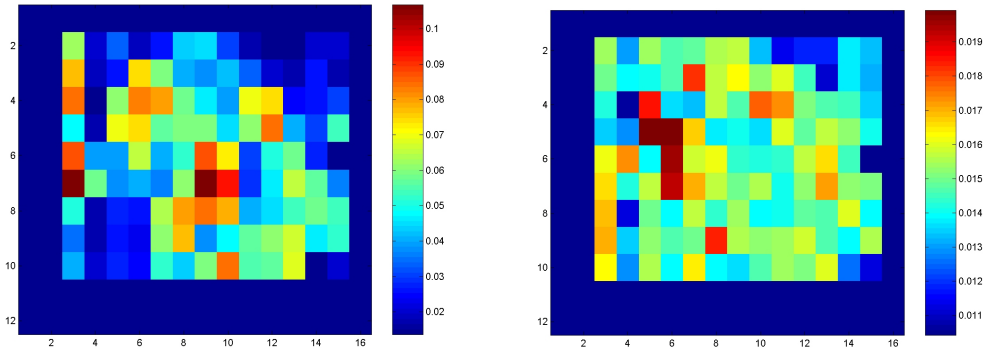

Figure 9: *Left panel*: Map with the mean values of the azimuthal reflectivity anisotropy at far offsets at the top of the reservoir. *Right panel*: Standard deviations associated with the mean reflectivity anisotropy.

4) Quantitative integration of the prior geological information with seismic data using rock physics.

Next we derive the prior joint PDF, $\rho(\mathbf{m}, \mathbf{d})$, for the fracture parameters and the data at each grid point, assuming that the prior geological information about the fracture parameters and the actual seismic data are statistically independent.

Finally, we quantitatively integrate the prior geological information and seismic data using the theoretical PDF, given by the rock physics theories. At each location we derive the *posterior* PDF, $\sigma(\mathbf{m}, \mathbf{d})$, over the fracture parameters and data by multiplying the prior joint PDF on the fracture parameters and the seismic data, which contains the information from geology and seismic, with the theoretical PDF, which represents the rock physics information. Then we integrate the *a posteriori* PDF, $\sigma(\mathbf{m}, \mathbf{d})$, over the seismic attributes space to obtain the updated distribution of fracture parameters, $\sigma_M(\mathbf{m})$. This posterior PDF, $\sigma_M(\mathbf{m})$,. represents the updated measure of uncertainty about the fracture parameters after integrating the prior geological information with the seismic data using rock physics theories.

From this *a posteriori* PDF of the fracture parameters, we can derive any statistical information, such as posterior expected values. More importantly, we can compute the probability that a certain model will satisfy any criteria, for example, the probability that the fracture density exceeds certain thresholds. These probability maps help us assess the uncertainty in our predictions, and therefore they can help us in making informed decisions regarding the reservoir management.

For example, Figure 10 shows a map with the spatial distribution of the posterior expected values for fracture density at the top of the reservoir, conditioned on the azimuthal anisotropy of reflectivity at far offsets.

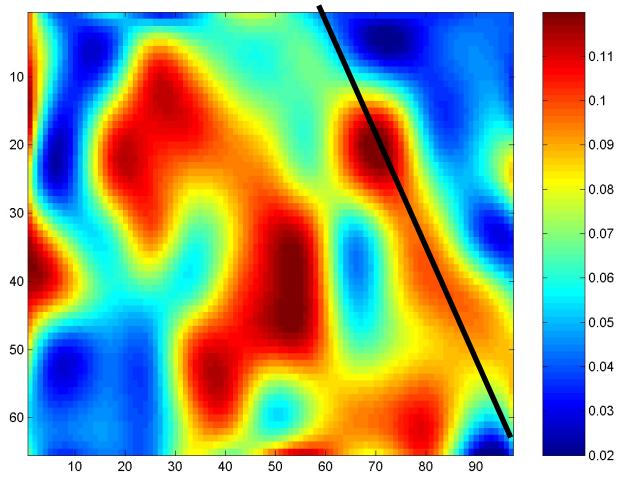

Figure 10: Map of the expected values for crack density derived from the *a posteriori* distribution, obtained by constraining the *a priori* geological information with the azimuthal anisotropy of reflectivity at far offsets, in the hypothesis of a vertical set of aligned fractures.

We observe a relatively higher fracture density in the proximity of the fault, sketched in Figure 10, which penetrates the carbonate reservoir, as the prior geological information also suggests. We can also observe the asymmetric distribution of the expected crack density with respect to the fault, with higher values of fracture density in the hanging wall. This result is in agreement with outcrop observations that suggest higher fracture density in the proximity of the fault, especially in the hanging wall (Florez, 2003). However, we also highlighted other zones of higher fracture density away from the fault. These zones may also correspond to possible subseismic faults.

Figure 11 presents on the left panel a probability map of fracture density exceeding a value of 0.09, which represents a relatively large degree of fracturing. We can observe the zones of higher probability of fracture density exceeding 0.09, which are the areas of interest for drilling new wells, since the fracture permeability may be controlling the reservoir production. Figure 11 presents on the right panel a probability map of fracture density being smaller than 0.04. According to Crampin (1994), rocks with fracture density smaller than this value behave almost like an intact mass of rock. Therefore, using these probability maps we can assess the risk of drilling a well in a zone a small fracture density.

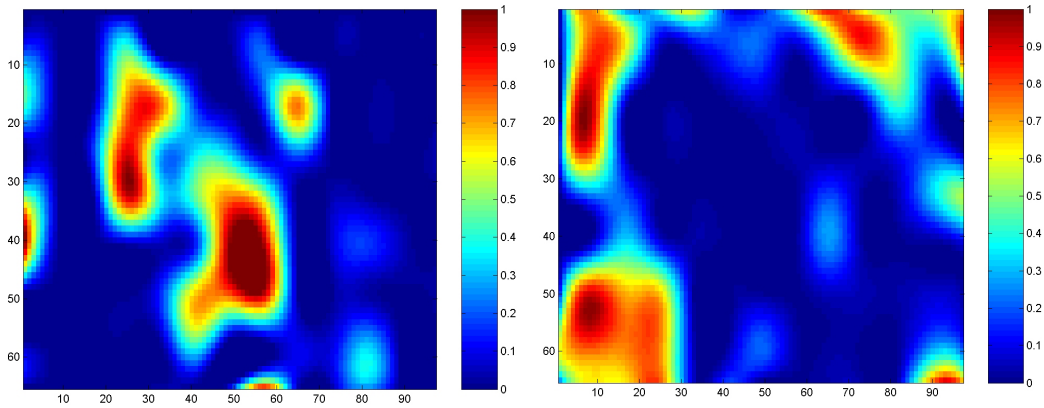

Figure 11: *Left panel*: Probability map for fracture density exceeding a value of 0.09, obtained by conditioning the prior geological distribution on the azimuthal reflectivity anisotropy at far offsets. *Right panel* . Probability map for fracture density being smaller than a value of 0.04, obtained by conditioning the prior geological information on the azimuthal reflectivity anisotropy at far offsets.

These probability maps serve as decision-making guideline for reservoir management, after we quantitatively integrate the geological, the seismic and the theoretical rock physics information.

3D Seismic data and AVAZ for fracture characterization.

In ATTACHMENT G, we focus on the analysis of the amplitude variation with offset and azimuth from a 3D seismic data set acquired over a fractured carbonate reservoir in eastern Texas, for determining the fracture orientations and the azimuthal anisotropy in reflectivity at the top of the reservoir, which is related to the intensity of fracturing.

In the first part of the Attachment, we show the impact of the 3D seismic acquisition footprint on analyzing the variation of the reflectivity with both offset and azimuth. The acquisition footprint of this survey affects significantly the seismic amplitudes, as we observe on the reflectivity time slices. The fold is not uniform, and it creates artificial stripes of low and high reflectivity that can mask the actual signatures of fractures.

Azimuthal analysis of the *PP* reflectivity involves partial stacking of the data on different ranges of azimuth. There is a tradeoff between the azimuthal resolution, which requires small ranges of azimuth, and the signal-to-noise ratio that requires larger fold, and implicitly larger azimuthal bins. For a fixed azimuthal range we can increase the fold by increasing the bin size, at the expense of reducing the spatial resolution.

In this Attachment, we show how increasing the spatial bin size can diminish the strong acquisition footprint, while increasing the fold and implicitly the signal-to-noise

ratio at each superbin location. The azimuthal range for stacking the reflectivity is kept constant, equal to 20 degrees. Based on the analysis, we determine that for this 3D seismic survey, the superbin size should be at least 800 ft, at 20º azimuthal range, to make a reliable interpretation of the reflectivity variation with offset and azimuth.

Once we observe an azimuthal variation in the seismic amplitudes, the challenge is to interpret it in terms of fracture density, orientation, and fluid saturation. Rock physics fracture modeling enables us to link the observed seismic attributes to the actual parameters of fractures. Therefore, in the second part of this Attachment we present more modeling results of the amplitude variation with incidence angle and azimuth (AVAZ) for the fractured carbonate reservoir. The rock physics fracture modeling shows that the interpretation of the azimuthal variation of the *PP* reflectivity in terms of fracture orientation and relative degree of fracturing requires careful rock physics modeling and additional geological constraints. The polarity of the azimuthal variation of the reflectivity changes with both gas saturation and the compressibility of the cracks. Therefore, the fracture strike can be given by the azimuth corresponding to either a maximum or a minimum in the azimuthal variation of the reflectivity. This result that may be used to differentiate between gas-filled and brine-filled fractures, assuming that the azimuthal anisotropy is due only to the presence of a vertical set of joints whose orientation is determined from other sources of information. On the other hand, this fact introduces an additional ambiguity when we want to determine the fracture orientation from the AVAZ alone. If we do not have information about the fluid that saturates the fractures, in some situations we may not be able to determine the fracture strike.

Based on the rock physics analysis, we consider that the fracture strike at the top of the James Limestone reservoir is given by the minimum in the azimuthal variation of the reflectivity. This criterion corresponds to the cases for which either the fractures are highly compressible, independently of the type of fluids that saturate them, or the fractures are less compressible and partially saturated with 90% or less of gas, in a patchy manner. Under these hypotheses, we derive a map with the fracture orientation and the associated azimuthal anisotropy in the reflectivity at the top of the reservoir (Figure 12). Using a bootstrap method, we also estimate the uncertainty in the fracture orientation and the azimuthal anisotropy in the reflectivity due to measurement errors.

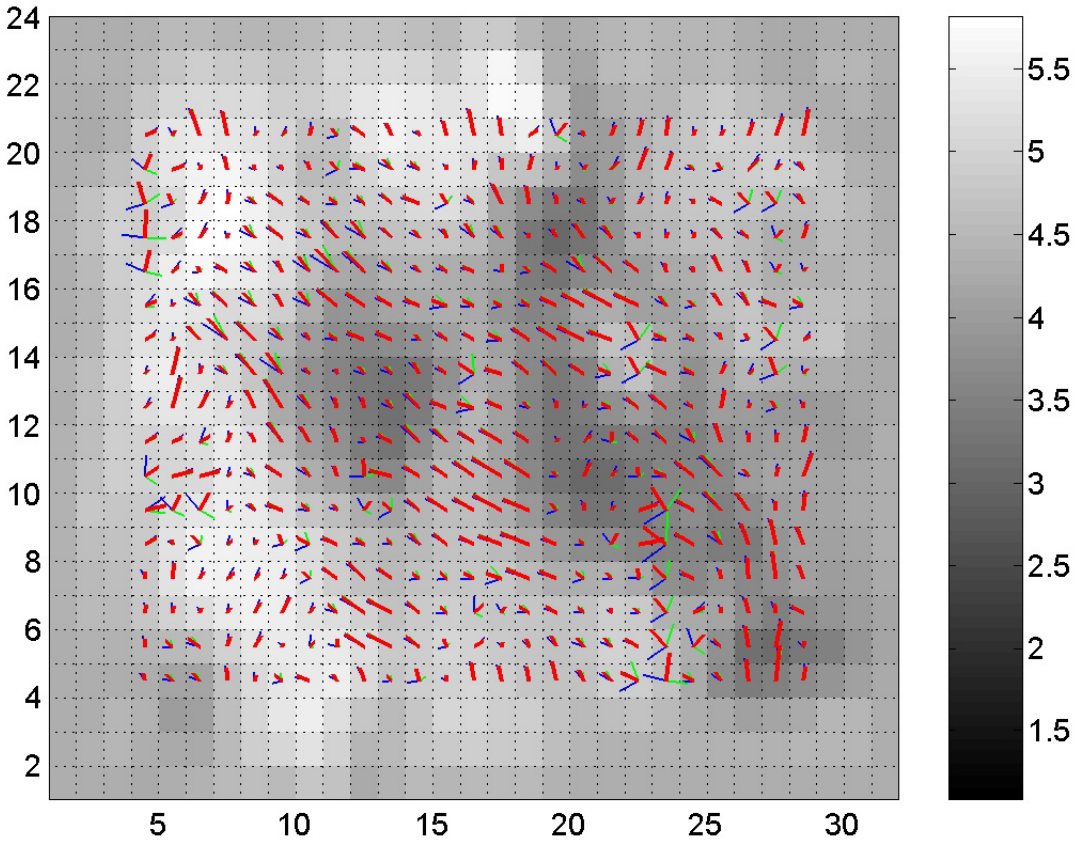

Figure 12: Fracture orientation at time slice of 1.3 seconds, corresponding to the top of James Limestone reservoir. The red segments represent the mean fracture strikes, while the blue and green segments represent the standard deviations from the mean orientation. The length of the red segments is proportional to the mean of the difference between the maximum and minimum amplitudes at each bin location (reflectivity anisotropy). The lengths of the blue and green segments give the standard deviations from this mean difference in the amplitudes. The fracture strikes are superimposed on the stack amplitude map for the same time slice. The superbin size is 800 ft.

We find excellent agreement between the mean fracture orientations derived from the azimuthal variation of the seismic amplitudes at far offsets and the fracture orientations derived from the FMI logs from a nearby well (Figure 13). There is also very good agreement between the mean fractures' strike from AVAZ and the present regional stress field. The mean fracture orientations are approximately parallel to the maximum horizontal stress in the region.

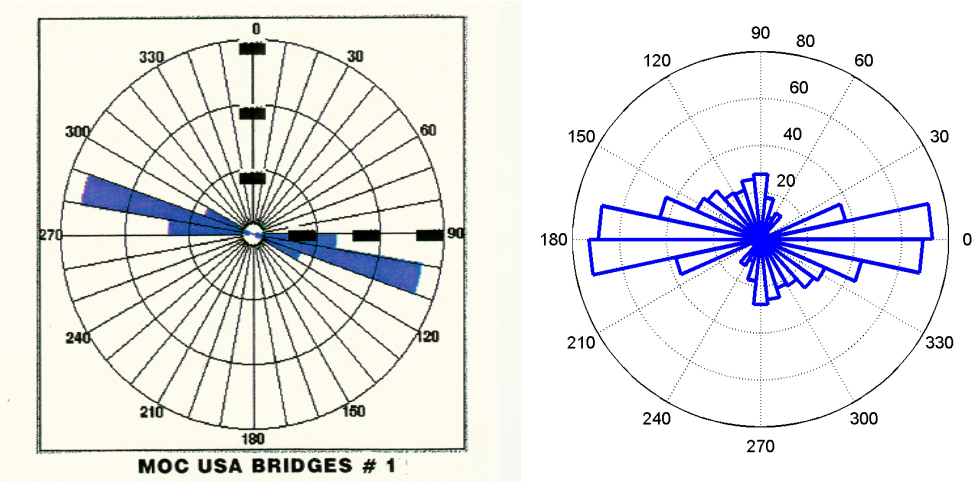

Figure 13: Comparison between the distributions of fracture strikes interpreted from a FMI log in James Limestone reservoir from a well in a nearby field (left) and the fracture strike interpreted from the azimuthal analysis of the seismic amplitudes at far offsets at the top of the James Limestone reservoir (right). Geographic North is the same for both rose diagrams. The observed fractures in the FMI log have dips of 89 degrees.

The distribution of the azimuthal anisotropy in the *PP* reflectivity at the top of the reservoir may be interpreted as a distribution of the relative degree of fracturing, assuming little variability in the fracture compressibility for the zone of interest, and uniform saturation for the fractures. We observe a relatively higher anisotropy in the proximity of an interpreted fault that penetrates the James Limestone reservoir. This may be due to higher fracture densities in the proximity of the interpreted fault. The anisotropy anomaly is slightly asymmetric, with higher values of the anisotropy in the hanging wall of the fault. This interpretation is in agreement with field observations, and with the geological model for the reservoir. However, we can also observe a zone of higher azimuthal anisotropy in the seismic amplitudes away from the fault. This zone may also correspond to larger fracture densities, perhaps associated with subseismic faults.

Fracture characterization from AVAZ requires careful rock physics modeling and additional geological and geomechanical information on fracture compressibility and fluids distribution. However, in the absence of such information, using multiple seismic attributes can also help reduce the uncertainty in the interpretation of fracture orientation and density. For example, using the azimuthal variation in the reflectivity together with

the seismic amplitude values either at the near- or far-offsets can better constrain the fracture distribution.

Analyses of Multi-Azimuth, Multi-Offset VSP Data

ATTACHMENT F summarizes our analysis of the VSP and interpretation of fracture-related anomalies, in terms of our rock physics models. Fracture modeling shows that the amplitude of the PP reflected wave from a fractured zone is lower than the amplitude of the PP reflected wave from an unfractured zone. We compare the position of the faults interpreted from the lateral boreholes and the positions of the faults interpreted on the VSP along the well trajectory. This comparison shows that there is a good agreement between the faults that are considered as very likely from the well information and the strong anomalies in the VSP. However, there are also cases where we do not see agreement between the borehole and VSP interpretations. In particular, the smaller faults interpreted from the borehole data do not generate amplitude anomalies. Other effects, like AVO effect caused by different angles of incidence along the well path are also superimposed on the VSP section. This comparison confirms that indeed fracture swarms associated with small-scale faults can generate an amplitude anomaly, but also shows that caution must be taken when interpreting every single amplitude anomaly as a fracture swarm.

Combining the seismic attribute analysis of VSP data and the geologic interpretation of LWD logs we have mapped the location of small faults along the path of Henderson-1 well. Amplitude anomalies, enhanced using zero-offset amplitude, and small offsets visualized using instantaneous phase, coincide with fault locations interpreted from drilling breaks, changes in calcite concentration and abrupt changes in gamma ray. These two independent sources of information provide the basis for a consistent interpretation of the VSP data.

PRACTICAL RECOMMENDATIONS

Introduction

In this section we summarize practical workflows and recommendations. As mentioned earlier, most published methods for seismic fracture detection focus heavily

on searching for evidence of seismic anisotropy, as might result from a single set of aligned fractures. Common among these are seismic shear wave splitting, azimuthal variation of P-wave AVO, and azimuthal variation in P-wave normal moveout (NMO) velocity. In this project, we also exploited azimuthal variation in amplitude as one of several controls on fracture intensity characteristics.

Pitfall: While seismic anisotropy can be a powerful fracture diagnostic, a number of situations can lessen its usefulness or introduce interpretation ambiguities. These include (a) multiple fracture sets at different orientations that combine to lessen the anisotropy, (b) the presence of nonfracture rock anisotropy as might occur with large differences in horizontal principal stresses, (c) fracture occurrence in narrow bands or swarms that are not sampled well by azimuthal methods, and (d) seismic acquisition geometries that provide limited azimuthal coverage – actually quite typical in spite of the name "3D seismic."

Solution: Laboratory, theoretical, and field studies indicate that a much broader spectrum of fracture seismic signatures can occur. Interpretation risk can be reduced by pursuing an integrated approach, exploiting as many sources of information as possible, and using the principles of rock physics as the link among seismic, geologic, and log data.

Workflow

The workflow that we developed and recommend consists of the following steps, which we have described in detail in the previous sections. The workflow is also illustrated schematically in Figure 5.

1) Establish and quantify prior information about fracture parameters.

Evaluate the possible geological hypotheses for the fracture distribution, based on the site-specific outcrop observations, if available, or outcrop analogs, as well as on the well-log information. Consider also the geological structure of the reservoir, which can be

obtained from the interpretation of seismic data. Parameters controlling fracture occurrence include: bed thickness, bed curvature, distance from the faults, local tectonic stresses, etc. The end results of this step are potentially a map of candidate fracture locations expressed as a PDF, and a list of likely fracture scenarios to evaluate. For example: Which intervals might be fractured? What is the local relation between lithofacies and fracture occurrence? How many fracture sets might exist? What pore fluids should be considered?

As we have been discussing, faults and fractures can have a range of seismic signatures. However, seismic can never resolve individual fractures and many of their geometric details. Hence, we believe it is critical to have a geologically sound model for the subresolution details of the fracture zones that we can use as inputs to our rock physics models. We have adopted the bowtie model, discussed in ATTACHMENT B, for fault and fracture occurrence in the James Lime play. It is also extremely valuable to FMI data in nearby wells, as a means to understand the fine-scale fracture patterns.

Examples of establishing the prior information are presented in ATTACHMENTS A, B, C, and D.

Pitfall: In some locations, outcrops and well control might be sparse or nonexistent.

Solution: Although site-specific information is most valuable, there are still constraints that can be applied when developing the prior model. These include: 1) estimates of stress, from local tectonic models, measurements from nearest wells, and from published stress maps, 2) structural controls, such as curvature, faulting, folding, determined from seismic, 3) estimates of facies types and bed thicknesses estimated from local depositional models and seismic sequence stratigraphy, 4) global observations of fracture density vs. depth, as discussed in ATTACHMENT D. A key advantage of our recommended probabilistic approach is that the prior fracture probabilities objectively express our state of knowledge. Weak constraints are still included and are quantified by a broad fracture probability.

2) Rock-physics modeling and stochastic simulations: Theoretical PDF

Next, perform rock-physics forward modeling and stochastic simulations based on the well-log data available, under the chosen geological hypotheses. The goals of this step are to identify the most informative seismic attributes for the site, and to predict the seismic signatures of fractured vs. unfractured rock, as well as of various pore fluids. Rock physics modeling via *Monte Carlo* simulations yield many realizations of sets of fracture parameters and seismic attributes that span the intrinsic natural variability. These variabilities include properties of the background unfractured rock and fracture parameters. The resulting "cloud" of realizations yields estimates of the theoretical joint PDF $\Theta(\mathbf{m}, \mathbf{d})$, which describes the physical relations between the fracture parameters (e.g. fracture density) and the seismic attributes. The theoretical joint PDF is site specific.

Pitfall: It is dangerous to apply the same interpretation rule to all locations where fractures are sought. For example, not all fractured reservoirs will be anisotropic; at some locations fractured zones will be seismic dim spots, and at others, bright spots; when fracture anisotropy is present, the relation between seismic amplitude and fracture direction is not always the same. Furthermore, serious nonuniqueness might occur. For example, a gas-filled fractured reservoir might look seismically similar to a water-filled fractured cap rock.

Solution: Interpretation risk can be reduced by following a comprehensive program of rock physics forward modeling of the geologically realistic fracture scenarios. The modeling allows us to explore the seismic signatures of the fracture distributions that are possible and likely at the site. We view this step as a natural extension of convention quantitative geophysical analysis for nonfractured targets. In those cases, it is accepted practice to compute synthetic seismic from well logs, and then explore how variations in rock and fluid properties will appear seismically. Very importantly, the results depend on the local geology, as well as seismic wavelet and acquisition parameters. The end results are physical insights into fracture signatures, and PDFs expressing the theoretical relations (with uncertainty) between the target fracture parameters and the data.

3) Analysis of seismic data and attribute extraction

Analyze field seismic data to ensure optimum processing, identify potential artifacts (such as acquisition footprint and non-uniform azimuthal coverage), and extract attributes that will be useful for the fracture interpretation, based on the rock physics modeling.

This step shares many of the processing and quality control steps that must be applied in any seismic work. Since many of the valuable attributes, whether isotropic or not, depend on amplitude, it is critical to apply state-of-the-art amplitude-preserving processing. For the cases of complicated geological structures, with steep dips, or for the cases where there are significant lateral velocity heterogeneities, the seismic amplitudes are less reliable. However, for the James Limestone reservoir, the geological structure is relatively flat, and the seismic amplitudes can be used to get information about the fracture distribution.

Azimuthal variations in seismic amplitudes are often handled by sorting the prestack data in azimuth bins, and then applying conventional processing to each bin.

Pitfall: Acquisition footprint and non-uniform azimuthal coverage can result in spatial and azimuthal variations in the seismic amplitudes that are entirely related to the geometric patterns of source and receivers, and not to geologic features of interest.

Solution: Design better acquisition surveys to provide a more uniform spatial and azimuthal coverage, or compensate these short-comes during processing, by using larger spatial bins and by normalizing the azimuthal stacks with the fold.

After processing, we extract attributes that the rock physics modeling predicts will be indicators of fractures: amplitudes, AVO, impedances, and azimuthal variations in all of these. As illustrated in ATTACHMENT G, we estimate the uncertainty of these attributes and fold them into PDFs.

4) Quantitative integration of the prior geological information with seismic data using rock physics.

Finally, we quantitatively integrate the prior geological information and seismic data using the theoretical PDF, given by the rock physics theories. At each location we derive

the *posterior* PDF, $\sigma(\mathbf{m}, \mathbf{d})$, over the fracture parameters and data by multiplying the prior joint PDF on the fracture parameters and the seismic data, which contains the information from geology and seismic, with the theoretical PDF, which represents the rock physics information.

Pitfall: The theoretical PDF, which gives the uncertainty in the physical correlations between the fracture parameters and the seismic attributes due to natural variability of the background rock properties, is considered stationary and representative over the area of study. This uncertainty is derived from the well-log data, and if the reservoir is not very well sampled with well-logs, we may underestimate the uncertainty due to geological variations of the target rock properties.

Solution: The methodology for quantitative data integration allows us to estimate the impact of larger uncertainty in the theoretical PDF on the final results for fracture parameters distribution. Therefore, we can play different "what if scenarios" and evaluate the impact of each of them on the posterior distribution for fracture parameters.

Then we integrate the *a posteriori* PDF, $\sigma(\mathbf{m}, \mathbf{d})$, over the seismic attributes space to obtain the updated distribution of fracture parameters, $\sigma_M(\mathbf{m})$. This posterior PDF, $\sigma_M(\mathbf{m})$,. represents the updated measure of uncertainty about the fracture parameters after integrating the prior geological information with the seismic data using rock physics theories.

From this *a posteriori* PDF of the fracture parameters, we can derive any statistical information, such as posterior expected values. More importantly, we can compute the probability that a certain model will satisfy any criteria, for example, the probability that the fracture density exceeds certain thresholds. These probability maps help us assess the uncertainty in our predictions, and therefore they can help us in making informed decisions regarding the reservoir management.

Attachment A

Geologic Model of Fracture Occurrence in the James Lime Field

Abstract

This chapter presents the basis for building a model for fault and fracture distribution at the Neuville field, where the VSP and 3-D seismic are located. In general, the concepts outlined here can be used for characterization of fractured reservoirs in East Texas. Lack of reservoir exposures prevents a direct outcrop analogue study. Nevertheless, we develop a conceptual model based on mechanical stratigraphy, tectonic evolution, pre-existing faults and loading conditions, since we consider they are the main factors controlling the mechanism of fracturing. In this particular case, the interposition of brittle and ductile layers at different scales, and the development of the Sabine uplift at the Texas-Louisiana border during the Cretaceous, are two factors with definite impact in the development and orientation of conjugate normal faults in the Cretaceous section.

The Mesozoic sequence of the Gulf of Mexico is characterized by the interposition of ductile and brittle layers at different scales. Similarly, the James Limestone is characterized by the interposition of meter-scale layers of limestone and calcareous shale. Joints and small fractures within the limestone do not propagate within the shale. In the same way as salt layers have played a significant role in the development of conjugate and listric normal faults in the Gulf of Mexico, shale intervals above, below and within the James Lime may constitute gliding planes for shearing and local faulting. Conjugate normal faulting is considered as the main deformation mechanism within James Limestone. Conjugate normal faults form narrow zones with high fracture density.

Fracture swarms or clusters are therefore associated to subseismic faults, or faults that cannot be detected with conventional seismic methods. Between these fracture swarms, the background fracture density may correspond to regularly spaced joints. The horizontal lateral sections of the Henderson-1 well confirm the presence of subseismic faults and fracture swarms within James Limestone.

Even though the model constrains the range of possible scenarios, there are still significant uncertainties regarding critical parameters like orientation and frequency of subseismic faults. We evaluate the different possibilities based on our current understanding of the region. Specifically, the probable impact of a large fault located just 2 km east of Henderson-1 has been evaluated using Poly3D, a boundary element method (Thomas, 1993). The results indicate that this fault does not affect significantly the orientation of subseismic faults at the well site under normal-fault loading conditions, but 3D seismic data is required to define more accurately the fault configuration.

Since the current results indicate that orientation of subseismic faults depends exclusively on loading conditions, three different possible orientations of a normal-fault state of stress are considered: (1) parallel to the Cretaceous depositional slope; (2) parallel to the current depositional slope; and (3) approximately normal to the fault affecting the James Limestone. The mechanic models confirm the expected fracture orientation and do not allow ruling out any of the possibilities.

Regarding fault spacing, we apply a systematic method for detection of subseismic faults in the horizontal sections of Henderson-1, using the gamma ray log as fault indicator. Six faults have been identified in the upper wellbore and just two in the lower. Since gamma ray detects basically lithology, it cannot be used to identify faults with very small offset. The use of other parameters sensible to rock fragmentation, like drilling rate, may be helpful to identify damage zones associated to incipient faults, but this requires calibration and further analysis.

Introduction

The James Limestone has been an exploration target for the onshore Gulf of Mexico since the discovery of the Fairway field in the East Texas basin in 1960 (Loucks et al,

1996). Traditionally it has been recognized as a series of sandstones, shale, and sandy, oolitic, coquinoid and dense limestone that occur above the Pine Island Formation and below the Rodessa Formation in the subsurface of Lower Cretaceous of South Arkansas, North Louisiana and East Texas (Crawford, 1951). In the study area (Fig. 1) the formation is characterized as a low-porosity microcrystalline fractured limestone, with porosities ranging from 3 to 15% and permeabilities between 0.001 to 0.1 md. Economic production from vertical wells is limited to areas where the carbonate facies exhibit high porosity and permeability (reefal limestone at Fairway field) or where the accumulation is large (Trawick field), but currently the formation is exploited by multiple-stacked horizontal wells, with horizontal sections in excess of 6000', which cut multiple fracture swarms probably associated to subseismic normal faults.

In general, characterization of fracture systems requires the determination of fracture types, orientation, time relationships, spatial distribution, average dimensions, average aperture, connectivity and hydraulic properties. Regarding faults, maximum offset and slip distribution are critical parameters that can be linked to thickness of gouge and fragmentation zones. Most of these parameters are difficult to determine, but 3D reflection seismology has provided a significant improvement in 3D fault imaging and slip distribution analysis (i.e. Gutierrez and Nur, 2001; Maerten and Pollard, 2001). Similarly, horizontal wells are giving the opportunity to estimate fracture densities along lateral sections, and showing the importance of small-scale faults in fracture distribution (i.e. Krystinik, 2000; Lloyd et al, 2000).

Fractures require heterogeneous stress concentrations to form and propagate. These concentrations can develop from material heterogeneities due to flaws, impurities or just due to the original rock fabric. Probably the most common sources of heterogeneous stress fields are due to geological structures induced by previous deformations at all scales (Pollard and Aydin, 1988). In this case, we think the depositional slope plays a key role in the orientation of faults since it determines the orientation of ductile horizons, which act as gliding planes that may create normal faults and the tips.

Slip along faults may alter significantly the stress field around the faults (i.e. Andersson, 1951; Pollard and Segall, 1987). The fault-related stress perturbation can be

significant within a region of about 2 times the fault dimension parallel to the slip direction (Segall et al, 1980). In that regard, we needed to evaluate the impact of the known fault configuration may have on the distribution of the orientation of smaller (subseismic) faults, given certain loading and boundary conditions. This approach resembles to some extent the methodology presented by Maerten *et al* (2000) for prediction of subseismic faults. For this purpose we use Poly3D, a boundary element method (Thomas, 1993).

Local stratigraphy plays a significant role in the mechanics of deformation. Fracture density due to flexure and curvature depends on the thickness of the brittle layer (i.e. Maerten and Maerten, 2001); joints can hardly cut across shale layers (Helgelson and Aydin, 1991) and ductile layers play an important role in fault evolution and fault architecture (i.e., Aydin & Koledoye, 2001). A strong relationship between fracture density and lithology of different carbonates was found within the Lisburne Group carbonates, in Alaska (Lorenz et al, 1997). Our study of Yates field illustrated also how facies can control fracture density (Sava et al, 2001). A conclusion derived from these results is that any study of structural deformation in sedimentary rocks should start by understanding the stratigraphy of the units deformed. This basically means that one needs to understand the rheology of the rocks deformed and the impact that the spatial distribution of each one of these lithofacies may have on the rock mechanical properties at different scales.

The lack of outcrops of James Limestone prevents a comprehensive characterization of the unit and its fracturing style. The structural model is based on well logs, seismic sections and structural sections provided by Marathon. Comparisons with analogue cases of sedimentary sequences with normal faults are based on two criteria: (1) the fact that the unit is composed of the interposition of ductile and brittle rocks; (2) the fact that the region is within a normal-fault stress regime and the orientation of these faults seems to have been controlled by the depositional slopes. We apply concepts developed from field observations and basic mechanical models to constrain the probable fault and fracture orientation within the James Limestone. Observations of small-scale faults at outcrops indicate that even faults with offsets smaller than 5 m can create significant high-density

fracture zones. These fragmentation zones may have a significant impact on acoustic and elastic impedance, seismic velocity and permeability anisotropy.

The chapter is divided in four main sections. The first three sections deal with the general geologic background of the area, the tectonic evolution of east Texas and the stratigraphy of both the whole section above James and the James Lime itself. The last section addresses the key points about characterization of the fracture systems at Neuville field: fracture types, orientation and spatial distribution.

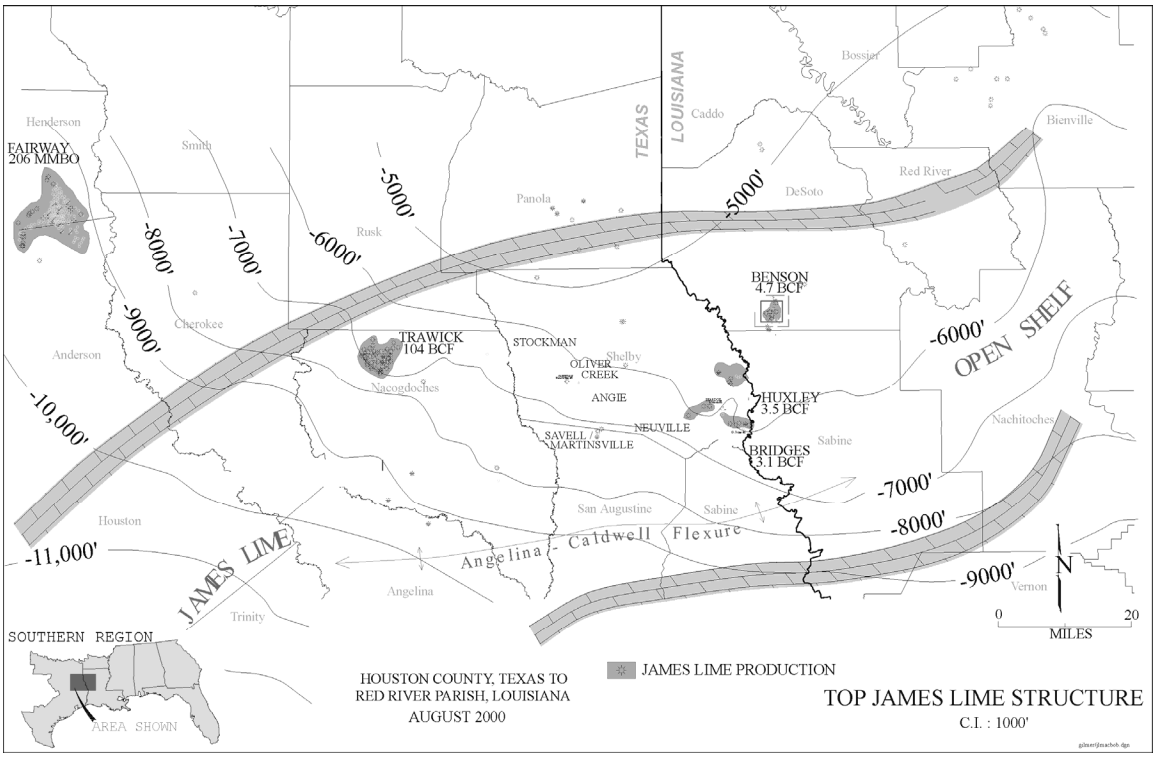

Figure 1. Location of James Lime study area, with the major oil and gas fields and the structural contours on top of the formation. The region of interest is at the Neuville, near the Texas-Louisiana border, (Courtesy of Marathon).

General Tectonic Setting

The area of interest is part of the northwestern inland border of the Gulf of Mexico (see inset Fig. 1). It is just west of the Mississippi River and involves counties in both Texas and Louisiana. The VSP survey was performed at Henderson-1, a well located

within the Neuville field, near the Texas-Louisiana border. However, we are going to also discuss information coming from other wells like Mccoy-1, within Louisiana, and Bridges, south of Henderson-1.

Geology of east and southeast Texas is characterized by Tertiary sediments gently dipping towards the Gulf of Mexico border and affected by localized normal faults (i.e. Renfro et al, 1984; Ewing, 1991). This area is basically under a normal-fault state of stress (Zoback and Zoback, 1980), where major normal faults occur oriented closely parallel to depositional strike of the basin (Fig.2). A relatively simple model can explain the development of normal faults as the result of basal shear or gliding along ductile (salt or shale) units, parallel to the depositional or structural dip (Fig.3). This model is implicit in the different regional cross sections of southern Texas and western Louisiana (i.e. Diegel et al, 1995; Peel et al, 1995) and is also implicit in the fault-initiation mechanism required for the glide systems and deep listric fault systems proposed by Ewing (1991).

The underlying Cretaceous rocks are marine sediments composed mainly of shale, limestones and sandstones. These rocks are also affected by normal faults, most of them detaching from the Louann Salt, a middle-Jurassic salt horizon that plays a very important role in the tectonics of the Gulf of Mexico. As shown by various authors (Diegel et al, 1995; Peel et al, 1995; Ewing, 1991) there are different detachment horizons (Fig. 3). In the Neuville region, the depositional slope during the Cretaceous was controlled by the Sigsbee uplift and the Triassic rift, therefore it was different than the current and depositional slope. Consequently, the structural trends and domains observed at surface within the Tertiary cannot be extrapolated directly to the Cretaceous at subsurface, without an analysis of the probable variations with depth.

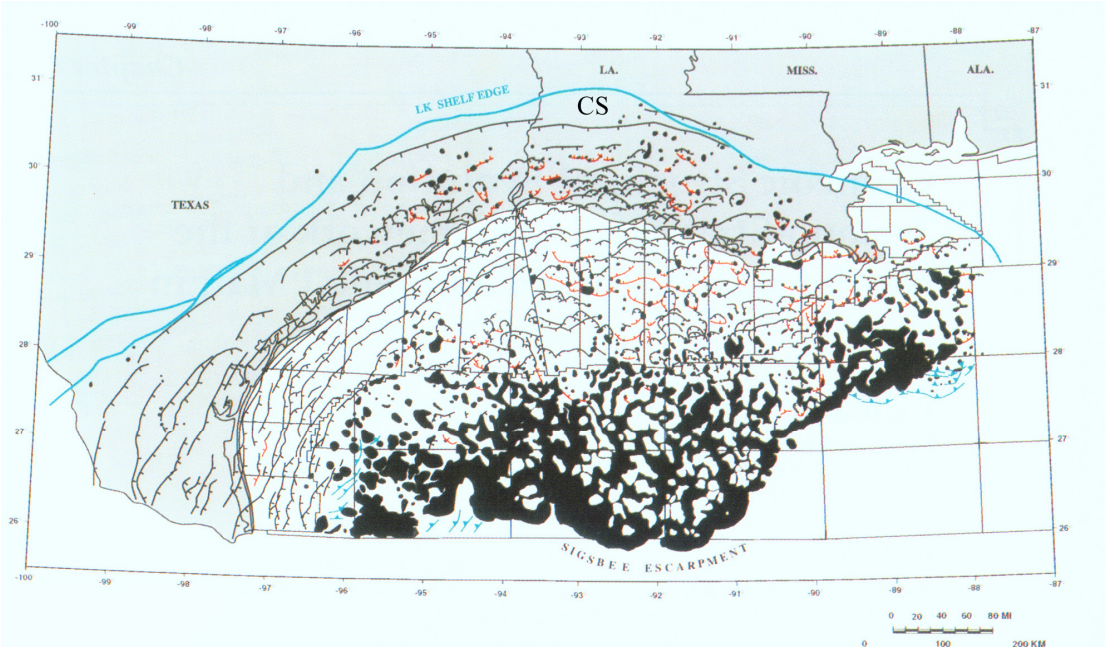

Figure 2. Regional tectonic map of the Gulf of Mexico Basin, showing the location of major normal faults (black lines with ticks), antithetic or conjugate normal faults (red lines), and salt domes (black patches). CS = approximate location of cross section of Fig. 3. After Diegel *et al* (1995).

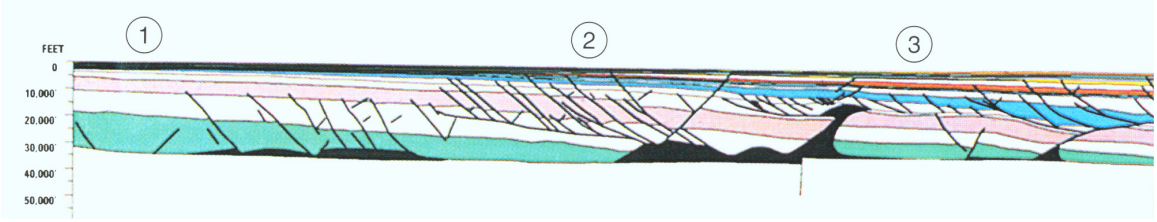

Figure 3. Cross-section at western Louisiana (see Fig. 2), sub parallel to the Texas-Louisiana border. Black = Louann Salt; Green = Upper Jurassic; White = Lower Cretaceous; Pink = Upper Cretaceous. After Diegel *et al* (1995). No vertical exaggeration.

Stratigraphy

Table1 summarizes the stratigraphy of East Texas around Neuville. There are lateral thickness variations, especially along the depositional dip. Here we present thickness reported west of the study area and at the Sabine uplift in Louisiana (Ver Wiebe, 1949). There are two main unconformities in the region, one at the Cretaceous-Tertiary boundary and other at the boundary between the Lower and the Upper Cretaceous. The Tertiary section is mostly composed of sandstone and shale, but with some shale and marl interposition at the base (Midway Formation). The Cretaceous section is

characterized by the interposition of limestone and shale, but becomes sandier towards the northwest. The Ferry Lake anhydrite seems to be an important stratigraphic marker in the Lower Cretaceous across the basin.

Table 1 . Stratigraphy of East Texas and West Louisiana, after Ver Wiebe (1949).

Series or Stage	**Name**	**Thickness (feet)**	**General Description**
EOCENE	CLAIRBONE GP	2100-1500	Interposition of sandstone, shale and glauconitic sandstones
EOCENE	Wilcox	700-800	Sandstone and shale
PALEOCENE	Midway	700-500	Shale and marls
		Unconformity	At Tyler Basin
UPPER CRETACEOUS	Navarro	400-525	Shale, marl and chalk
	Taylor	550-900	Chalk and shale, basal sandstone
	Austin	200	Mostly chalk and shale
	WOODBINE GP		
Turonian?	Eagle Ford	50-200	Mostly shale
Cenomanian	Lewisville	100-200	Sandstone, shale and redbuds
	Dester or Euless	350-150	Mostly sandstone
		Unconformity	At Sabine Uplift
LOWER CRETACEOUS	WASHITA GP		Shale, limestone and claystone
Albian	Fredericksburg		Shale, limestone and claystone
	TRINITY GP	Include Glen Rose, Hoston Gps.	
	Paluxy	1000	Shale and sandstone
	GLEN ROSE GP		
	Mooringsport	800	Mostly shale
	Ferry Lake	250	Anhydrite, regional marker
Aptian	Rodessa	200	Limestone and shale (Bexar shale at the base)
	James	50-400	Mostly limestone
	Pine Island	300	Mostly shale
	Sligo	100	Limestone
	HOSTON GP	900	Mostly shale, some sandstone

Stratigraphy of James Limestone

The "James Limestone" is a lithostratigraphic concept established from wellbore descriptions at Arkansas, Louisiana and east Texas. The unit is not present at surface exposures, since the Lower Cretaceous cropping out further northwest presents different lithologies, basically facies related to more continental depositional settings. In spite of being a lithostratigraphic concept, the lithology of the unit varies from calcareous sand, at the northwest, to microcrystalline and argillaceous limestone at the southeast. The James Limestone is part of the Lower Cretaceous Trinity Group; it underlies the Bexar Shale and overlies the Pine Island Formation. Here we describe the lithology at the type locality (Crawford, 1951) as well as more modern descriptions from other localities. In addition to this, we present a brief analysis of the lithologic sequence at McCoy-1, a well near to Henderson - 1.

Type Locality

The Arkansas Fuel Company's No.1 well, drilled in 1925 and located in the section 14- Twp, 20 N-Rge, 1E, Union Parish, Louisiana, has been designated as the type locality of the James limestone (Crawforth, 1951). The cores, between 3820' to 3915', revealed the presence of a distinct stratigraphic unit composed primarily of gray, medium-grained, calcareous, porous sandstone.

Lithofacies

According to Crawforth (1951), in the surroundings of the type locality the James Limestone is composed of brown to gray, porous to non-porous calcareous sand. Westward, the sandstone grades into oolitic limestones that are locally coquinoid. All the limestones in this area are arenaceous to some extent. Across southern Arkansas, the James limestone is predominantly tan, saccharoidal, sandy and chalky. In the eastern part of the area, the formation is made up almost wholly of sandstone. Reddish-brown and gray shale are interbedded with the limestone throughout most of southwestern Arkansas. Down-dip, in the northwest Louisiana-East Texas area, the James sediments are typically shale and shaly limestone. Oolitic and coquinoid limestone occurs only in a few local

areas. Whereas the limestone is typically arenaceous in the area to the north and east, in east Texas it is proportionally argillaceous. Poorly preserved foraminifera and ostracoda are present in a few of the limestone and shale beds. Although ammonites have been recovered from the Pine Island Formation, immediately below the James, no ammonites have been reported from the James itself.

Loucks *et al* (1996) describe the James Lime in Louisiana as a Lower Cretaceous formation that forms part of the Glen Rose Subgroup, equivalent to the James Lime in east Texas and the Cow Creek Limestone in south Texas. The unit is predominantly terrigenous siliciclastics in the northeastern, updip portions of the Mississippi Salt basin and grades into a carbonate facies in the southwestern, seaward part of the basin, where open marine conditions prevailed. They consider the James Lime as a shoal-water complex that developed on a shallow-water shelf with variable conditions of low to high-energy waves and currents. They divide the unit into 8 lithofacies (Table 2) deposited within one third-order depositional sequence but arranged into three parasequences. The high-porosity lithofacies (4 to 6) seems to be restricted to syndepositional paleo-highs, whereas the other muddy lithofacies (2, 3, 7 and 8) are more widely distributed. The depositional settings vary from deep water, low-energy, open-marine shelf environments, to shallower, higher-energy bottoms (lithofacies 4 to 6). According to that study, the distribution of the facies was controlled by paleostructures associated with underlying salt domes.

In the study area, James Limestone is characterized as a low-porosity microcrystalline fractured limestone. Porosity ranges from 3 to 15% and permeability varies between 0.001 to 0.1 md. The limestone layers alternate with carbonate-rich shale intervals that do not have fractures. Total thickness of the unit is about 400 feet, but net thickness of carbonate facies ranges from 295’ (east) to 135’ (west). The main facies are fossiliferous wackestone and mudstone deposited in an open shelf environment. The facies present two main types of porosity, intercrystalline and vugular. Better reservoir properties are expected at paleo-structural highs not only because they imply a shallower depositional environment, but also because increased diagenetic effects have been found on those highs.

In McCoy-1, the formation is composed of the interposition of limestone and shale, as indicated by the GR and the Vp/Vs ratios (Fig. 4). The well log s (FMI, GR and velocity logs) shows that limestone and lime-rich shale alternate in layers about 1.3 m thick, forming single parasequences. A comparison of the vertical fracture frequency in well McCoy-1, against the well log response (Fig. 5), illustrates how the background fractures are confined to the limestone intervals indicated by the low GR. This comparison shows that shale-rich intervals act as fracture barriers and are more ductile than limestone layers. The contrast in ductility is an important factor in the evolution of faults and fractures in sedimentary sequences.

Table 2. Main lithofacies of the James Limestone at east Louisiana, Mississipi Salt Basin (Loucks et al, 1996), east of Marathon's James play area.

Lithofacies	**Description**	**Distribution**	**Mean ϕ**	**σ**	**Mean K**	**σ**
8	Burrowed Wackestone	Regional	1.92	0.43	0.005	.016
7	Wackestone to Grainstone	Regional (Wackestone)	2.92	2.75	0.257	.831
6	Packstone and Boundstone	Paleo-highs	6.25	3.59	0.150	0.388
5	Stromatolite Bindstone	Paleo-highs	2.81	0.72	0.042	0.116
4	Packstone to Grainstone	Paleo-highs	7.13	3.21	0.181	0.444
3	Borrowed Wackestone	Regional	2.94	0.71	0.001	0.000
2	Tight Lime Packstone	Regional	-	-	-	-
1	Argillaceous Wackestone	Regional	-	-	-	-

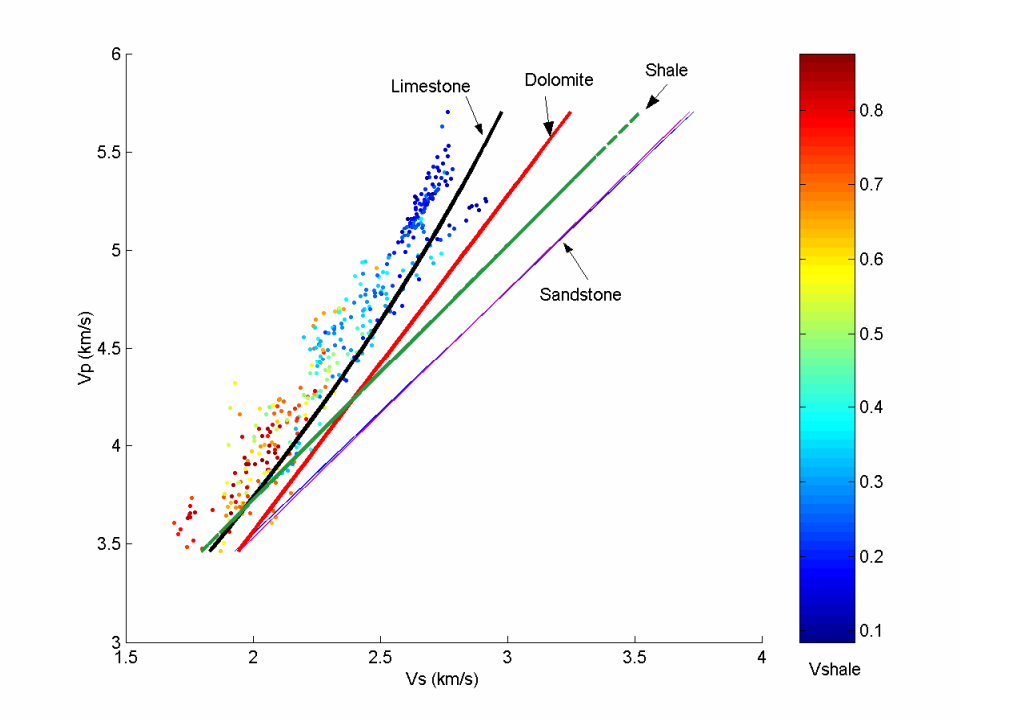

Figure 4. Scatter plot of Vp and Vs for the interval 5750'-6150' at well Mccoy-1, corresponding to James Limestone. Rocks with low Vshale correspond to pure limestones, whereas rocks with high Vshale seem to be a mixture of shale and limestone.

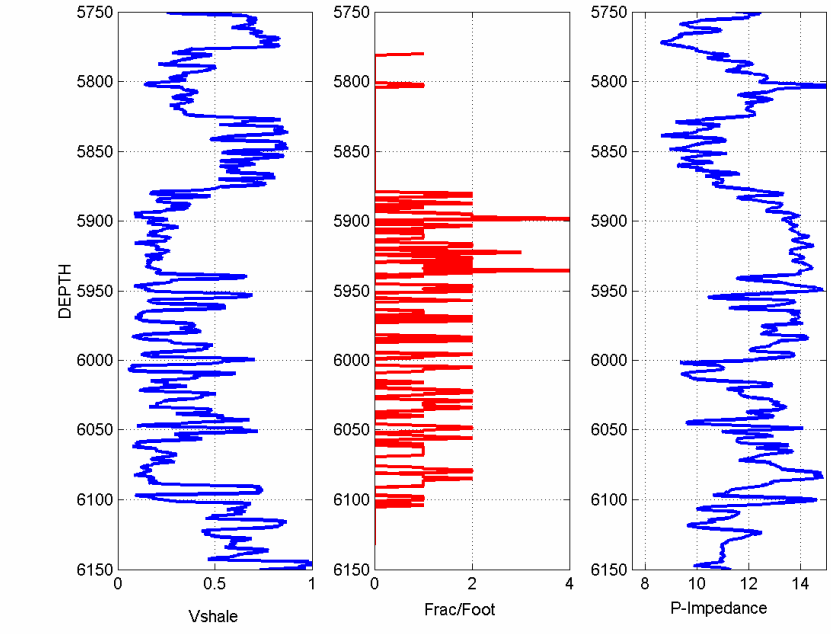

Figure 5. Comparison of fracture frequency, Vshale, and acoustic impedance. Fractures are confined to the brittle limestone layers and absent in the ductile shale.

Tectonostratigraphic Evolution of East Texas

A comprehensive summary of the tectonic evolution of Texas is given by Ewing (1991). According to Ewing, major tectonic events can be arranged as a series of tectonic cycles somehow equivalent to Wilson's cycles of continental rifting, subduction, collision and concomitant periods of intracontinental deformation. Each cycle produces characteristic stratigraphic sequences, or tectonostratigraphic units, that record the onset and development of rifts and passive continental margins, eventually followed by sequences associated to compress ional tectonics, as well as magmatism, uplift and erosion. Four main cycles have been recognized in Texas: (1) The SierraGrande-Chaves cycle, that extends from the Early to Middle Proterozoic; (2) The Llano cycle, Middle Proterozoic; (3) The Ouachitan cycle, which comprises all the Paleozoic; and (4) The Gulfian cycle, that started with continental rifting in the Late Triassic at about 220 m.y. ago and is still going on.

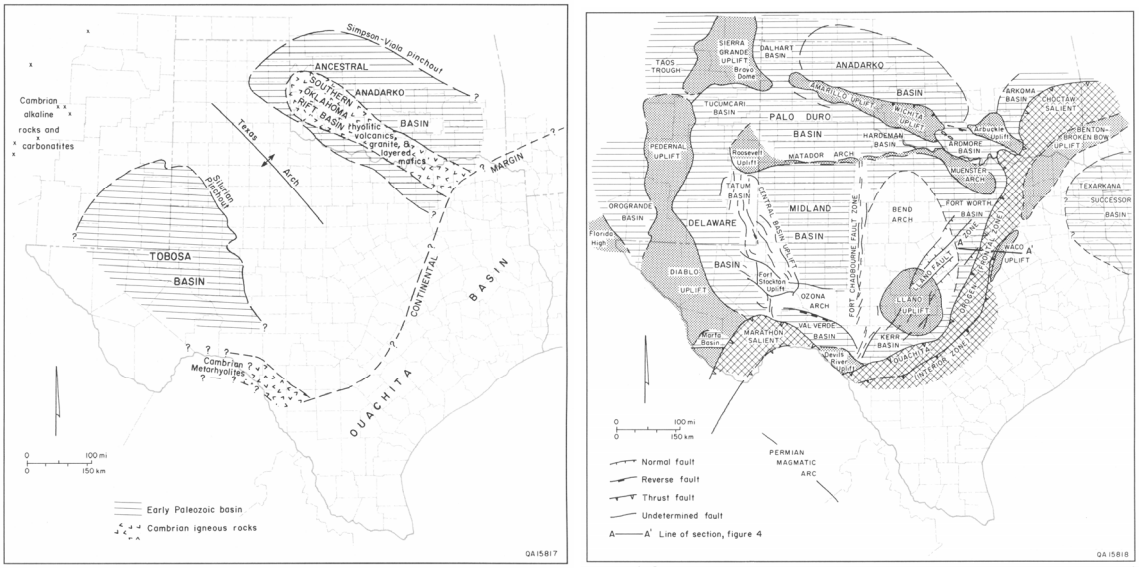

Figure 6. Left: Map showing location of main Cambrian features, failed rifts, continental margin and ancestral basins. Right: Map showing location of major late Paleozoic structural elements of the Ouachita orogen and foreland deformed belts. After Ewing (1991).

The metamorphic and igneous rocks related to the Precambrian tectonic cycles can be considered part of a crystalline basement with similar mechanical properties, therefore they are thought to have little influence in the geometry of overlying features. On the

contrary, the current structural configuration of Texas started to form since the Cambrian. Rifting of the southern margin of North America during the Cambrian led to development of several failed rift basins (Ewing, 1991), two of them led to the Anadarko and Tobosa basins in Texas, separated by the Texas Arch (Fig. 6, left). The late Paleozoic tectonics of Texas is quite complex, but one of the outstanding features is the Ouachita orogen frontal zone (Fig. 6, right), which outlines the edge of a thrust system trending northwest. The shape of this front has controlled the development of subsequent features along east Texas. Another remarkable feature in east Texas is the development of the Texarkana basin, considered to be a successor basin (Ewing, 1991) just in the same region where the Sabine uplift formed during the Mesozoic.

Structures created by the early Mesozoic rifting are poorly known because they are deeply buried. According to Ewing (1991) an outline of the early Mesozoic rifts can be obtained from the distribution of the salt diapirs and the extension of the Louann salt, deposited during the middle Jurassic (Fig. 7, left). Extension continued during the Jurassic and early Cretaceous, nevertheless the thick sedimentary sequence composed of upper Jurassic Limestones, upper Jurassic to lower Cretaceous clastics, and Aptian to Albian carbonate platforms is interpreted as a post rift passive-margin fill (Ewing, 1991). The James Limestone was deposited during the Aptian, as part of the carbonate platform sequence.

The post rift sequence mobilized the Louann Salt into pillows and diapirs in East Texas and led to the development of a peripheral graben system. These grabens formed at or near the pinch-out of salt and created the headwall of basinward sliding of the post-salt sedimentary sequence (Fig. 8), which began in Late Jurassic and probably is still going on (Jackson, 1982). During Late Cretaceous to Paleocene times the structural configuration is modified by the development of the Sabine uplift at east Texas and north Louisiana (Fig. 7, right). The origin of this uplift is still controversial, since some authors relate it to the Laramide Orogeny (Lauback and Jackson, 1990) whereas others explain it as the result of stress relaxation of deep lithosphere (Nunn, 1990). Up to 2500 m of lower Cretaceous strata was eroded from this uplift at about 100 m.y. (Albian), and several hundreds of meters of Cenomanian strata were also eroded, before deposition of

the Late Cretaceous Austin Chalk (Ewing, 1991). The structure was, therefore, very active during the Late Cretaceous and should have played a significant role in the configuration of structural features at the East Texas-Louisiana border during that period of time.

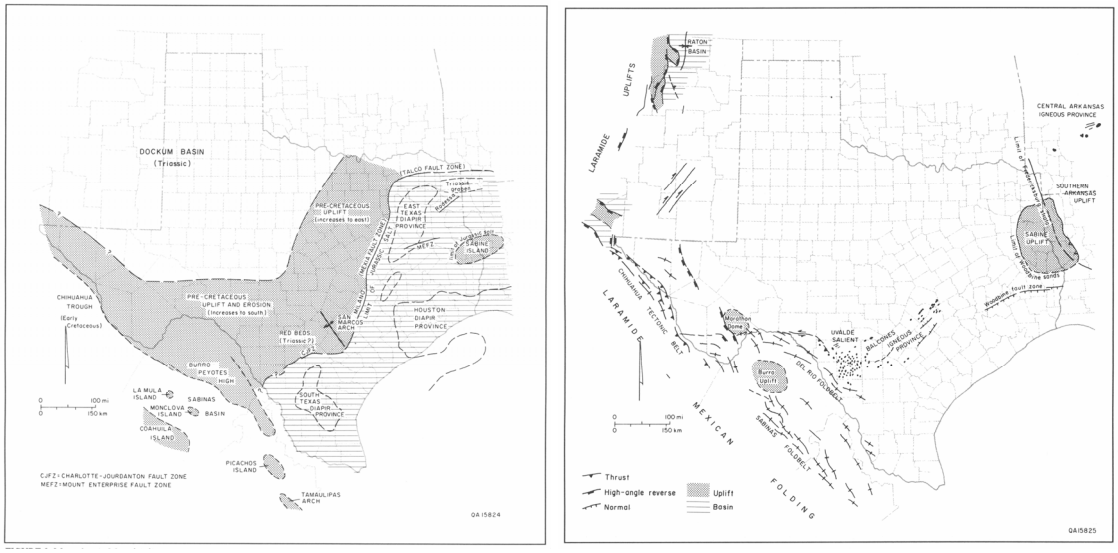

Figure 7. Left: Early Mesozoic features, diapir provinces may correspond to areas of higher extension. Right: mid-Cretaceous to Eocene tectonic elements of Texas. Notice that the study area is within the Sabine uplift, just at the Louisiana-Texas border. After Ewing (1991).

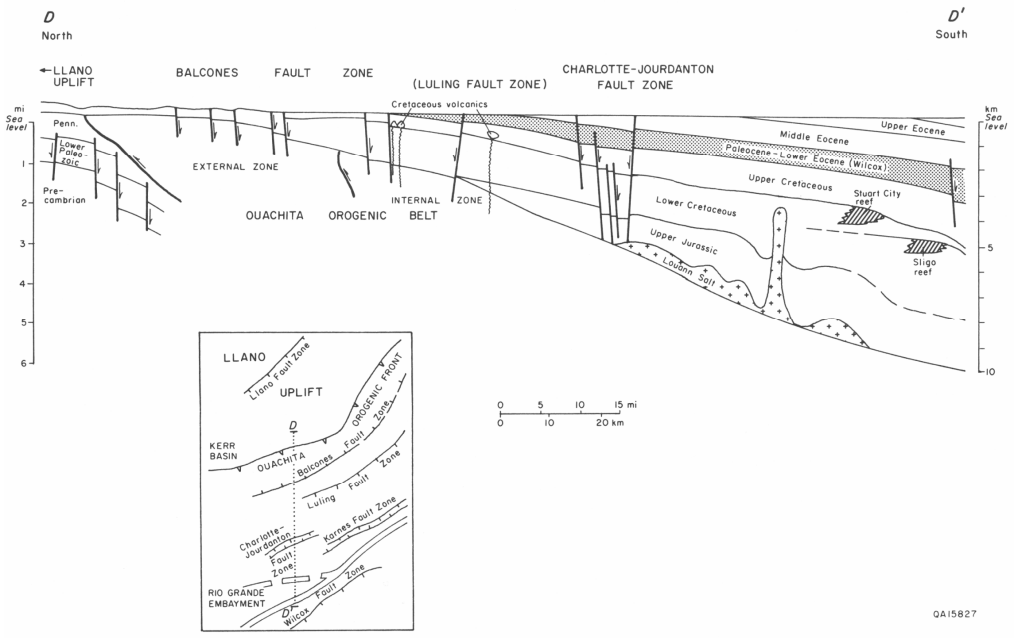

Figure 8. Cross section of the peripheral Gulf Coast, showing Cretaceous the development of graben and basin-margin faults at the pinch out of salt deposits. After Ewing (1991).

The Cenozoic is characterized by the syndepositional development of normal faults, or growth faults (Fig. 9). Large river systems with headwaters in the Rocky Mountains drained toward the Gulf of Mexico. Major deltas built and prograded for more than 200 km seaward from the Cretaceous shelf margin. High sedimentation rates generated overpressure on deep, mud-rich units producing a mechanically unstable section that led to syndepositional normal faulting (Fig.10), known as growth faulting (Ewing, 1991). The fault systems are named according to the major shelf-margin progradational unit associated. The faults systems and the depositional units are progressively younger towards the shelf edge (southeast). The proposed mechanism explains why each fault system is detaching from higher stratigraphic horizons, but the presence of salt in upper detachment horizons indicates a more complex history (Peel et al, 19955). Ewing (1991) classified growth faults into two main groups: (1) glide systems, in which horizontal displacements are larger than vertical displacements; and (2) deep listric fault systems, in which vertical subsidence of hangingwall rocks is greater than horizontal displacement.

In summary, the main tectonic episodes that have influenced the structures at the Texas-Louisiana border, the region of interest, are: (1) Cambrian failed rifts; (2) Triassic rifting and deposition of the Louann Salt; (3) Faulting and tectonism associated to both the Sabine uplift and the mobilization of the Louann Salt; and (4) Cenozoic extension and development of syndepositional normal faults.

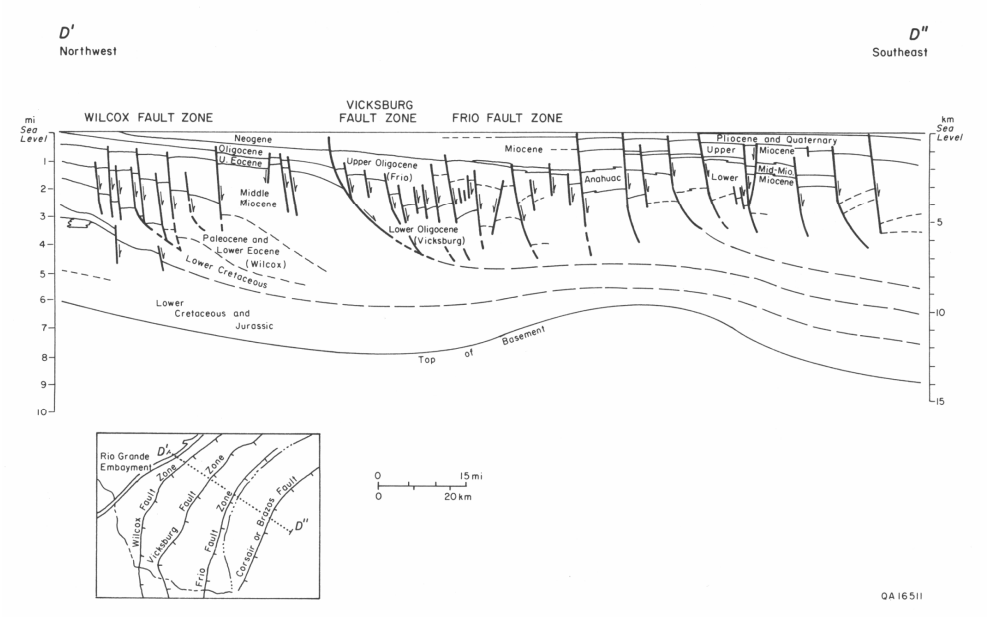

Figure 9. Cross-section of the inland Gulf Coast Basin, showing Cenozoic growth faults. After Ewing (1991).

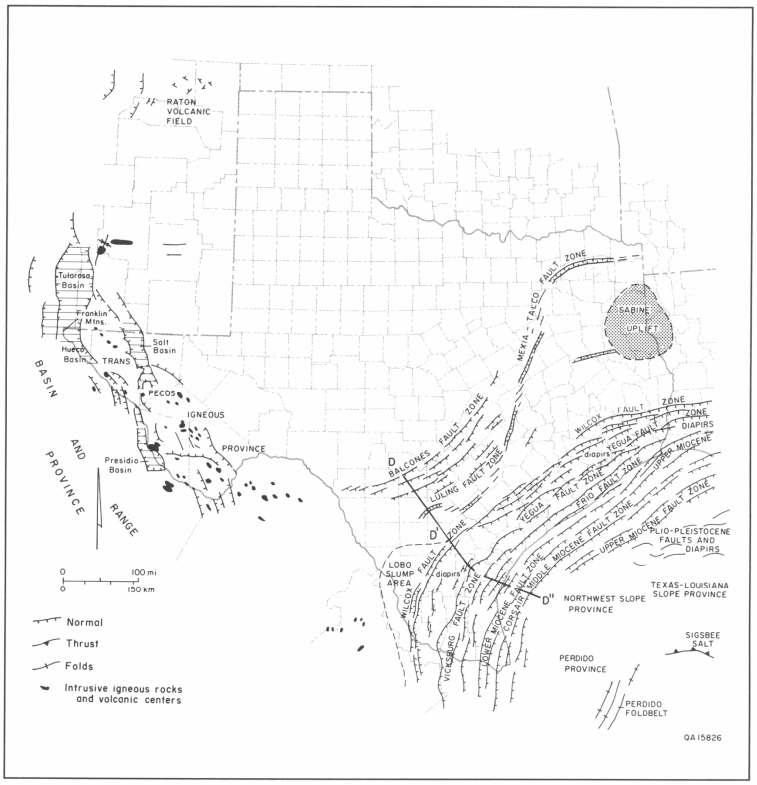

Figure 10. Major Cenozoic tectonic elements of Texas. Growth faults surrounding the Gulf Coast. The Sabine uplift still stands out in the Louisiana-Texas border. After Ewing (1991).

Faults and Fractures at Henderson-1

For characterization of faults and fracture systems within the James Limestone at the Neuville field, we have two key pieces of information. First we have the two horizontal wellbore sections through the main productive intervals of James Limestone (Fig. 11). The wellbore is oriented at 150° azimuth, and was thought to be normal to the main fault set in order to cut as many fractures as possible. As will be discussed later, it is probable that this is not actually the case. The wellbore may not be normal to the main fault system. Nevertheless, at least six small-scale faults or subseismic faults were found along these horizontal wells. These are normal faults according to the interpretation of offsets in the drilled section, but also based on the structural style of the region. The second piece of information is the coherence cube from Marathon's 3D seismic (Fig. 12). The time slices show clearly a normal fault trending N 67°W, affecting the James

Limestone. Additional smaller faults have also been proposed based on some weak trends in amplitude anomalies or the coherence cube, but the orientation of these smaller faults is subjective and therefore uncertain. Nevertheless, these two sources of information indicate that normal faults at different scales are the dominant features at Henderson-1.

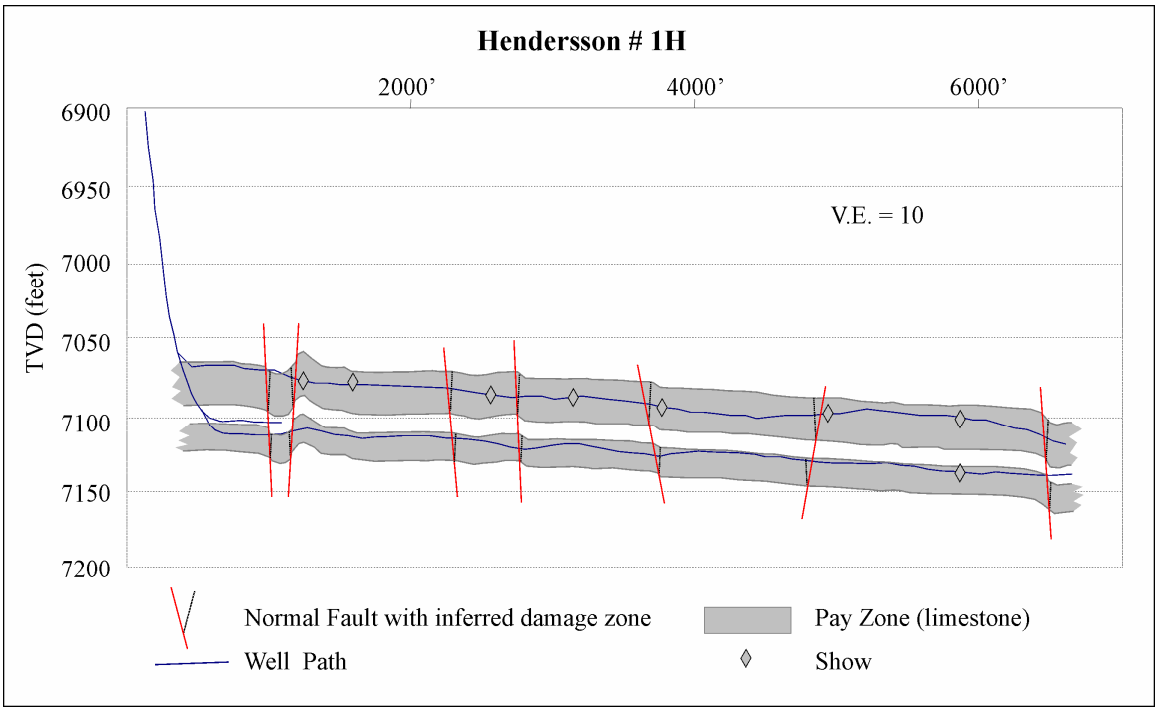

Figure 11. This cross section illustrates the horizontal sections of Henderson-1 laterals, (Courtesy of Marathon). VE = Vertical Exaggeration.

Fracture/ Fault Types

As explained in the tectonic evolution, the dominant structural style in this region is extensional. Normal faults have been developing from the Triassic up to the present. Specifically in the east Texas-Louisiana border, the faults affecting the Cretaceous rocks formed during Early to Late Cretaceous times, whereas faults that involve the Tertiary formed during the Eocene. Often the case, normal faults in sedimentary sequences develop conjugate sets. When the rocks involved in the deformation are brittle, like in this case, conjugate normal faults create narrow zones with high fragmentation (see Attachment C). Therefore, fracture swarms characterize fault-related damage zones,

whereas intact-rock intervals are characterized by low fracture density, most likely regularly spaced joints. This conceptual fracture distribution has already been documented at some outcrops of the Austin Chalk in Texas (Fig. 13), and constitutes the basic model for fracture systems of James Lime at Neuville.

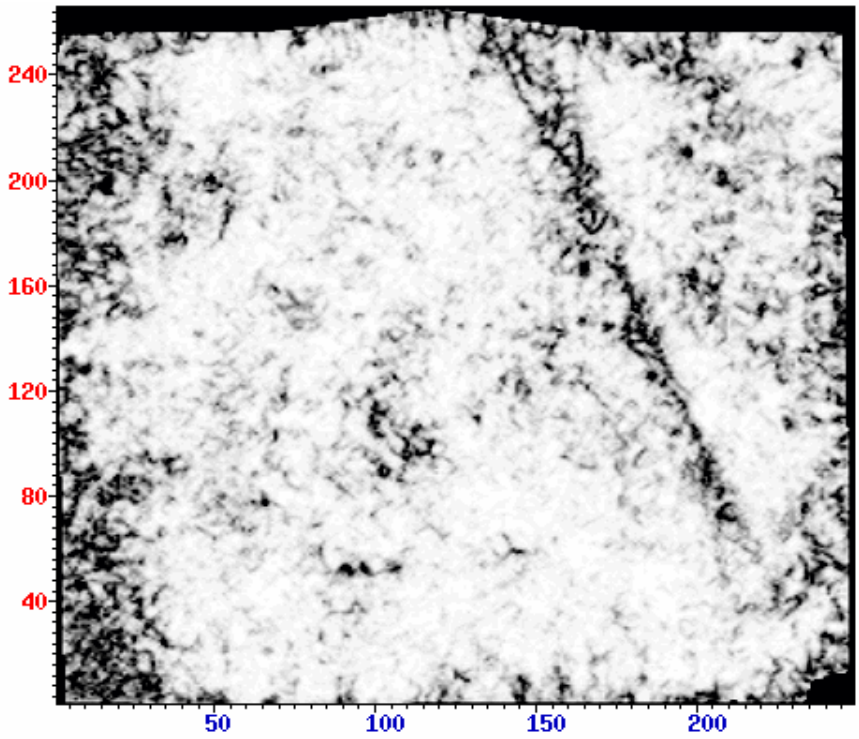

Figure 12. Coherence cube slide near top James Lime, showing a fault located east of Henderson-1. The fault azimuth is 293°, and Henderson-1 is located about x=100, y=120. The slice is rotated about 30° clockwise in respect to the north, which is approximately pointing out in the direction of the upper–right corner.

The proposed model (Fig. 13) agrees with observations of conjugate normal faults in sedimentary packages with similar lithologic contrast in ductility (see Attachment C). Field observations of normal faults in different settings document the presence of significant fragmentation and fracturing even for faults with less than 1 m slip (Fig. 14). Often the case, faults with slip larger than 1 m develop a core zone made of gouge or very fine-grained material (Figs. 15 and 16). For a given lithology, thickness of the gouge and the fragmentation zones varies according to fault offset. But large-offset faults can be easily identified in seismic; therefore our interest is focused on faults that cannot

be detected even with a semblance-based coherency algorithm (Marfurt *et al*, 1998). The fault-offset below seismic resolution depends on signal frequency and seismic velocity. If we assume that seismic resolution is approximately $\lambda/4$, where λ is the wavelength, and given a velocity (v) and a certain offset (u) the frequency required to resolve a fault is given by $v / 4u$. For 5 m offset in sediments with a seismic velocity of 2000 m/s we could image the fault with a 100-hertz signal, but we need a 200-hertz signal to image a fault in carbonates with velocities of 4000 m/s.

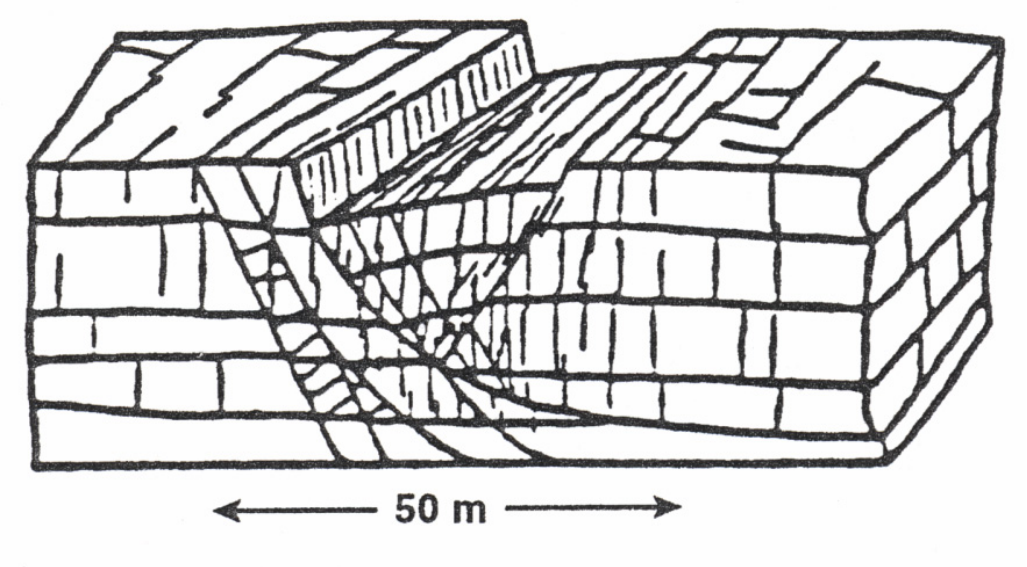

Figure 13. Schematic model that illustrates the most likely distribution of joints and fractures associated to the normal faults within James Lime. The vertical fractures correspond to an orthogonal set of joints, one parallel to the main fault, that abut against bedding surfaces. The oblique fractures correspond to the main fault and sub parallel faults dipping in the same direction, and a conjugate normal fault dipping in opposite sense. This description from outcrops of the Austin Chalk at Texas (Friedman and Wiltschko, 1992) is proposed as the basic model for fault and fracture systems of James Limestone at Neusville field**.**

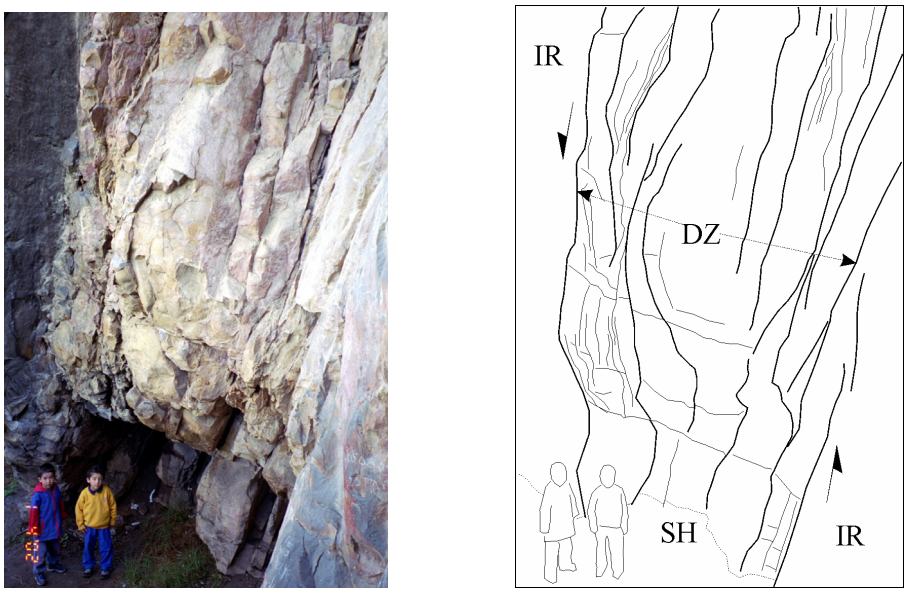

Figure 14. Photo and sketch of the damage zone associated to a normal fault with less than 1 m of vertical slip (the boys are about 1 m tall). Subparallel, closely spaced fractures with localized breccia zones are the main features of the damage zone. IR= Intact rock; DZ= damage zone; SH= Shale layer. Maastrichtian sandstones in Colombia.

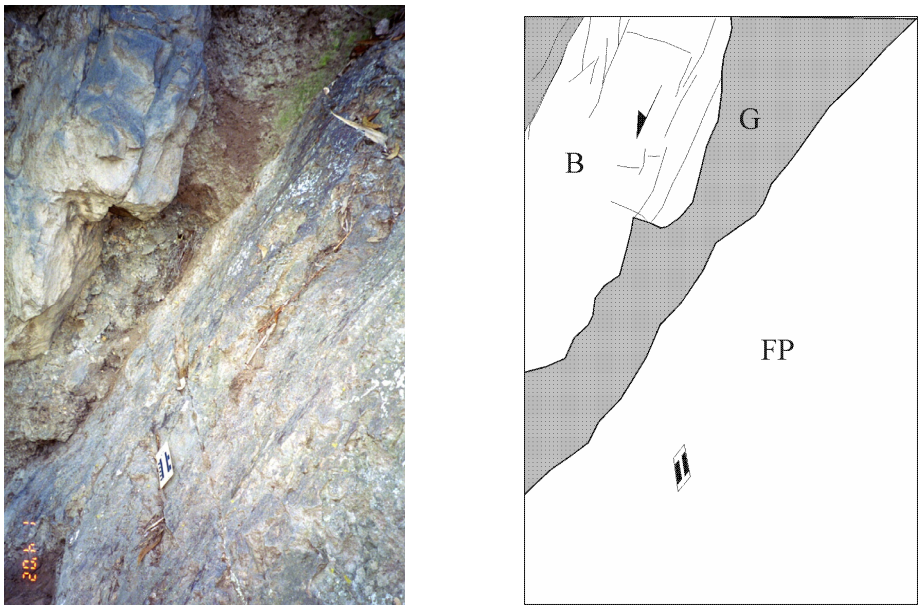

Figure 15. Gouge zone (G) associated to a normal fault with vertical slip larger than 1 m, but smaller than 5 m, in the same stratigraphic interval of Fig. 7. B= Breccia; FP = Fault plane. The scale rule is about 15 cm long.

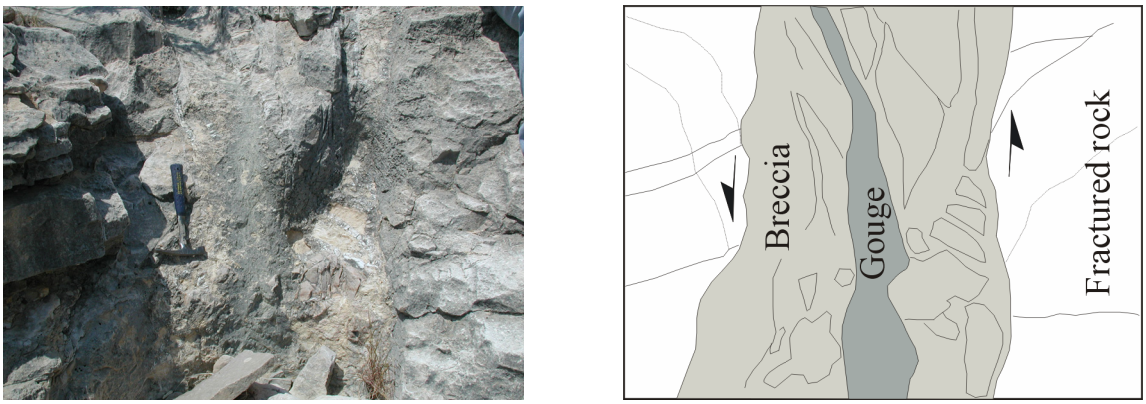

Figure 16. Fault zone architecture, photo (left) and sketch (right), which corresponds to a 6-m-slip fault. Albian limestones near Yates oil field, Texas.

Fault and Fracture Orientation

The horizontal sections of Henderson-1 document the presence of small normal faults that offset the strata enough to generate a jump in the gamma ray signal (Fig. 11). As explained before, these faults have been interpreted as normal faults, because this is the dominant structural style in the region. The well azimuth, 150°, was proposed to be normal to the dominant fracture azimuth, but the actual fracture orientation is unknown since additional fracture-imaging logs (FMI or borehole televiewer) were not acquired. In that regard is important to point out that information obtained from these logs is not always definitive, since two or three orientations can be present and the more frequent orientation is not necessarily the dominant one (Wu and Narr, 2000). The VSP was acquired in two directions, one parallel to the wellbore (150°) and the other at 80°(230°), as will be explained in the Attachment F, anomalies in reflection amplitudes along the VSP seem to correlate with the fault zones identified in the wellbore, but they are observed in both orientations. There are three possible explanations for this observation: (1) the faults are oblique to both orientations rather than parallel to one of them; (2) there are two different fault systems; (3) some amplitude anomalies may not correspond to fault zones.

Information regarding fracture orientation at subsurface comes from McCoy-1 and USA Bridges-1. McCoy-1 is located to the east of Henderson-1, in Louisiana. Bridges-1 is located some miles south of Henderson-1. The orientation of fractures obtained from

FMI logs in these two wells (i.e. Fig. 17), indicates a consistent single set of fractures oriented at E-W to ENE-WNW. Fracture density at McCoy-1 is low and fractures do not cut across shale, therefore it is very likely that they correspond to joints. The probable presence of an orthogonal secondary set of joints is inferred from observations made at Albian limestones in our previous study at Yates field (Fig. 18), but also from other documented studies of Cretaceous limestones in Texas (Fig. 13). The consistency of the single-set orientation of fractures systems at subsurface suggests a strong influence of the stress field, since fractures with other orientations must be closed (Fig. 19). Based on this observation, we conclude that the most likely model for Henderson-1 is the one with subparallel open fractures and faults. Therefore, the next question is: What is the orientation of these fractures? Based on seismic interpretation and the current understanding of the tectonic setting, we consider three different scenarios: (1) subseismic faults are parallel to observed normal fault 2 km east of the well (Fig. 20); (2) subseismic faults are parallel to the normal faults observed in the Tertiary, related to the known regional stress field (Fig. 21); and (3) subseismic faults are perpendicular to the observed normal fault (Fig. 22). We will analyze these different possibilities of fracture orientation, which we are going to refer to as scenario A, scenario B and scenario C respectively, based on well-known fracture mechanics principles, data available, outcrop analogue studies and the tectonic evolution of the region.

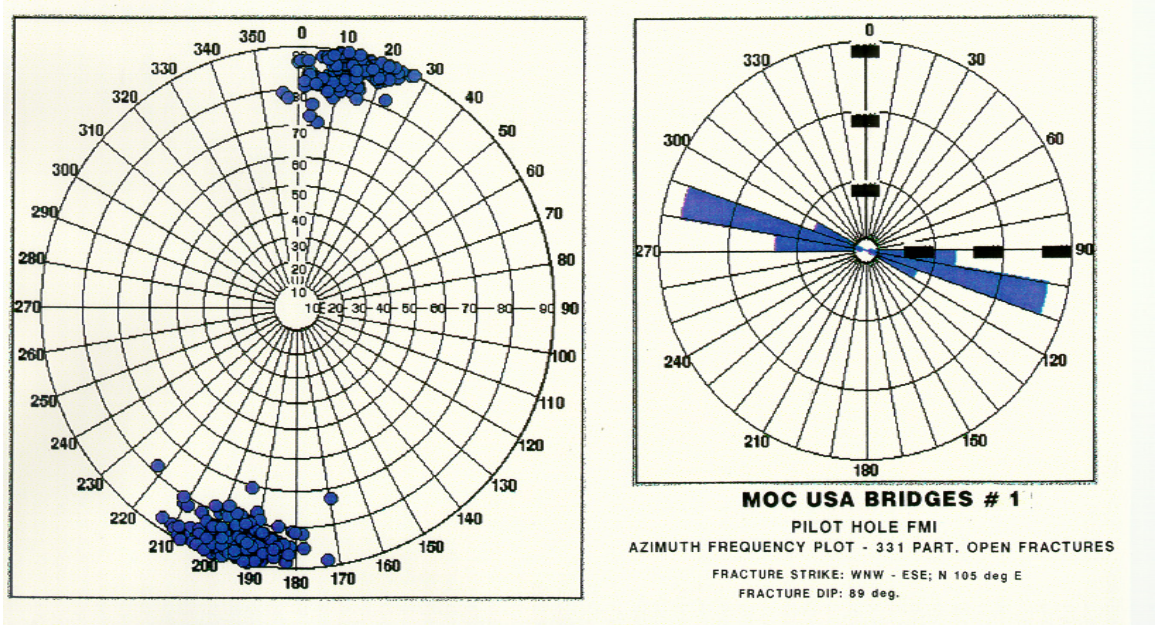

Figure 17. Schlumberger's interpretation of fracture sets in well Moc Usa Bridges # 1 from FMI logs. In well McCoy-1 the strike of this single set is E-W, indicating small variations in the general trend. The orientation of these fractures is parallel to the fault observed 2 km east of Henderson-1, parallel to the open fractures at McCoy-1 and also parallel to the Cretaceous depositional slope. All these observations together suggest that fault/fracture trends within James Lime may be different from fault/fracture trends within the Cenozoic at surface.

Figure 18. Two orthogonal sets of joints observed in outcrops nearby Yates field, in Albian limestones.

Figure 19. Two orthogonal sets of joints near a large normal fault. The joints filled with calcite (veins) are parallel to the fault trace. The set normal to the fault trace, therefore normal to the maximum horizontal stress, is closed. Permian rocks at Algerita Escarpment.

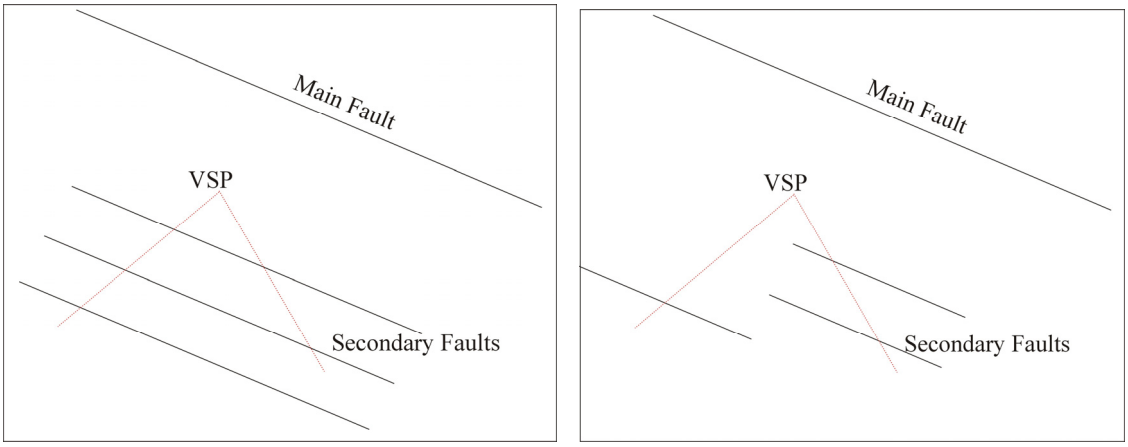

Figure 20. Sketch showing the situation for scenario A: subseismic faults parallel to the main fault and oblique to both VSP azimuths.

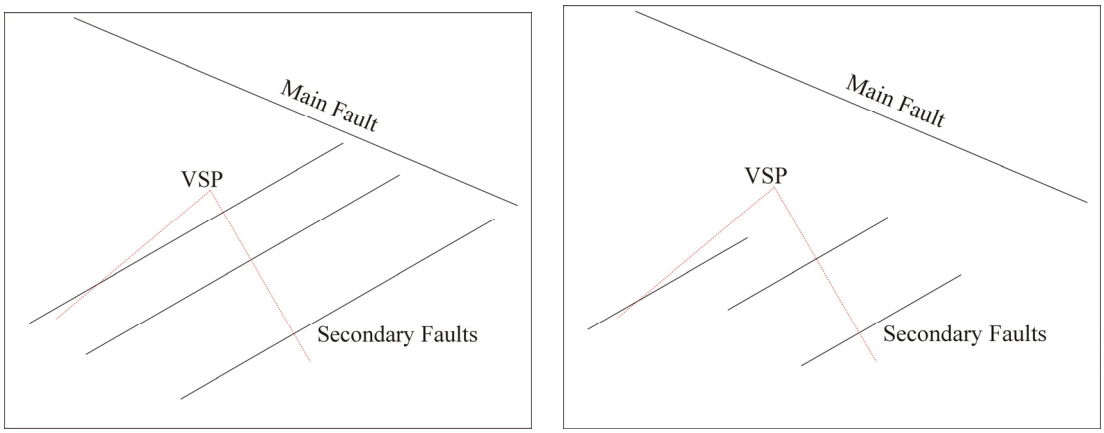

Figure 21. Sketch illustrating the situation for scenario B: subseismic faults are parallel to the Cenozoic faults at surface, perpendicular to the wellbore (150°) and subparallel to the other VSP azimuth (230°).

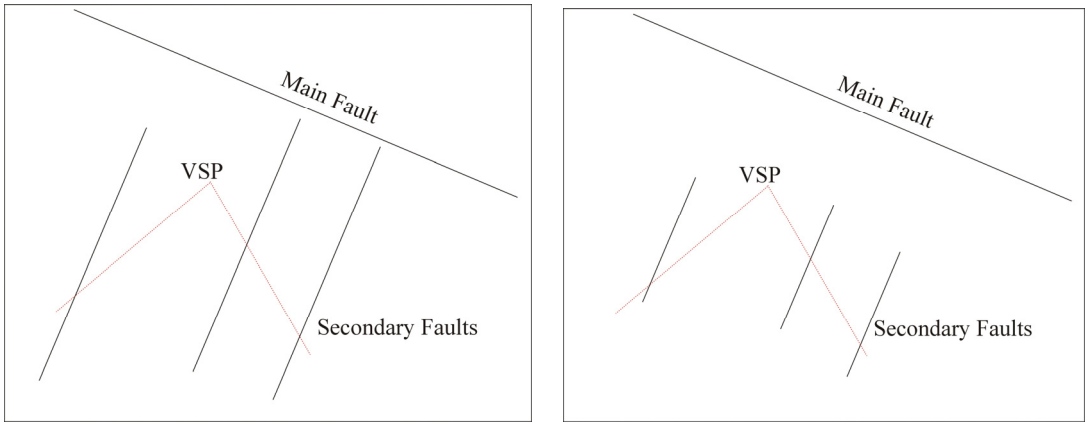

Figure 22. Sketch showing the geometric configuration of scenario C: subseismic faults are normal to the main fault and therefore slightly oblique to the 230° VSP and oblique at high angle to the 150° VSP.

The hypothesis of small faults and fractures parallel to the major fault within the Cretaceous (scenario A) is based on the fact that faults are detaching from different stratigraphic horizons. The mechanical model for development of these faults is similar: faults may have originated from splay joints formed within brittle layers, generated due to stress concentrations associated to slip along weak planes that could have been either salt horizons or overpressured shale. The original dip of these horizons should correspond to the original depositional slopes. Current configuration of the Gulf Coast fault system (Figs. 2 and 10) indicates that depositional slope controls the slip direction of Cenozoic detachments. Consequently, normal faults are parallel to the depositional strike. It turns

out that because of the presence of the Sabine uplift in the region of interest, the depositional strike of Cretaceous sediments (Fig. 23) is different than the depositional strike of Tertiary sediments. Therefore, orientation of faults within the Tertiary may not correspond to the orientation of faults within the Cretaceous. The Cretaceous depositional strike coincides with the orientation of fractures at USA Bridges-1 (Fig. 17) and with the orientation of the fault observed in the coherence cube (Fig. 12).

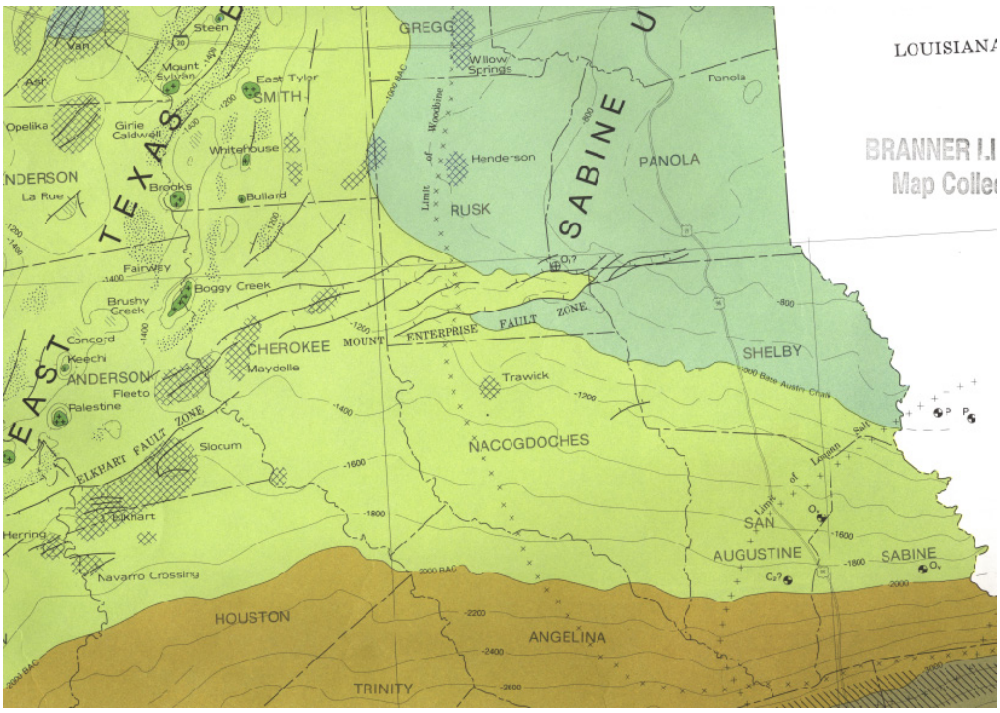

Figure 23. Tectonic Map of southeast Texas (Ewing et al, 1990) showing the structural contours on top of Austin Chalk (Upper Cretaceous), the limit of Louann Salt and the extension of the Sabine uplift indicated by the limit of Woodbine deposits. The normal faults shown crops out at surface and affect the Cenozoic section.

The second hypothesis, that subseismic faults are subparallel to the faults observed in the Tertiary (scenario B), seems to be the idea that led original Marathon's interpretation. The majority of faults at surface are trending to the ENE (Figs. 10 and 23), orientation that is in agreement with the current state of stress in the area (Zoback and Zoback, 1980). As will be shown in the geomechanical modeling, the presence of the pre-existing WNW-trending Cretaceous fault does not affect significantly the orientation of the new faults. In addition to this, some ENE-trending normal faults actually involve the Upper

Cretaceous Austin Chalk, as shown in Fig. 23. This model, therefore, makes mechanical sense and cannot be ruled out.

Another model proposed by Marathon's geologists, is that small faults and fractures are perpendicular to the Cretaceous fault (scenario C). This interpretation is based on some linear trends observed in the coherence cube. Joints normal to the associated normal fault are documented in the literature (Kattenhorn *et al*, 2000) but they require basically a rotation of the stress field that originated the normal faults. Such rotation may result from tensional stresses derived from bending, but a detailed analysis of curvature and flexure at James Top would be necessary to completely evaluate this hypothesis. For the Poly3D modeling, this case is somehow similar to the previous one, since the geomechanical models show that the Cretaceous fault does not affect significantly the orientation of new features due to change in the loading conditions. Even though we think this is a less likely option, it cannot be ruled out completely before further analysis.

Geomechanical Models

The fault located 2 km east of Henderson-1 is a normal fault with about 200 feet of maximum offset near the well. The fault is more than 17 km long but its actual dimensions are not known. Its azimuth is 113° and dip direction is southwest (right-hand rule). This fault is labeled as the main fault on Figs. 20, 21 and 22. There is another normal fault parallel to the previous one, located about 5 km west of Henderson-1. Even though the exact dimensions of the faults are unknown, we can evaluate the impact of these faults on the orientation of new faults and fractures at Henderson-1, since the major stress perturbations are located at the fault tips. In order to evaluate the different possibilities of fracture and subseismic faults orientation based on this configuration for different loading conditions, we need to assume the dimensions for the two rectangular faults. For the main fault we estimate 34 km length and 1 km height. For the smaller fault we assume 17 km length and 0.5 km height. Incorporation of the actual fault dimensions may improve the accuracy of the results obtained.

Boundary Conditions

The material properties and boundary conditions at the fault surfaces are the same for all the realizations. For each different case we modified the loading boundary conditions. Poisson's ratio (ν) is 0.3 and Young modulus is 40000 MPa. The boundary conditions at each fault are: t1 = 0; t2 = 0; b3 = 0. Where t1 is the traction resistance for dip-slip along the fault, t2 is the traction resistance for strike-slip along the fault and b3 is the Burger's vector (displacement) normal to the fault surface. For the loading boundary conditions we assumed a normal-fault stress state with three different orientations of the minimum compressive horizontal stress: (1) normal to the faults at subsurface; (2) normal to the faults at surface, which is coincident with the current state of stress (Fig. 24; and (3) about 80° oblique to the faults. In addition to these three models, we run another two with strain boundary conditions with the maximum strain normal to the main fault. The first strain boundary conditions was shear strain = 0.08, the second was uniaxial strain = 0.08.

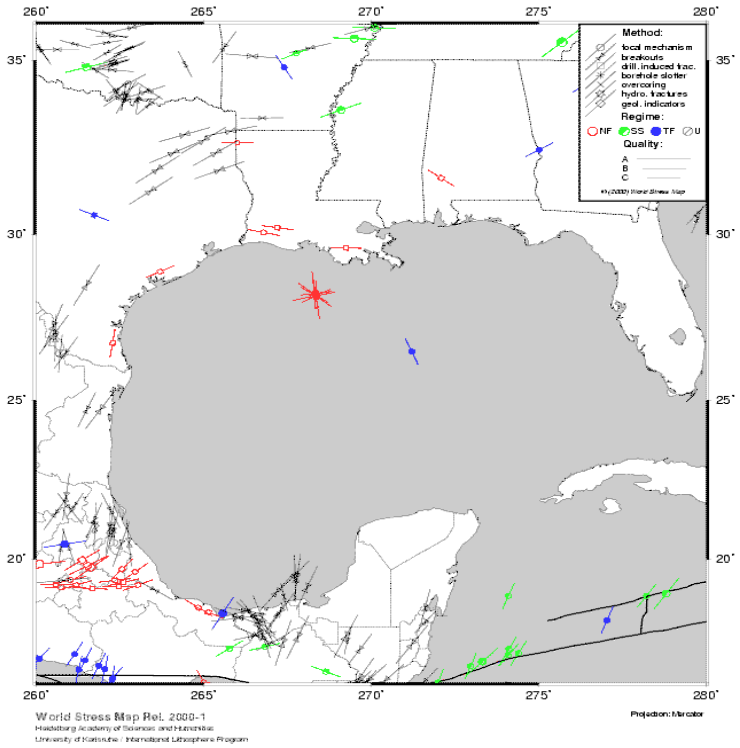

Figure 24. Map of the stress field in the Gulf of Mexico. World Stress Map (Mueller et al, 2000).

Results from Stress Boundary Conditions

We put three parallel observation grids at different heights, in the region corresponding to the location of Henderson-1. They allow us to obtain a three dimensional view of the distribution of the stress field. We have created two different types of plots for each realization or model. The first plot shows the distribution of the mean stress and illustrates the extension of the stress perturbation. In general blue colors show areas of lower compressive stress and red colors show areas of higher compression. For the normal state of stress we could not obtain tension and actually this is still an unresolved question: What is the minimum dimension of the slip patch that can produce tension? But for our current purposes this question is not critical. The second plot shows the orientation of the intermediate (black) and maximum (red) compressive stresses, they

both define the plane where new joints can be formed. Following Anderson's theory of faulting (Anderson, 1951), the intermediate compressive stress is always parallel to the fault strike, therefore is showing the orientation of new subseismic faults for each case.

The comparison of the first type of plot for the different stress boundary conditions, figures 25, 26 and 27, shows no significant variation in the spatial distribution of the perturbed stress field. In all three cases we obtain a normal fault, although the actual slip magnitudes are different for each case and the oblique shear is especially noteworthy in the second case (Fig. 26). In general, the perturbation of the stress field due to slip along the faults does not seem to have a major impact on the orientation of faults and fractures at Henderson-1. As a result, the orientation of the faults at Henderson-1 is basically controlled by the loading conditions, as can be deduced from the comparison of figures 28, 29 and 30, which illustrate the orientation of the intermediate compressive stress. Nevertheless, the actual dimensions of the fault and the slip distribution along the fault constitute critical parameters for a more accurate analysis.

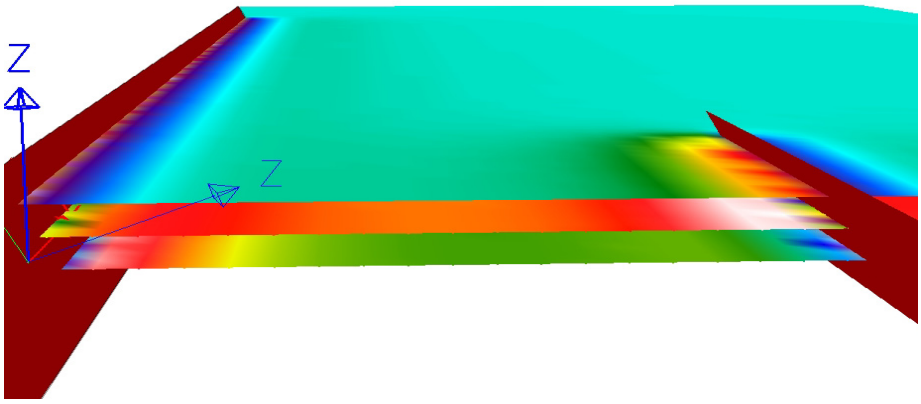

Figure 25. Scenario A. Lateral view. Mean stress due to slip along the faults (purple) under normal-fault state of stress. The minimum compressive horizontal stress is normal to the faults. Blues indicate zones of lower compressive stress and reds zones of higher compressive stress

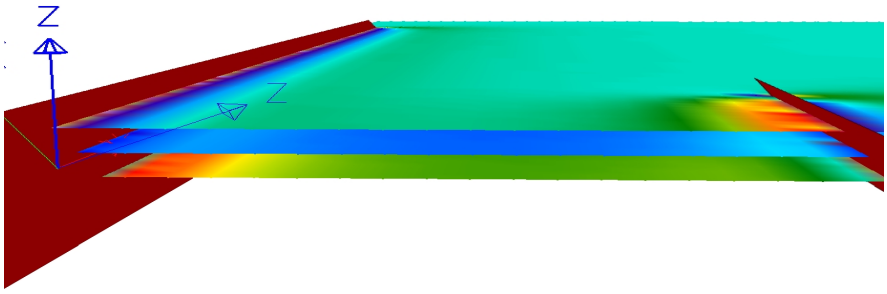

Figure 26. Scenario B. Lateral view. Mean stress due to slip along the faults (purple) under normal-fault state of stress. The minimum compressive horizontal stress is oblique to the faults, resembling the current state of stress in the region. Blues indicate zones of lower compressive stress and reds zones of higher compressive stress.

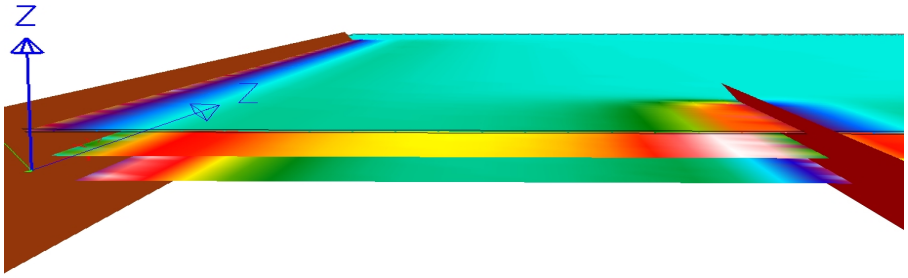

Figure 27. Scenario C. Lateral view. Mean stress due to slip along the faults (purple) under normal-fault state of stress. The minimum compressive horizontal stress is at high-angle (about 85°) in respect to the faults strike. Blues indicate zones of lower compressive stress and reds zones of higher compressive stress.

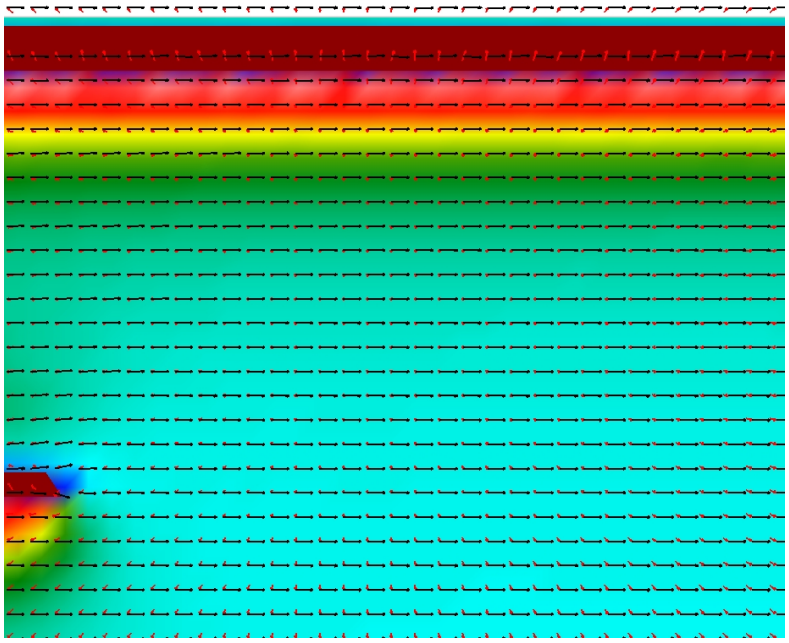

Figure 28. Scenario A. Plane view showing the distribution of the mean stress around the faults, and the orientation of both intermediate (black arrows) and maximum compressive stresses (red arrows). New faults would be parallel to the intermediate stress, and new joints would be within the plane defined by both the intermediate and the maximum compressive stress. Minimum compressive stress normal to the faults.

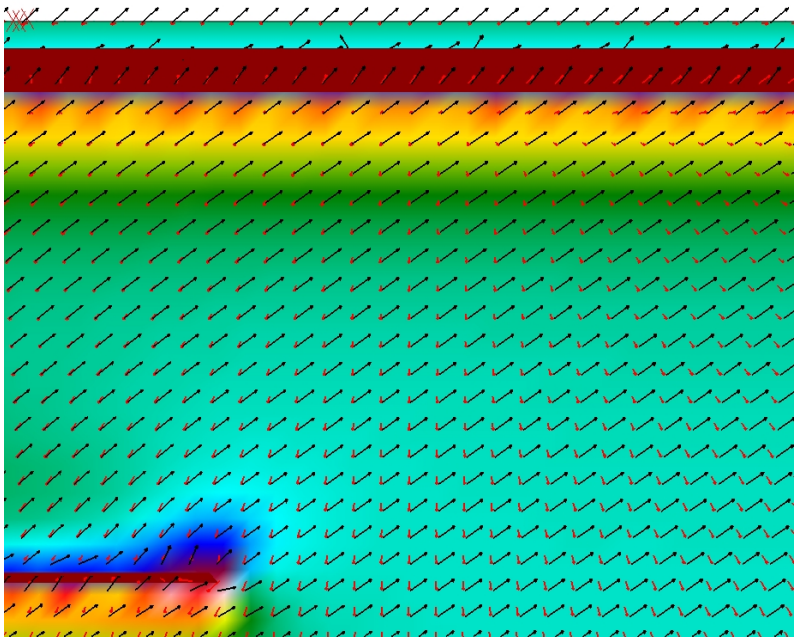

Figure 29. Scenario B. Plane view showing the distribution of the mean stress around the faults, and the orientation of both intermediate (black) and maximum compressive stresses (red). New faults would be parallel to the intermediate stress, and new joints would be within the plane defined by both the intermediate and the maximum compressive stress. Minimum compressive stress is oblique to the faults.

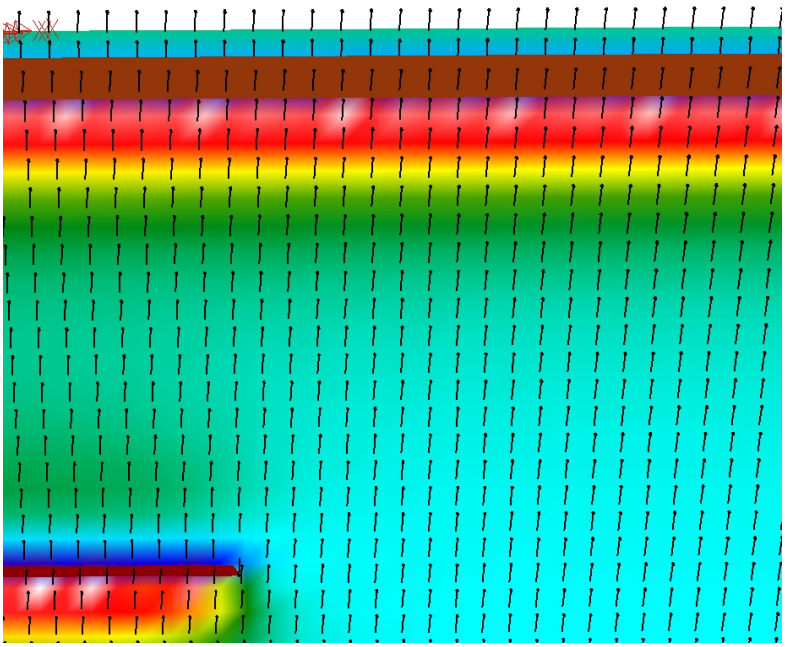

Figure 30. Scenario C. Plane view showing the distribution of the mean stress around the faults, and the orientation of both intermediate (black) and maximum compressive stresses (red). New faults would be parallel to the intermediate stress, and new joints would be within the plane defined by both the intermediate and the maximum compressive stress. Minimum compressive stress is at 80° angle to the faults.

Results from Strain Boundary Conditions

Models with specified stress boundary conditions have always the problem of the uncertainty in stress magnitudes. Strain boundary conditions can be more easily specified since strain can be estimated from the geometry and kinematics. In that regard, it is necessary to have 3D seismic to estimate the slip distribution along the faults, the actual fault geometry and the James horizon geometry. Shear strain boundary conditions are of particular interest since we think these faults are related to a ductile detachment at subsurface, but again additional data is required to determine the actual geometry of the system. Nevertheless, for comparison purposes we ran two models with strain boundary conditions, as explained in the boundary conditions section.

The results from these models show no major differences in the spatial distribution of the perturbed stress field, with respect to the previous models (Figs 31 and 32). The orientation of the expected faults and joints is parallel to the main fault, as in the case of the stress boundary conditions, according to the orientation of the intermediate

compressive stress. Nevertheless, two important changes should be noted: (1) the uniaxial strain boundary conditions produces a flip of the intermediate and maximum compressive stresses around the tip of the secondary fault (Fig. 33); (2) the shear strain boundary condition generates tilted, not vertical, joints since the maximum compressive stress is tilted (Fig.34).

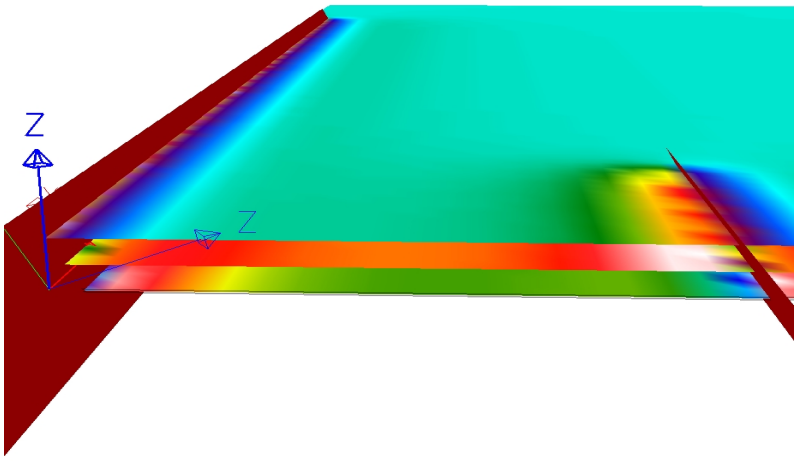

Figure 31. Scenario A. Uniaxial strain boundary conditions. Lateral view of mean stress due to slip along the faults (purple). Blues indicate zones of lower compressive stress and reds zones of higher compressive stress. Maximum strain is normal to the fault azimuth.

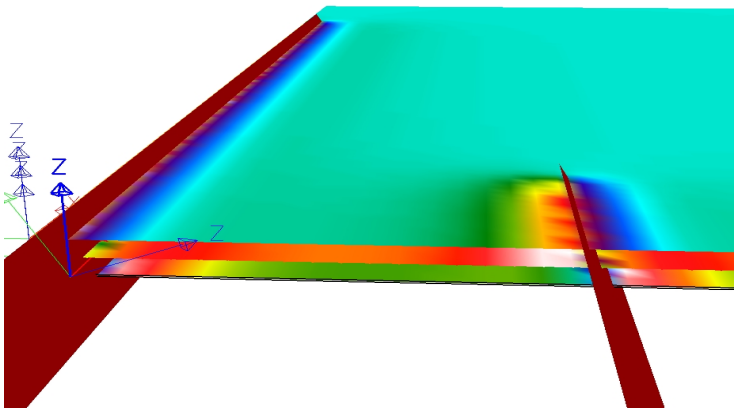

Figure 32. Scenario A. Shear strain boundary conditions. Lateral view of mean stress due to slip along the faults (purple). Blues indicate zones of lower compressive stress and reds zones of higher compressive stress. Maximum strain is normal to the fault azimuth.

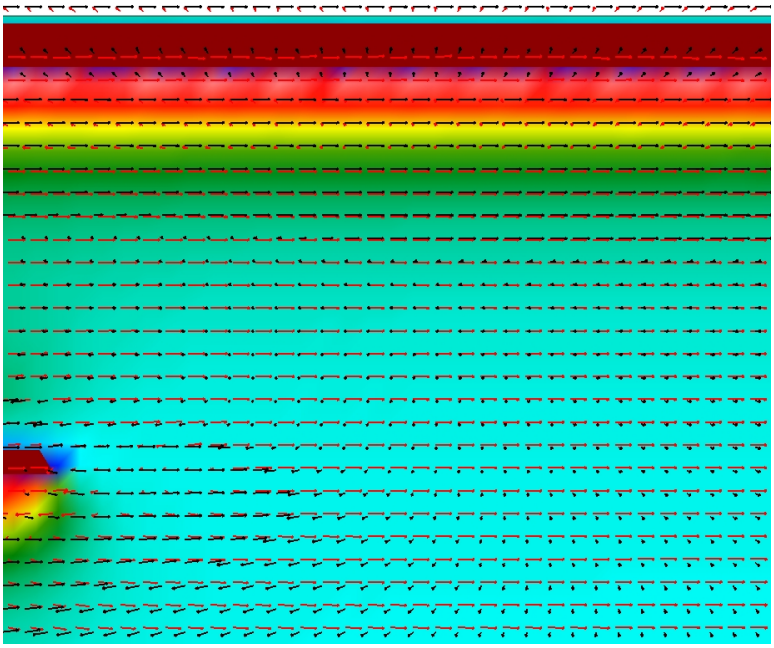

Figure 33. Scenario A. Uniaxial strain boundary conditions. Plane view of mean stress around the faults, and orientation of principal stresses. Blues indicate zones of lower compressive stress and reds zones of higher compressive stress. Arrows correspond to the intermediate (black) and maximum (red) compressive stress and indicate the orientation of new faults and joints.

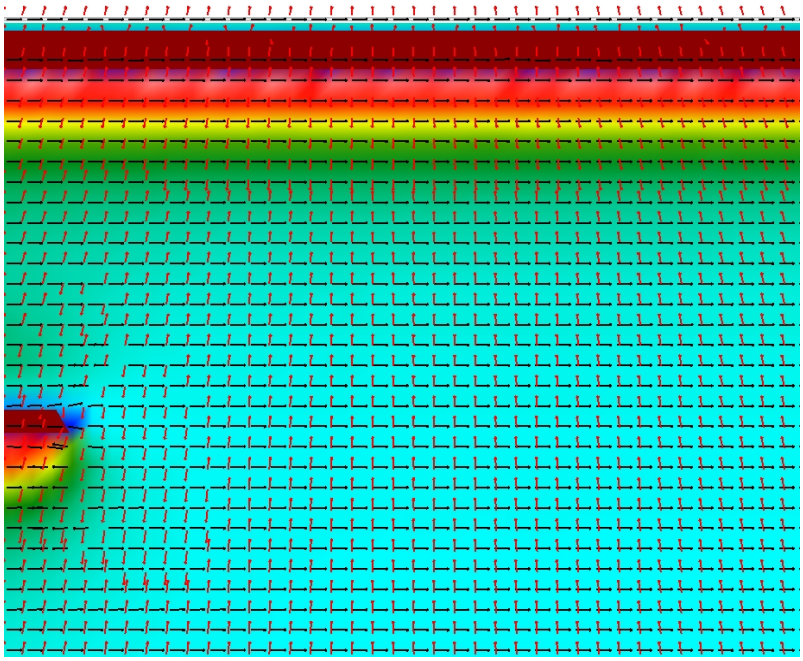

Figure 34. Scenario A. Shear strain boundary conditions. Plane view of mean stress around the faults, and orientation of principal stresses. Blues indicate zones of lower compressive stress and reds zones of higher compressive stress. Arrows correspond to the intermediate (black) and maximum (red) compressive stress and indicate the orientation of new faults and joints.

Frequency of Subseismic Faults and Fracture Zones

The two horizontal wellbores at Henderson-1 indicate the presence of small faults and fracture swarms at subsurface. The same observations are reported from other horizontal wells. The occurrence of regularly spaced small-scale faults and joint zones has been documented from outcrop observations (i.e. Florez, 2000). Therefore, horizontal wells are confirming that many of the characteristics of fracture systems at surface can be extrapolated to the subsurface. Fracture-imaging logs can be used to determine fracture characteristics along horizontal sections, but there are not FMI logs in Henderson-1.

Marathon's technique for distribution of small faults relies upon the analysis of cuttings and the gamma ray. Definitely, there is not a better indicator of faults than a well-established and detailed stratigraphy. Biostratigraphy can be a quite useful tool to determine offset within similar lithologies, when a fine biostratigraphic zonation is available. But in this case we have just the following parameters: drilling rate, gamma ray, calcite, flare, total gas, casing pressure and shows. Here we present the results obtained from the analysis of the gamma ray alone. In this analysis we define three indicators: the gamma ray, the derivative of the gamma ray and the sum of both of them. They are identified as Find1, Find2 and Find3 respectively. We put thresholds values for Find2 (20) and Find3 (50) in order to identify the major changes. There are six major changes in Find3 in the upper lateral section (Fig. 35), but just two in the lower lateral (Fig. 36). They seem to correspond to the faults with larger offset in Henderson-1. Further analysis of other parameters sensitive to fault zones, like drilling rate, may help to define the frequency of smaller faults and fracture swarms.

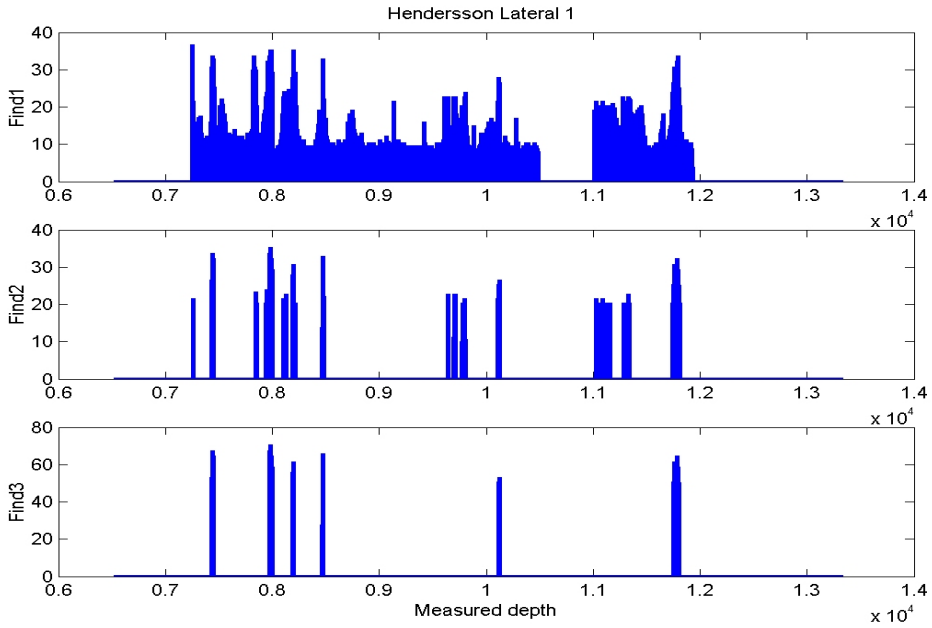

Figure 35. Systematic analysis of gamma ray log as a fault indicator in the upper lateral horizontal section of Henderson-1. Find1, Find2 and Find3 correspond to the original gamma ray log, the derivative, and the sum of both of them respectively. Threshold values are used for plotting Find2 (20) and Find3 (50). The six peaks observed in Find3 are interpreted to correspond to subseismic normal faults.

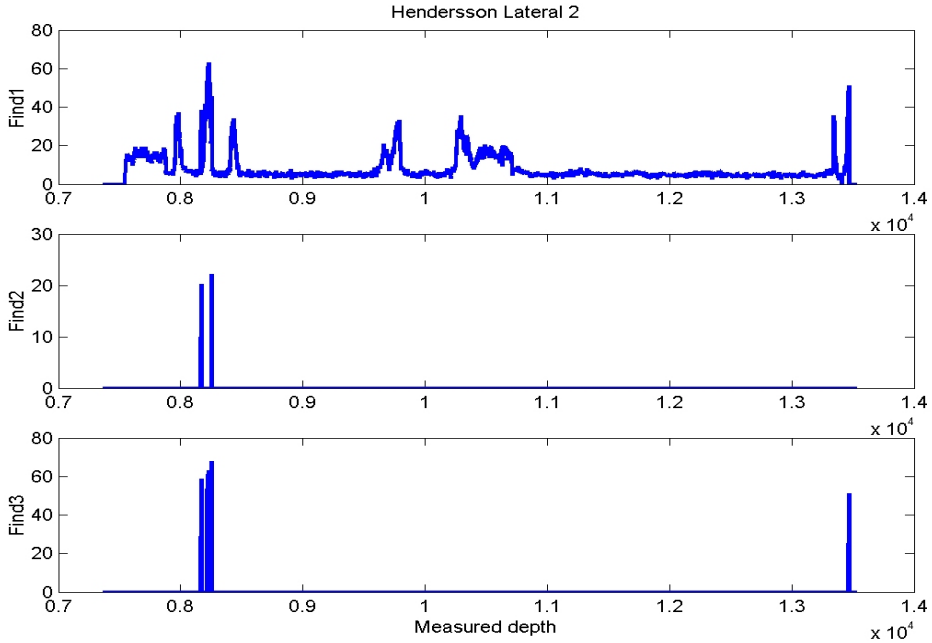

Figure 36. Systematic analysis of gamma ray log as a fault indicator in the lower lateral horizontal section of Henderson-1. Find1, Find2 and Find3 correspond to the original gamma ray log, the derivative, and the sum of both of them respectively. Threshold values are used for plotting Find2 (20) and Find3 (50). The two peaks observed in Find3 are interpreted to correspond to subseismic normal faults.

Conclusions

The mechanical stratigraphy of the Mesozoic at East Texas, characterized by the interposition of ductile and brittle layers and a basal salt horizon (the Louann salt), has played a significant role in the style of deformation at the Gulf Coast. Listric and conjugate normal faults seem to have developed as the result of basal shear along the salt horizon. The orientation of these faults at the Texas-Louisiana border is controlled by depositional slope, apparently determined by the presence of the Sabine uplift.

In a similar way but at different scale, the James Limestone presents the interposition of meter-scale layers of limestone and calcareous shale. Joints and small fractures within the limestone do not propagate within the shale. Conjugate normal faulting is considered as the main deformation mechanism within James Limestone. Conjugate normal faults form narrow zones with high fracture density. Fracture swarms or clusters are therefore associated to subseismic faults, or faults that cannot be detected with conventional seismic methods. Between these fracture swarms, the background fracture density may correspond to regularly spaced joints.

The presence of subseismic faults and fracture swarms has been confirmed from the horizontal sections of Henderson-1. But there is uncertainty about the orientation and spacing of these features. The probable impact of a normal fault affecting the Lower Cretaceous, located just 2 km east of Henderson-1, has been evaluated using Poly3D (Thomas, 1993). The results indicate that this fault does not affect significantly the orientation of subseismic faults at the well site under normal-fault loading conditions, but these results depend on the geometric configuration and the slip distribution of the fault which are not well constrained. A better, more accurate, model can be built using 3D seismic data. Nevertheless, the current results indicate that orientation of subseismic faults depends exclusively on loading conditions. Three different possible scenarios for orientation of the normal-fault state of stress are modeled, based on our understanding of the tectonic evolution of the region and some proposed interpretations: (1) parallel to the fault affecting James Limestone; (2) parallel to the faults at surface and to the current state of stress; and (3) quasi-normal to the fault affecting James Limestone. These three different hypothesis are referred as scenario A, B and C respectively. The models based

on stress boundary conditions confirmed the expected fracture orientation but did not allow ruling out any of the possibilities.

Two additional models, using strain boundary conditions, showed similar results when compared to an equivalent model using stress boundary conditions, but the shear-strain model showed different fracture inclination. Stress boundary conditions are difficult to determine since there is uncertainty about stress magnitudes. On the contrary, strain boundary conditions could be constrained if the three-dimensional geometric configuration of the reservoir was known. In consequence, more appropriate boundary conditions can be specified from the analysis of 3D seismic data.

The interposition of shale and limestone layers within James Limestone, allows the use of gamma ray log as an indicator of small faults. We have applied a systematic method for detection of subseismic faults in the horizontal sections of Henderson-1. Six faults were identified in the upper wellbore but just two in the lower. Since the tool depends on the presence of contrasting lithologies on opposite fault walls, it cannot be used to identify faults with very small offset. The use of other parameters sensible to rock fragmentation, like drilling rate, may be helpful to identify damage zones associated with incipient faults, but this requires calibration and further analysis.

Attachment B

Evolution Of Conjugate Normal Faults In Sedimentary Sequences With High Brittle/Ductile Contrast

Abstract

Conjugate normal faults are a common geometric fault configuration that occurs in different natural settings at different scales. The origin and evolution of these faults is poorly understood. Here we propose a model for evolution of conjugate normal faults in sedimentary sequences with high brittle/ductile contrast. The model is based on field observations and numerical modeling. It is shown that conjugate normal faults patterns are the result of sequential events of slip and hierarchical splay jointing. Basically, slip along ductile bedding surfaces or layers generates a stress perturbation that results in the formation of subvertical splay joints. Slip along these subvertical splay joints (sheared joints) generates a new stress perturbation that creates a new set of splay joints. The azimuth of the new set of splay joints is parallel to the sheared joints, but they have opposite dip direction. The new splay joints constitute new low-friction planes that slip, forming a set of conjugate normal faults. Interaction between bed-confined, subparallel sheared joints (normal faults) is required in order to form larger normal faults.

This sequential evolution of conjugate normal faults results in a particular shape that we call *the tectonic bowtie*. The limits of the bowtie are defined by the parent (synthetic) normal fault and the main two opposite-dipping antithetic faults. In respect to the parent fault, the antithetic faults are located at the upper quadrant of the hanging wall and the lower quadrant of the footwall. The zones between the parent fault and the antithetic faults are characterized by high-density of fractures, or fracture swarms, which are parallel to the parent fault. The bowtie can be well-preserved or partially preserved depending upon the actual geometry of the parent fault.

The deformation documented in this paper is associated to faults with less than 1 m of vertical offset, and therefore corresponds to faults that are below the limit of seismic resolution. Nevertheless, these fracture swarms may have a significant impact on both rock impedance and rock permeability.

Introduction

Conjugate normal faults have been observed in a variety of natural settings and at various scales, from outcrops (i.e. Aydin, 1973; Horsfield, 1980; Selsing, 1981; Antonellini and Cruikshank, 1992; Watterson *et al*, 1998; Young, 2000) to 2D and 3D seismic data (Nicol et al, 1994; Gutierrez and Nur, 2001). They have been found in a variety of tectonic settings, at the crest of salt anticlines (Nilsen *et a*l, 1995), salt withdrawal basins (Maoine and Pickford, 2001), in the hanging walls of listric normal faults (Dula, 1991), and associated to wrenching (Gutierrez and Nur, 2001). They have been also generated in sandbox and clay models (McClay, 1995; Withjack *et al*, 1995). They are particularly conspicuous in the northern Gulf of Mexico basin (Diegel *et al*, 1995; Peel *et al*, 1995).

Understanding the genesis and mechanical evolution of these faults may have important connotations for certain disciplines like earthquake seismology and hydrology, but especially for the oil industry, given that conjugate normal faults can play a significant role in accumulation of hydrocarbons and reservoir compartmentalization (Jev *et al*, 1993; Morley et al, 1990; Gutierrez and Nur, 2001). According to Ferril *et al* (2000), conjugate normal faults may be an important factor in the development of permeability anisotropy in reservoirs. Understanding the potential effects of normal faults on reservoir

permeability provides a key to understanding the development of migration pathways and traps, reservoir compartments and baffles, and reservoir permeability anisotropy. From the rock physics point of view, understanding the structure of subseismic faults provides a way to interpret and model their impact on elastic properties and, therefore, in seismic impedance and anisotropy.

This study documents and analyzes the evolution of conjugate normal faults in a specific sequence of sedimentary rocks. The main characteristic of these rocks is the interposition of layers with different mechanical properties: thick layers of brittle, low-porosity sandstone interpose with thin layers of ductile, fissile shale. The study documents field observations from the same locality, throughout which the progressive evolution of faulting can be discerned. Basically it shows the evolution of conjugate normal faults from splay joints created by slip along bedding surfaces, associated with thin shale layers or clay-rich lamina. Slip along these subvertical splay joints creates a secondary set of splay joints, trending in the same azimuth of the former ones but dipping in opposite direction. These new surfaces slip again due to the remote stress field, but the sense of shear differs from the original splay joint because of the different orientation in respect to the remote stress. The final result of this sequential alternation of slip events and subsequent splay joints is a system of conjugate normal faults with high density of fractures in between.

All the deformation described in the sequence of evolution of these conjugate normal faults is associated to faults with less than 1 m of dip-slip, which is probably the total displacement. Significant deformation and gouge core-zones are reported for faults with about 5 m of slip (Myers and Aydin, *in prep.*). Such faults are rarely documented in geological literature because of their small slips and are impossible to image within the ranges of frequencies and velocities of current seismic reflection techniques. They can hardly be identified with seismic interpretation techniques such as coherence analysis. The impact of these features on seismic and permeability is different than the impact of cracks and joints. Fracture swarms due to normal faults are predicated to be parallel to the fault and have better connectivity than joints. A random distribution of cracks may be a better representation for fracture swarms, since splay joints are always formed out of the plane of the parent sheared joint.

Field Observations of Conjugate Normal Faults

The following description comes from outcrops in the Andean foldbelt. All the pictures come from the same outcrop, near a thrust fault. In the following discussion is implicit the interpretation that normal faults formed at an early stage of deformation, when the beds were not tilted. We are not going to extend on the discussion of the tectonic setting, since our analysis is focused on two aspects: (1) the role of weak, ductile layers as shale; (2) the progressive fragmentation associated to normal faults. In that regard, the sequence of evolution that we are describing here can be applied to other tectonic settings.

The different stages of fracture development and progressive fracturing can be summarized in the following steps:

1. Slip along ductile layers or bedding surfaces due to high pore pressure, subtle inclination or any other factor that lowers the coefficient of friction. This slip alters the stress field within the overlying brittle layer (figures 1 and 2).
2. Generation of splay fractures (joints) within the adjacent brittle layers due to the stress field created by slip along the ductile layer (figures 1 and 2).
3. The new subvertical splay joints are weak planes with favorable orientation for failure under a normal state of stress. These splay joints transform into small faults and slip along these planes generates a new stress perturbation around the splay joints.
4. Generation of new splay joints derived from the stress perturbation created from slip along the pre-existing splay joints. These second-order splay joints have the same strike than the previous ones, but opposite dip (Fig. 3).
5. Slip along the second generation of splay joints. This failure process transforms the splay joints into small normal faults, with the same strike than the previous normal faults but opposite dip. They form, therefore, the conjugate or antithetic set of the conjugate normal faults system (figures 4 and 5).
6. Link and interaction of meter-scale faults create a larger scale (10 m) fault system, which presents a more complex fracture architecture, but still preserves the basic elements of the system.

The sequence of deformation and fracturing starts with slip along weak planes. The coefficient of internal friction of shale or clay-rich layers can be lower than brittle layers, because of montmorillonite content (Lockner and Beeler, 1999), organic-matter content or just anisotropy. It could also be decreased by pore pressure (Hubbert and Rubey, 1969) derived from water, gas or oil content. Just a few degrees of inclination can produce slip along a low friction layer. Our field observations indicate that slip along shale layers does occur and generates splay fractures in the adjacent brittle layer (figures 1 and 2). A noteworthy example is the development of a tail fracture at the pinching out of a shale lamina, and the absence of fractures beyond this point (Fig. 1). The presence of splay fractures created from slip along bedding planes dipping on both directions, is actually evidence that these splay joints formed before beds were tilted, otherwise they should always be dipping in just one direction.

After slip has occurred, the stress field around the slip patch changes to an asymmetric distribution of areas with higher tension (or lower compression) and areas of higher compression. Our interpretation of the observations is that splay joints are generated within the tensional quadrants (or least compressive quadrants) either at the boundary of the slipping patch, or from irregularities within the brittle layers. In any case, some of these joints propagate all the way through the brittle layer, up to the next bedding surface (figures 2 and 3). These splay joints are inclined about 80° to 60° respect to the quasi-horizontal bedding surface.

Once these splay joints have been created, the stress distribution has also changed, since the stress perturbation has been equilibrated by the formation of splay joints. The inclination of the new splay joints is favorable for slip under a normal-fault state of stress (Anderson, 1942; Hubbert, 1951). As shown in the mechanical modeling, dip-slip along these recent splay joints transform them into normal faults and create a new perturbation of the stress field. Slip along the bedding planes may also occur, and the interaction between these two weak planes, the bedding surface and the splay joint, produces the asymmetric localization of maximum tension (or least compression) at the left-upper and right-lower quadrants in respect to the splay joint.

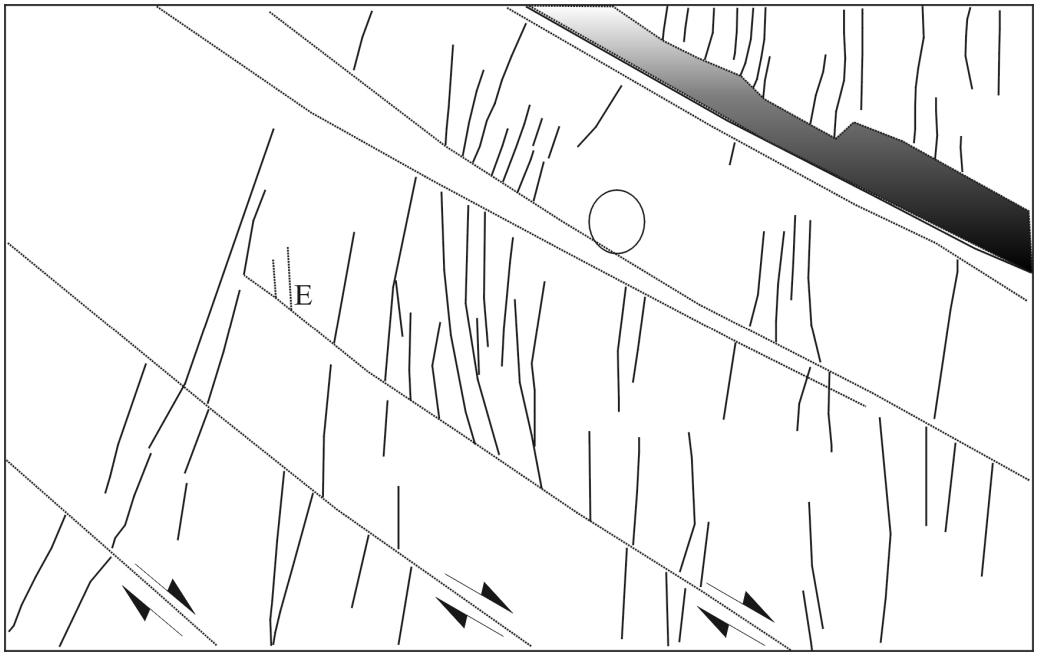

Figure 1. Photograph (above) and sketch (below) of an example of the generation of subvertical splay joints (subvertical lines) due to slip along clay-rich or shale lamina (dotted, subhorizontal lines).

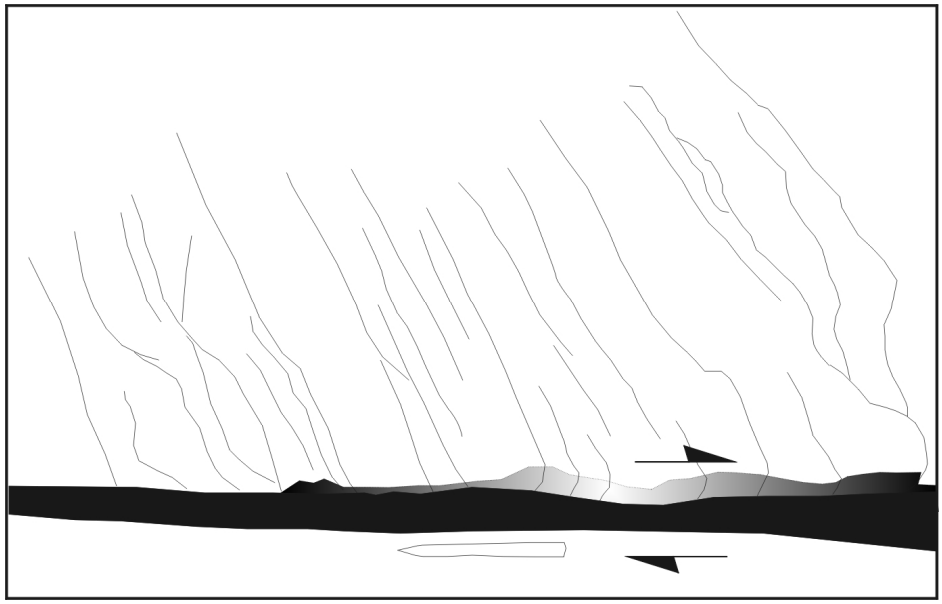

Figure 2. Example of development of splay joints due to slip along a shale layer about 3 cm thick. The angle between the layer and the splay joints is about 70°, as predicted from fracture mechanics models.

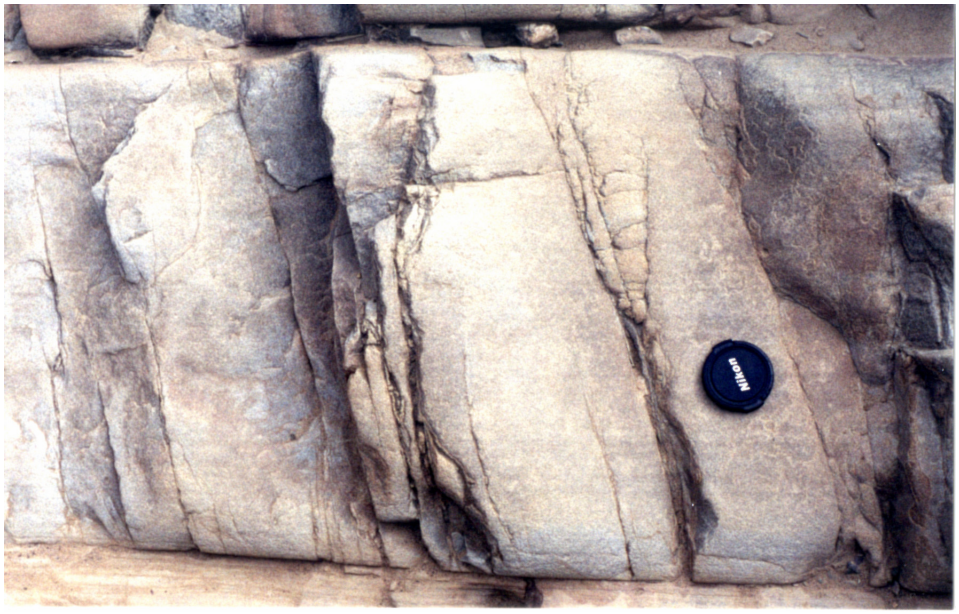

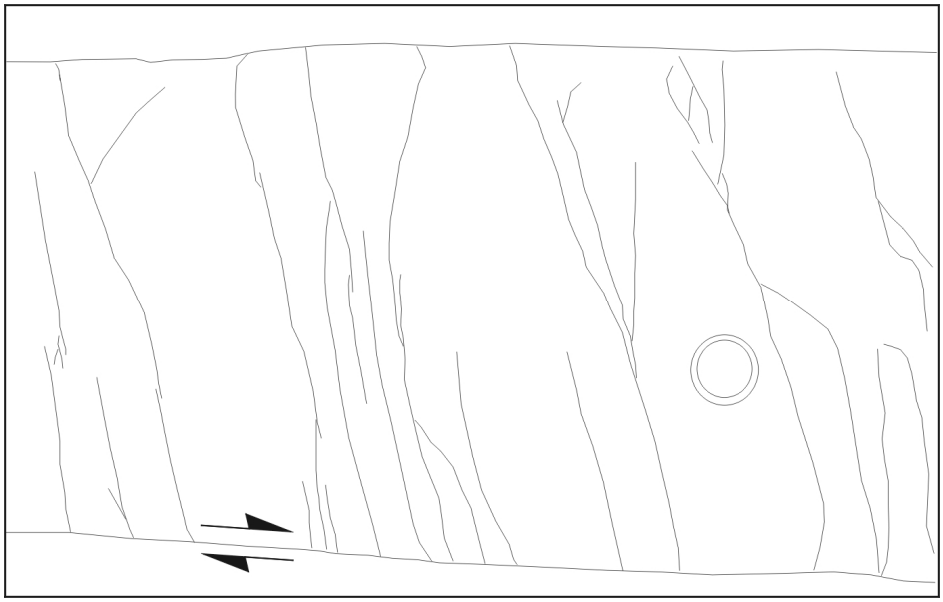

Figure 3. Splay joints formed from slip along a sandstone-sandstone bedding surface, with some clay-rich lamina. Notice that the splay joints propagate upwards from one bedding interface to the other, but abut against the upper interface.

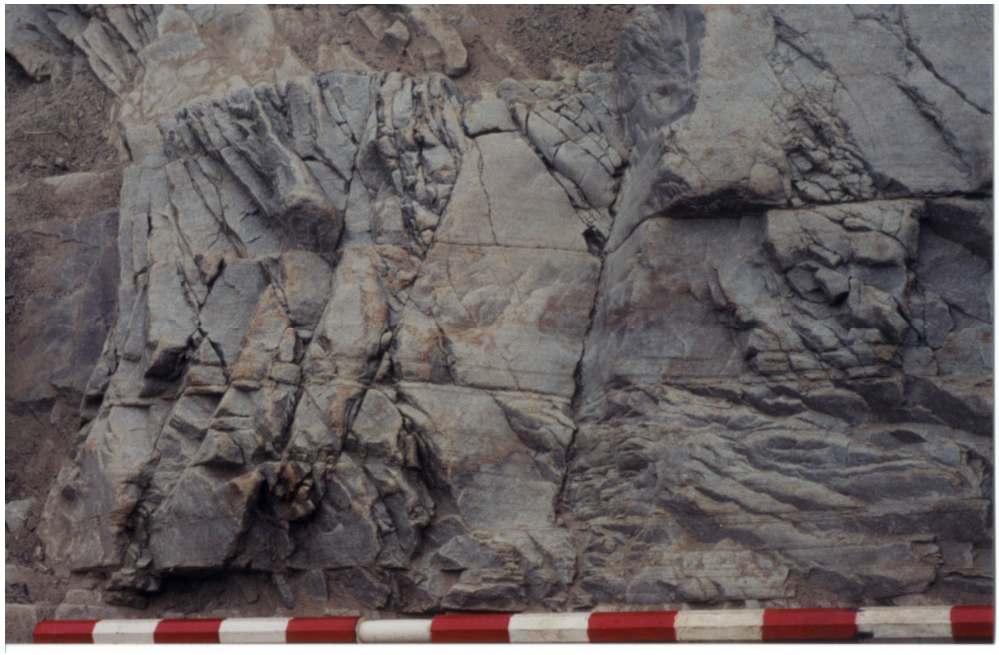

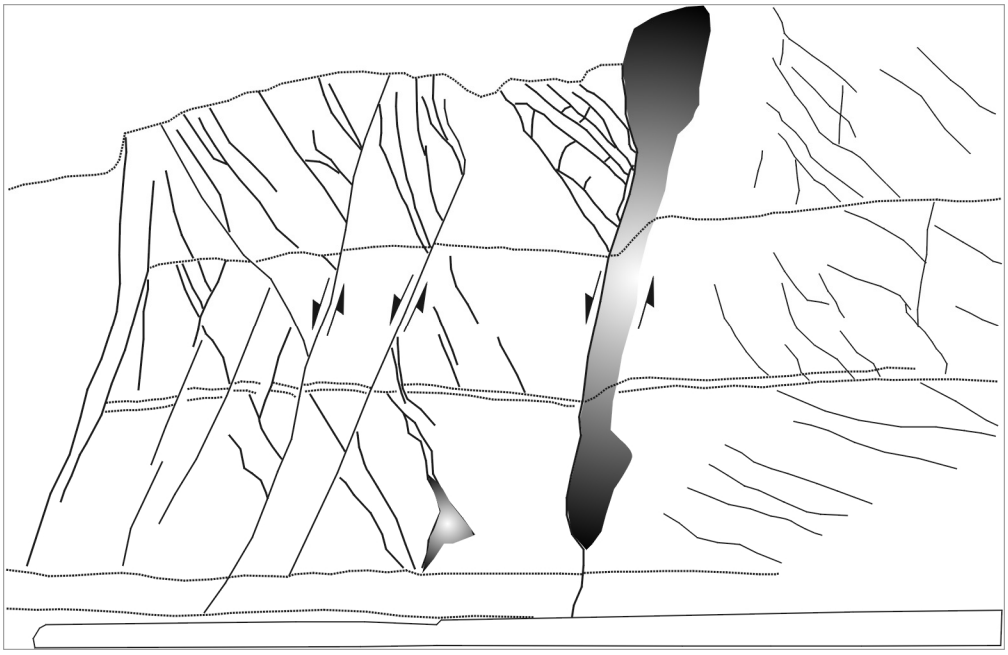

Figure 4. Subvertical splay joints, formed due to slip along bedding planes, constitute new weak planes along shear failure may occur. Slip along these splay joints (arrows indicating shear) generates a new stress perturbation that creates new splay joints. If the failure is dip-slip, as this case, these new splay joints will have the same azimuth of the previous one but opposite dip direction.

The new stress distribution facilitates the generation of a new set of splay joints. They form either at the boundary of the pre-existing splay joint or away from it, but within the tensional (or least compress ional) quadrants. These new splay joints have the same strike as the former splay joints (now normal faults) but opposite dip, these splays will constitute the new conjugate or antithetic set of normal faults. Formation of these splay joints equilibrates the stress perturbation. The asymmetric distribution of these new splay joints gives rise to a bowtie shape (figures 4 and 5), occasionally described as an X-shaped style (Young, 2000). Since they are generated from the parent fault, the new splay joints do not cut across that fault, they abut against it.

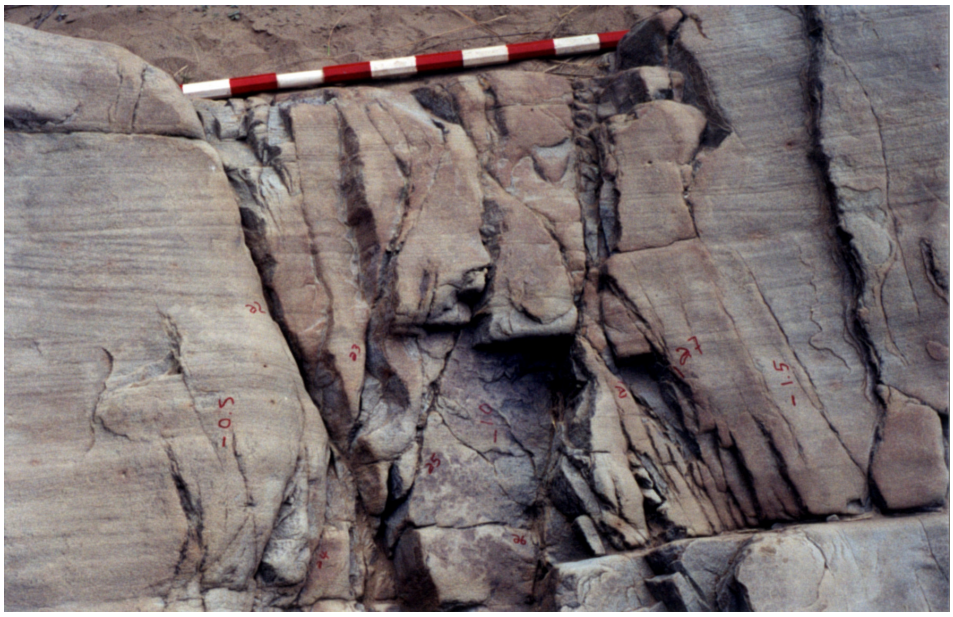

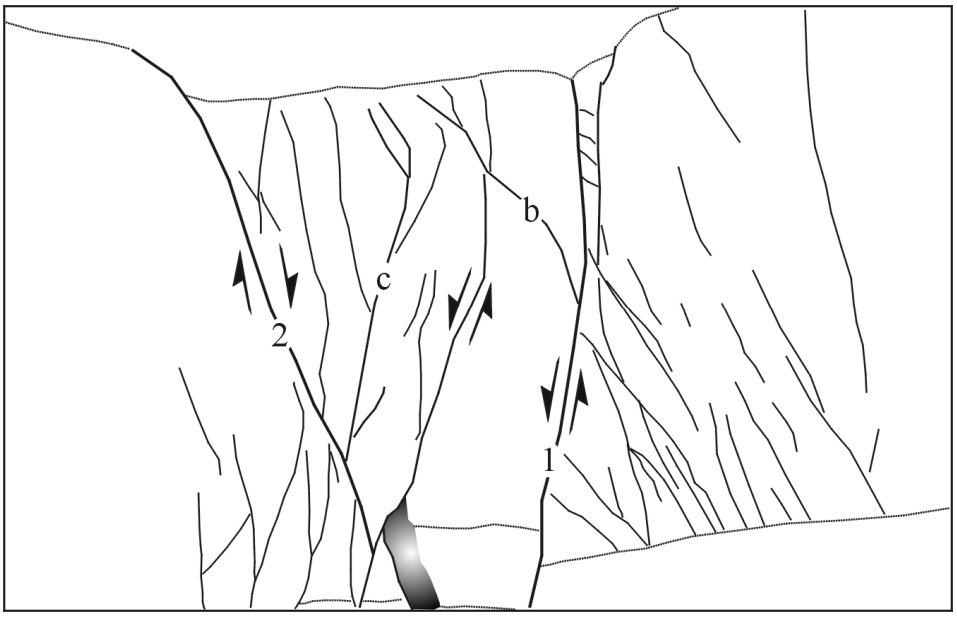

Figure 5. Slip along first generation of splay joints transform them into normal faults (1), and creates the stress perturbation that generates a new set of splay joints (b). Slip along these new splay joints transform them into an antithetic or conjugate set of normal faults (2) and creates a new stress perturbation that generates another set of splay joints (c). This sequential and hierarchical process creates a narrow zone with localized high-density of fractures.

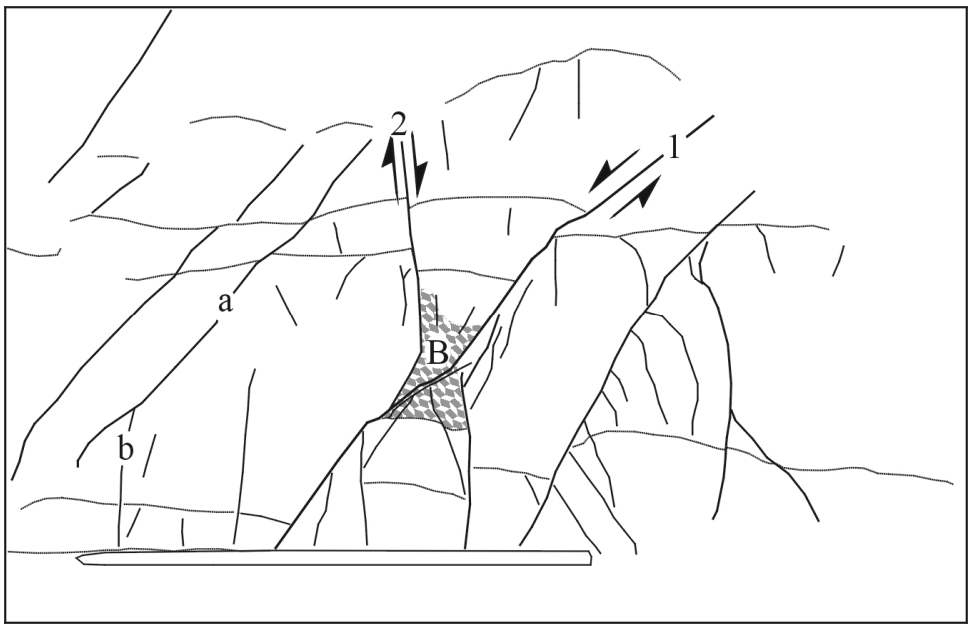

Figure 6. The tectonic bowtie. The parent fault (1) creates two sets of conjugate secondary faults (2), at the tensional quadrants of the stress perturbation created by slip along the parent fault. The secondary faults do not cut across, but abut against the parent fault. A region affected by mechanical compaction and brecciation (B) is created at the intersection of the parent and secondary faults.

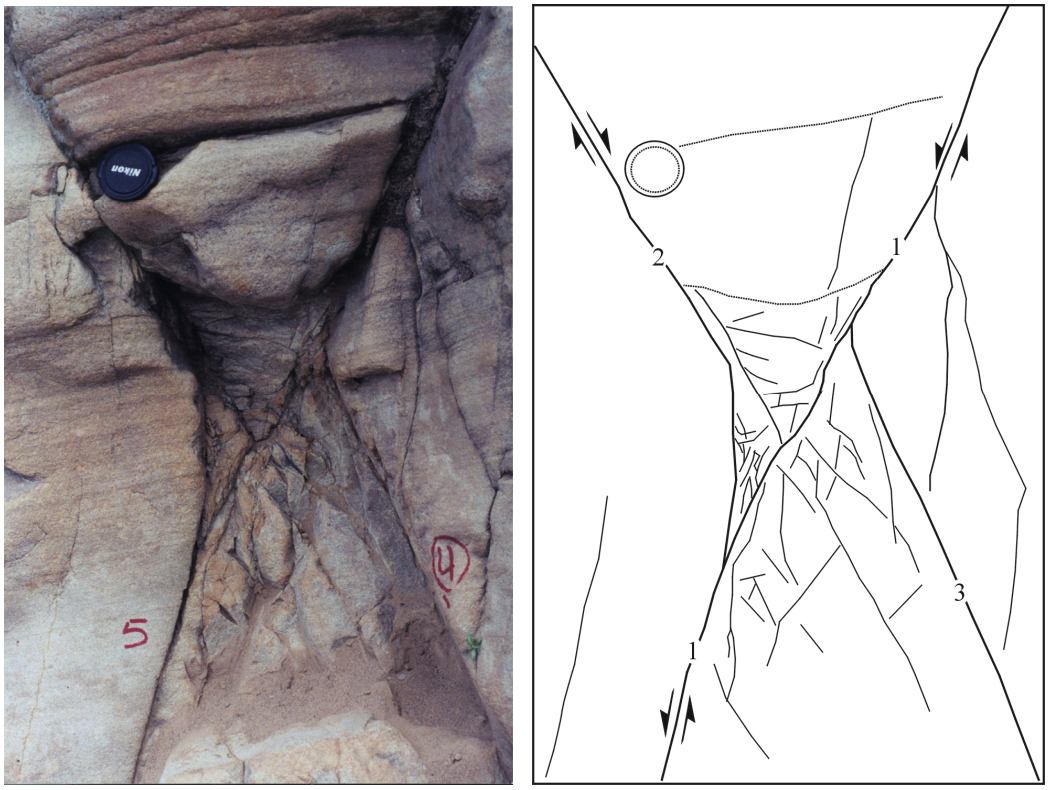

Figure 7. Picture and sketch showing a detailed view of the intersection between the parent fault, 1 in the sketch, 5 in the photograph, and the secondary faults, 2 and 3 in the sketch (one of them 4 in the photograph). Notice the contrast in fragmentation of the rock between the faults and the rock outside the faults. Also notice that the secondary faults bend and abut against the parent fault.

These second-generation splay joints are also favorably oriented for failure. Slip along these surfaces and the parent fault creates a new perturbation of the stress field. Because of the orientation of the surfaces, the areas of higher tension are now localized between the conjugate faults at the extremes of the parent fault, and outside the conjugate faults near the fault intersection. This configuration leads to the localization of fracturing and fragmentation within the area bounded by the conjugate normal faults. At the intersection of the parent fault and the main secondary faults new fractures may form outside the fault boundaries and may accommodate some of the slip along the new conjugate or antithetic fault. Slip along the conjugate antithetic faults can also be accommodated either by fracturing, slip along the parent fault or mechanical compaction. The antithetic faults do not cut across the parent fault (see figures 5 and 6), since both fault systems are active.

The next step in this process is the interaction and link of meter-scale faults to form a larger scale (10 m) normal fault. The product of this process is a more complex fault geometry and architecture of the damage zone (figure 6). The trace of the faults is not

smooth and continuous and staircase steps can be formed at the intersection of fault segments and bedding surfaces. Local high-density fracture zones, derived from the fault segments, can stand outside the main fault zone, but the overall architecture of the conjugate fault system is preserved since new, larger conjugate faults are formed. Faults can be ranked according to their age relationships since younger faults are derived from slip along older ones. The fragmentation is localized within the zone between the main fault and the main secondary faults (figure 6). No evidence of younger faults cutting older faults was observed within these early stages of fault development.

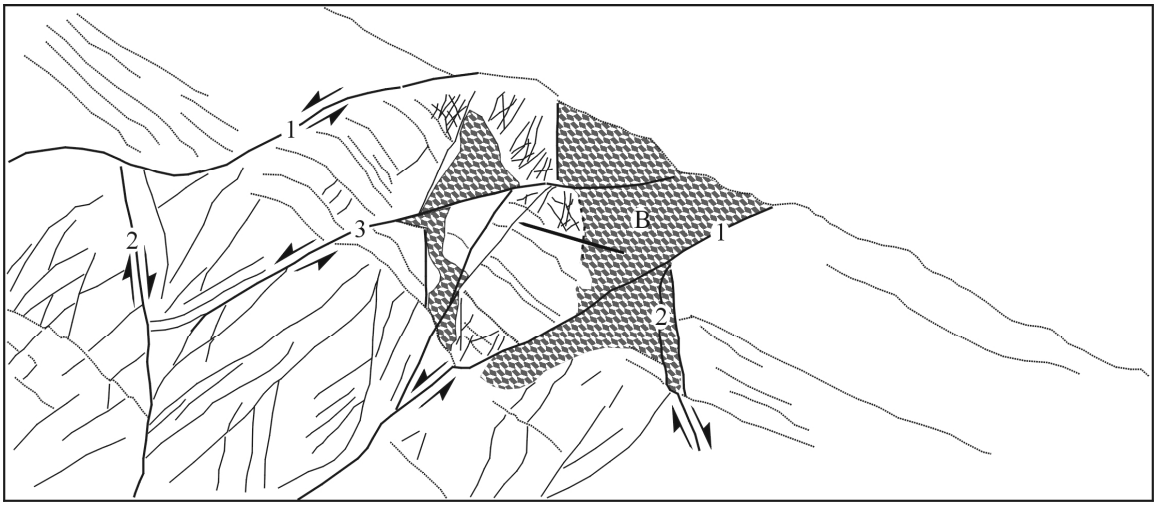

Figure 8. Tilted conjugate normal faults at 10-m scale. The number on each fault indicates the age relationship and the hierarchy of the faults: (1) parent faults created by link and interaction of

splay fractures derived from slip along bedding planes: (2) main conjugate or antithetic set formed from splays created by slip along 1: (3) secondary synthetic set formed from splays created by slip along 2. The stick scale is 1.5 m long. B= Breccia zones

Numerical Modeling

In order to test the mechanical feasibility of the ideas derived from our field observations, we ran a numerical modeling using Poly3D (Thomas, 1993). Poly3D is a computer program that calculates the displacements, strains and stresses in elastic whole or half-space using planar, polygonal-shaped elements of displacement discontinuity (Maerten et al, 2001). The polygonal element must have minimum three sides. Poly3D will calculate the component of displacement, strain and stress at specified points or observation grids defined by the user. The polygonal element may represent a fault or fracture surface, or a portion of it. The displacement discontinuity is constant on each element, therefore to model a fault or a fracture it is necessary to use more than one element. Indeed, accuracy of the model near the fault surface relies on the density of elements used to model the surface.

General Specifications

The models described below have the same specified remote stress boundary conditions and present solutions for both slip and stress distributions around the fault planes. The remote stresses are specified in terms of the effective stress (σ) defined as (Hubbert and Rubey, 1951):

$$\sigma_{xx} = S_{xx} - Pp \quad (1)$$

where S_{xx} are the principal stresses and Pp is pore pressure. The applied stress boundary conditions for all the cases were:

$$\sigma_{11} = -1 \text{ MPa}$$
$$\sigma_{22} = 0 \text{ MPa}$$
$$\sigma_{33} = -10 \text{ MPa}$$

since a normal-fault stress state is characterized by $S_{33}<S_{11}<S_{22}$, using the convention of tension as positive. S_{33} is the vertical stress or overburden. S_{11} and S_{22} are the

maximum and minimum horizontal compressive stresses. The material properties are also the same for all the models:

Young's modulus (E) = 50 GPa
Poisson's ratio (n) = 0.25

The boundary conditions in the cracks are always ttb=000. Which means traction (t) in the crack for dip-slip is zero, traction (t) for strike-slip is zero and Burger's vector (b), or displacement, for opening mode or interpenetration between the crack surfaces is zero. The observation grid, to visualize the results, is an YZ-plane that bisects the models.

Sequential modeling

We have run three different models trying to reproduce the deformation sequence we observed in the field. So the modifications made at one step are a direct consequence of the results obtained in the previous step. All the following graphs are color coded in the same way, from blue to red and white. Blue colors represent higher values, green colors intermediate, reds colors lower values and white is the lowest one. In the observation grid we are always showing the first invariant of the stress field (σ_{mean}), whereas in the fault surfaces we are showing the displacement field.

The first model simulates slip along the bedding surfaces. It contains, therefore, just a 7-m-long squared crack tilted 3° in respect to the horizontal X-axis. This crack represents a slip patch within a bedding plane. The results show that slip along this surface creates and asymmetric perturbation of the stress field, as expected (Fig. 9). Green colors in the observation grid show areas of lowest compression and reds show areas of highest compression. The maximum slip in the crack (blue at the center) is just 0.11 mm. The mean stress varies from –6.59 MPa to 1.107 MPa, therefore even for a very small slip like this we obtain localized tension near the tip of the slipping surface. This tension combined can be enough to initiate a joint at that point. The probable propagation direction of that joint is at a high angle in respect to the slipping surface, about 70° according to models derived from mixed mode crack propagation, as shown in Fig. 10.

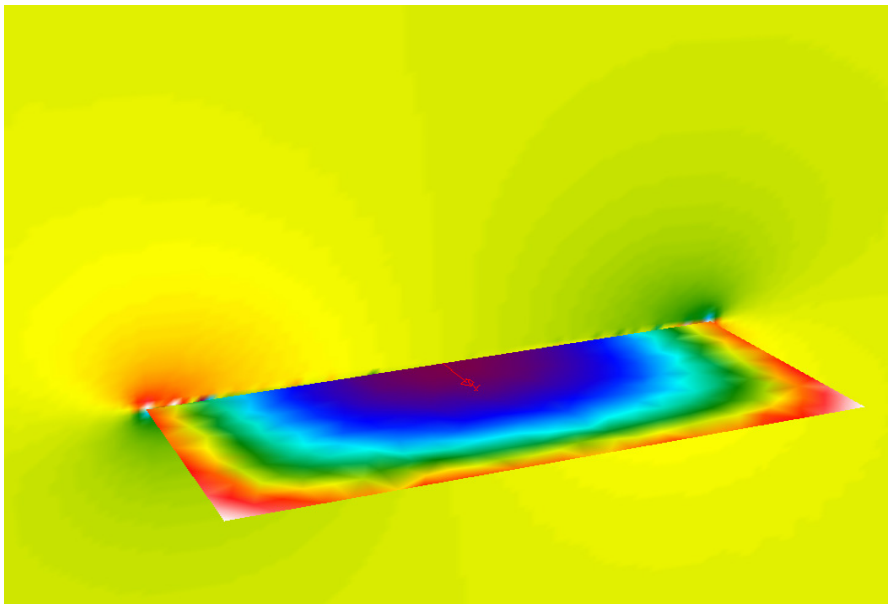

Figure 9. First model: slip along a subhorizontal free-traction surface. The vertical plane is the observation grid, showing the mean stress field. The subhorizontal plane is the crack with the displacement field within the crack. Blue colors indicate higher values; reds and white colors indicate lower values.

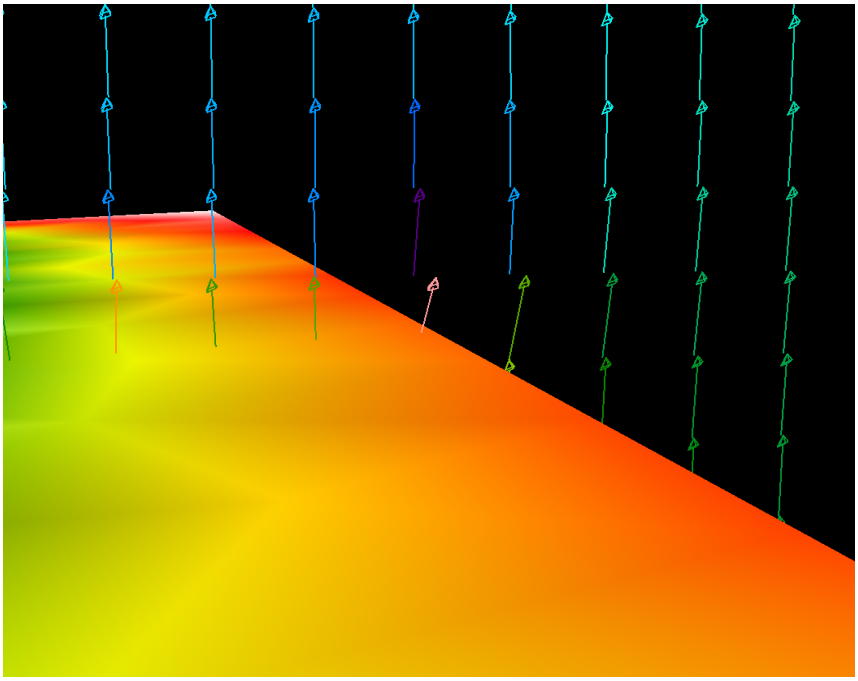

Figure 10. First model: slip along a subhorizontal traction-free crack. The arrows indicate the orientation of the maximum compressive stress (1) at the tip of the crack, therefore the direction of propagation of new joints. Notice the slightly tilted arrows at the crack tip.

The second model incorporates a new crack, generated at the tip of the pre-existing one. The new crack is 5 m high by 7 m long, so it represents a joint that after being created at the tip of the slipping surface has growth up to the next bedding plane and extended laterally along the slipping patch. The results obtained in this model (Fig. 11) show that the stress distribution due to slip along both the subhorizontal and the subvertical cracks is asymmetric in respect to the subvertical crack, but not in respect to the subhorizontal one. The maximum slip in the subvertical surface is 0.2 mm and its distribution is symmetric through the crack The maximum slip along the subhorizontal surface is 0.5 mm, larger than in the previous model, and its distribution is skewed to the intersection with the new crack (Fig. 12). The maximum tensile stress is 5.68 MPa (blue colors) and the maximum compressive stress is –14.94 MPa (white). The areas where new joints will most likely be generated are shown in green colors and bounded by yellow in Fig. 9. Notice that the localization of yellow colors coincides closely with the location of main secondary splays in figures 3, 4 and 5. The possible orientation of new joints generated at this point can be inferred from the orientation of the maximum compressive stress around the subvertical crack (Fig. 13), which coincides with the orientation of the secondary splay joints observed in figures 3 and 4.

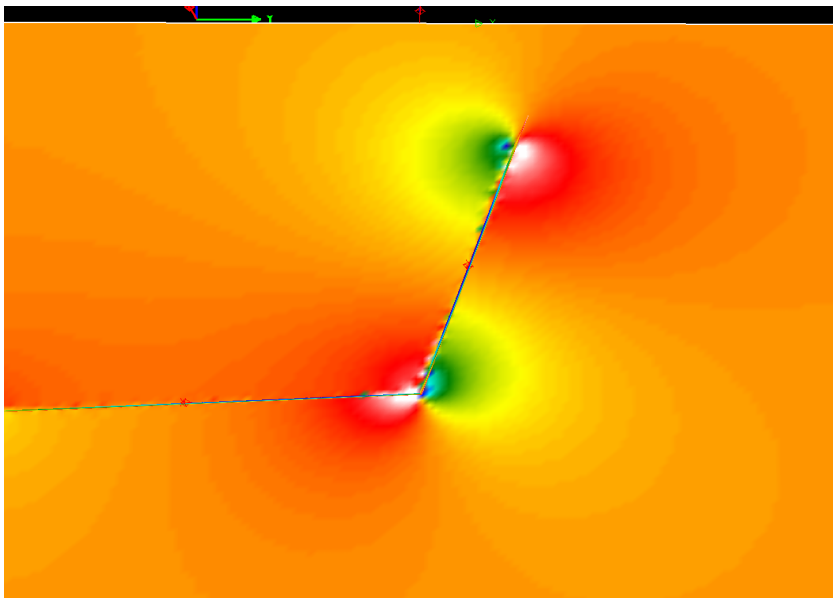

Figure 11. Second model: Slip along intersecting subvertical and subhorizontal traction-free surfaces. Side view showing the distribution of $_{mean}$ within the observation grid. Blue colors indicate highest tension; reds and whites indicate areas of highest compression.

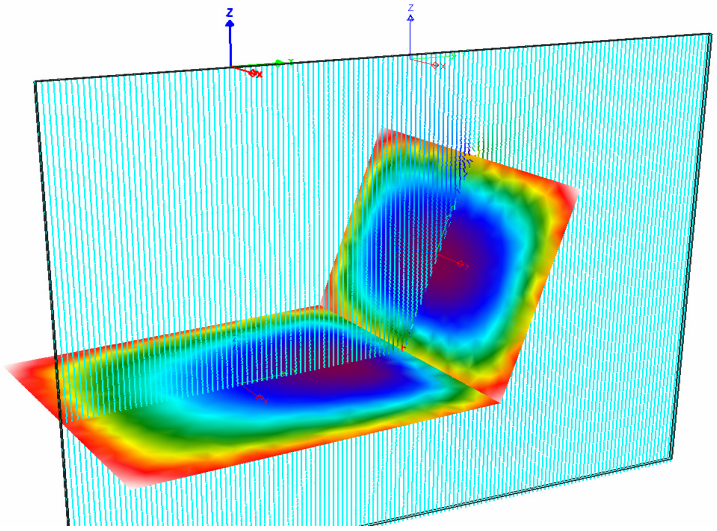

Figure 12. Second model. View showing the observation grid (light blue plane) and the crack surfaces with the slip distribution. Blue colors indicate larger slips; reds and whites indicate lower slips. Notice the asymmetry of slip distribution in the subhorizontal crack.

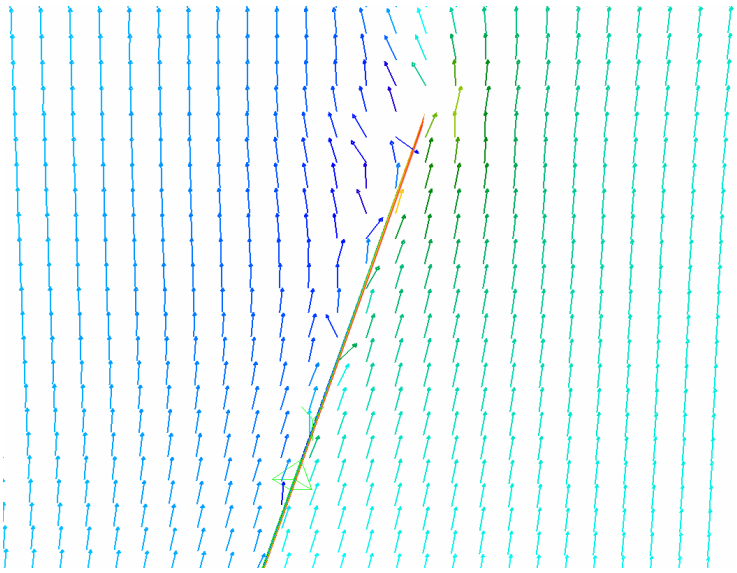

Figure 13. Side view showing the orientation of maximum compressive stress (s1) at the tip of the subvertical crack. Notice the arrows with opposite dip direction than the crack plane, at the left side of the crack. These arrows show the possible orientation of new joints generated within the areas of highest tension (lowest compression) around the crack**.**

Finally, the third model incorporates the splay joints that can be created in the areas of highest tension of the second model (Fig. 13). The two new cracks are parallel to the pre-existing subvertical crack, but have opposite dip direction. They are 2 m high by 5 m wide. The results from the model illustrate that regions between the main subvertical crack and the conjugate cracks are zones of very low compressive stress, or probably tension (Fig. 14). In fact, the areas of tension are now localized in a vertical band around the main fault, but the regions bounded by the cracks are the areas of lowest compressive (highest tensile) stress. These results are in agreement with our field observations (figures 4, 5 and 6), and corroborate our interpretation about evolution of the conjugate normal faults. The slip distribution along the faults is shown in Fig. 15. Slip along the bedding surface is null, slip along the new splay cracks is about 0.3 mm, and slip along the main crack has now increased up to 1.1 mm. Therefore, the presence of the new joints inhibits slip along the bedding surface but enhances slip along the subvertical crack. The range of σ_{mean} magnitudes is now between 8.32 MPa (maximum tension) and –27.42 MPa (maximum compression).

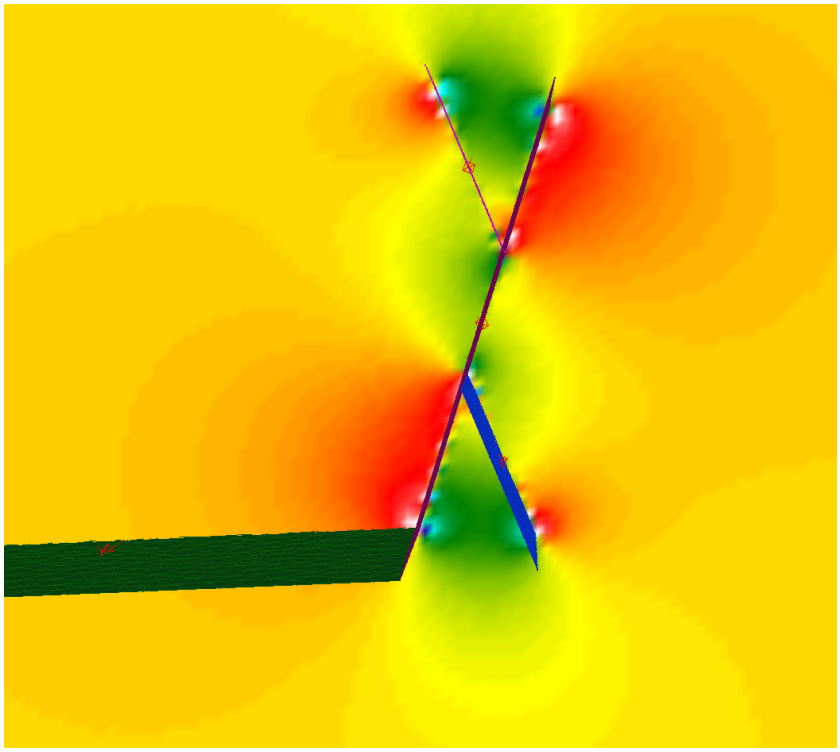

Figure 14. Third mode. Distribution of the mean stress due to slip along both the old and the new splay cracks (or splay joints). Reds indicate areas of highest compression; blues and greens correspond to regions of tension or lower compression. Notice that tension (or least compression) is mostly localized within the two opposite-dipping sheared joints (or conjugate normal faults).

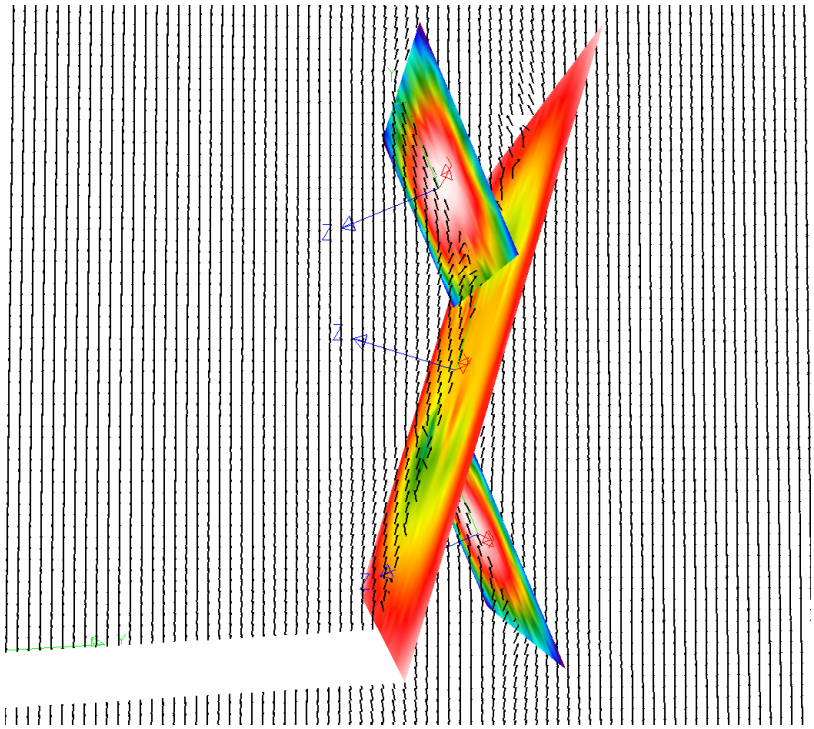

Figure 15. Third model. Slip distribution within the faults (colors) and orientation of the maximum compressive stress (black arrows). In the subvertical cracks, reds and whites correspond to larger offsets (shear is negative), and blues and greens to lower offsets. Notice that in the parent fault the slip distribution is not symmetric anymore. Also notice that slip along the subhorizontal crack is negligible.

Discussion

Both the field observations and the numerical modeling provide evidence to propose a progressive and sequential deformation steps for the development of conjugate normal faults. The basic mechanism is that slip along weak planes generates a stress perturbation that creates a new set of cracks or joints. The formation of these joints implies relaxation of the perturbed stress field. Shear failure due to the remote stress field creates a new perturbation of the stress around the sheared planes and produces a new set of splay joints. The relationship between old sheared joints and new splay joints is hierarchical, and the younger features abut against the older ones. The formation of long, unconfined normal faults requires the interaction between subparallel, bed-confined faults.

The sequence and mechanisms of deformation proposed in this paper are somewhat similar to those proposed by Segall and Pollard (1983), Maertel (1990), Cooke *et al* (2000) and Myers and Aydin (*in prep.*). Nevertheless, whereas most of these papers deal with the evolution of strike-slip, this paper deals with the evolution of normal faults. The

faults described in this paper show high-density fracture zones, even though slip along these faults is less than 1 m, and a few cm in some cases. The high-density of fractures and fragmentation observed, is considered to be the result of rock brittleness. On the other hand, it has been shown that the deformation has been localized because of slip along weak, ductile, clay-rich layers. Therefore, it can be concluded that the same style of deformation should be expected in rocks with the same high brittleness/ductility contrast.

Finally, since the conjugate faults are subparallel to the parent fault, and the fracture swarm is confined within both the conjugate and the parent fault. It is expected that fracture swarms formed by this mechanism will be parallel to the parent fault. A direct consequence of this observation is that faults with very small offset, seismically not detectable, can create subparallel fracture swarms that may have a significant impact on rock permeability and impedance.

Conclusions

We are presenting a model for genesis and evolution of conjugate normal faults in sedimentary sequences with high contrast in rock ductility/brittleness. The model is based on field observations made in the same locality, where different stages of fault evolution are present. These stages are basically: (1) slip along the bedding surfaces between the ductile and the brittle layers; (2) generation of subvertical splay joints due to the stress perturbation created by the bedding-parallel slip; (3) slip along the subvertical splay joints; (4) generation of secondary splay joints, derived from the pre-existing faulted joints, strike-parallel but with opposite inclination that the parent joints; (5) slip along both the secondary and the main splay joints, forming a conjugate set of normal faults; (6) link and interaction of meter-scale faults to form a larger (10 m) fault; (7) incremental slip along this new fault, generation of larger conjugate faults and localization of rock fragmentation within the area bounded by the parent fault and the main conjugate fault.

The observations and models presented in this paper indicate that a system of conjugate normal faults in a normal-fault state of stress will create high-density fracture zones, confined within the parent and the main secondary faults. The shape of the conjugate fault system resembles a bowtie, and it is proposed to use the term *tectonic bowtie* for that geometry. The tectonic bowtie defines a zone where fracture density is higher than the adjacent rock due to conjugate normal faults. There can be variations in the fault configuration due to the actual dimensions of the parent fault, but in general it can be established that a higher density of fractures is expected at the hanging wall near

the upper fault tip, and at the footwall near the lower fault tip. In a normal-fault state of stress, the orientation of these fracture swarms is expected to be parallel to the parent fault.

The deformation documented in this paper is associated with faults with less than 1 m of vertical offset. A high degree of fragmentation can be expected in rocks with high brittleness, even with a few meters of offset. As a consequence, high fragmentation associated to subseismic faults should be expected in highly brittle rocks. The impact of subseismic faults on seismic impedance, seismic anisotropy and permeability anisotropy can be as important as the impact of cracks, joints and the stress field.

Attachment C

Probabilistic modeling of fracture density constrained by outcrop data and geomechanics

Abstract

This paper presents a methodology for building static geologic models of fractured reservoirs using outcrop data, stochastic simulation and geomechanics. First, a comparison of outcrop and subsurface data shows the relevance of outcrop information to characterize deformation mechanisms and spatial heterogeneity at subsurface. Then, the descriptive statistics of fault and fracture systems collected at an outcrop is used to create geostatistical models of fracture-density distribution, which replicate the spatial heterogeneity observed at the outcrop.

The probability density function characterizing the fracture density within a limited area may vary between exponential, lognormal or normal, depending on the degree of fracture localization. The mean of these distributions depends not only on the strain, but also on the stratigraphic architecture. In general, low fracture-density zones are the rock volumes with relatively low shear-strain, bounded by localized fracture swarms associated with faults. Mean fracture density within the faults' damage zones can be up to one order of magnitude higher than the background fracture density.

We test the applicability of sequential Gaussian simulation (SGS), and sequential indicator simulation (SIS) to generate models of joint frequency. SGS can reproduce the

statistics of the outcrop data, even though cannot replicate the architecture. Variogram-based SIS can generate large and continuous high fracture-density zones, which resemble the fracture corridors associated with small faults, however it cannot successfully handle diverse orientations for the background, low-fracture-density zones.

In order to generate models with different orientations for large faults, small faults and joints, an object-based indicator approach is used. In this approach, maps of the spatial distribution of faults and damage zones are first generated using the statistics of outcrop data, stochastic techniques and some geomechanical principles. The maps are filled with SGS realizations for high and low fracture-density zones, using the cookie-cutter technique. This technique assures the lateral continuity of high-density fracture corridors associated with faults, regardless of the orientation of the low-density fracture background.

Outcrop Analog Information for Fractured Reservoirs

Seismic methods for fracture detection provide direct information about the elastic properties of the reservoir; however the limited resolution, the inherent uncertainties, and the on-uniqueness of the solutions to the inversion of seismic properties require the use of additional information about the subsurface fracture system, such as analog outcrop data (Teng, 1988). In her dissertation, Teng (1998) showed that seismic analysis can help to constrain predictions of the spatial distribution of fracture densities, which have a very important impact on fluid flow responses. However, the inference of fracture densities from shear wave splitting analysis can be unreliable due to uncertainties about some key parameters, including fracture specific stiffness, fracture orientation, and background lithology. She explained that the length, connectivity and orientation distribution of the fractures are crucial factors of the fracture systems and have important impact on fluid recovery.

Outcrop studies supply significant qualitative and quantitative information for geologic modeling of fractured reservoirs. From the perspective of reservoir characterization, there are two basic approaches to tackling this problem, stochastic simulation of fracture networks and deterministic modeling based on mechanical

principles. For any of these approaches, outcrop descriptions provide constrains to the modeling parameters since: (1) they show the spatial variability of fracture density at reservoir scale, which can be translated to the subsurface modeling using statistical parameters such as the mean, the standard deviation, and the distribution function of fracture populations; (2) they indicate the different mechanisms that generate fractures for specific rock types and deformation styles; and (3) they fill the scale gap between core, well-log and seismic data (Figure 1).

Contrary to the case of stratigraphic heterogeneities, where detailed outcrop studies and geostatistical modeling are widely used for reservoir modeling, there are not standard techniques to incorporate outcrop studies or geostatistical methods into the modeling of fractured reservoirs. In the case of stratigraphic heterogeneities, conceptual stratigraphic models, combined with relevant statistical data, are commonly used as constrains or conditioning data for sequential Gaussian simulation (SGS) or sequential Indicator simulation (SIS). On the contrary, the direct use of outcrop data for geologic modeling of fractured reservoirs is commonly limited to the comparison of fracture orientation at outcrops and subsurface.

The problem we intend to solve in this paper is: how can we translate the descriptions and data obtained at outcrops, into relevant information for seismic modeling and engineering characterization of fractured reservoirs? Along the paper, we are going to use the results we obtained from an outcrop analogue study in Bolivia, and explore different geostatistical techniques to create an static numerical model that reproduce the spatial heterogeneity observed at the outcrops. The following section reviews the data and main conclusions derived from an outcrop study of faults and fractures in a fold and thrust belt (Florez et al, 2003). After that section, we discuss the statistical parameters required to generate geostatistical models. Then, the results from SGS and SIS are presented. That section also shows an alternative technique for modeling fracture density; in this method an indicator map of tectonic-facies (or damage-zone indicator) is modeled, and then filled with realizations from SGS using different fracture densities. Finally, we discuss the results in terms of their applicability to seismic and reservoir modeling, and present the conclusions.

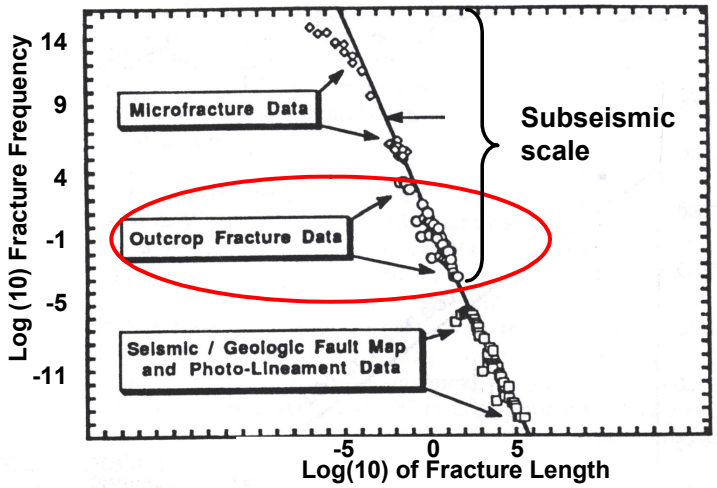

Figure 1: Log to Log plot of fracture length frequencies, normalized for area and class intervals (after Heffer and Bevan, 1990). The figure shows how outcrop data fills the gap between core or well-log data, and seismic data.

Results from an Outcrop-Analog Study

In their study of the Abra del Condor-Canaletas (ADCC) fold and thrust belt, Florez et al (2003) show that faults and joints occur at different scales in a hierarchical fashion, as a consequence of progressive shearing (Figure 2). The first generation of fractures is an orthogonal set of joints, one parallel and the other perpendicular to bedding azimuth. Shear along these joints transformed them into small faults and created new sets of fractures, oblique to the bedding attitude. Linkage of these small faults facilitated the formation of larger faults with significant strike-slip offset. Shear along bedding planes created sub-vertical splay joints that induced the formation of conjugate normal faults. Subordinate strike-slip and normal faults are concomitant products of compressive deformation, in this thrust belt.

They also document a hierarchical correspondence between spacing of structural heterogeneities and stratigraphic architecture. They measured spacings of joints and outcrop-scale faults along the backlimb of Abra-del-Condor Anticline, and subdivided the structural discontinuities into four main groups: joints, small faults, intermediate faults, and fault zones. Spacing of joints, small faults and intermediate faults have a lognormal distribution, whereas spacing of fault zones shows a normal distribution. The mean of these distributions is about the same as the thickness of the confining stratigraphic intervals. Therefore, spacing and dimensions of joints and faults have a first-order relationship to the thickness of the confining stratigraphic sequences.

Conceptual Model

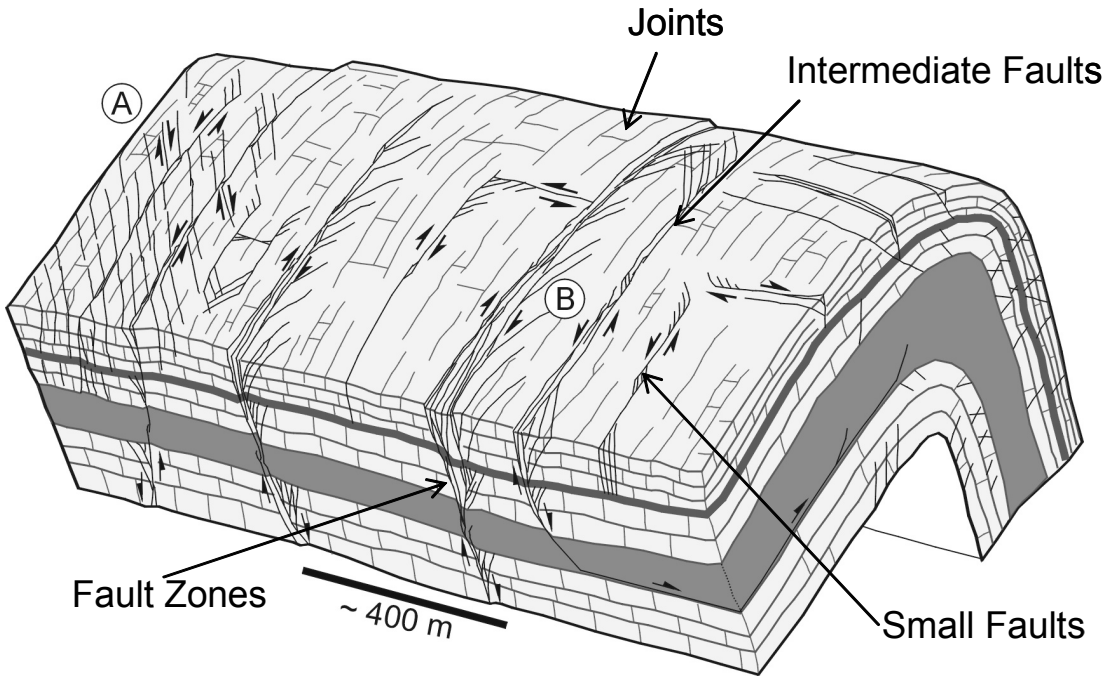

Figure 2: Conceptual model of distribution of faults and fractures in a fault-cored Anticline (Florez et al, 2003).

Figure 2 presents a conceptual model of faults and fractures in an anticline, as part of a fold and thrust belt (Florez et al, 2003). The model shows the hierarchical relationships that exist between faults zones, intermediate faults, and smaller features (sheared joints, joints and splay joints). This conceptual model also illustrates the relationship between the scale of stratigraphic intervals and structural discontinuities. Fault zones extend across the different stratigraphic intervals (which form a sequence), whereas intermediate faults stop at the thick, shaly interval in the middle. Similarly, sheared joints can extend throughout some bedding surfaces but may stop at meter-thick shale layers. Finally, joints are confined within single mechanical layers and splay joints related to flexural slip always abut against the sheared bedding planes.

For the case of ADCC fold and thrust belt, the dominant faults and fractures are either parallel or normal to the structural grain (determined by the folds axis), however in areas with relatively higher deformation the splay fractures extend and form a secondary oblique pattern, as illustrated in Figure 3. This variation in fracture pattern is schematically illustrated in Figure 2, and is interpreted to be associated with an increase in shear strain. Therefore, as a general rule we can establish that areas with parallel faults

and joints are characteristic of low shear-strain domains, whereas areas with abundant oblique splay fractures are characteristic of intermediate shear-strain domains. The high shear-strain domains are basically the wide damage zones associated with fault zones.

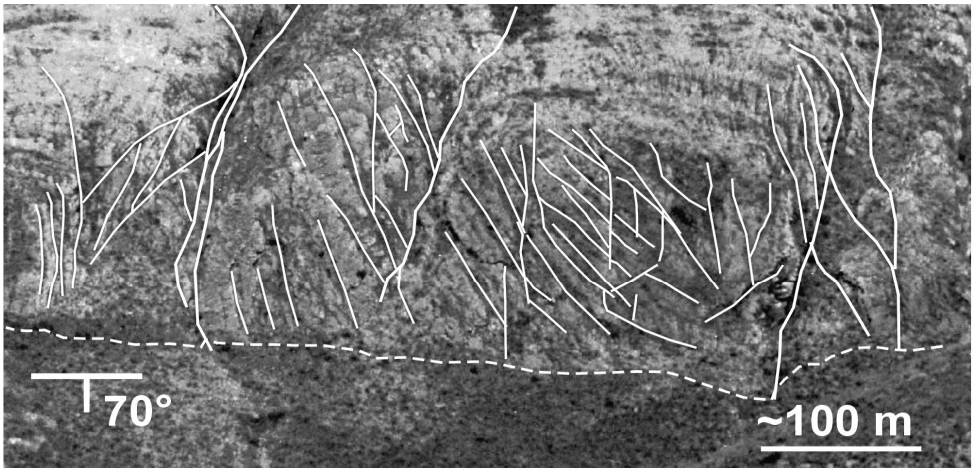

(a)

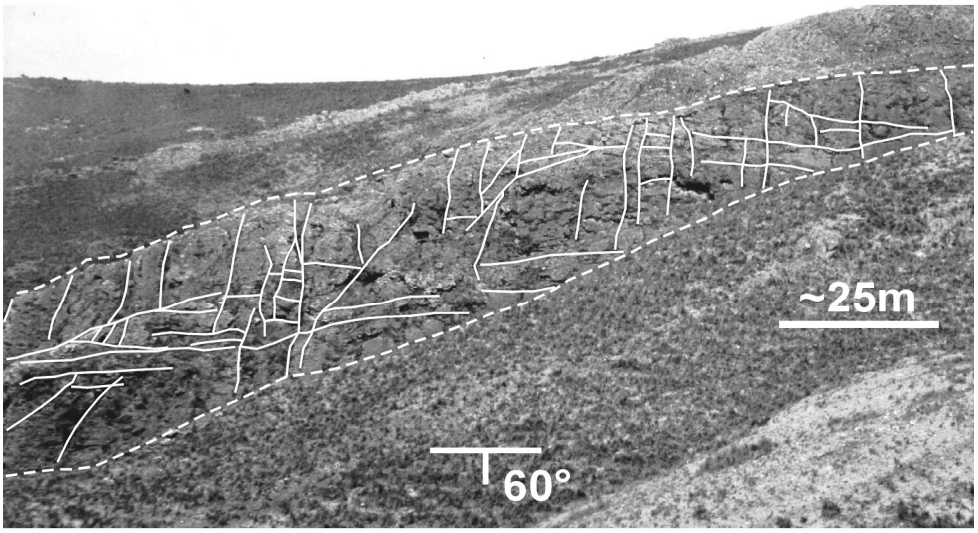

(b)

Figure 3: Variation of fault and fracture patterns along the azimuth of an Anticline: (a) Dip-parallel faults bound a block with dominant oblique splay fractures, a geometry characteristic of intermediate shear-strain areas; (b) orthogonal (dip-parallel and azimuth-parallel) small faults and joints, a geometry characteristic of low shear-strain domains.

Factors Controlling Fracture Density

Shear strain and stratigraphic architecture are among the most important factors controlling the distribution of fracture density. Other well-known factors are rock

properties, stretch and loading mode (Wu and Pollard, 1995; Bai and Pollard, 2000). In order to illustrate the influence of shear strain on fracture density, we took the fracture density scanline shown in Figure 4, and calculated the average fracture frequency for intervals of 50 m (164 ft). Shear strain was obtained by adding the offset of all the faults within each interval and dividing by 50. In order to avoid the effect of the adjacent fault zones, we excluded the initial and the final 50-m intervals. The results show the increment of fracture density as shear strain increases (Figure 5).

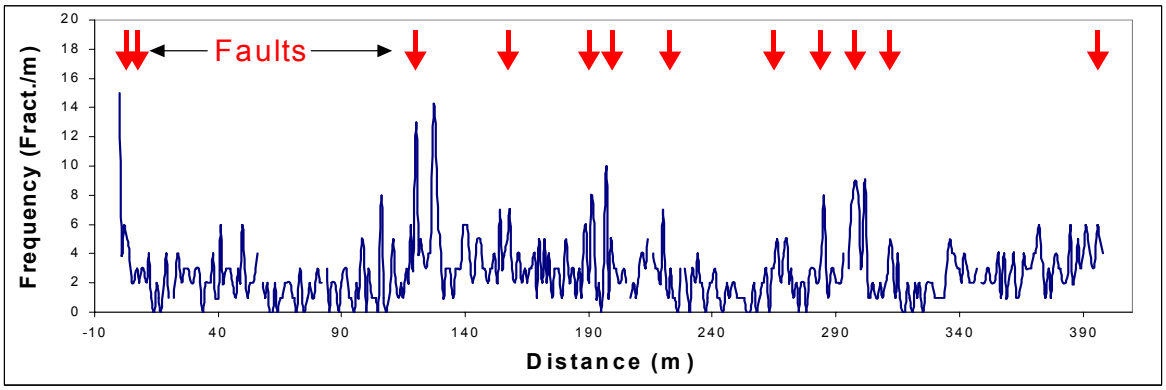

Figure 4: Scanline along the azimuth of a low shear-strain block, within the backlimb of the Abra del Condor Anticline.

The effect of stratigraphic architecture on fracture density is likely to be similar to that of bed thickness on joint spacing, explained by Wu and Pollard (1995), and Bai and Pollard (2000). Narr (1990) defined the fracture spacing index *(I)* as the ratio of layer thickness *(T)* to average fracture spacing *(S)*. Bai and Pollard (2000) proposed that there is a threshold value of the fracture index $(I \leq 1)$, above which the stress field between the joints becomes compressive, inhibiting additional joint infilling. They called this stage fracture saturation.

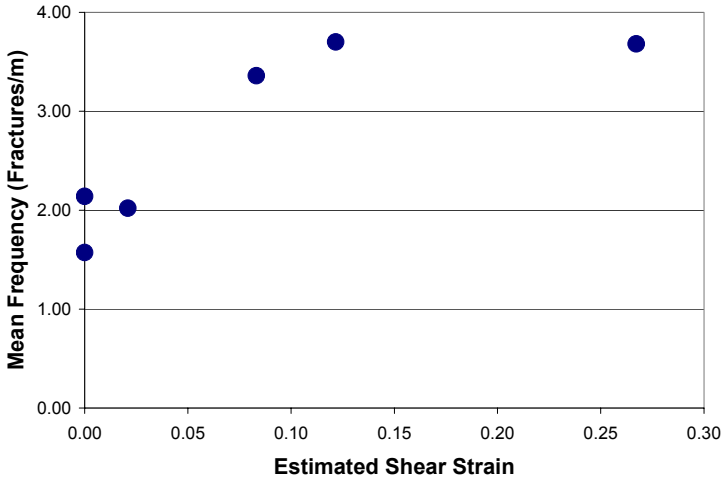

Figure 5: Relationship between mean fracture frequency and shear strain, as calculated for intervals of 50 m along the scanline shown in Figure 4. The extremes of the scanline are not taken into account because of the influence of the adjacent fault zones.

In the ADCC fold and thrust belt, fracture-density distributions vary between exponential, lognormal and normal (Figure 6). These variations depend on shear strain and scale of observation. Florez et al (2003) reported a lognormal distribution for fracture spacing, which is the inverse of fracture density. Lognormal distributions of joint spacing have been previously documented by Rives et al (1992) and Narr and Suppe (1991). Narr and Suppe (1991) also found a relationship between the median of joint spacing and thickness of mechanical layers. Rives et al (1992) showed that distribution of joint spacing may evolve from exponential to lognormal and normal, as extensional strain increases. The former shows a clear lognormal distribution, whereas the later has a more symmetric, less skewed, distribution.

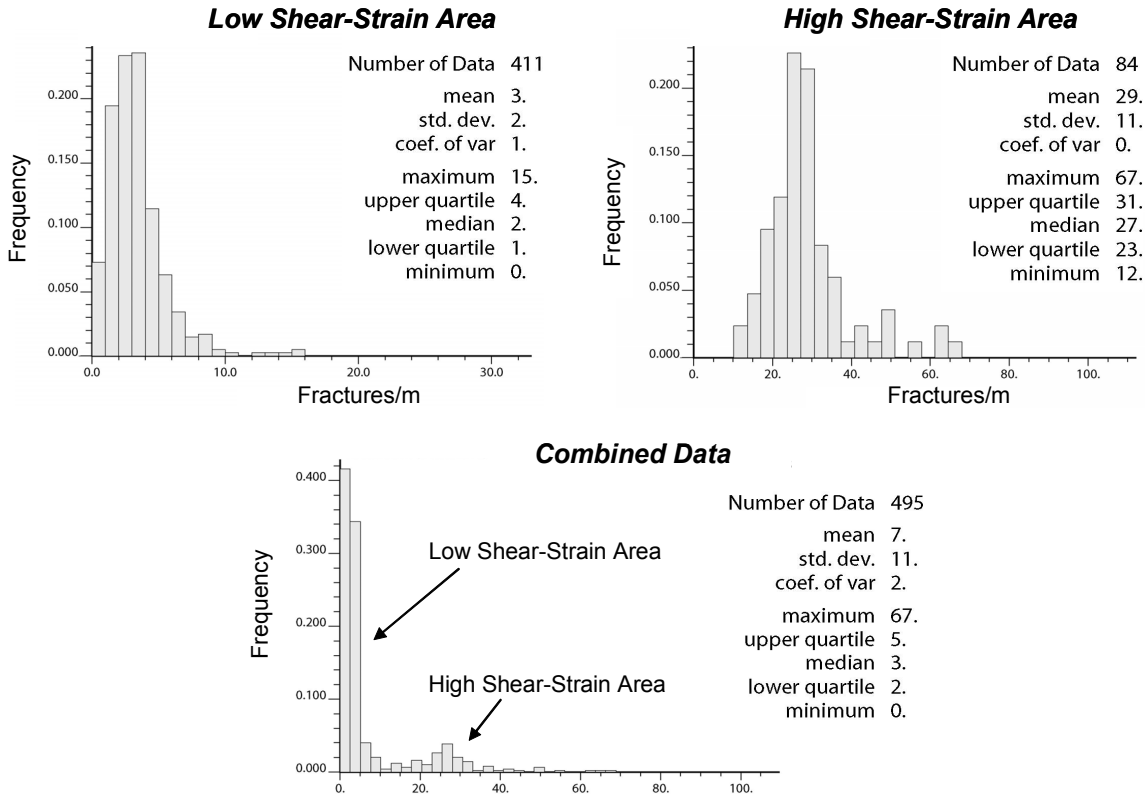

Figure 6: Histograms of fracture densities from areas with different degree of shear strain.

Stratigraphy, Fracture Spacing and Fracture Density Distributions

There is a correspondence between the mean spacing of the different fracture hierarchies (from joints to fault zones) and the stratigraphic unit that contains them: mean joint spacing keeps a first order relationship with respect to bed thickness, while mean spacing of small faults is of the same order of magnitude as thickness of sandstone bedsets (Florez et al, 2003). Similar relationships exist between intermediate faults and parasequences and fault zones and sequences. Figure 2 shows a conceptual model of the scale hierarchical correspondence between fractures and stratigraphic sequences. Since there are other factors, like stretch (Wu and Pollard, 1995; Bai and Pollard, 2000) or shear strain, that also influence fault and joint spacing, this correspondence should be expressed as:

$$M = \alpha T \tag{1}$$

where α is a factor related to shear or extensional strain, *T* is the thickness of the relevant stratigraphic package and *M* is the mean spacing of joints or the confined faults.

Table 1: Mean spacing of fracture hierarchies, compared to the thickness of the confining stratigraphic intervals. The ratios T/S for intermediate and small faults increase significantly at Canaletas outcrop (higher shear-strain), with respect to those observed at the backlimb of Abra del Condor Anticline.

Outcrop	Fracture Hierarchy	Mean Spacing (S) in m	Confining Stratigraphic Interval	Measured or Estimated (~) Thickness (T)	Ratio T/S
Backlimb of Abra del Condor Anticline; Huamampampa Formation	Fault Zone	361	Sequence (Fm.)	365	1.0
	Intermediate Fault	59	Parasequence Set	64.5	1.1
	Small Fault	4.2	Bedset	10	2.4
	Joint	0.49	Bed	~0.5	1.0
Canaletas; Santa Rosa Fm.	Intermediate Fault	19.3	Parasequence Set	82.5	4.3
	Small Fault	0.76	Bedset	~9	11.8

Comparison to Subsurface

There are many similarities between the fracture systems observed at outcrops and those found at subsurface, as can be deduced from the comparison of FMI images from the subsurface to the outcrop data. First of all, fracture orientations found at subsurface resemble those observed at outcrops (Figure 7). The abundance of oblique fractures with respect to either bedding-dip or bedding strike, is interpreted as the result of the development of splay fractures from cross and axial faults. The dominant orientation depends on the sense of shear. For example, in the case illustrated in Figure 7, the subsurface data show fracture orientations consistent with left-lateral shear along cross faults.

The comparison between subsurface and outcrop observations indicates that fracture mechanisms and types are also similar. Figure 8 shows a high-fracture density zone overlying ay a low-fracture density interval. A similar contrast in fracture density has been observed at outcrops, and corresponds to the damage zone associated with small normal faults, like the one shown at the bottom of Figure 8. Similarly, splay fractures abutting against bedding surfaces are observed both at subsurface and at outcrops, as illustrated in Figure 9.

In spite of the striking similarities found, the extrapolation of outcrop data to the subsurface must be cautiously done. Many fractures may have formed during the uplifting process of rocks to the surface. In addition to this, the confining stresses at subsurface will tend to close many of the fractures observed at outcrops. This implies the need to apply a correction factor, from fracture densities measured at outcrops to the expected fracture densities at subsurface.

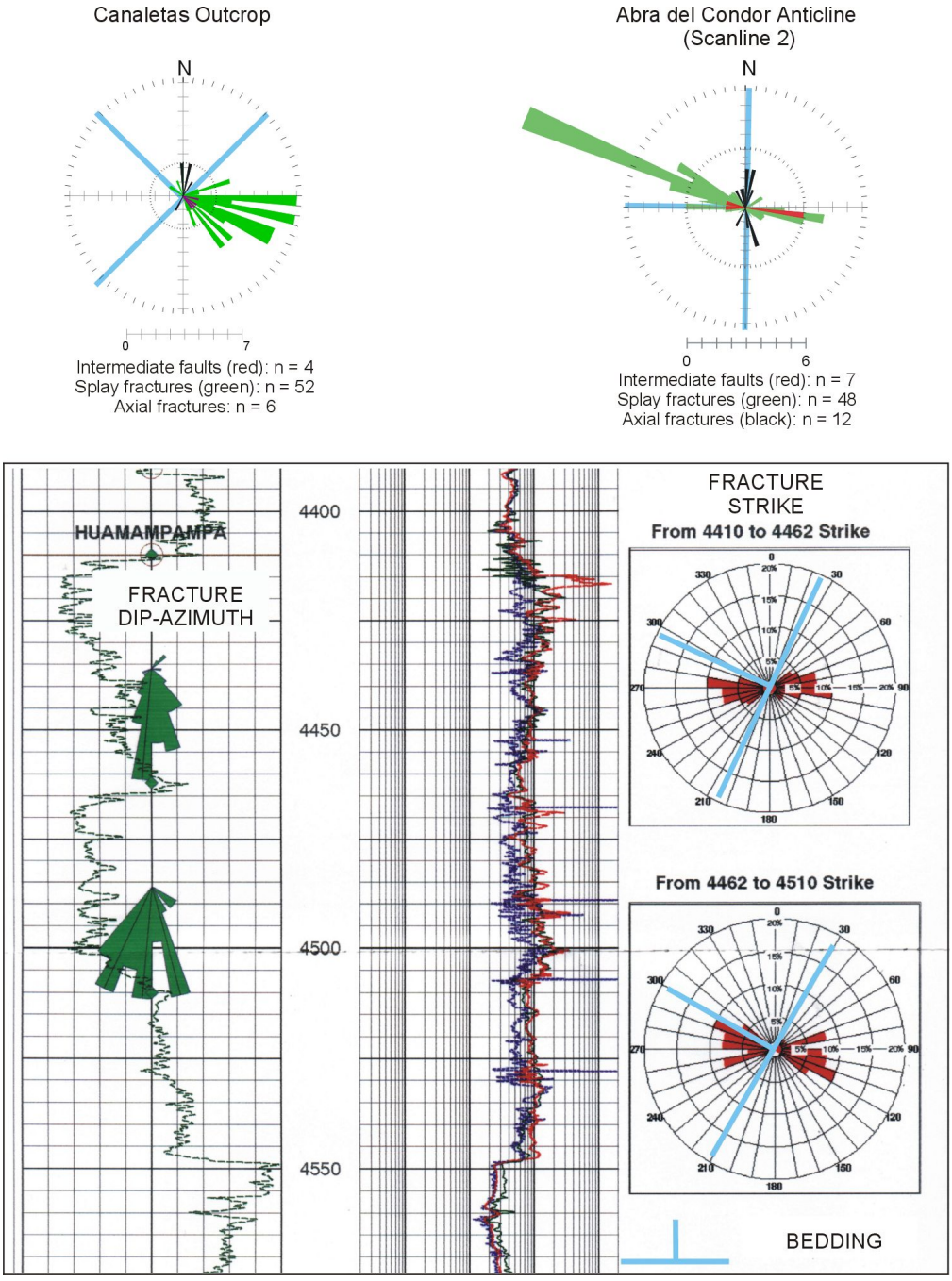

Figure 7: Comparison of the orientation of fracture systems at outcrops (above) to the fracture systems at subsurface. The hierarchical relationships observed at outcrops provide a conceptual framework to understand the observations at subsurface.

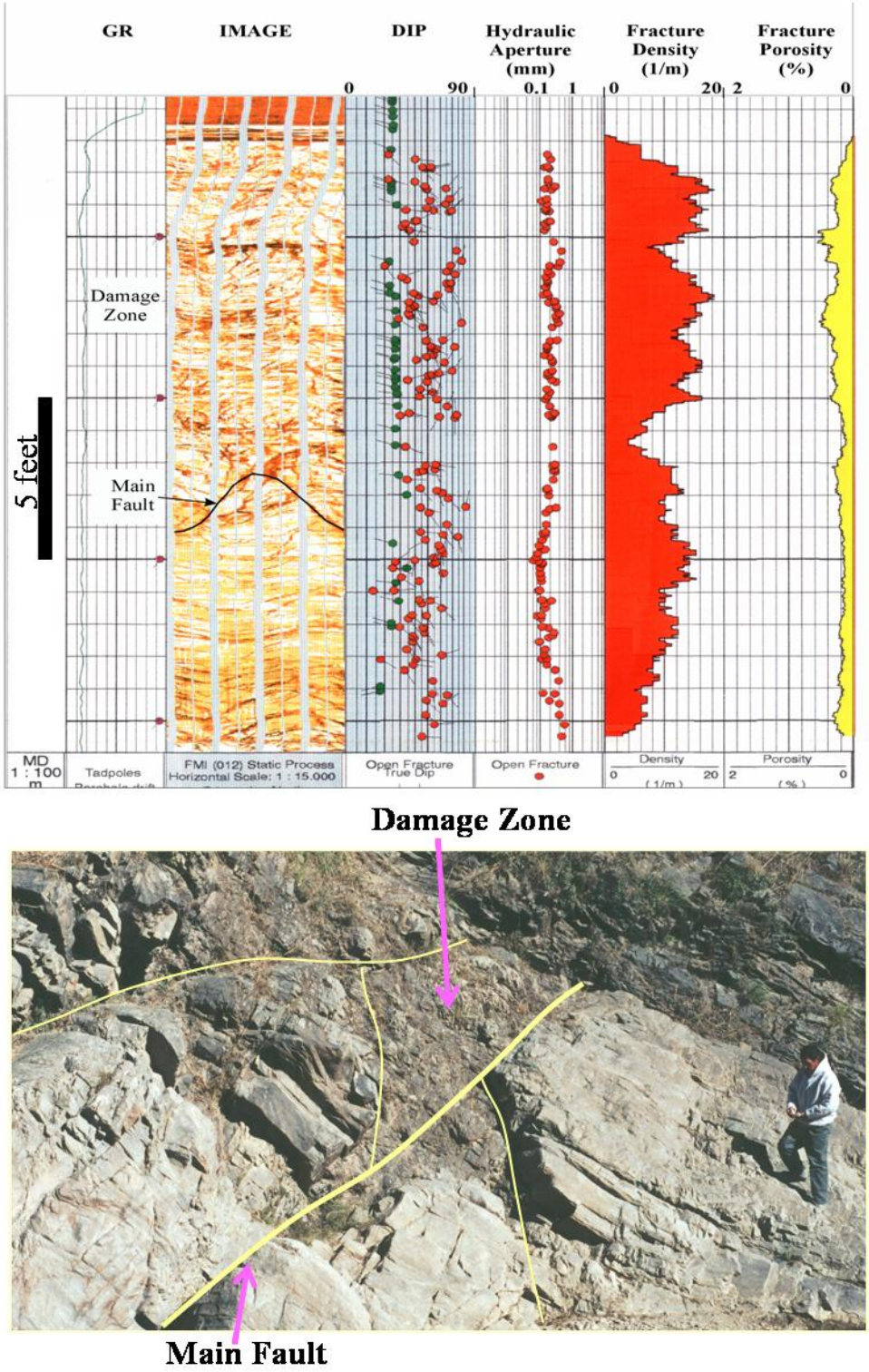

Figure 8: Comparison between subsurface and outcrop observations. The contrast in fracture density observed at subsurface can be interpreted as a damage zone associated to a small fault, like the one shown below.

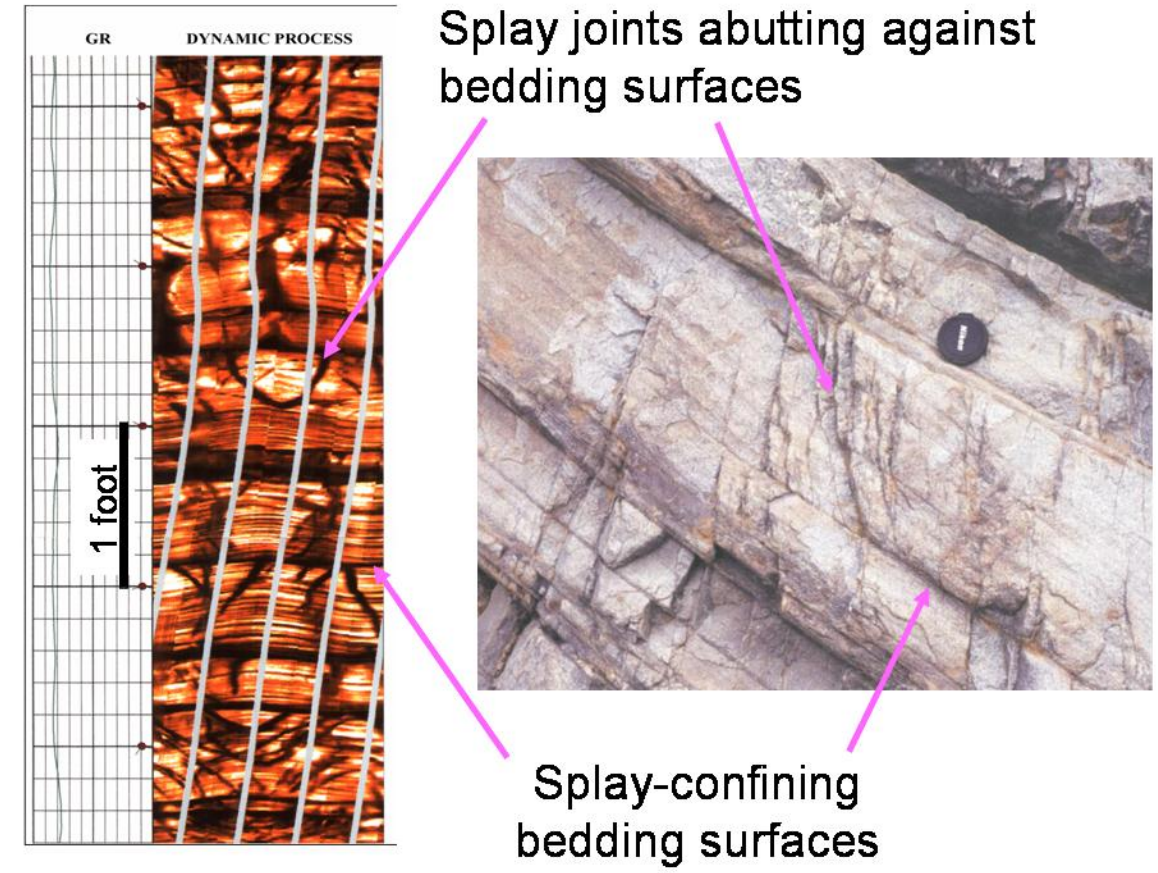

Figure 9: Comparison between subsurface and outcrop observations. Small fractures abutting against bedding surface are observed both at subsurface (left) and at outcrops (right).

Statistical Parameters for Sequential Simulation

The use of outcrop analogues, or any analogue, is a decision of stationarity (see Deutsch and Journel, 1998, p. 12), on which we decide that the analogue information is relevant and representative of what we should expect in the reservoir. The purpose of geostatistical simulation is to reproduce the spatial heterogeneity and the statistics of the constraining information, which in this case is the analogue data. The parameter that is going to be modeled is fracture density, defined as fractures per meter, as measured along a scanline. The constraining information is the histogram of fracture density as measured along scanlines, in particular the histogram of fracture density along the scanline shown in Figure 4, and the variograms obtained from this scanline.

Histograms: Equally-Probable Fracture-Density Distributions

The first source of uncertainty comes from the fact that there are many fracture-density distributions that can generate the same histogram. The histogram we want to reproduce is that of the low shear-strain area, shown in Figure 6. This histogram can be approximated by a lognormal distribution with mean and variance obtained from the data. We can generate many statistical replicates of the scanline shown in Figure 4, by randomly drawing from this distribution a large number of samples (Figure 10). However, the spatial order of the fracture-density values will be different for each case. One of these realizations is shown in Figure 11. In practical terms this means that even though is possible to predict the presence of fracture swarms associated to faults within a given rock volume, it is not possible to predict the exact location of these fracture swarms. For simulation purposes the empirical cumulative distribution function (CDF) derived from the original data has been used.

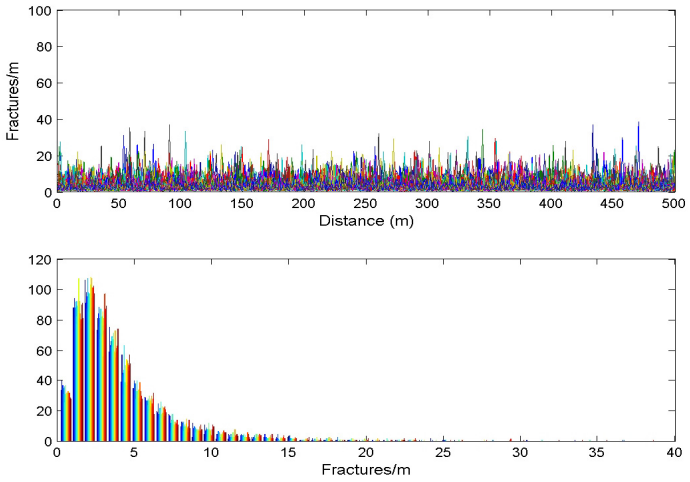

Figure 10: Many fracture-density distributions obtained from Montecarlo simulation using a lognormal distribution of fracture density. All these equally-probable fracture-density distributions honor the histogram of fracture density obtained from the scanline shown in Figure 4.

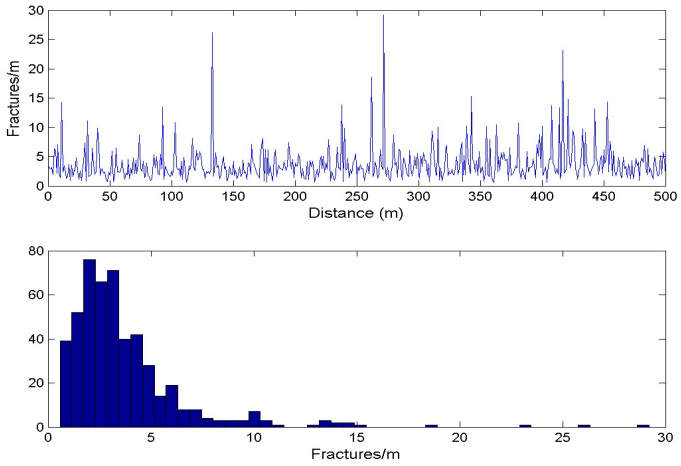

Figure 11: Randomly selected fracture-density distribution. This virtual scanline is statistically equivalent to the scanline measured along the low shear-strain zone, shown in Figure 4.

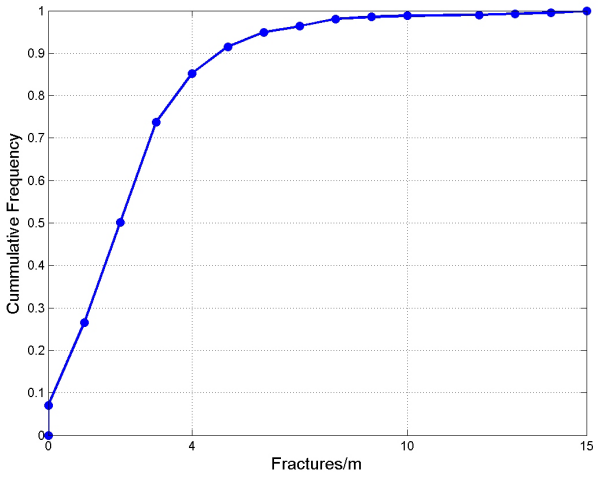

Figure 12: Empirical Cumulative Distribution Function (CDF) obtained from the original scanline shown in Figure 4.

Variogram Models

In Sequential Gaussian simulation (SGS) the spatial heterogeneity of the reservoir model is constrained by the variogram model. Since for the particular case of Abra del Condor outcrops, the dominant fractures are either parallel or normal to the dip direction, the variogram is defined following these two orientations. The data from the scanline (Figure 4) indicates that an exponential variogram is a good approximation (Figure 13). The correlation length, or range, for the azimuth direction can also be obtained from the

scanline data. The focus of this simulation is on dip-parallel fractures, therefore we apply a large correlation length in this direction.

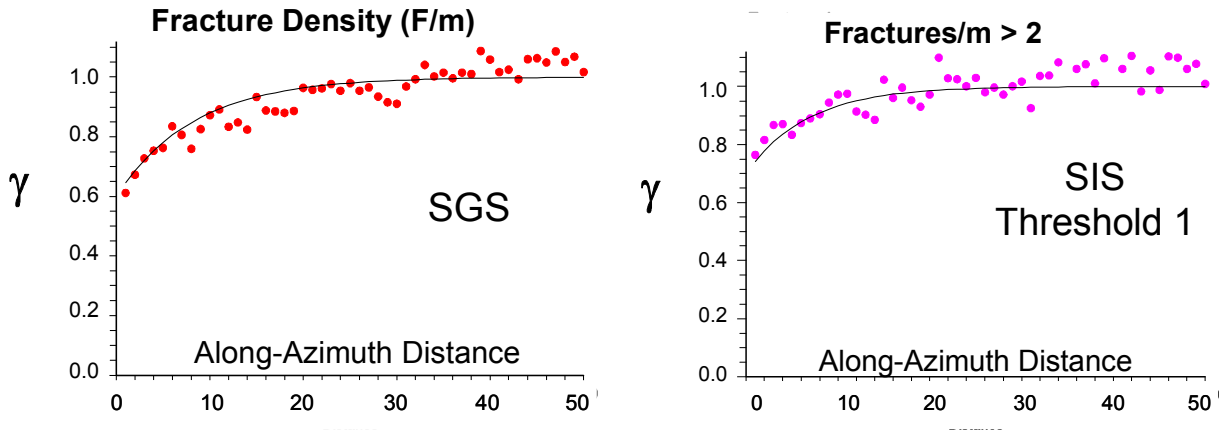

Figure 13: Along-Azimuth Variogram models from the scanline shown in Fig. Left: variogram model for the whole data set. Right: variogram model for fracture densities larger than 2 fractures per m.

In variogram-based Sequential Indicator Simulation (SIS) we can use threshold values of fracture-density, and apply different variogram models for each threshold. The threshold values can be related to fracture hierarchies in terms of the fracture density. For example, the presence of 10 fractures per m can be used as an indicator of small or intermediate faults. In principle, this technique should allow us to put different correlation lengths and anisotropies for each fracture-density class. The variogram models used for each threshold value are illustrated in Figure 14.

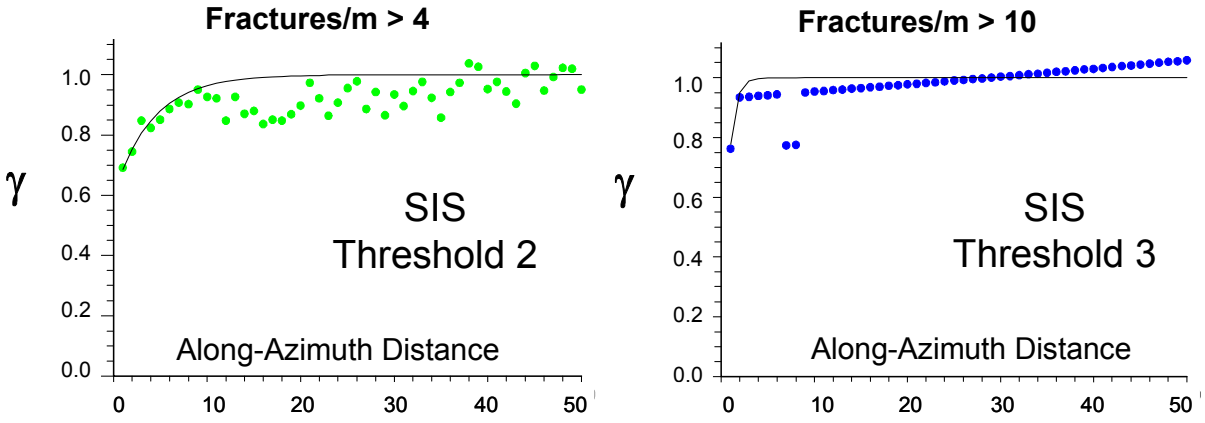

Figure 14: Variogram models for sequential indicator simulation, for thresholds 2 (left) and 3 (right). Fracture density of 10 fractures per meter is used as an indicator of small or intermediate faults.

Stochastic Modeling

This section explores different geostatistical methods to generate numerical models that reproduce the spatial variability of fracture density observed at outcrops. First we use variogram-based sequential simulation techniques: sequential Gaussian simulation (Figure 15) and sequential Indicator simulation (Goovaerts, 1997; Deutsch and Journel, 1998) to try to reproduce this variability and spatial continuity. After that we use a more deterministic approach that resembles the object-based indicator simulation method (Deutsch and Journel, 1998). In this approach, the spatial distribution of faults and fault zones is modeled first, generating an indicator map of the damage zones and faults. This volume can be considered a tectonic-facies indicator map. Afterwards, this indicator map is populated with realizations obtained from SGS. The damage zones and faults are populated with results from SGS realizations for high fracture densities and their respective variograms, whereas the background areas are filled with results from SGS realizations for low fracture densities and their respective variograms. This combination of stochastic fault modeling and SGS allows us to reproduce the spatial heterogeneity observed at outcrops.

Sequential Gaussian Simulation (SGS)

Sequential Gaussian simulation performs stochastic sequential simulation under the assumption of a multiGaussian random function model (Goovaerts, 1997). Figure 15 presents a sketch diagram of the steps to perform SGS, and the algorithm sgsim implemented in GSLib (Deutsch and Journel, 1998).

As can be observed in Figure 16, SGS generates statistical replicas of the outcrop data, however it can not reproduce the geometric or architectural distribution of fracture densities. In this technique we are using the global variogram for fracture density, shown in the left side of Figure 13. However, the large azimuth-parallel range observed in this variogram, about 25 m, corresponds more to the correlation length of low fracture-density areas. Along the azimuth, the high fracture-density areas have an almost pure nugget effect, as shown in the right side of Figure 14. The ability of SGS to reproduce the architecture of a fractured reservoir may improve if we have more data. However, from these results we conclude that SGS is not the most appropriate technique to model fractured reservoirs.

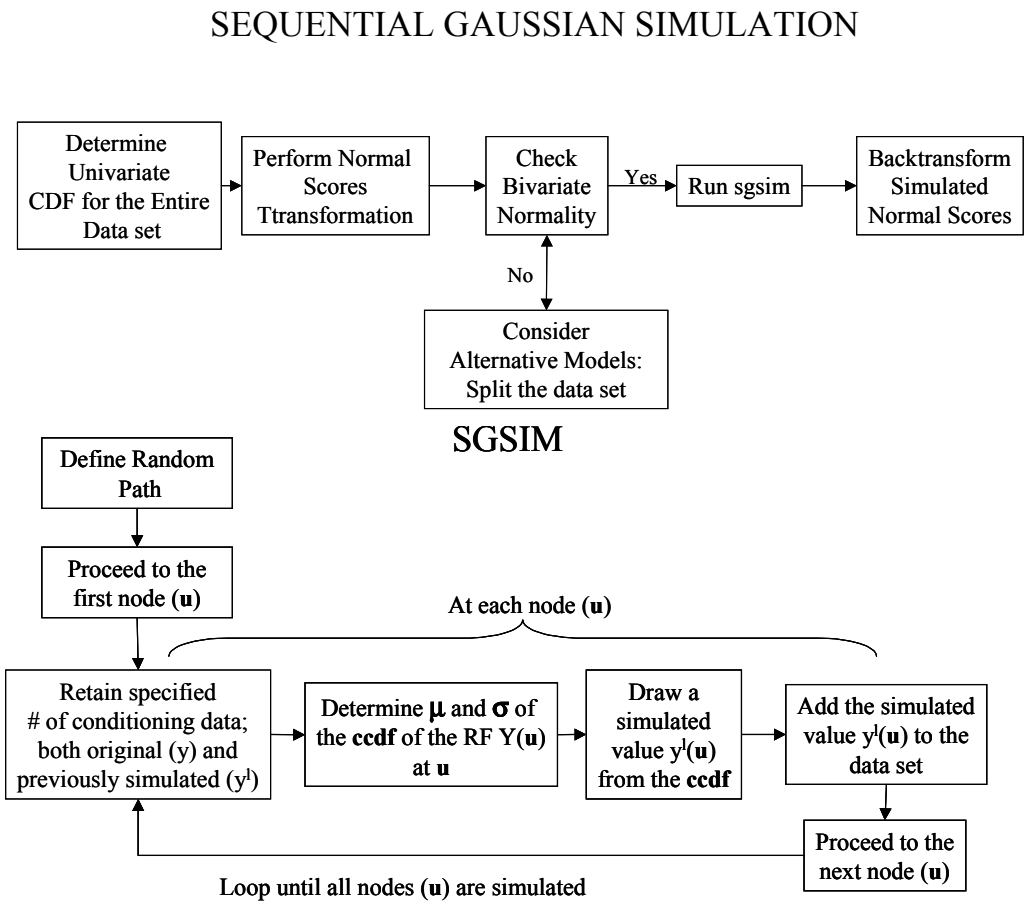

Figure 15: Sketch diagram showing the different steps for Sequential Gaussian Simulation, and the algorithm that follows sgsim (After Deutsch and Journel, 1998).

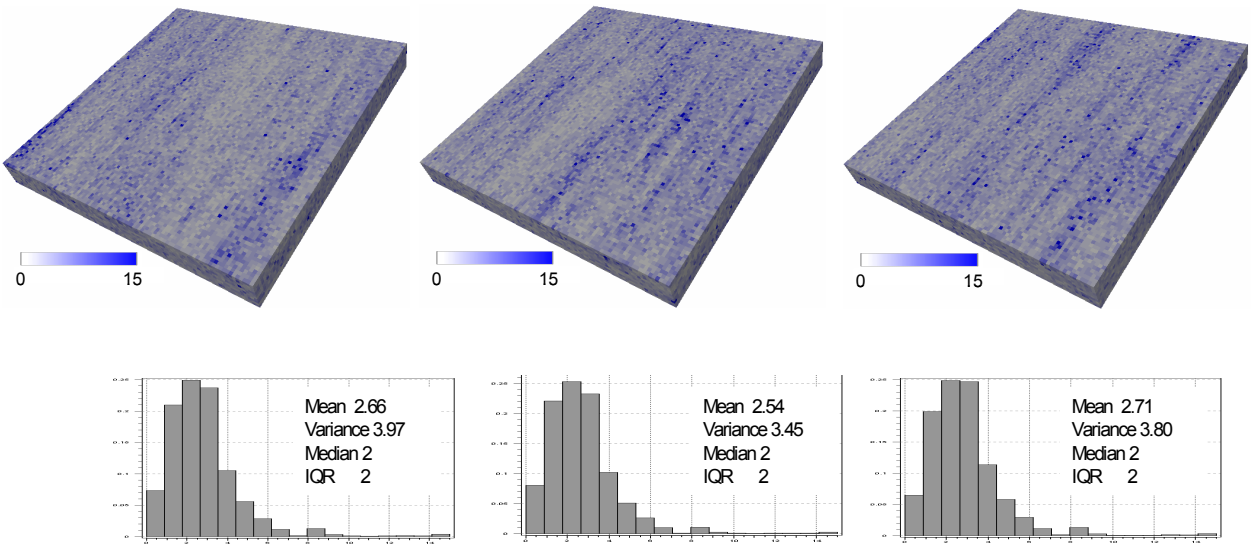

Figure 16: Equally-probable realizations for fracture density (fractures per meter) obtained from Sequential Gaussian Simulation (SGS), and their respective histograms.

Variogram-Based Sequential Indicator Simulation

Sequential indicator simulation (SIS) is a non-Gaussian simulation technique, which allows one to account for class-specific patterns of spatial continuity through different variogram models (Goovaerts, 1997, p.395). Figure 17 schematically illustrates the algorithm for SIS. The variograms for the different threshold values are shown in Figure 13 (right side) and Figure 14.

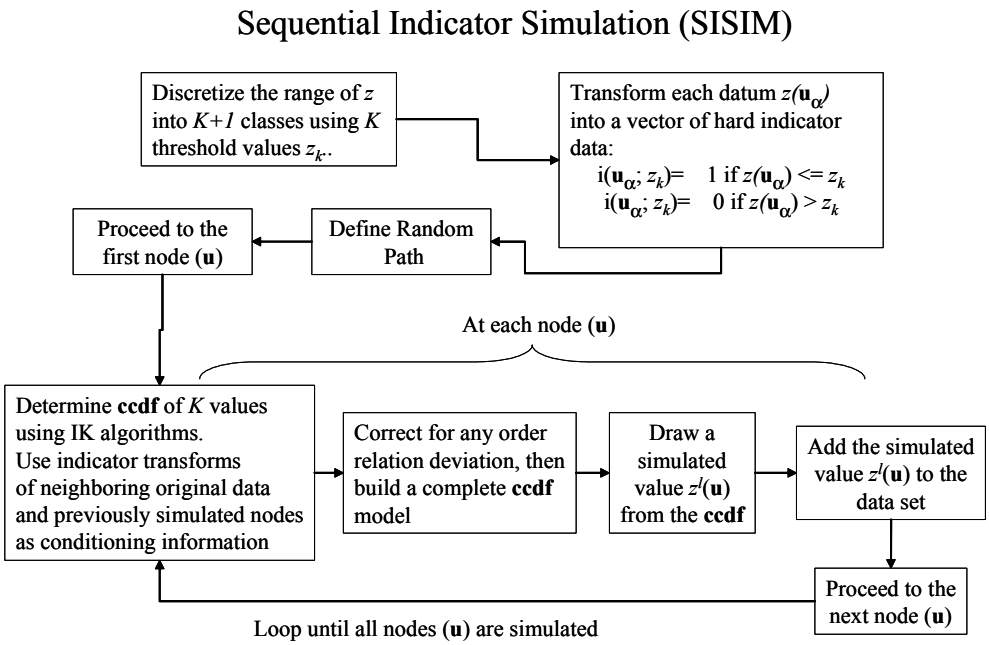

Figure 17: Diagram illustrating the sequential indicator simulation algorithm (Goovaerts, 1997; Deutsch and Journel, 1998).

In the case of parallel high and low fracture-density zones, corresponding to faults and joints respectively, SIS generates fracture-density models that replicate the architecture observed at outcrops. As shown in Figure 18, SIS generates high fracture-density corridors similar to those associated with small faults at outcrops. The fracture density models in Figure 18 are more appropriate for fractured reservoirs than those presented in Figure 16.

However, for the case of diverse orientations for high and low fracture-density zones, SIS cannot generate the laterally continuous high-fracture density corridors. In other words, the anisotropy of the low-fracture density class, which is the most likely and dominant class in the empirical CDF (Figure 12), overrides the anisotropy of the high fracture-density corridors (Figure 19).

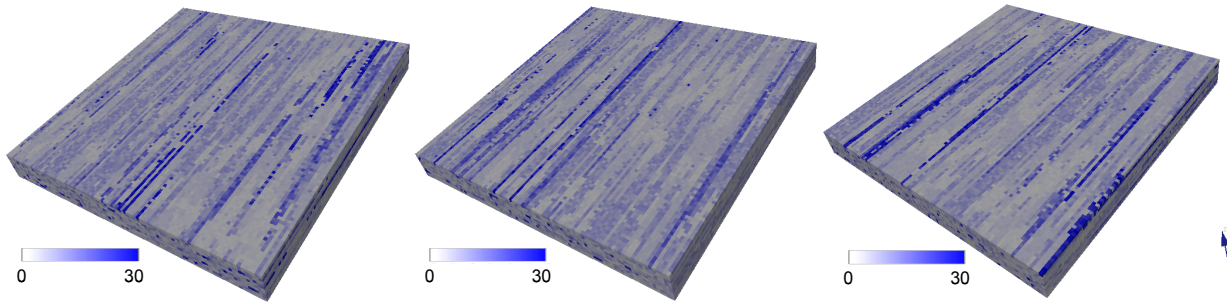

Figure 18: Results from sequential indicator simulation algorithm (sisim), for the case of parallel variograms for both high and low fracture-densities.

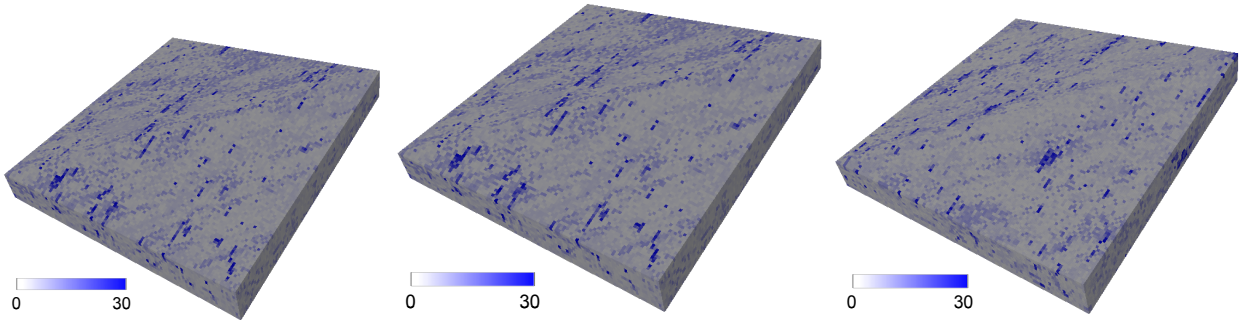

Figure 19: Results from the variogram-based sequential indicator simulation algorithm (sisim), for the case of diverse orientations of high fracture-density zones and low fracture-density background.

Stochastic Fault Modeling and Sequential Simulation

In order to overcome the limitations of SGS and SIS for modeling of fractured reservoirs, we propose to use an object-based indicator approach: first simulating the distribution of faults and damage zones, a tectonic-facies indicator map, then populating this indicator map with realizations from SGS.

We propose stochastic fault modeling as a method to generate maps of tectonic-facies indicators. Starting from one of the equally probable scanlines illustrated in Figure 10, this method uses Montecarlo simulation to model fault locations, fault dimensions, and the width of the fault damage zone, as outlined in Figure 20. The tectonic-facies architecture is modeled in 2D, for un-deformed grids (stratigraphic framework). Further improvements of this method will require the implementation of three-dimensional models and the interpolation to a deformed, structural grid.

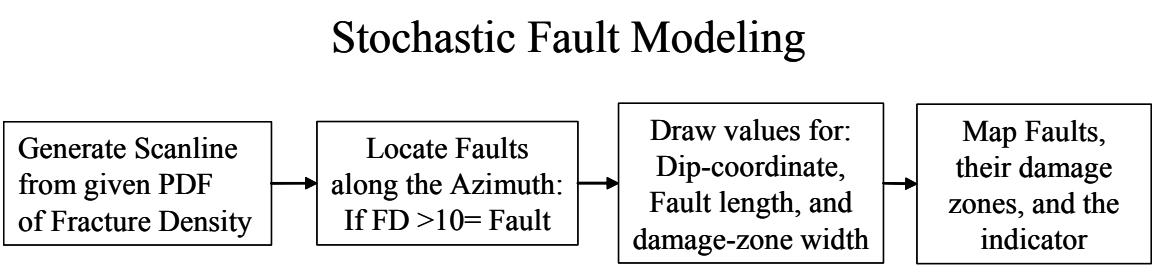

Figure 20: Flow diagram for stochastic fault modeling. Currently the method is implemented for simple fault two dimensional configurations in un-deformed grids.

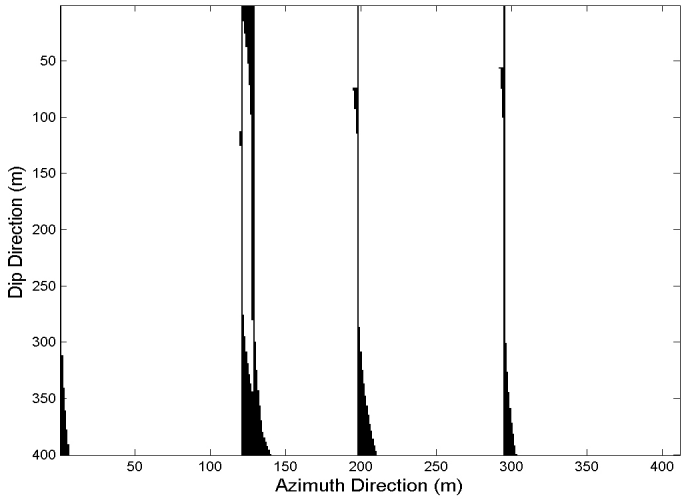

Figure 21: Stochastic fault model for an area with low shear-strain. The architecture corresponds to small strike-slip faults with left-lateral shear.

The indicator maps obtained from stochastic fault modeling are shown in Figure 21 and Figure 22. In the first case (Figure 21) the indicator map reproduces the fault architecture expected for an area with low shear-strain, with large spacings between faults and narrow damage zones. In the second case (Figure 22), the indicator map replicates the most likely fault architecture for an area with moderate shear-strain, where the spacing between faults decreases, and the width of damage zones increases. In both cases, the architecture corresponds to that generated by left-lateral strike-slip faults, with wider damage zones asymmetrically localized towards the tip of the faults. The asymmetric distribution of damage zones follows the asymmetric distribution of tensional and compressional stresses expected from fault-induced stress perturbations.

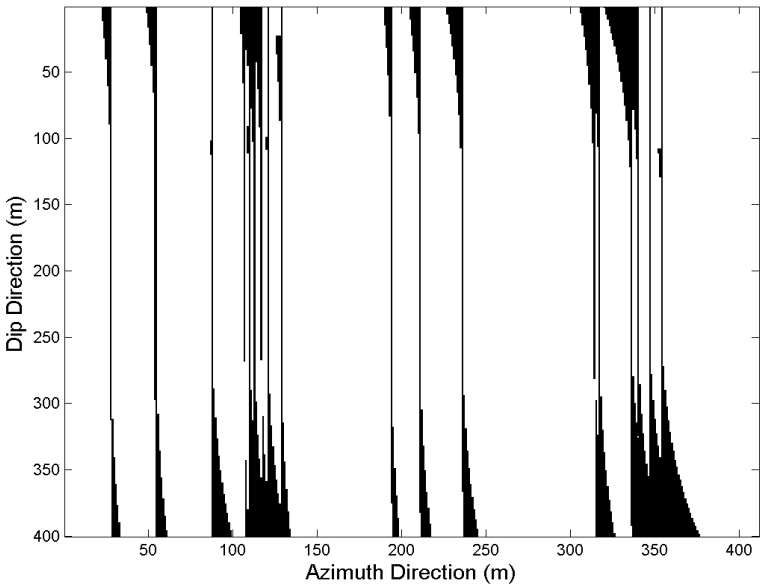

Figure 22: Tectonic-facies indicator map obtained from stochastic fault modeling. The model resembles the architecture expected for small faults with left-lateral shear, in a region with moderate shear-strain. Fault spacings are smaller and damage-zone widths are larger than those simulated for a low shear-strain area (Figure 21).

The tectonic-facies indicator maps are populated with fracture-density values obtained from SGS realizations. The low fracture-density areas, background areas in the indicator maps, are populated with realizations for low fracture densities. Similarly, the high fracture-density zones, or damage zones, are filled with realization from SGS with higher fracture densities. The final result is the combination of the two populations. This technique is basically and object-based indicator simulation method, extensively discussed by Wang (1998), and outlined by Deutsch and Journel (1998). The final fracture-density maps are illustrated in Figure 23, for the low shear-strain area, and Figure 24 for the high shear-strain area. Figure 25 presents a comparison between the two models, representing areas with different degree of shear strain.

It is important to emphasize that a reservoir model should, at least, reproduce the mean and variance of your analogue. In many cases the outcrop data is reduced to use the mean spacing for specific areas, without regarding the variance. For example, a comparison of the histograms of the two reservoir models, shown in Figure 26, demonstrates that the mean of these histograms is relatively close, about 3, however the variance is significantly different. The higher variance in the histogram corresponding to the moderate shear-strain area reflects the presence of more high fracture-density

corridors in this area. The overall higher fracture density of the moderate shear-strain area is clearly illustrated by the quantile-quantile plot (Figure 27).

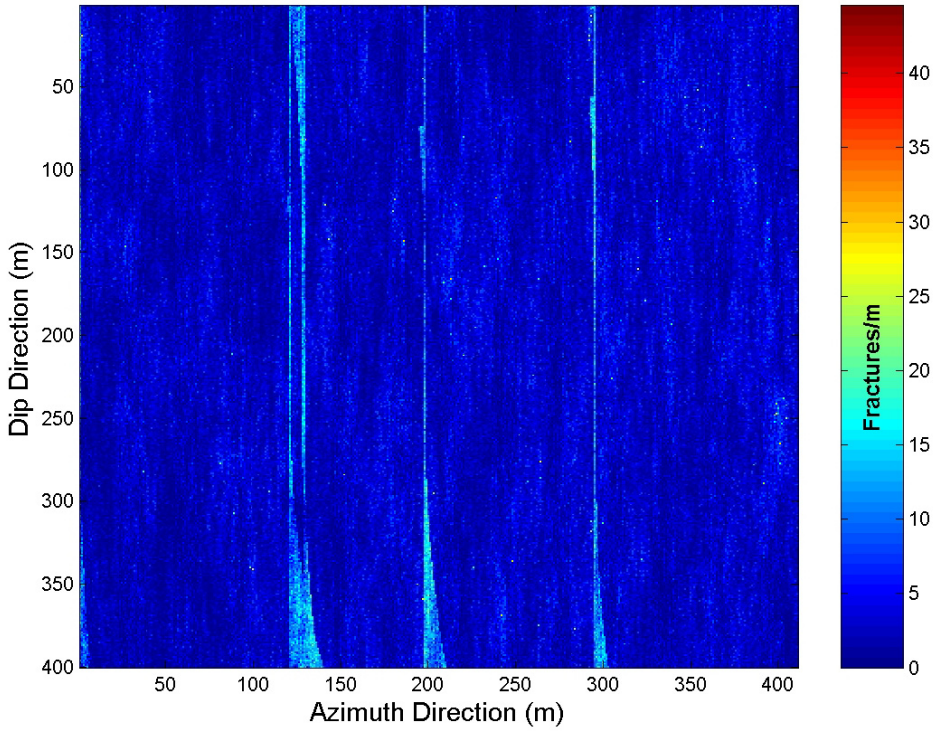

Figure 23: Fracture-density map obtained from the combination of SFM and SGS. Low shear-strain area.

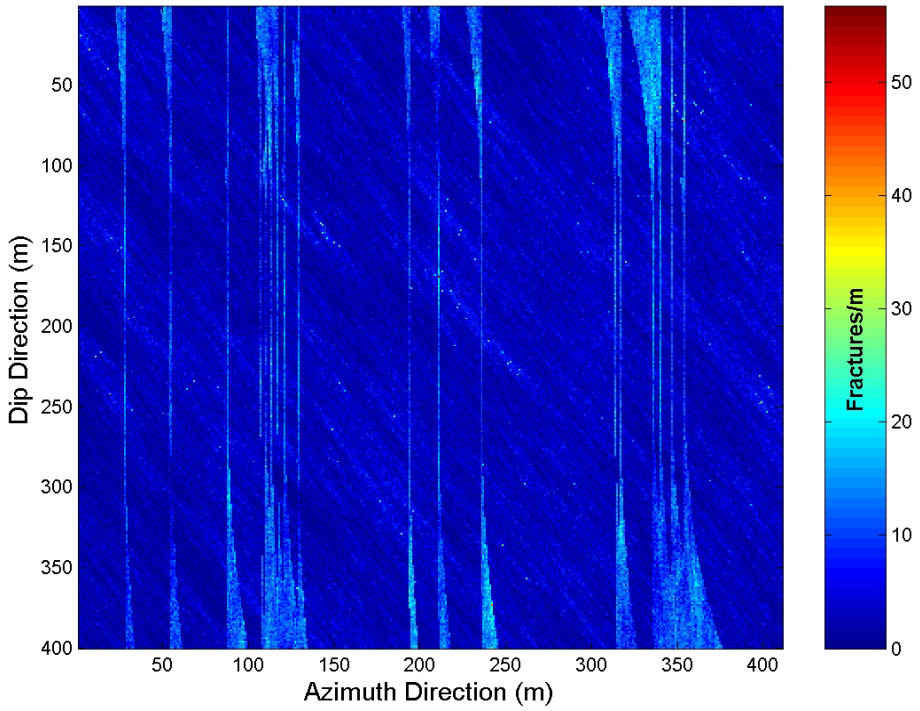

Figure 24: Fracture density model obtained from the combination of SFM and SGS. The model reproduces the spatial heterogeneity of FD observed at areas with moderate shear-strain.

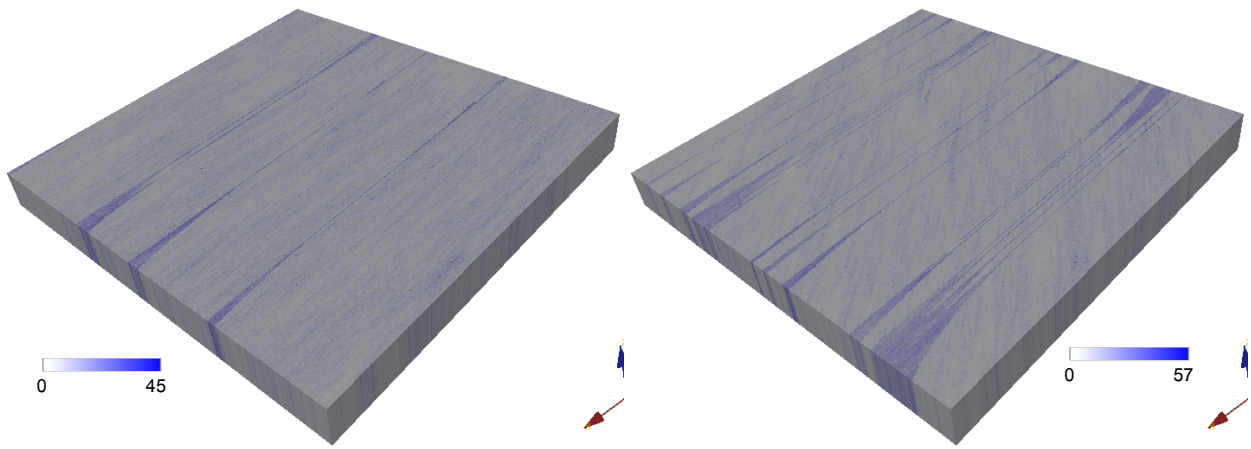

Figure 25: Comparison of the models obtained from combining SFM and SGS. The model to the left represents a low shear-strain area, where faults and fractures are parallel. The model to the right represents a moderate shear-strain area, where faults are parallel and secondary fractures are oblique, replicating the geometry of splay fractures derived from shear along the faults.

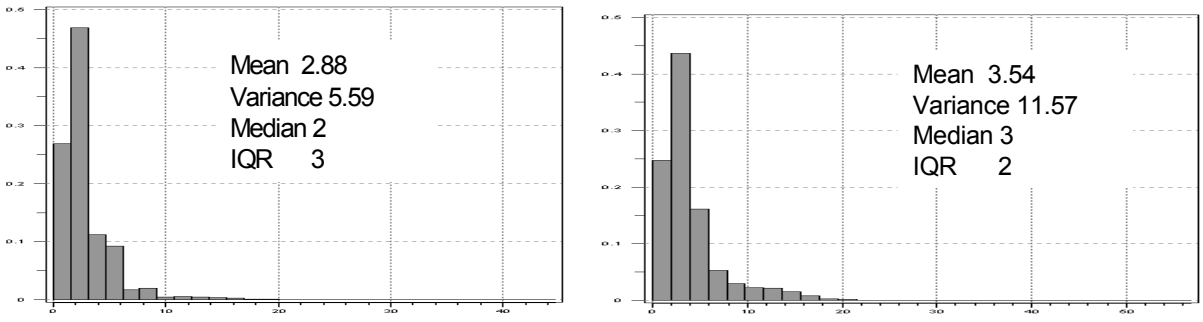

Figure 26: Left: histogram for the low shear-strain area. Right: histogram for the moderate shear-strain area. Notice that the mean of these two histograms is about the same, however the variance is significantly different. The higher variance in the model of the moderate shear-strain area reflects the overall higher fracture density in this model.

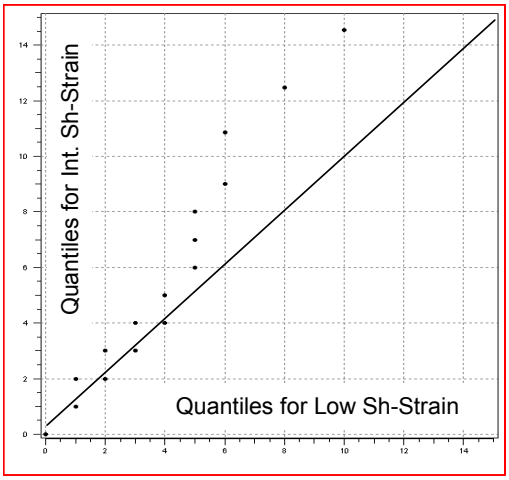

Figure 27: Quantile-Quantile plot comparing the fracture density populations of the two models. These plot shows that the fracture density in the model of the moderate (intermediate) shear-strain area is higher than the fracture density in the model of the low shear-strain area.

The combination of stochastic fault modeling (SFM) and sequential Gaussian simulation (SGS) generates statistical replicas of the outcrop data, which reproduce the spatial heterogeneity observed at outcrops. Figure 28 presents a comparison between the generated models and the outcrop architecture. This method is basically an object-based indicator technique. The indicator maps are generated using stochastic methods to select the values for parameters that describe the fault architecture. The maps obtained reproduce the lateral continuity of narrow fault zones, which could not be reproduced using pixel-based simulation techniques like SIS.

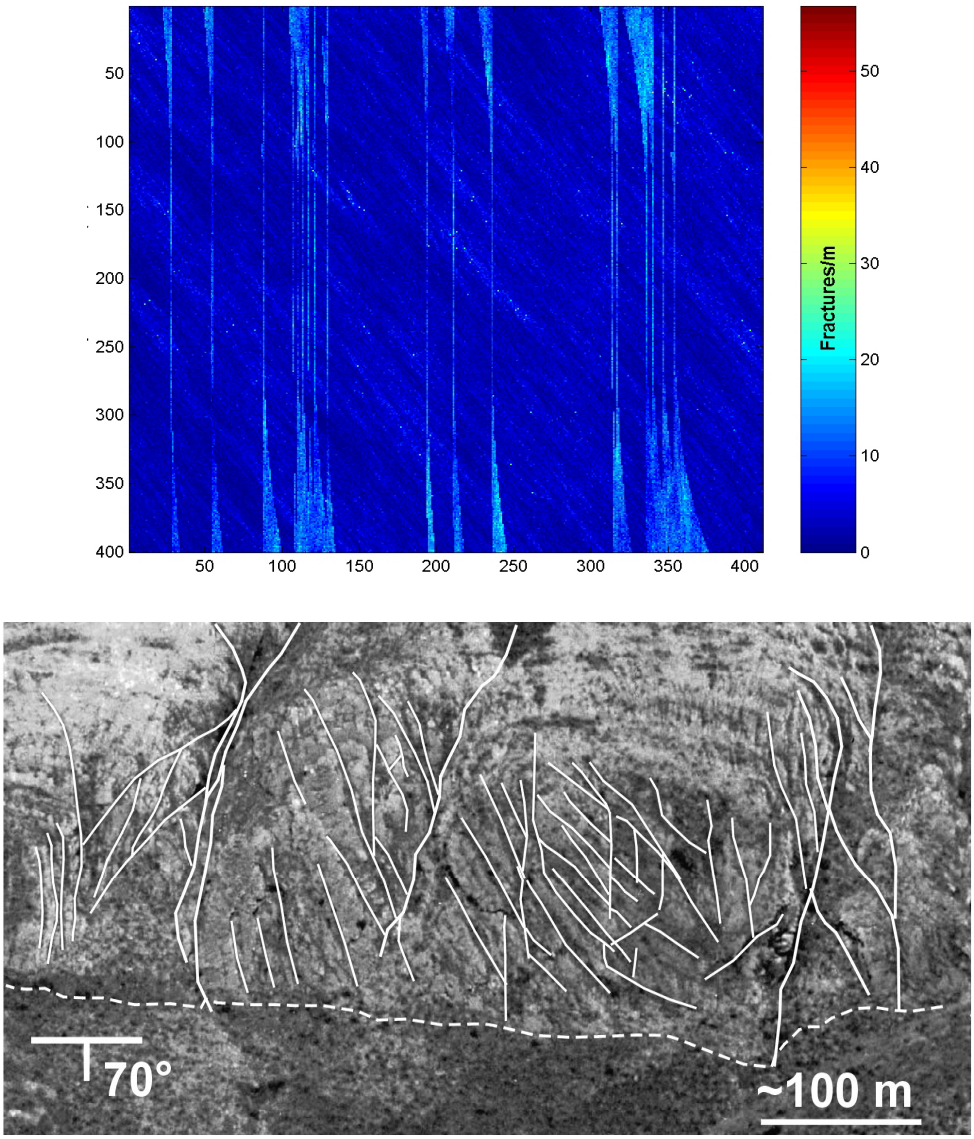

Figure 28: Comparison of the spatial heterogeneity simulated from the SFM-SGS technique, and the fracture distribution observed at outcrops.

Discussion

The combination of SFM and SGS allowed us to reproduce the spatial heterogeneity of fracture density observed at outcrops, however the method requires further improvements. The technique, which falls within the object-based indicator methods, is as an alternative method for modeling fractured reservoirs. The fact that fracture density is the modeled variable might facilitate the implementation of methods for seismic modeling that use crack density as the main parameter; i.e. Hudson model (Mavko et al,

1998). However, there are still many issues to be resolved before this technique can be applied to real cases: How can you go from fracture density to crack density? How do you incorporate the fracture orientation at meter (pixel) scale? How do you upscale these models? Ho do you incorporate the effect of confining stress on these fracture-density values? We briefly discuss these questions in the following paragraphs.

Fracture Density, Crack Density and the Effect of Confining Stress

The transformation from fracture density to crack density strongly depends on the applied stress field and the rugosity of the fracture surfaces. To better understand this, it is convenient to think of each fracture as a set of aligned cracks. The closure of each crack will depend on the applied normal stress and the aspect ratio of the crack. As a rule of thumb, the crack-closing stress is numerically proportional to $\alpha_0 E_0$, where α_0 is the crack initial aspect ratio and E_0 is the Young's modulus of the intact material (Mavko et al, 1998). The rugosity of the fracture surfaces, or mismatch, controls the original aspect ratios. The final closure of a fracture depends on the initial aspect ratios of the aligned cracks along the fracture. This concept is essentially similar to the concept of crack-induced stress anisotropy and the crack-induced velocity dependence on pressure (Nur and Simmons, 1969), however applied at a larger scale.

For a specific stress field, the relationship between fracture density and crack density can be approximated as linear. In general, for a set of fractures larger that the volume under study, the relationship between number of fractures per volume *(N)* and the volumetric crack density *(ε)* can be expressed as:

$$\varepsilon \approx K(\sigma)\frac{N}{8} \tag{4}$$

where $K(\sigma)$ is a scaling factor that largely depends on the applied stress field. In fact, K not only depends on the magnitude of the normal stress applied to the fracture, but also on the shear stress. That is the essence of the role of active faults on fractured reservoirs documented by Barton et al (1995) and Wiprut and Zoback (2000). Other factors like diagenesis and cementation may affect the final number of open cracks and their proportional ratio to the number of fractures. In short, the total number of fractures within a reservoir may remain the same, nevertheless the number of open cracks is sensitive to the applied stress field. As a first approximation to extrapolate from outcrops to subsurface, we can assume that the crack density decreases non-linearly with confining stress (depth), however is linearly proportional to the fracture density.

Fracture Orientation at Meter Scale and Upscaling

Incorporating the meter-scale fracture orientation and upscaling are two issues intimately related. The fracture density models generated so far implicitly assume a random or isotropic fracture orientation, which also implies that these fracture-density values can be treated as a scalar for upscaling purposes. A more rigorous approach requires the incorporation of fracture orientation. In order to take into account the orientation of fractures at meter (or pixel) scale, the upscaling procedure becomes more complicated. In that case, it is necessary to define a tensor of the property to be upscaled. For example, in order to upscale the elastic properties, we need to establish a stiffness tensor based on the crack density values, and apply the backus average to these stiffness tensors. A somewhat similar procedure would be required for permeability. In addition to this, the average fracture or crack densities of different fracture sets have to be computed first, and then added all together. Even though this upscaling scheme would not take into account the effect of crack interaction, it seems to be the viable approach. Upscaling is a complex issue that requires a more extensive and detailed analysis, and it has to take into account the anisotropy induced by fracture orientation.

Conclusions

Rigorous outcrop-analogue studies provide relevant information for understanding the spatial heterogeneity and deformation mechanisms of fractured reservoirs in the subsurface. We have shown examples of striking similarities between the FMI data from a subsurface reservoir, and its outcrop analogue.

Sequential Gaussian simulation (SGS) can reproduce the statistics of the outcrop analogues, but cannot replicate the architecture. The different equally-probable realizations obtained from SGS do not generate the laterally continuous high fracture-density corridors associated with faults.

Variogram-based sequential indicator simulation can replicate both the statistics and the architecture of parallel fracture sets of different hierarchies, faults and background joints, however it cannot successfully handle fracture hierarchies with different orientations.

The combination of stochastic fault modeling (SFM) and sequential Gaussian simulation allows us to reproduce the spatial heterogeneity of fracture density observed at outcrops. This approach is basically an object-based indicator approach, on which the

SFM method maps the distribution of damage zones associated with faults, or tectonic facies indicator map. Afterwards, the indicator map is populated with realizations of different fracture densities generated with SGS.

The technique illustrated in this paper provides an alternative method for modeling fractured reservoirs, however there are still important issues to be solved. The most important issues are the reduction of crack density as a function of the applied stress field, and upscaling of elastic and hydraulic properties.

Attachment D

Field Data on Shear-Wave Anisotropy: Practical Bounds on Crack Density

Introduction

In this attachment we present the collection of field data on shear-wave anisotropy reported by different authors and summarized by Crampin (1994). We use this dataset to obtain insights into the distribution of shear-wave splitting, and implicitly crack density, as a function of depth. The results of the analysis presented in this section constitute valuable *a priori* information that can be used to constrain the crack density values for fracture modeling, depending on the depth of the reservoir.

Analysis of the data

The field data on shear-wave anisotropy were acquired in various environments, from sedimentary basins to igneous/volcanic and metamorphic rocks, and at different depths, from near surface, to more than 30 km depth. The shear-wave data were collected either from earthquakes or from controlled sources, such as reflection surveys, VSP, reversed VSP, and cross-hole surveys.

Table 1 presents this collection of the field data on azimuthal shear-wave anisotropy after Crampin (1994). The first column gives the types of rocks, or the environment, the second column gives the method used for acquiring the data, the third column presents the place where the data were collected, the fourth column gives the corresponding depth

for the recorded anisotropy, the fifth column presents the percentage of shear-wave splitting anisotropy, while the last column indicates the reference.

Table 1: Observed percentage of azimuthal shear-wave velocity anisotropy from field data reported by different authors and collected by Crampin (1994).

type of rock	method	place	depth	anis%	reference
volcanic rocks	shear-wave splitting/ aftershocks	Campi Flegrei, Italy	<15km	1.4	1
gabbro	shear-wave splitting/earthquake	Anza, CA, USA	<17km	1.5	2
above subduction zone	shear-wave splitting/earthquake	Wellington, New Zealand	<60	2	3
mixed metam/sedim rocks	shear-wave splitting/earthquake	Los Angeles Basin, CA	<15	2,2.5	4
gabro	shear-wave splitting/earthquake	Anza, CA, USA	<3.5	2.3+ - 1.7	5
welded fractured tuff	shear-wave splitting/earthquake	Tazawako, Akita, Japan	<0.5	3	6
unspecified	Vs information omitted	Charlevoix Zone, Canada	unspec	3	7
crystalline rock	shear-vave splitting/earthquake	Mojave Desert, CA, USA	<0.45	3.5	8
metamorphic rocks	shear-wave splitting/earthquake	W. Deep Levels, S. Africa	<5	<4	9
granite	shear-wave splitting/earthquake	Manitoba, Canada	0.4-0.5	4	10
granite and mixed geology	shear-wave splitting/earthquake	Kinki, Honshu, Japan	<15	4	11
volcanic rocks	shear-wave splitting/earthquake	Rift zone, Japan	<10	4	12
mixed metam/sedim rocks	shear-wave splitting/earthquake	Los Angeles Basin, CA	<15	4.3	4
volcanic caldera	shear-wave splitting/earthquake	Long Valley, CA	<10	4.3	13
mixed metam/sedim rocks	shear-wave splitting/earthquake	TDP Izmit, Turkey	<12	4.5	14
mixed metam/sedim rocks	shear-wave splitting/earthquake	Shikoku, Japan	<10	4.5	15
volcanic rocks	shear-wave splitting/earthquake	E Rift Zone, Hawaii	<10	5	16
volcanic/ sedimentary rocks/ geothermal area	shear-wave splitting/earthquake	Takinoue, Honshu, Japan	<2	6	17
volcanic caldera	shear-wave splitting/earthquake	Long Valley, CA	<10	6.4	18
volcanic caldera	shear-wave splitting/earthquake	Phlegraean Fields, Italyl	<3.1	7	16
metamorphic rocks/aftershocks	shear-wave splitting/earthquake	Nahami, NWT, Canada	<20	7	19
granite/geothermal area	shear-wave splitting/earthquake	Cornwall, England	<2	8	20
volcanic caldera/resurgent dome	shear-wave splitting/earthquake	Long Valley, CA	<10	9.6	18
principally lower crust	shear-wave splitting/earthquake	TDP Izmit, Turkey	<30	10	21
above subduction zone	shear-wave splitting/earthquake	Wellington, New Zealand	<15	10	3

granulite facies	shear-wave splitting/earthquake	Arunta Block, Australia	<1	10	22
volcanic caldera/fault zone	shear-wave splitting/earthquake	Long Valley, CA	<10	15	23
volcanic/sedimentary rocks /geothermal area	shear-wave splitting/earthquake	Takinoue, Honshu, Japan	<2	18	17
mixed sediments	shear-wave splitting/VSP	Devine, TX, USA	<0.47	0.7-3.8	24
unspecified sediments	shear-wave splitting/RFL	Pennsylvania, USA	<6	1.4	25
mixed sediments	shear-wave splitting/RFL	Dimmit, Zavala, Frio Counties, TX	<2	1.5, 2, 2.5	26
clay, sandstones, limestones	shear-wave splitting/VSP	Caucasus Basin, Russia	<.9	1.4	27
shale, limestone	shear-wave splitting/VSP	Paris Basin, France	1.1-2	1.6	28
mixed sediments	shear-wave splitting/RFL	Silo Field, WY, USA	<2.4	1.0-4.0	29
unspecified sediments	shear-wave splitting/RFL	unspecified, USA	<3	2	30
mixed sediments	shear-wave splitting/RFL	Giddings Fld. TX, USA	<2.6	2	31
Palaeozoic sedim	shear-wave splitting/EQ	Enola, Arkansas, USA	<6	2	32
shale, limestone	shear-wave splitting/VSP	Paris Basin, France	0.6-1.1	3	33
shale, carbonates	shear-wave splitting/VSP	Romashkino, Russia	<1	3.3-4	34
mixed sediments	shear-wave splitting/VSP	Dilley, TX USA	<3	3.5+-0.5	35
unspecified sediments	shear-wave splitting/VSP	CBTF, OK, USA	<.6	4	36
unspecified sediments	shear-wave splitting/VSP	Lost Hills Field, CA	<.64	7	37
fractured chalk	shear-wave splitting/VSP	Silo Field, WY, USA	2.5	>7	38
fault zone	shear-wave splitting/VSP	Orroville, CA, USA	0.3	7.2-7.6	39
fault zone	shear-wave splitting/VSP	Parkfield, CA, USA	<1.4	8	40
unspecified sediments	shear-wave splitting/VSP	Railroad Gap Field, CA, USA	<0.4	9	41
fractured sandstone	shear-wave splitting/VSP	S. Casper Creek, WY, USA	0.8-0.85	10	42
clay, limestones	shear-wave splitting/RVSP	CBTF, OK, USA	<0.04	10.5	43
clay, limestones	shear-wave splitting/CHS	CBTF, OK, USA	<0.04	12	44
unspecified sediments	shear-wave splitting/VSP	Cymric Field, CA, USA	<0.47	14	41

(1) Iannaccone & Deschamps (1989); (2) Peacock et al. (1988), (3) Gledhill (1991); (4) Du (1990); (5) Aster &Shearer (1991); (6) Kuwahara, Ito & Kiguchi (1991); (7) Buchbinder (1985); (8) Li, Leary & Aki (1990); (9) Graham, Crampin & Fernandez (1991); (10) Holmes, Crampin & Young (1993); (11) Kaneshima, Ando & Crampin (1987); (12) Kaneshima, Ito & Sugihara (1989); (13) Savage, Peppin & Vetter (1990); (14) Booth et al. (1985), (15) Kaneshima & Ando (1989); (16) Savage, et al. (1989); (17) Kaneshima et al. (1988); (18) Shih &

Meyer (1990); (19) Buchbinder (1990); (20) Roberts & Crampin (1986); (21) Graham & Crampin (1993); (22) Greenhalgh et al.. (1990); (23) Savage, Peppin & Vetter (1990); (24) Yardley & Crampin (1993); (25) Lynn & Thomsen (1990); (26) Li, Mueller & Crampin (1993); (27) Slater et al. (1993); (28) Bush & Crampin (1991); (29) Martin & Davies (1987), (30) Lynn & Thomsen (1986); (31) Mueller (1991); (32) Booth et al. (1990); (33) Lefeuvre, Cliet & Nicoletis (1989); (34) Cliet et al. (1991); (35) Alford (1986); (36) Queen & Rizer (1990); (37) Winterstein & Meadows (1991a); (38) Lewis, Davis & Vuillermoz (1991); (39) Leary, Li & Aki (1987); (40) Daley & McEvilly (1990); (41) Winterstein & Meadows (1991b); (42) Shuck (1991); (43) Liu et al. (1993a); (44) Liu, Crampin & Queen (1991);

As shown in Table 1, shear-wave splitting in crustal rocks has been widely observed in controlled-source reflection surveys, as well as associated with earthquakes. There are cases when the shear-wave splitting may be attributed to phenomena other than cracks, such as rock foliation or crystal alignment, but typically the anisotropy appears to be the result of aligned fractures or microcracks and preferentially oriented pore space.

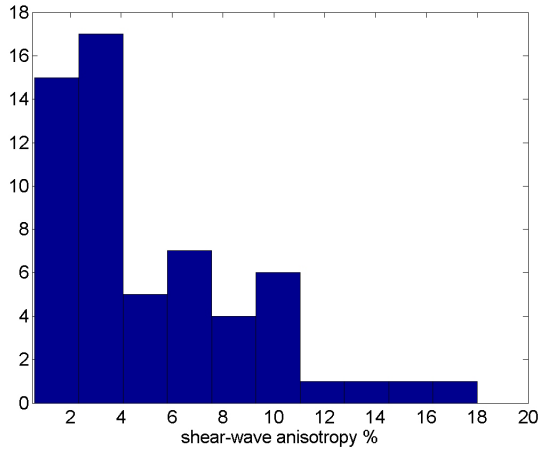

Figure 1: Histogram for the shear-wave splitting data from Table 1. Data collected by Crampin (1994).

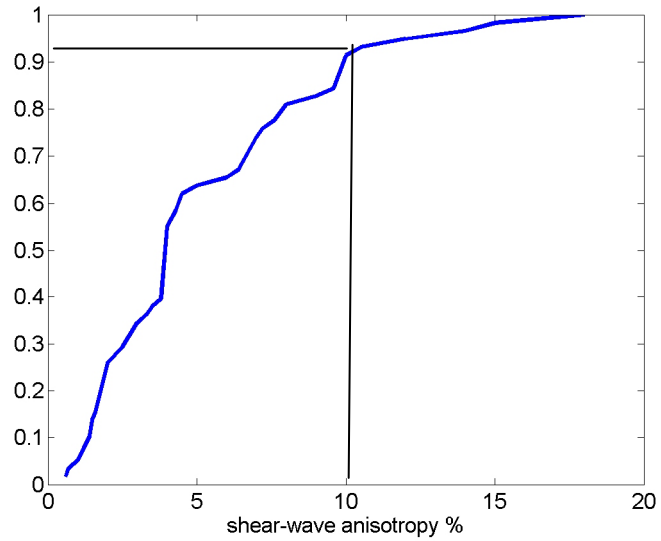

Figure 2: Cumulative distribution function for the shear-wave splitting data from Table 1. Data collected by Crampin (1994).

Figure 1 presents the histogram for the shear-wave splitting data from Table 1, while Figure 2 presents its corresponding cumulative distribution function. We can observe from Figure 2 that more than 90% of the reported data corresponds to the shear-wave anisotropies of less than 10%.

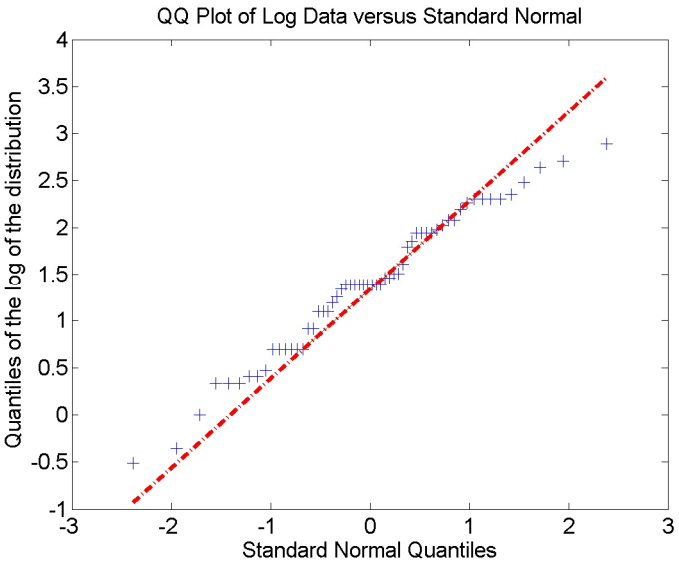

Figure 3: Q-Q plot for the logarithm of the shear-wave splitting data from Table 1. A linear trend close to the red line indicates a log-normal distribution for the data.

We can also observe from Figure 1 that the world-wide shear-wave anisotropy data does not follow a Gaussian distribution. From the shape of the histogram from Figure 1, it appears that the distribution of the shear-wave splitting data is more likely log-normal or exponential. In Figure 3, we show a quantile-quantile plot that compares the logarithm of the S-wave anisotropy distribution from Figure 1 with a normal distribution. The trend in Figure 3 is close to linear. This suggests that the world-wide *S*-anisotropy data follows more or less a log-normal distribution. Of course, there are departures from a log-normal distribution, as we can see in Figure 3. These departures are more significant especially for the large values of the shear-wave anisotropy.

We can obtain more insights about the world-wide shear-wave anisotropy data if we plot it against the depth, as in Figure 4. Figure 5 is similar to Figure 4, zooming on the first 6 km in depth.

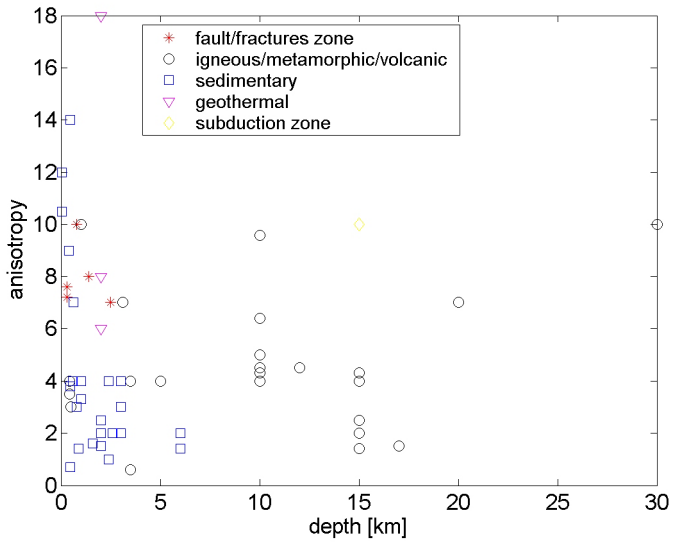

Figure 4: Shear-wave anisotropy data as a function of depth. Data collected by Crampin (1994).

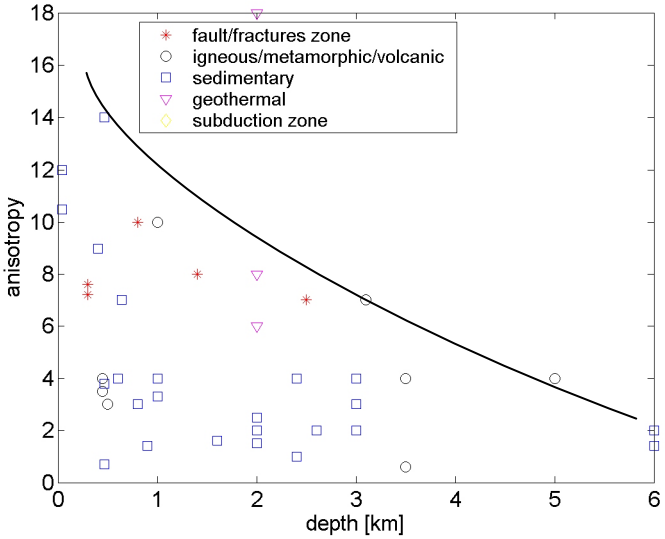

Figure 5: Shear-wave anisotropy data as a function of depth, for the first 6km. Data collected by Crampin (1994). The curve represents schematically the upper bound for the shear-wave data as a function of depth.

The data in Figure 5 acquired around the globe by different authors, suggests that there is an upper bound for shear-wave anisotropy that decreases with depth. For example, this data set suggests that at 0.5 km depth we may expect shear-wave anisotropy values between 0 and 14%, while at 6 km depth we should expect shear-wave anisotropy values between 0 and 3%. The upper bound on the shear-wave anisotropy decreases from 14% at the surface to about 3% at 5 km depth.

Shear-wave splitting phenomena can sometimes be attributed to factors other than the presence of aligned cracks, such as rock foliation, crystal alignment, or structural effects. However, in most situations the azimuthal shear-wave anisotropy in the shallow crust appears to be the result of aligned fractures, or aligned microcracks.

The interpretation of the shear-wave splitting as crack-induced anisotropy requires elasticity theories that relate the observable seismic parameters to fracture parameters. For example, we can use Hudson's (1981, 1997) model to derive the corresponding crack densities that would generate the observed shear-wave anisotropy. In the weak anisotropy approximation, the relationship between the crack density of a fractured medium with aligned cracks, and the shear-wave splitting is given by (Bakulin, 2000):

$$e = \frac{3(3-2g)}{8}\gamma . \qquad (1)$$

In the formula above, e is the crack density as defined in Hudson's model, g is the square of the S to P-wave velocity ratio $(V_S/V_P)^2$ of the unfractured background rock, and γ is the induced shear-wave anisotropy.

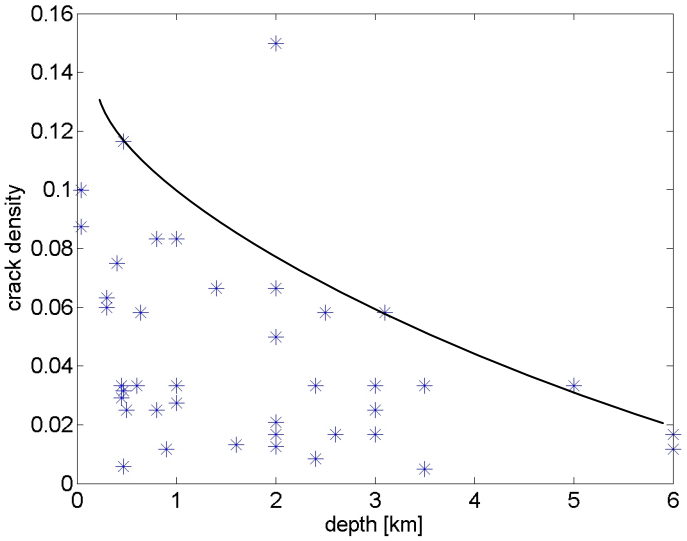

Figure 6: Computed crack density from the shear-wave anisotropy data using Hudson's penny-shaped crack model with volumetric distribution of cracks. We assume the V_P/V_S ratio of the host rock to be 1.7. The curve represents schematically the upper bound for the crack density as a function of depth.

The computed values of the crack density using Equation 1 are presented in Figure 6. The V_P/V_S ratio is assumed to be 1.7.

As expected, the computed crack densities also exhibit an upper bound, which decreases with depth, as is shown schematically in Figure 6. For example at 0.5 km depth the computed crack density varies approximately between 0 and 0.12, while at 6 km depth, the crack density varies in a narrower range, between 0 and 0.02. This may be explained by the effect of stress on cracks. Normally, increasing depth implies also increasing effective stress on the fracture planes. The stress is closing the cracks, therefore reducing the crack density. Another observation is that more than 95% of the computed crack density values are smaller than 0.1, which is the limit of validity for the Hudson's penny-shaped crack model. Therefore, this collection of field data also suggests that a crack density of 0.1 represents a relatively large degree of fracturing,

which may be encountered especially at small depths, where the stresses are smaller. However, as the depth increases, the normal effective stress on the fracture planes increases as well, increasing the contact area on the fracture planes, and reducing the crack density. This collection of data suggests that in most practical situations we should expect crack density values smaller than 0.1.

Hudson also models fractures as linear, planar arrangements of cracks (Hudson, 1997). However, he shows that, to first order, it does not matter if the cracks are volumetrically distributed in the rock mass, or if they are confined in parallel planes. Therefore, in the assumption of planar distribution of cracks, we can obtain the average relative area of cracking on the fracture planes from the crack density from Figure 6. We assume that the ratio between the average radius of the cracks and the distance between fracture planes is constant and equal to 1. The relative area of cracking, r, is given by:

$$r = \pi \frac{H}{a} e \,. \tag{2}$$

Here, H is the distance between the fracture planes, a is the mean radius of the crack on the fracture plane, and e is the total crack density of the fractured rock mass computed from the shear-wave anisotropy data using Hudson's model (1981).

Figure 7 presents the relative area of cracking on the fracture planes as a function of depth, in the assumption that the ratio of the spacing between fracture planes to the radius of the cracks is 1. We can see, as expected, that the relative area of cracking on the fracture planes decreases with increasing depth. This is because the effective stress on the fracture planes is larger at higher depth, pressing the faces of the fractures closer together, and increasing the area of contact between them.

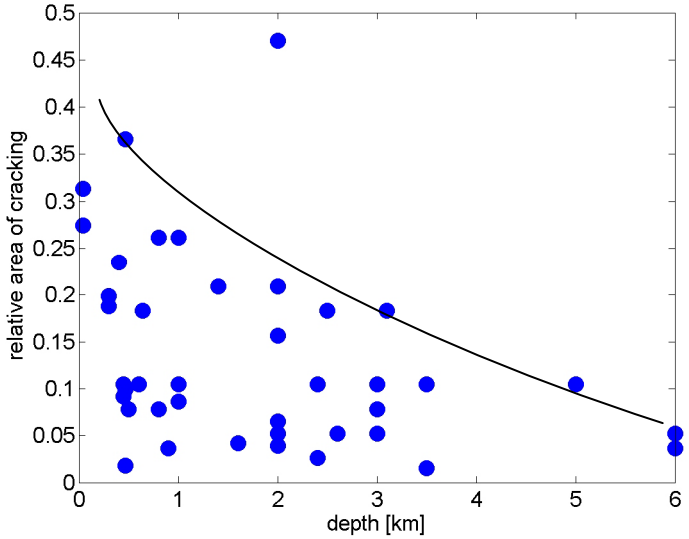

Figure 7: Computed relative area of cracking for planar distribution of cracks using Hudson's (1997) penny-shaped crack model. We assume the V_P/V_S ratio of the host rock to be 1.7. The curve represents schematically the upper bound for the relative area of cracking as a function of depth.

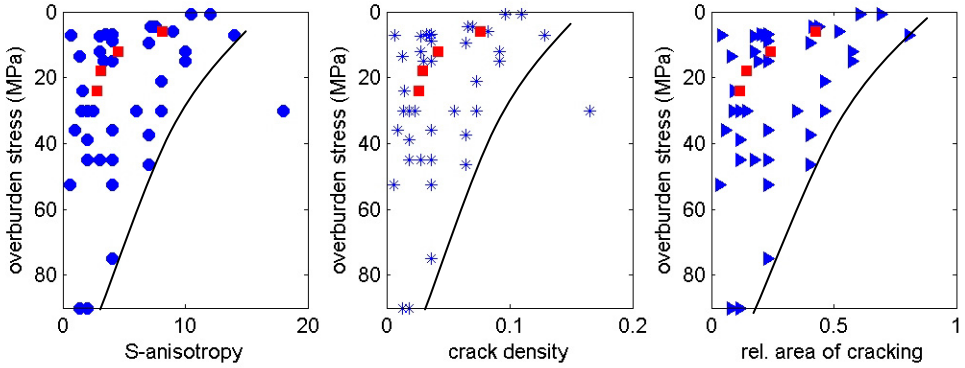

Figure 8: From left to right: Shear-wave anisotropy, crack density and the relative area of cracking as a function of the effective overburden stress computed using Crampin's collection (1994). Superimposed with red squares are the calculated values using Hsu and Schoenberg (1993) laboratory measurements. The effective overburden stress is estimated assuming a gradient of 15 MPa per km.

Figure 8 presents a summary for the analysis of the shear-wave anisotropy data. We converted the depth into the effective overburden stress, using a gradient of 15 MPa per km. The first panel shows the shear-wave anisotropy data as a function of effective overburden stress, the second panel shows the crack density as a function of effective overburden stress, and the third panel shows the relative area of cracking as a function of the effective overburden stress. On the panels from Figure 8 are superimposed also the

corresponding computed values from Hsu's and Schoenberg's (1993) measurements on simulated fractured media.

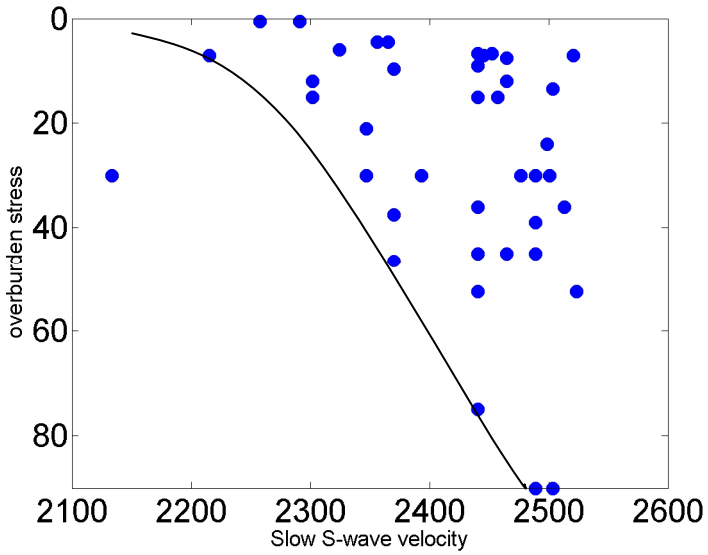

Figure 9: Computed S-wave velocity orthogonal to the fractures, using Hudson's model and the crack density, evaluated from the shear-wave anisotropy data from Crampin's collection.

Figure 9 presents the computed shear-wave velocity in the direction orthogonal to the fractures as a function of the overburden stress. The velocity is derived by using Hudson's model and the crack density evaluated from the shear-wave anisotropy data from Crampin's collection. We assume the same velocity for the unfractured background rock properties for all of the observed shear-wave anisotropy data. For the fractures, we assume an aspect ratio of 0.001. As expected, the computed shear-wave velocity increases with the estimated overburden effective stress. This happens because the cracks are closed gradually by the increasing stress as we go deeper in the Earth's crust, which has a stiffening effect on the elastic moduli. The increase in velocity with increasing pressure due to the closing of the cracks is one of the fundamental rock physics observations in the laboratory (Nur, 1971).

In conclusion, from the collection of the shear-wave anisotropy data acquired in various places around the globe, we observe a general trend of decreasing anisotropy with depth. More precisely, at each depth, the shear-wave anisotropy may vary from 0 to an upper bound. The upper bound values decrease with depth. Using elasticity theories that

relate shear-wave anisotropy with fracture characteristics, we compute the crack density and the relative area of cracking on the fracture planes, and display them as a function of depth, as well as the corresponding effective overburden stress. The analysis puts valuable constraints on the values of fracture parameters we should use in the modeling, depending on the depth of the reservoirs.

Based on the collection of data by Crampin, we also observe that the shear-wave anisotropy values of all of the reported data taken together do not exhibit a Gaussian distribution, but rather a log-normal or exponential distribution. Therefore, the prior distribution for the crack density should also follow a log-normal or exponential distribution, as geological outcrop studies also suggest (Snow, 1968; Priest and Hudson, 1976; Sen and Kazi, 1984; La Pointe and Hudson, 1985; Rouleau and Gale, 1985; Bouroz, 1990; Villaescusa and Brown, 1990, Narr and Suppee, 1991). This is also an important result that can be used in assigning prior distributions to crack density as a measure of uncertainty due to natural variability.

Conclusions

The analysis of the field data on shear-wave anisotropy acquired in various environments by different authors and summarized by Crampin (1994) helps us calibrate the fracture density parameter as well as the relative area of cracking on the fracture planes as a function of depth. The assumption is that the observed shear-wave splitting is due to alignment of vertical, parallel fractures.

More than 95% of the computed crack-density values based on these S-wave anisotropy data are smaller than 0.1. The larger values of crack density (around 0.1) correspond to data acquired at shallower depths, where the stress is smaller.

We also observe that the shear-wave anisotropy values of all reported data taken together exhibit not a Gaussian distribution, but rather a log-normal or exponential distribution. Therefore, the prior distribution for the crack density should also follow a log-normal or exponential distribution, as geological outcrop studies suggest. This is also an important result that can be used in assigning prior distributions to crack density as a measure of uncertainty due to natural variability.

This collection of data suggests also that there is an upper bound on the shear-wave anisotropy, and implicitly on the crack density, that decreases with depth. For example, the upper bound on the shear-wave anisotropy decreases from 14% at the surface to about 3% at 5 km depth. This helps us put powerful constraints on the crack density values as a function of depth. For example, for a reservoir at 1 km depth the crack density values may vary between 0 and 0.09, while for a deeper reservoir around 5 km depth, the crack density values may vary within a narrower interval from 0 to 0.04.

The results of the analysis of the laboratory and field data are valuable *a priori* information that we can use to constrain the crack density in our fracture modeling. This can help us to estimate the feasibility of various seismic methods to detect fractures, depending on the depth of the reservoirs.

Attachment E

Rock Physics Analysis and Stochastic Fracture modeling of the James Limestone Reservoir

Abstract

The first part of this attachment presents the rock physics analysis, based on well logs, of the fractured James Limestone reservoir. The objective is to understand if it is possible to seismically differentiate the gas-filled fractured zones from the other heterogeneities in the reservoir.

Using the information from the cross-dipole and FMI logs from one of the wells, we show that most of the fractures are associated with high velocity rocks, characterized by low porosity and a small amount of shale. This observation can be used to directly delineate fractured zones from seismic measurements. The association of fractures with high-velocity rocks also constrains the seismic properties of the background rocks that we use in our fracture modeling.

Based on the rock physics analysis, we consider that the reservoir may exhibit three main types of facies: 1) unfractured, clean limestones, 2) shaly limestones, and 3) fractured, clean limestones. The goal is to find the optimal combination of seismic attributes for distinguishing the gas-filled fractured zones from the shaly and unfractured limestones in the reservoir.

The second part of the attachment presents the results of the stochastic simulations of various seismic attributes for different models of fractures in the James Limestone reservoir. The modeling suggests that for the James Limestone reservoir, the interface

attributes, such as amplitude variation with offset (AVO), as well as with azimuth (AVAZ), may be more useful than travel-time techniques. The advantage of using interface attributes, defined at the boundary between two layers, is that they provide localized information at the target of interest, unlike the travel-time methods. Besides, for thin reservoirs, travel-time techniques are not very useful for fracture detection.

Based on the modeling, we conclude that the fractures at this site do have a seismic signature, especially if they are saturated with gas. For example, the modeling predicts low PP reflectivity values for the gas-filled fractured zones. However, we also expect low amplitudes from the shaly rocks in the reservoir, which are less likely to get fractured. The *AVO gradient* can help resolve this ambiguity. Modeling shows that the shaliness moves the *AVO gradient* to smaller negative values as compared to the clean, unfractured limestones, while the gas-filled fractured zones move the *AVO gradient* to larger negative values as compared to the clean, unfractured limestones.

In summary, rock physics fracture modeling and stochastic simulations for seismic attributes of the James Limestone reservoir provide a framework for delineating gas-filled fractured zones from seismic data, and for estimating the uncertainty in fracture characterization due to natural variability.

Introduction

The James Limestone formation has been an exploration target on the onshore Gulf of Mexico since the discovery of the Fairway field in Texas basin in 1960 (Loucks et al, 1996). In the study area, the formation is a microcrystalline fractured limestone, with the unfractured matrix permeability between 0.001 and 0.1 mD (Marathon Oil Co., Internal Report). However, the presence of fractures can locally increase the permeability. Therefore, precise fracture localization can have a big impact on gas production.

The rock physics analysis of the cross-dipole and FMI logs from one of the wells suggests that most of the fractures are associated with rocks which have the least amount of shale, characterized by high velocity and small porosity values. The same preferential association of the fractures with a particular type of facies was also observed for the San Andres carbonate reservoir (Sava et. al, 2001). The association of the fractures with the

high-velocity rocks constrains the seismic properties of the background rocks that we use in the fracture modeling.

The area of study is situated in a normal faulting regime. The maximum horizontal stress in the region is oriented E-W. In a normal faulting regime, the orientation of the faults is expected to be parallel to the maximum horizontal stress. A geological model based on the logs from horizontal wells suggests that the fractures are in part controlled by subseismic normal faults (Meeder, personal communication). These small faults can generate narrow damaged zones with high fracture density, due to increasing strain in the proximity of the faults (Nelson, 1985). Between these fracture swarms, the background fracture distribution may correspond to regularly spaced, vertical joints. This interpretation is supported by the FMI data from a nearby field. The fracture distribution interpreted from FMI log suggests the presence of a single set of vertical joints oriented approximately on the E-W direction. Therefore, for fracture modeling we consider the cases of both isotropic and anisotropic distributions of fractures. The isotropic distribution corresponds to the fracture swarms in the vicinity of faults, where the crack distribution is more chaotic, such as in brecciated zones. The anisotropic distribution corresponds to a single set of vertical joints that generates an azimuthally anisotropic elastic medium with HTI symmetry.

For the interface properties, we consider the boundary between the cap rock (Bexar shale), and the underlying James Limestone reservoir, modeled with different distributions of fractures.

We use *Monte Carlo* simulations for both fracture properties as well as for the background rocks to assess the feasibility of the seismic methods to delineate and characterize the fractured zones. The stochastic approach helps to incorporate the natural variability of the rock properties into deterministic models (Mavko and Mukerji, 1998; Mukerji et al., 2001). In this attachment, we show how we estimate the uncertainty due natural variability of both the background rock properties and the fracture parameters using Monte Carlo simulations.

Rock Physics Analysis

In this section, we use the well-log data available from two wells in the region to understand how the reservoir heterogeneities, and especially fractures, influence the seismic properties (V_P and V_S).

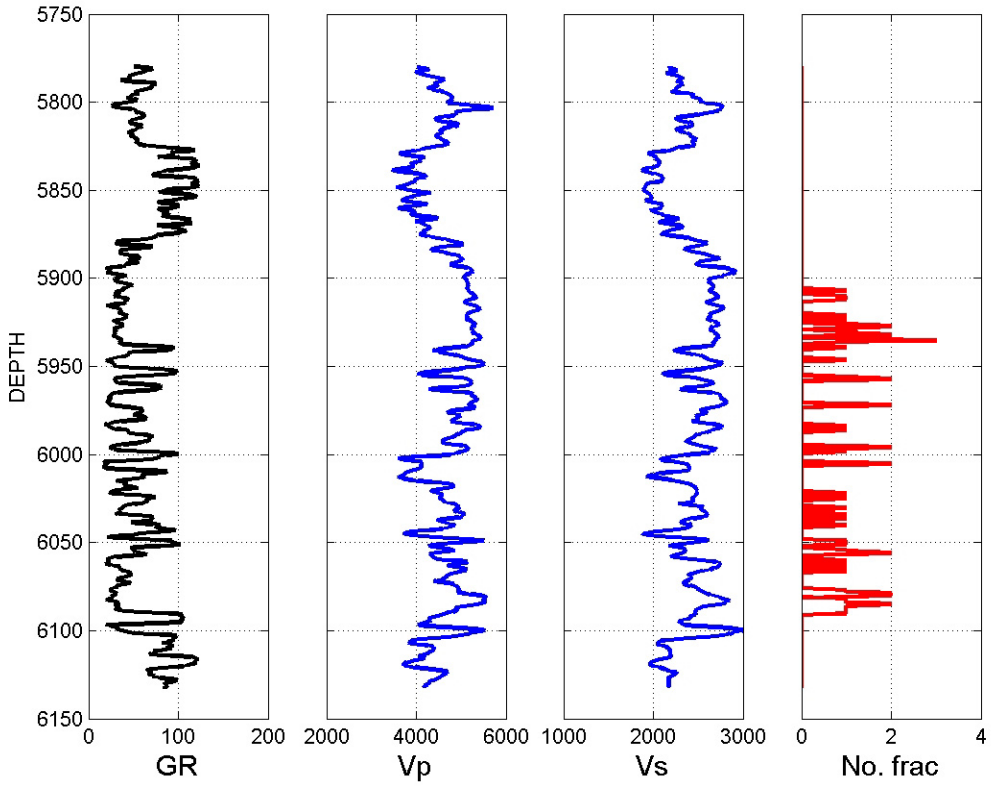

Figure 1: Well A: Well-log data over a depth interval corresponding to James Limestone reservoir. The depth is in feet. Gamma-Ray in first column is given in API, the V_P and V_S from the second and third columns respectively are in m/s, while the fourth column gives the number of fractures per foot interpreted from FMI data.

Figure 1 presents the well-log data from one of the key wells (Well A). The depth interval corresponds to the James Limestone reservoir. The first column gives the Gamma-Ray, the second and the third columns present the ultrasonic *P*- and *S*-wave velocities, while the fourth column shows the number of fractures per foot, interpreted from an FMI log. From Figure 1 we see a large variability in the gamma-ray, usually interpreted in terms of the volume of shale. This suggests that the reservoir is a heterogeneous limestone with intercalations of shaly rocks. As expected, the fractures

occur primarily in the more brittle rocks, with lower content of shale, characterized by lower Gamma-Ray values.

Figure 2 presents the porosity as a function of the Gamma-Ray for the James Limestone reservoir. The data are color-coded by the number of fractures per foot, interpreted from the FMI. We see a trend of increasing porosity with Gamma-Ray. This implies that the rocks with higher shale content exhibit also higher porosities. The important observation is the association of the fractures with the reservoir rocks that have low Gamma-Ray and low porosity values. This implies that the fractures occur preferentially in the more brittle and tighter rocks inside the reservoir, as expected (Nelson, 1985).

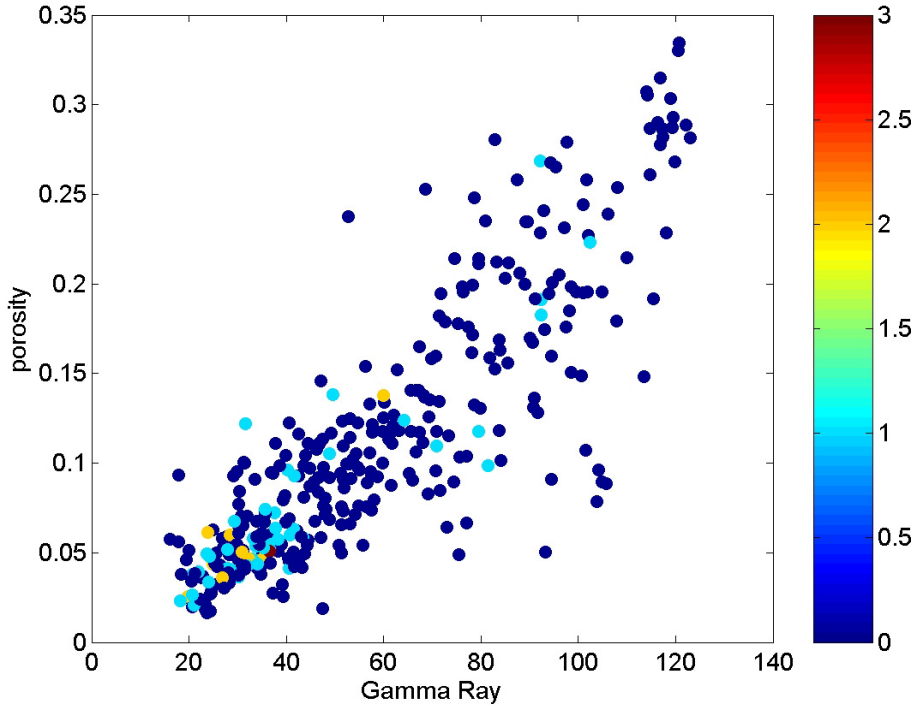

Figure 2: Porosity as function of the Gamma-Ray for the James Lime reservoir. The data are color-coded by the number of fractures per foot, interpreted from FMI. (Well A).

In the following sections we present the rock physics analysis, emphasizing the impact of shale content and fracture distribution on the seismic properties, such as the *P*- and *S*-wave velocities, using the well-log data from two wells.

V_P-porosity relation

A very common and useful plot in any rock physics analysis is the *P*-wave *velocity vs. porosity* scatter-plot, which gives information about the diagenetic processes that the rocks have experienced, as well as about the pore types (Anselmetti and Eberli, 1977).

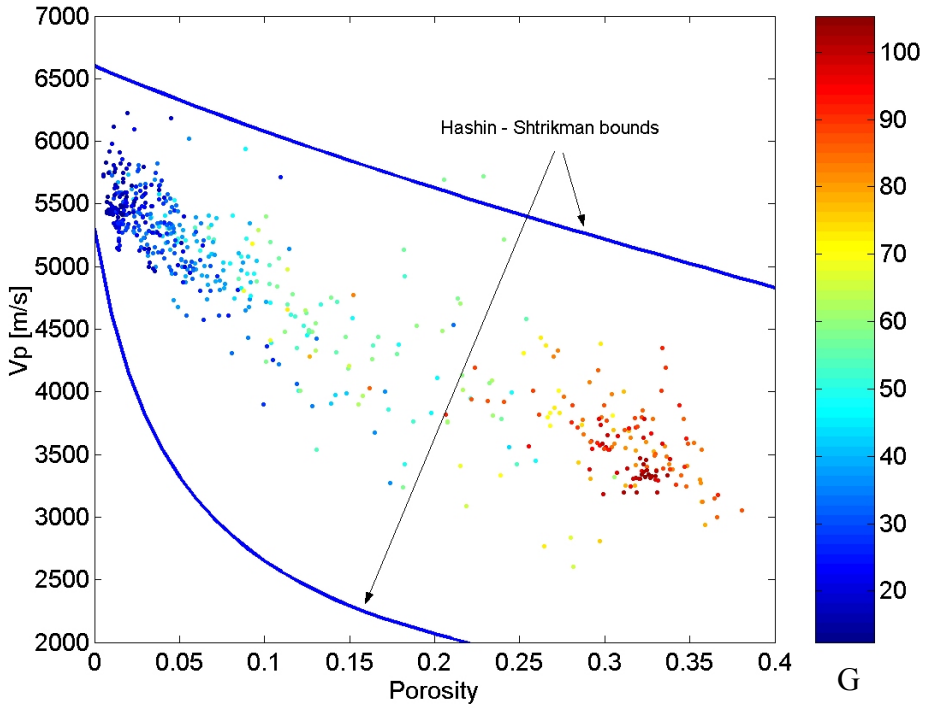

Figure 3: V_P-porosity scatter plot for James Lime reservoir. Data are color-coded by Gamma Ray (Well B).

Figure 3 presents the V_P *vs. porosity* scatter-plot for the James Limestone interval from one well (Well B). The data are color-coded by Gamma-Ray intensity (API). We observe the expected trend of decreasing velocities with increasing porosity. We can also see that the higher velocities correspond to cleaner limestones (smaller values of Gamma-Ray), while the lower velocities correspond to rocks with higher shale content (larger values of Gamma-Ray). The porosity values for the shaly rocks are large, while those for the clean limestones are significantly smaller. This indicates that the cleaner limestones are tight, densely cemented rocks. Therefore, fracture permeability can have a big impact on the fluid flow in the areas of tight, clean limestones.

From Figure 3 we observe a larger scatter in the V_P-*porosity* domain for the shaly rocks than for the cleaner limestones. The scatter increases with porosity and shale content.

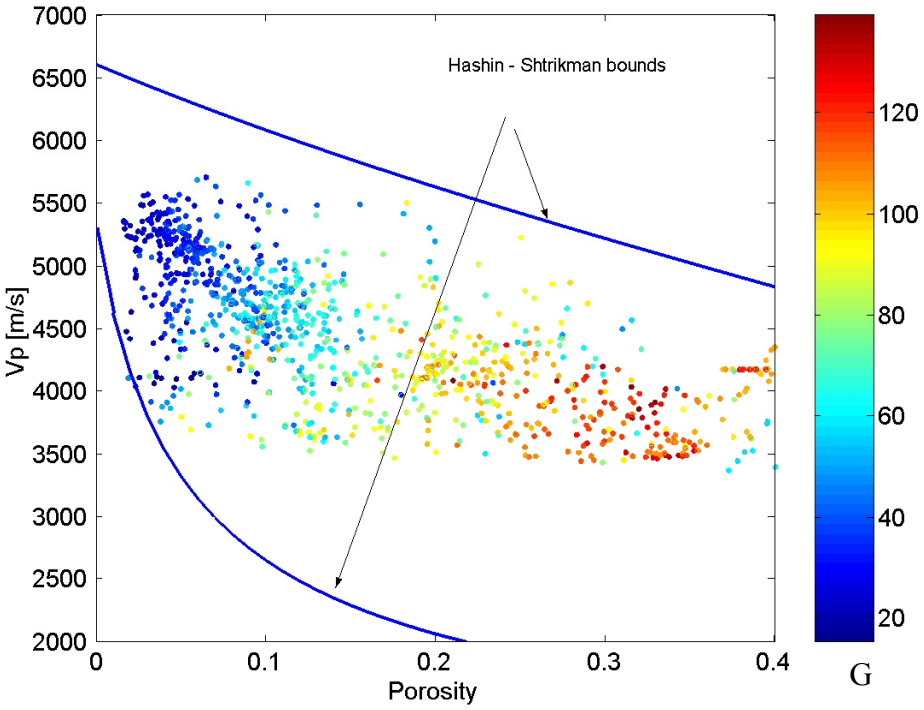

Figure 4: V_P-porosity scatter plot for the James Limestone reservoir. Data are color-coded by Gamma-Ray (Well A).

Figure 4 shows again a V_P *vs. porosity* scatter-plot, but for data from one of the key wells (Well A). We can observe the same expected trends of decreasing velocities with porosity, and decreasing velocities with Gamma-Ray, due to higher shale content. However, in this well there is more scatter in the velocities for the lowest porosities, in contrast with what we observed in the previous well (Figure 3). The *P*-wave velocities vary significantly, from approximately 5700 m/s to 4000 m/s, at about 5% porosity. We see from the color-coded Gamma-Ray that at these small porosities the shale content is relatively low. We also know from FMI data that fractures occur preferentially in the rocks with lower shale content. Therefore, we hypothesize that this large variation in the *P*-wave velocity at low porosities is the result of fractures. Fractures can greatly lower the velocities, without significantly increasing the porosities.

If we compare the V_P-*porosity* scatter plots for the two wells, we may interpret from the velocity variation, that Well A encountered more fractures than Well B. However, we can not verify this interpretation, since Well B does not have an FMI log.

Fracture distribution in the V_P-porosity domain

Figure 5 shows the same V_P *vs. porosity* scatter-plot for the James Limestone reservoir from Well A, but the data are color-coded by the number of fractures per foot. The fractures are interpreted from FMI log. we interpolated the number of fractures per foot to match the sonic log depth sampling. We can see that most of the fractures are in the brittle rocks, characterized by higher velocities, smaller porosities and lower shale content.

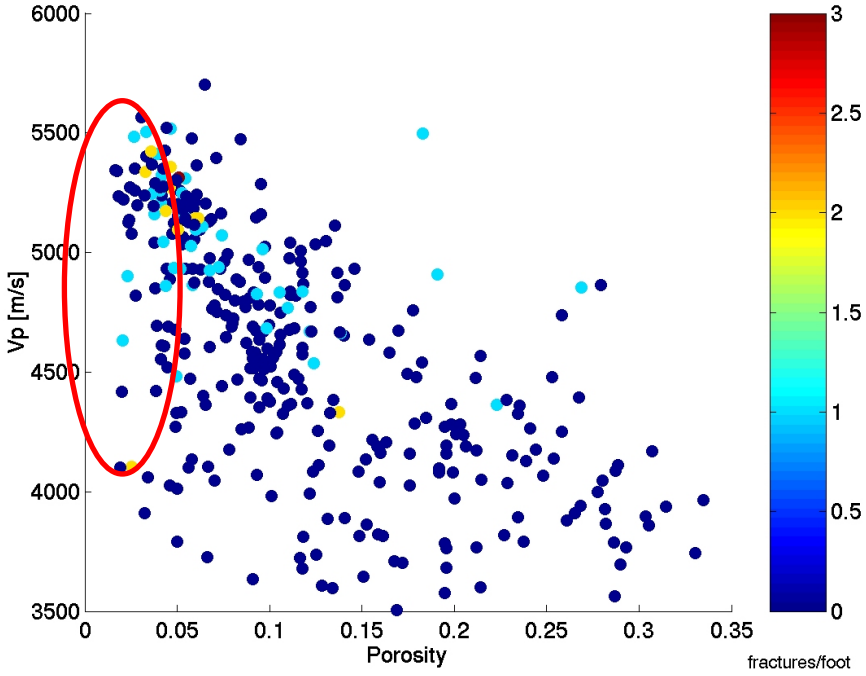

Figure 5: Fracture distribution in the James Limestone in the V_P-porosity domain. The data are color-coded by number of fractures per foot, determined through FMI in Well A.

In Figure 5, we highlight a zone of highly varying V_P at small porosity. This zone corresponds to intervals with a relatively larger number of fractures per foot, and it supports the hypothesis that the scatter in the velocities is due to fractures.

V_P-V_S relationship

Another very important relation that we consider in any rock physics analysis is the one between the *P*-wave velocity and the *S*-wave velocity, since this is the key to lithology, and also to fluid discrimination from seismic or sonic-log data. This relation is also very important for predicting V_S in cases when we have only *P*-wave information.

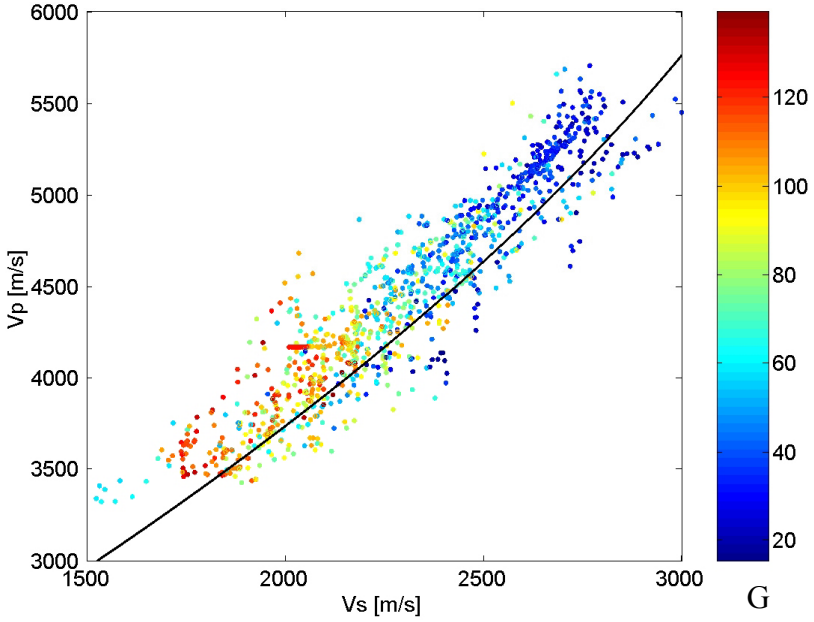

Figure 6: V_P-V_S scatter plot for James Lime reservoir. Superimposed is Castagna's line for Limestones. (Data from Well A).

For the area of study, we use the V_P-V_S relation from Well A, the only one which has shear-wave information. Figure 6 presents the V_P-V_S scatter plot for the James Limestone reservoir. Data are for brine-saturated rocks. We also superimposed the least-squares polynomial fit derived by Castagna et al. (1993) for limestones:

$$V_S = -0.05508\, V_P^2 + 1.0168\, V_P - 1.0305 \qquad (1)$$

We can see that for this data set, the *S*-wave velocity is slightly lower than the one predicted by the Castagna's empirical relation. In other words, the V_P/V_S ratio is a little higher for the James Limestone than is predicted by Castagna's relation. Nevertheless, there is a very distinct correlation between V_P and V_S, as expected.

Fracture distribution in the V_P-V_S domain

Figure 7 presents the same V_P-V_S scatter plot for an interval from the James Limestone reservoir. The data are color-coded by the number of fractures per foot.

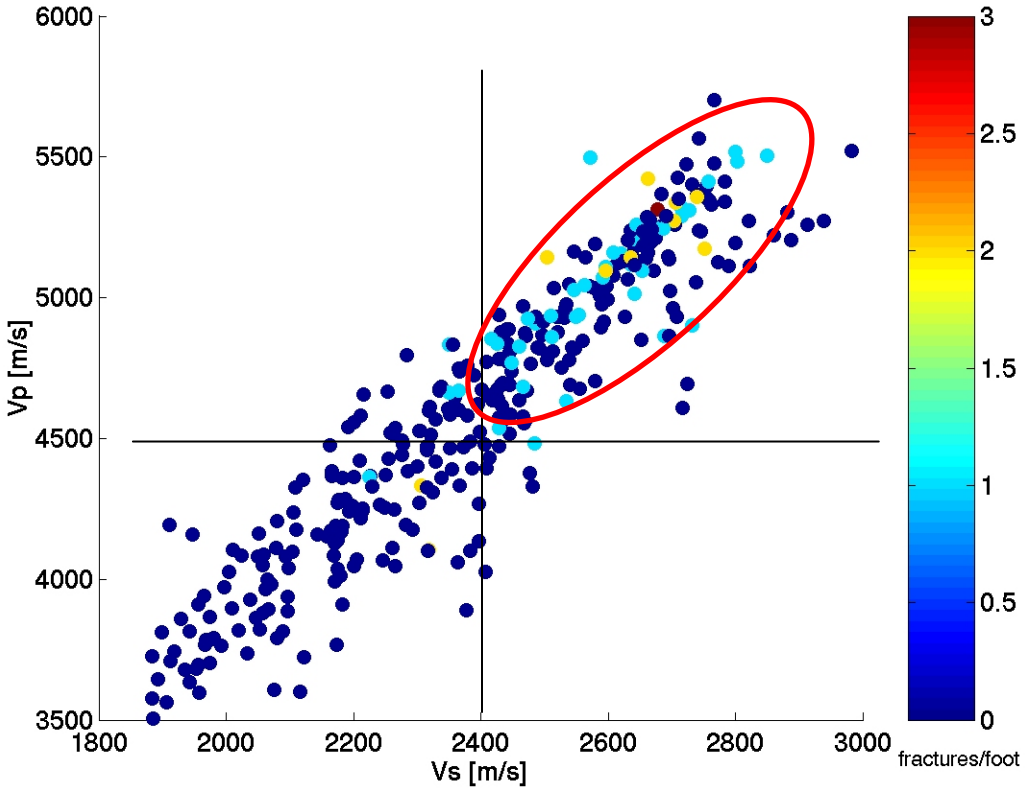

Figure 7: Fracture distribution in the James Limestone in the V_P-V_S domain. The data are color-coded by number of fractures per foot, determined through FMI. (Well A).

We observe that the fractures are mostly present in rocks with high *P*- and *S*-wave velocities. As a consequence, in the modeling we assume that the fractures are associated with high-velocity rocks, whose unfractured background properties exceed certain limits, such as 4500m/s for V_P and 2400m/s for V_S.

This association of the fractures with the high-velocity rocks was observed also for the San Andres reservoir, in the Yates Field (Sava et al, 2001). The association can play an important role in fracture delineation from seismic data. Even if the fractures will lower the velocity significantly in the most fractured zones, on average the velocities of the fractured regions may be larger than the velocities of the unfractured rocks, characterized by higher shale content. Therefore, on average, higher impedance may

correspond to the zones with higher probability of fractures, as the results from fracture modeling show in the next sections.

Gassmann fluid substitution

Another very important task in any rock physics analysis is to assess the fluid sensitivity in the seismic response. For this, we use Gassmann's (1951) low-frequency fluid substitution method (Mavko et al., 1998). Figure 8 shows the brine-saturated (blue) and the gas-saturated (red) properties of the James Limestone reservoir in the V_P-V_S domain. As expected, the fluid sensitivity is a little larger at smaller velocities. The superimposed lines are least-square linear fits to the data, for the brine and gas cases, respectively. We can observe that the variability in V_P and V_S from rock stiffness, clay content, and porosity is as large as the sensitivity to the fluid changes.

The average elastic fluid properties in the area of interest are presented in Table 1, and are evaluated using Batzle's and Wang's (1992) empirical relations:.

Table 1: Fluid properties for the James Limestone reservoir.

	Bulk modulus [GPa]	Density [g/cm3]
brine	2.51	1.018
gas	0.048	0.032

However, we expect the fluid sensitivity to be significantly enhanced by the presence of the fractures, as the modeling results show in the next sections.

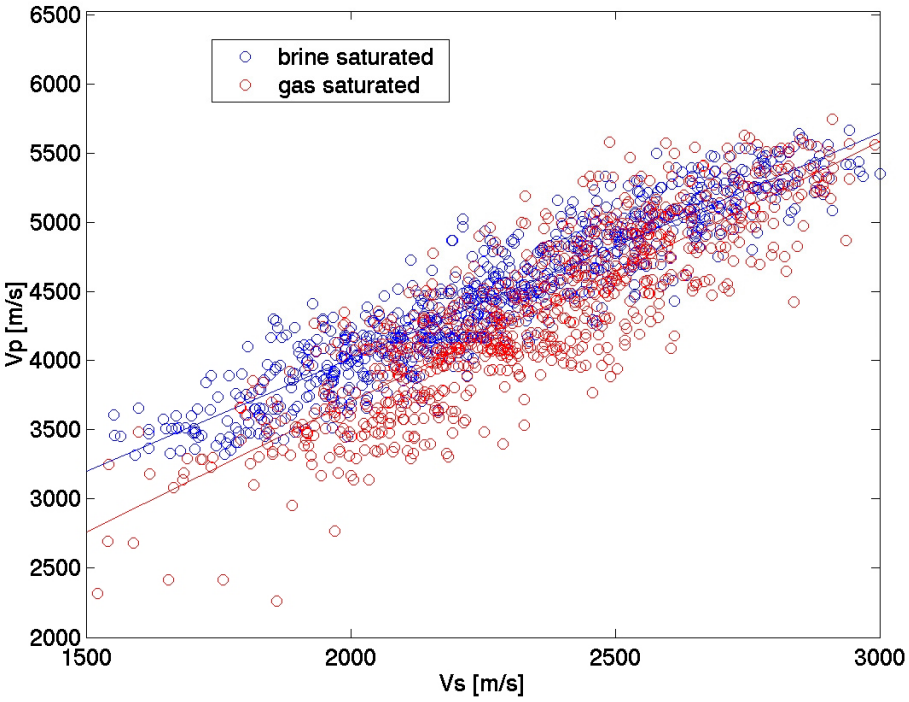

Figure 8: V_P-V_S scatter-plot for brine and gas-saturated cases for the James Limetone reservoir. Velocities are stochastically simulated.

Summary of the observations

In this section, we give a brief summary of the preceding rock physics analysis, based on the well-log data.

From the V_P-*porosity* scatter-plots color-coded by the Gamma-Ray, we see that the velocities decrease with porosity and shale content, as expected. The cleaner limestones have lower porosities and higher velocities than the more shaly rocks.

From the V_P-V_S scatter-plot color-coded by the number of fractures per foot, we can see that most of the fractures are associated with high V_P and V_S. This association can play an important role in fracture delineation from seismic data. As we show in the next section, high density of gas–filled fractures can significantly lower the velocities of the clean limestones. However, on average, the velocities of the fractured regions may still be larger than the velocities of the shaly rocks. Therefore, higher impedance values may correspond to the zones with higher probability of fractures.

This association of fractures with higher velocity rocks helps us in choosing the unfractured background properties that we need to input in the modeling. The elastic properties should correspond to rocks with velocities higher than certain limits, such as 4500 m/s for V_P and 2400m/s for V_S.

Based on these observations, we consider that the reservoir may exhibit three main types of facies: 1) unfractured, clean limestones, 2) shaly limestones, and 3) fractured, clean limestones that we model with various distributions of cracks.

Monte Carlo simulations and fracture modeling

In this section, we present the results of the fracture modeling and stochastic simulations of various seismic signatures, with the objective of determining the optimal seismic attributes for delineating the gas-filled fractured zones in the reservoir. The stochastic approach allows us to incorporate the natural geologic variability of rock properties into deterministic elastic models (Mavko and Mukerji, 1998; Mukerji et al., 2001, Avseth et al., 2005).

Fractures affect both the interval properties, such as velocities and travel-time, and the interface properties, such as reflectivity and AVO. If the fractures are aligned, they can also induce anisotropy for both interval and interface properties.

In most cases, seismic field studies for fracture detection are designed to find near-vertical and open joints (Teng, 1998; Grimm, 1999; Perez, 1999; Lynn, 1999). However, in the proximity of the faults, sometimes the host rock can be very fractured, giving rise to the so-called “breccia zone”. In these cases the faults may have systematic alignment, but the smaller fractures can be distributed in all possible directions. Therefore, for this situation a more appropriate fracture model is one that assumes isotropic distribution of crack orientations.

For both isotropic and anisotropic distribution of fracture orientations, we use Hudson’s (1981) penny-shaped crack model.

In this section, we consider the fractures to be 100% saturated with either brine or gas, but not necessarily with the same fluid as in the matrix porosity. We substitute the fluids in the fractures by changing the elastic moduli of the inclusion material in Hudson’s (1981) equations. This procedure assumes that there is little communication between the

fluids in the matrix pores and the fluids in the cracks during wave excitation. This assumption is most appropriate when the matrix porosity and permeability are small (Hudson, 1997, Teng, 1998). For the clean limestones that are most likely to get fractured, the porosity of the unfractured background rocks is smaller than 10%, while the permeability has also very low values, between 0.001 and 0.1md (Marathon Oil Co., Internal Report).

To assess the uncertainty of fracture detection and characterization from seismic data, we run Monte Carlo simulations on the input parameters in the Hudson's model (1981). The input parameters are the crack density, aspect ratio of the ellipsoidal cracks, bulk modulus of the saturating fluid, and the V_P, V_S and *density* of the isotropic, unfractured background rocks.

For the crack density, we choose a uniform distribution between 0.01 and 0.1. The upper value of 0.1 corresponds to the limit of validity of Hudson model. As discussed in Attachment D, this value represents a relatively large degree of fracturing, especially for a reservoir at approximately 2 km depth. By choosing a uniform distribution We assume maximum uncertainty over the interval considered for the crack density. For the aspect ratio of the penny-shaped cracks, defined as the ratio between the aperture and the radius of the crack, we also use a uniform distribution, on a logarithmic scale (from 0.001 to 0.1).

For the unfractured matrix properties (V_P, V_S, *density*), we derive the distributions from the well-log data. . Figure 9 presents in the upper panels the histograms for the V_P, V_S and *density* of the clean limestones in the reservoir, obtained from the well logs. The lower panels in the same figure present the probability distribution functions (PDFs) of the V_P, V_S, and *density* derived from the histograms. Since the fractures occur preferentially in the high velocity rocks, as the rock physics analysis shows, we consider for the background properties of the host rocks only P-wave velocities greater than 4500m/s.

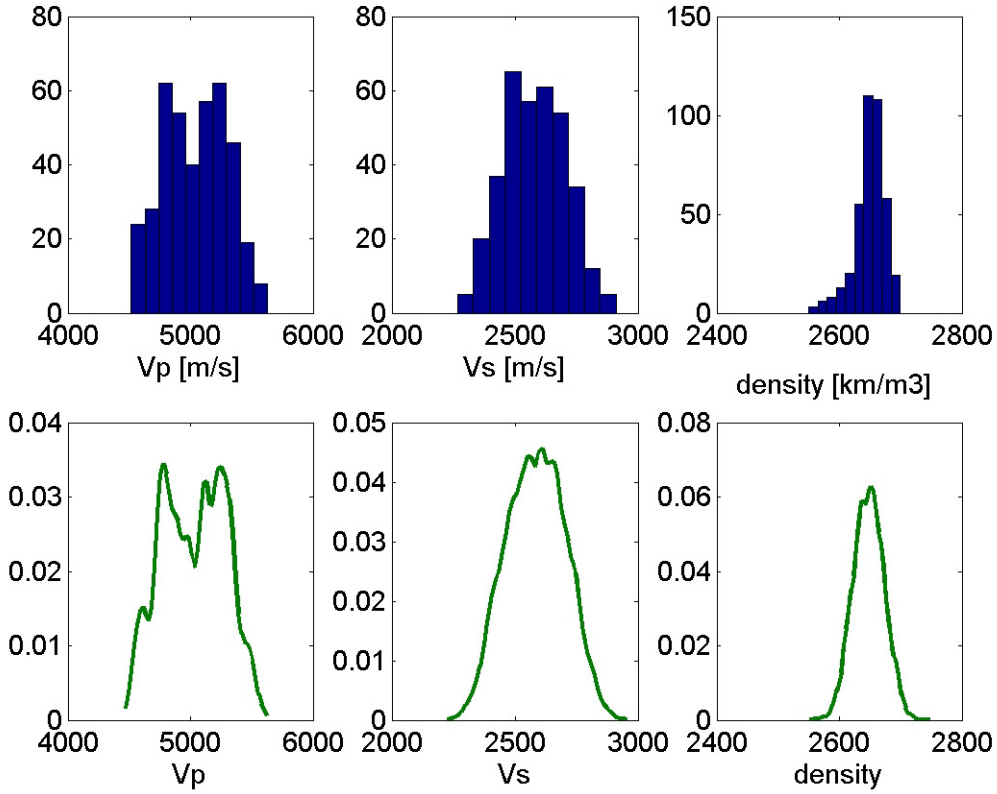

Figure 9: Upper panels: V_P V_S and density histograms derived from the well logs for the unfractured background rock properties. Lower panels: Corresponding probability density functions (PDFs).

The V_P, V_S, and *density* derived from the well logs are also upscaled to seismic wavelengths. The upscaling is performed on the well data using Backus (1962) averages for the bulk and shear modulus, and volumetric averages for density (Mukerji, 1995). The fluid that saturates the fractures is considered to be either gas or brine.

The *Monte Carlo* procedure consists in randomly drawing correlated sets of V_P, V_S, and *density* from the distributions derived from the well-logs for the unfractured background rock properties, and also from the assumed distributions for the crack density and the aspect ratio of the ellipsoidal cracks. For each realization of a set of V_P, V_S, and *density*, together with the crack density and the aspect ratio of the cracks, we compute the elastic properties for the fractured medium, using Hudson's model. If we repeat this procedure many times, we obtain a large number of realizations of elastic properties for the modeled fractured medium, to span the intrinsic natural variability.

We also simulate multiple realizations for the elastic properties for the other possible facies in the reservoir, such as the shaly rocks and the unfractured, clean limestones. In order to model the interface properties, we also simulate multiple realizations for the *Vp*, *Vs* and *density* of the cap rock, based on the distributions derived from the well logs.

Based on this large number of correlated realizations of elastic properties, we derive the joint probability density functions (PDFs) of various seismic attributes for each facies in the reservoir: 1) clean, unfractuered limestone, 2) shaly limestone, and 3) fractured, clean limestone. We compute both the interval and the interface seismic properties, to understand how we can separate the fractured zones filled with gas from the other facies in the reservoir, in different possible scenarios.

Interval properties

In this section, we present the results of our stochastic simulations for interval properties, such as *P*- and *S*-wave velocities, *P*-Impedance and Poisson's ratio and travel-times, in the hypotheses of a vertical set of fractures, and of randomly oriented cracks in the reservoir.

Interval velocities

Fractures can lower significantly the velocities of the initially unfractured host rock. We consider first the hypothesis of an isotropic distribution of fracture orientations, which corresponds to breacciated zones associated with faults.

We use *Monte Carlo* method and fracture modeling, as previously presented, and obtain the joint probability density function for the interval *P*- and *S*- wave velocities.

Figure 10 shows one of the results of the stochastic simulations for the three different possible facies in the reservoir. The contours represent the joint probability density functions (PDF) of V_P and V_S for the unfractured, clean limestone (blue), for the shaly rocks in the reservoir (red), and also for the fractured, clean limestone, modeled with randomly oriented cracks (green). The fractures are filled with gas.

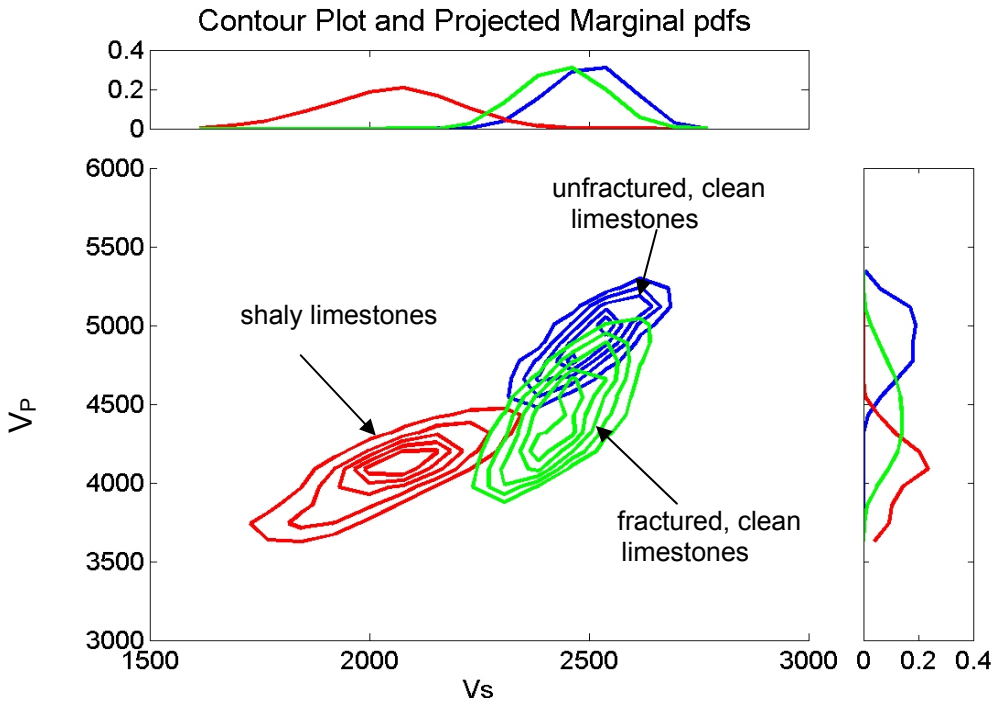

Figure 10: Joint probability distribution functions of V_P and V_S for the Monte Carlo simulations of the unfractured clean limestones (blue), fractured limestones with randomly oriented cracks (green), and shaly rocks (red). Fractures are filled with gas. The upper and right panels show the marginal distributions for V_S and V_P for each facies.

The uncertainty in the PDFs is due to the variability in the unfractured background properties. For the fractured facies, the scatter is also due to the variability in both the crack density and the aspect ratio of the cracks.

We can see that in the V_P-V_S *domain* there is some overlap of the joint probability distribution functions (PDF) between the modeled fractured rocks and the unfractured ones. The *P*-wave velocity of the fractured rocks filled with gas decreases more than the *S*-wave velocity. From the marginal distribution, presented in the right-side panel of Figure 10, we see that on average, the V_P of the fractured, clean limestone is larger than the V_P of the shaly rocks. However, as the fracture density increases, the *P*-wave velocity of the fractured, clean limestone becomes closer to the *P*-wave velocity of the shaly limestone. At the same time, the decrease in V_S due to fractures is smaller, such that the S-wave velocities of the fractured, clean limestones remain significantly higher than the

V_S of the shaly rocks. Therefore, the shear-wave information is valuable for discriminating between the gas-filled fractured zones and the shaly zones in the reservoir.

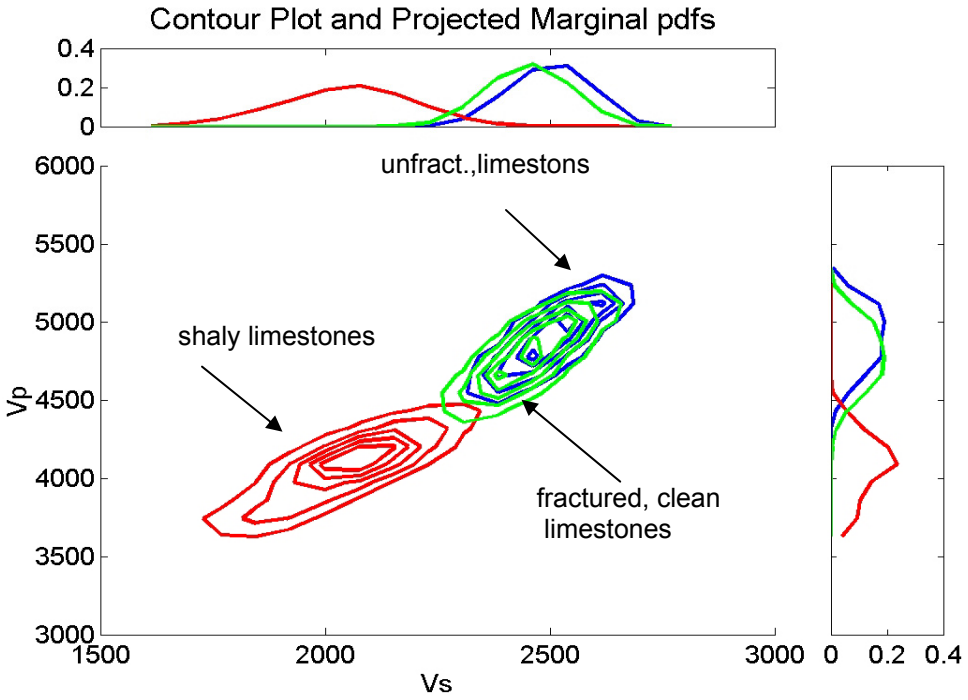

Figure 11: Joint probability distribution functions of V_P and V_S for the Monte Carlo simulations of the unfractured, clean limestones (blue), fractured limestones with randomly oriented cracks (green), and shaly rocks (red). Fractures are filled with brine. The upper and right panels show the marginal distributions for V_S and V_P respectively, for each facies.

Figure 11 presents the joint PDF of V_P and V_S for the three main facies in the reservoir. In this case, however, the fractures are saturated with brine. We observe very small decrease in both *P* and *S*-wave velocities as compared with the properties of the unfractured limestones. Modeling shows that in the V_P-V_S domain it is difficult to distinguish between unfractured, clean limestones and fractured zones, if the randomly oriented fractures are saturated with brine.

In the case of a vertical set of aligned fractures, the medium is anisotropic, and velocities vary with direction. Figures 12 and 13 show the joint PDF of V_P and V_S for the three possible facies in the reservoir.

The modeled V_P and V_S of the fractured limestones correspond to the waves polarized parallel to the fracture planes. In Figure 12, the cracks are gas-saturated, while in Figure

13, the cracks are brine-saturated. As Hudson's model predicts, the V_S of the fractured rocks polarized along the crack plane is not at all affected by the presence of the fractures. However, the *P*-wave velocity propagating parallel to fracture planes is slightly lowered, if the cracks are filled with gas. However, this decrease in V_P is not very large, such that the *P*-wave velocities propagating along the fracture planes remain higher than those of the shaly limestones in the reservoir.

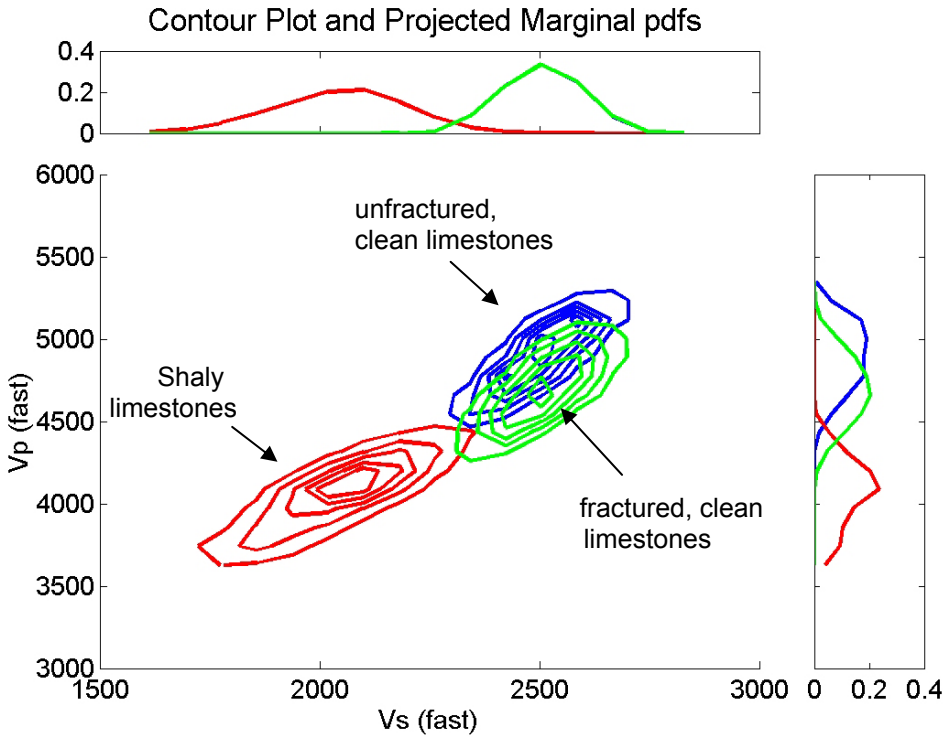

Figure 12: Joint PDFs of V_P and V_S for the Monte Carlo simulations of the unfractured clean limestones (blue), fractured limestones with a set of vertical cracks (green), and shaly rocks (red). Fractures are filled with **gas**. The V_P and V_S for fractured facies correspond to polarization **parallel to fractures**. The upper and right panels show the marginal distributions for V_S and V_P respectively, for each facies.

If the fractures are saturated with brine, then the fractured rock cannot be distinguished from the unfractured, clean limestones, as Figure 13 shows.

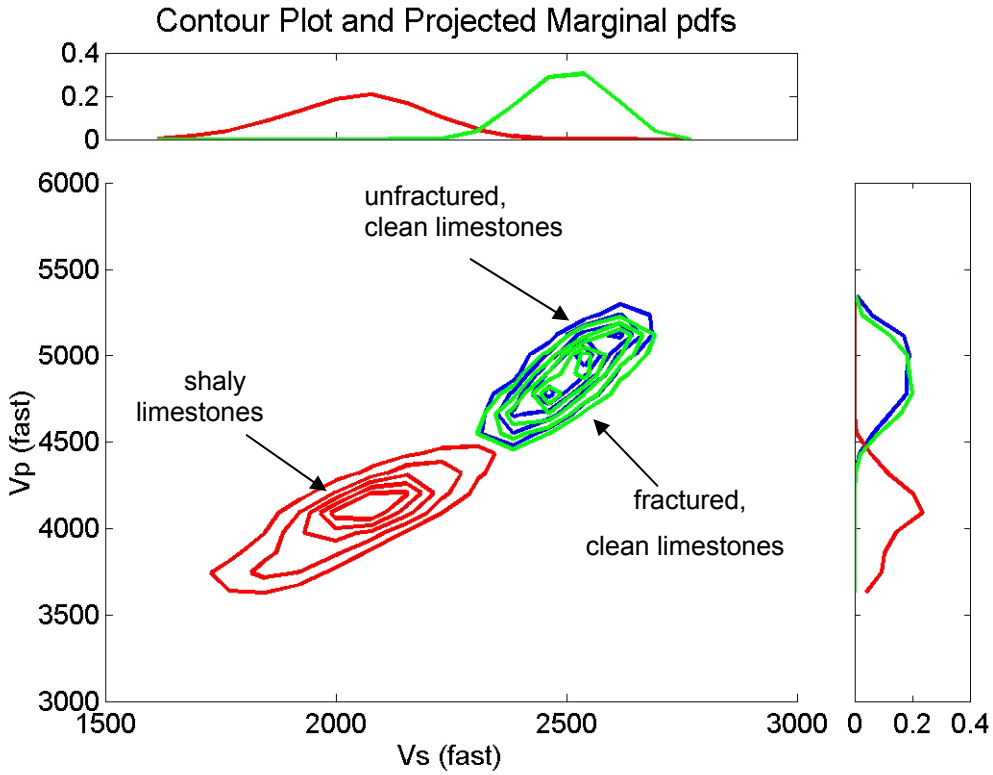

Figure 13: Joint PDFs of V_P and V_S for the Monte Carlo simulations of the unfractured clean limestones (blue), fractured limestones with a set of vertical cracks (green), and shaly rocks (red). Fractures are filled with **brine**. The V_P and V_S for fractured facies correspond to polarization **parallel to fractures**. The upper and right panels show the marginal distributions for V_S and V_P respectively, for each facies.

Figures 14 and 15 show again the joint PDFs for V_P and V_S. In these cases the properties of the fractured facies correspond to the wave polarization orthogonal to the fracture planes. The cracks are filled with gas (Figure 14), and brine (Figure 15), respectively. For the gas-saturated fractures, both V_P and V_S decrease significantly as compared with the properties of the unfractured, clean limestones. However, the modeling predicts a larger decrease in V_P, than in V_S. The *S*-wave velocities polarized orthogonal to the fracture planes remain significantly higher than the *S*-wave velocities of the shaly limestones, in contrast with the *P*-wave velocities. This result suggests that the shear information from waves polarized orthogonal to the fracture planes is important for discriminating between the gas-filled fractured zones and the shaly zones in the reservoir.

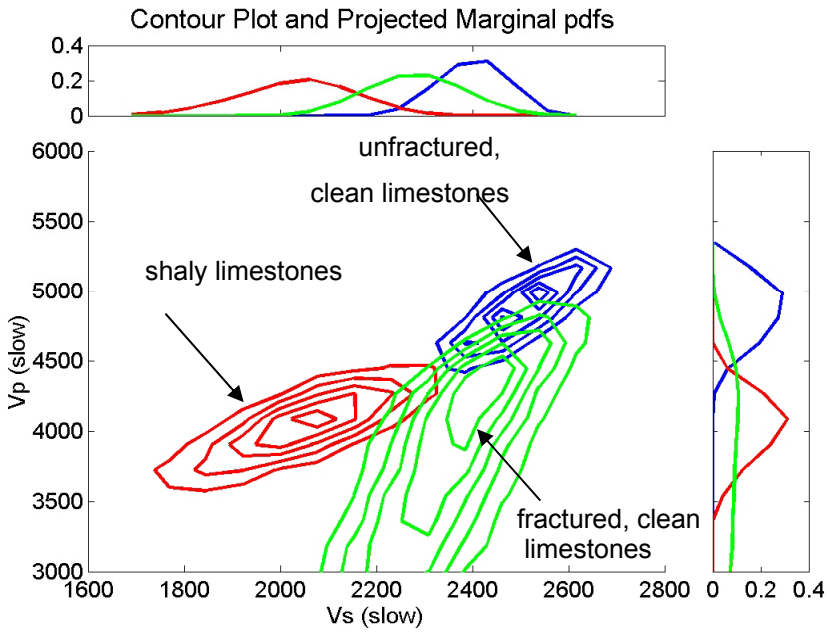

Figure 14: Joint PDFs of V_P and V_S for the Monte Carlo simulations of the unfractured clean limestones (blue), fractured limestones with a set of vertical cracks (green), and shaly rocks (red). Fractures are filled with **gas**. The V_P and V_S for fractured facies correspond to polarization **orthogonal to fractures**. The upper and right panels show the marginal distributions for V_S and V_P respectively, for each facies.

Figure 15 shows that, if the fractures are saturated with brine, the *P*-wave velocity polarized orthogonal to fractures decreases less than the corresponding *S*-wave velocity with the same polarization. Both V_P and V_S polarized orthogonal to brine-filled cracks are larger than the velocities of the shaly rocks in the reservoir.

From the modeling, we observe that in the V_P -V_S domain the gas-filled fractures are much more easily distinguishable from the unfractured rocks than the brine-filled fractures, for both isotropic and anisotropic distributions of fracture orientations.

If the fractures are saturated with gas, the modeling shows that the *P*-wave velocities are more sensitive than the *S*-wave velocities. As expected, the *P*-wave velocity decreases the most in the case of a vertical set of aligned fractures, if the waves are propagating orthogonal to the cracks. For large crack densities, the V_P of the fractured zones becomes comparable to the V_P of the shaly limestones in the reservoir, which are less susceptible to be fractured. The S-wave velocity decreases less than *P*-wave velocity, and its expected values remain larger than the *S*-wave velocity of the shaly rocks. Therefore, V_S

is a valuable piece of information to discriminate between the gas-filled fractured zones and the shaly limestones in the reservoir.

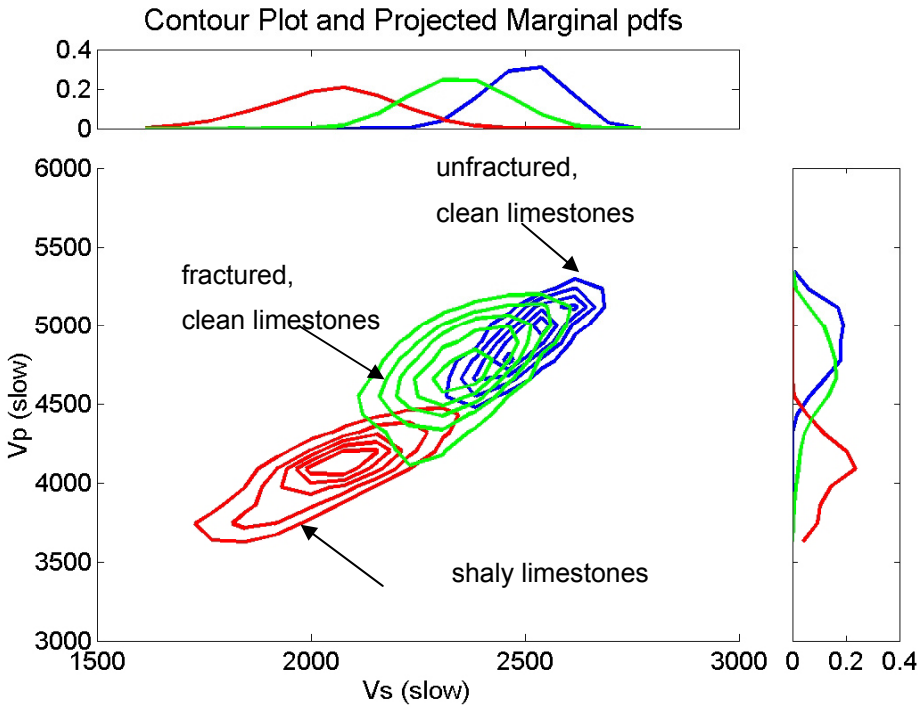

Figure 15: Joint PDFs of V_P and V_S for the Monte Carlo simulations of the unfractured clean limestones (blue), fractured limestones with a set of vertical cracks (green), and shaly rocks (red). Fractures are filled with **brine**. The V_P and V_S for fractured facies correspond to the polarization **orthogonal to fractures**. The upper and right panels show the marginal distributions for V_S and V_P respectively, for each facies.

If the fractures are brine-saturated, it is more difficult to distinguish the fractured zones from the unfractured ones. Both *P*- and *S*-wave velocities are little affected by the presence of the fractures, for both isotropic and anisotropic distribution of cracks. The fractured zones saturated with brine are the most visible in the V_P -V_S domain, when the waves are polarized orthogonal to the aligned fracture planes. This is the only case in which V_S is more sensitive to fractures than V_P (Figure 15). However, on average, *S*-wave velocity of the fractured zones remains larger than the *S*-wave velocity of the shaly limestones in the reservoir.

P-Impedance – Poisson's Ratio

Besides the V_P -V_S domain, we also consider the *P-Impedance* - *Poisson's Ratio* domain, in the case of an isotropic distribution of fractures.

Figures 16 and 17 present the joint PDF for the *P-Impedance* and *Poisson's Ratio*, again for the three possible facies in the reservoir: unfractured, clean limestones (blue), fractured limestones (green), and shaly rocks (red). Fractures are randomly distributed and filled with gas (Figure 16) and brine (Figure 17), respectively. The pores in the matrix rocks are brine-saturated.

From Figure 16 we can see very little overlap between the three different possible facies in the reservoir. The *P-Impedance* of the fractured rocks filled with gas may drop significantly, especially for high fracture density, as compared with the *P-Impedance* of the unfractured, clean limestones. However, as we observe from the marginal distributions of the *P-Impedance* for each facies (right panel of Figure 16), the expected value for the *P-Impedance* of the fractured zones is still larger than the one corresponding to the shaly limestones in the reservoir. Therefore, higher impedance may correspond to zones of higher fracture probability. *Poisson's ratio* is a good discriminator between the fractured, clean limestones and the shaly rocks. If the fractures are filled with gas, the *Poisson's Ratio* of the fractured limestones decreases drastically as compared to the *Poisson's Ratio* of both the shaly limestones and the unfractured, clean limestones.

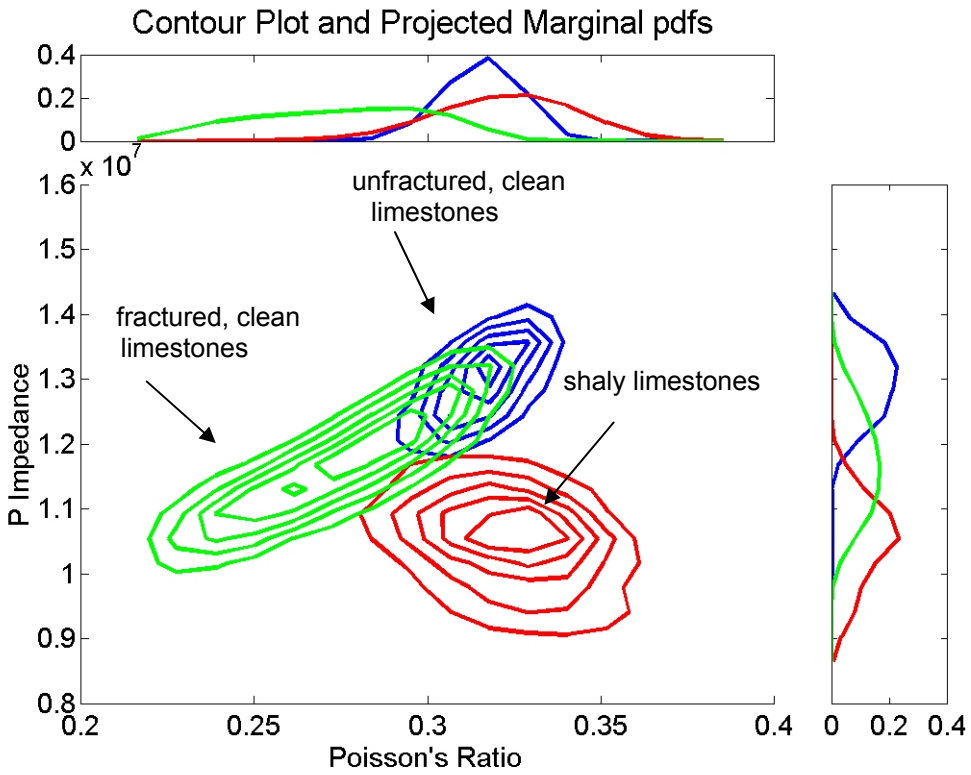

Figure 16: Joint probability distribution functions of the P-Impedance and Poisson's Ratio for the Monte Carlo simulations of the unfractured, clean limestones (blue), fractured limestones with **randomly oriented cracks** (green), and shaly rocks (red). Fractures are filled with **gas**. The upper and right panels show the marginal distributions for Poisson's Ratio and P-Impedance respectively, for each facies.

If the fractures are saturated with brine (Figure 17), then they are not distinguishable from the unfractured, clean limestones. We can observe very small decrease in the P-Impedance, and practically no change in the Poisson's Ratio, as compared to the unfractured properties.

These modeling results suggest that it is the gas in the fractures that makes the Poisson's ratio drop, not the fractures themselves, since the Poisson's ratio of the brine-filled fractured zones does not change significantly in comparison with the unfractured facies.

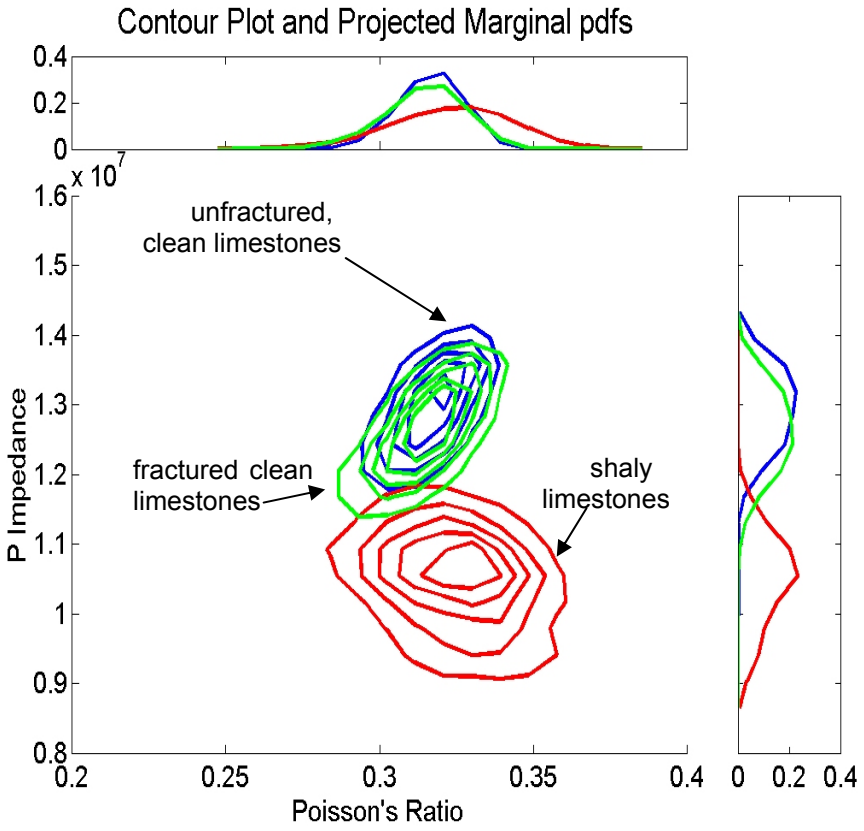

Figure 17: Joint probability distribution functions of the P-Impedance and Poisson's Ratio for the Monte Carlo simulations of the unfractured, clean limestones (blue), fractured limestones with randomly oriented cracks (green), and shaly rocks (red). Fractures are filled with **brine**. The upper and right panels show the marginal distributions for Poisson's Ratio and P-Impedance respectively, for each facies.

Thomsen's anisotropic parameters

A single set of aligned vertical fractures generates a transversely isotropic medium with horizontal axis of symmetry (HTI). Most of the seismic attributes for an HTI medium are given in the literature in terms of Thomsen's (1986) anisotropic parameters and modification of these developed by Tsvankin (1997).

We use again Hudson model (1980, 1981), together with stochastic simulations, to compute the anisotropic Thomsen's type parameters. The background properties are simulated through a correlated *Monte Carlo* approach, based on the V_P ,V_S and *density* derived from well-log data.

Figures 18 and 19 present the stochastically simulated epsilon, gamma and delta anisotropic coefficients defined with respect to the vertical axis (Tsvankin, 1997a). The

scatter in the data is due to the variability in the unfractured background properties, and also in the crack density and aspect ratio of the fractures. We use the same distributions of the crack density and the aspect ratio for both gas-filled and brine-filled fractures.

In Figure 18 the data are color-coded by fracture density, which increases from 0.01 to 0.1. The anisotropy coefficients increase in absolute value with increasing fracture density, as expected.

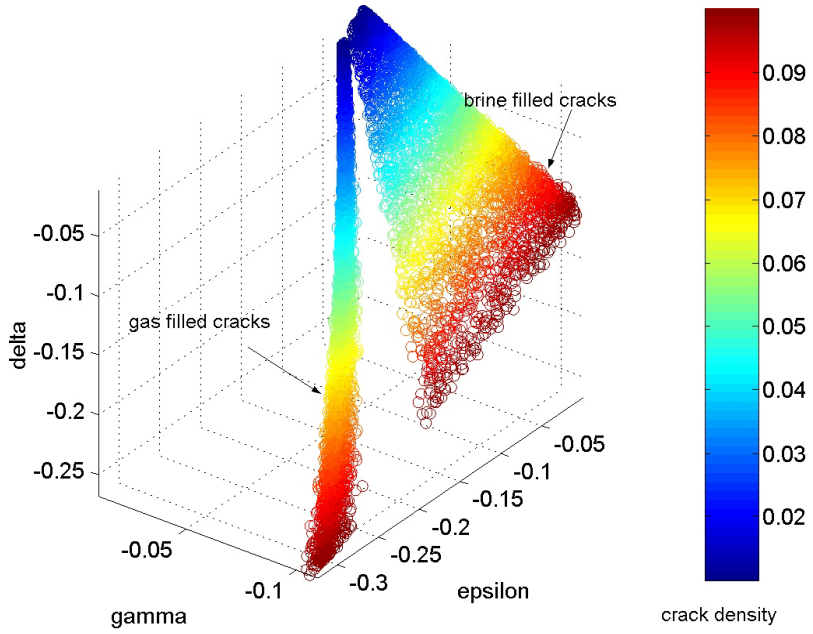

Figure 18: Stochastically simulated Thomsen type anisotropic parameters epsilon, gamma and delta defined with respect to vertical axis for HTI medium. Matrix porosity is brine saturated. Fractures are filled with gas and brine, respectively. Data are color-coded by the crack density.

We observe that the gas-filled and the brine-filled fractures have different signatures in the Thomsen's-parameter domain. More specifically, absolute values of the epsilon and delta parameters are larger for gas-filled fractures than for brine-filled fractures. However, as expected, the gamma parameter, which is a measure of the shear-wave anisotropy, does not change with the fluid.

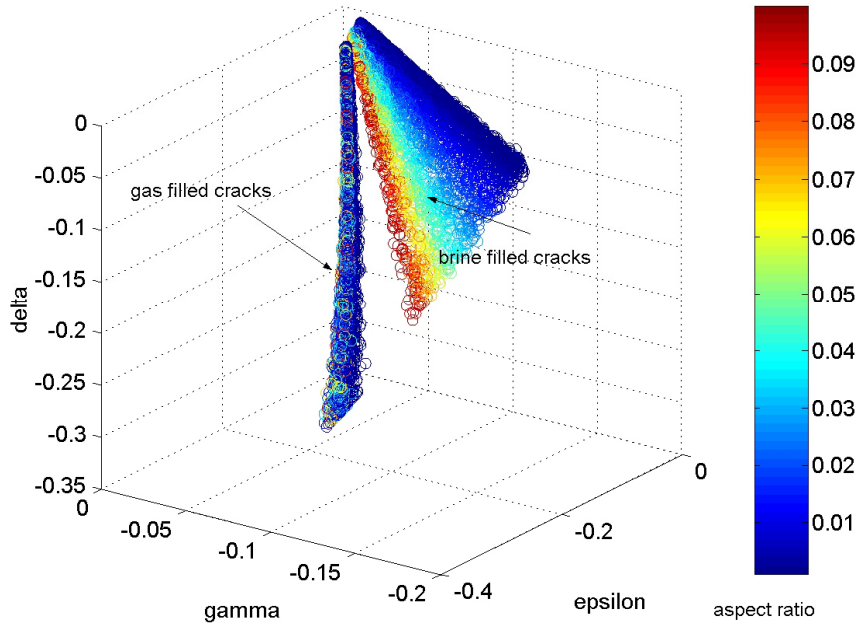

Figure 19: Stochastically simulated Thomsen type anisotropic parameters epsilon, gamma and delta for HTI medium, defined with respect to vertical axis. Matrix porosity is brine saturated. Fractures are filled with gas and brine, respectively. Data are color-coded by aspect ratio of the cracks.

In Figure 19 the data are color-coded by the aspect ratio of the fractures. We see that the brine-filled cracks are more sensitive to the aspect ratio than are the gas-filled fractures. As a result, the scatter in the data for the brine-filled fractures is larger than for the gas-filled fractures. At fixed crack density, the higher the aspect ratio of the brine-filled cracks, the larger the absolute values of epsilon and delta. For smaller aspect ratios, i.e., for very thin cracks, the presence of brine stiffens the cracks significantly, making them almost invisible to the seismic waves.

For gas-filled fractures, we verify the weak anisotropy approximation for fracture density, given by Bakulin (2000):

$$e = -3/8\varepsilon^{(V)}. \tag{2}$$

Here, e represents the fracture density, while $\varepsilon^{(V)}$ represents the epsilon parameter defined with respect to the vertical axis (Tsvankin, 1997).

We vary the crack density in a deterministic way, and we use *Monte Carlo* method and Hudson's model to simulate the elastic stiffness matrix of the fractured medium,

taking into account the variability in the unfractured background rock properties and in the aspect ratio of the cracks. Then, for each realization of elastic stiffness matrix, we derive the Thomsen's epsilon parameter with respect to vertical, and use Equation 2 to compute the crack density. These computed values of crack density are shown in Figure 20 (the open circles). To check the approximation from Equation 2, we superimposed the actual values of crack density used in the modeling (the horizontal lines).

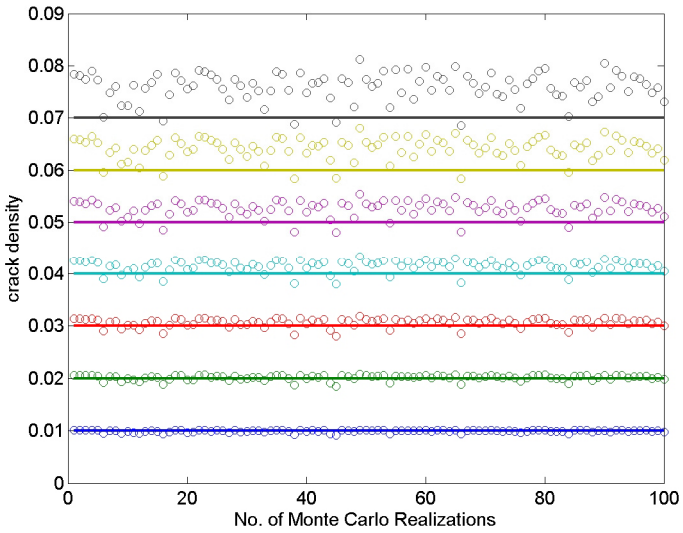

Figure 20: Verification of the weak-anisotropy approximation for crack density as a function of the Thomsen's epsilon parameter with respect to the vertical axis, for gas-filled fractures. The circles represent the computed crack density using the Equation 2 and Monte Carlo simulations for the elastic stiffness matrix of the fractured medium. The horizontal lines represent the actual values of crack density used in the modeling. The scatter in the data is due to variability in the background rock properties and aspect ratio of the cracks.

From Figure 20, we observe that, for small crack density up to 0.04, the Equation 2 gives good results for crack density. However, for larger crack density values, the weak anisotropy approximation overestimates the actual crack density. For example, in this case, for a crack density of 0.07 the overestimation is approximately 8%. Therefore, for gas-filled fractures, the crack density can be approximated by 3/8 of the absolute value of Thomsen's epsilon parameter expressed with respect to vertical axis, especially for relatively small crack densities.

For the brine-filled fractures the absolute values of the epsilon parameter are smaller than those of the gas-filled fractures, as we can observe in Figures 18 and 19.

The delta parameter is also a function of the fluid type, and its absolute values are larger for the gas-filled fractures than for the brine-filled fractures, as we can observe in Figures 18 and 19.

The gamma parameter, also a linear function of the fracture density in the weak anisotropy approximation, does not change with fluid. This parameter represents the *S*-wave anisotropy. Bakulin (2000) gives an expression for the gamma parameter as a function of the ratio between V_P and V_S of the unfractured background rock:

$$\gamma^{(V)} = -\frac{8}{3(3-2g)}e, \tag{3}$$

$$\text{with } g = \left(\frac{Vs}{Vp}\right)^2. \tag{4}$$

Therefore, when the fluid is not known, gamma, the *shear-wave splitting parameter*, may be useful to predict fracture densities.

Travel time

In the hypothesis of a vertical set of aligned fractures in the reservoir the *P*-wave travel time varies with the direction of wave propagation.

Grechka and Tsvankin (1998) give the travel time variation for an HTI medium as a function of azimuth. Figure 21 is a contour plot of the difference between the P-wave travel time from the bottom of the James Limestone for the fractured and unfractured cases, as a function of azimuth and offset. The fractured James Limestone reservoir is modeled with vertical fractures filled with gas. In the modeling, we consider the crack density to be constant and equal to 0.07. The contour values in the plot are in seconds. We can see that the difference in travel time is larger in the direction perpendicular to fractures (azimuth 180) than in the direction parallel to fractures (azimuth 90), as expected. Therefore, in principle, travel time may be used to determine the orientation of the main fracture system, and also to estimate fracture density. However, for the James Limestone reservoir, the difference in *P*-wave travel time between fractured and unfractured cases is very small. This is due because the reservoir is thin (approximately 200 ft).

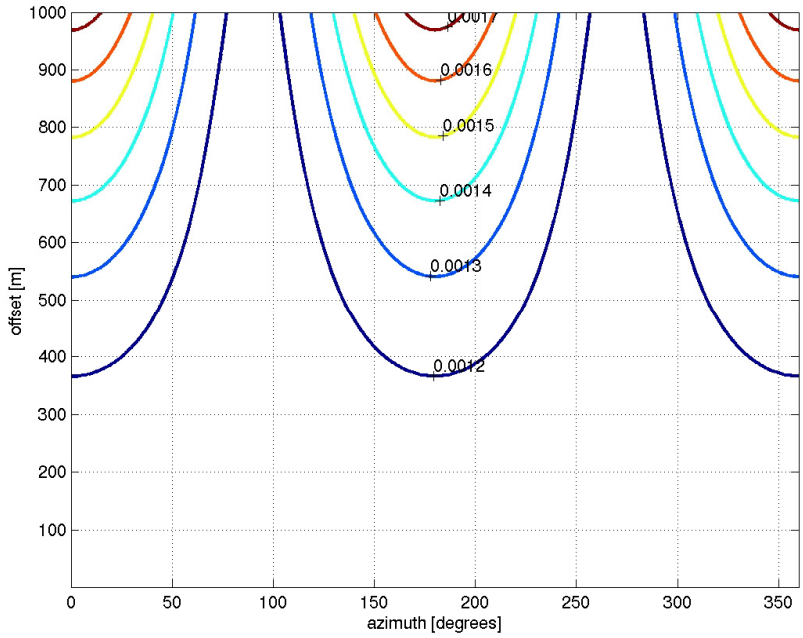

Figure 21: Contour plot for the travel time differences between the fractured and unfractured simulated James Limestone reservoir as a function of azimuth and offset. The values on the curves are in seconds.

For example, at the azimuth orthogonal to fractures and at an offset of 700m, the difference between the fractured and unfractured cases is approximately 1.4 milliseconds. Therefore, *P*-wave travel time difference between the fractured and unfractured zones through the James Limestone reservoir is not a practically useful attribute.

We also consider the hypothesis of a more chaotic distribution for fracture orientations, such as near the faults. Figure 22 shows the travel time from the bottom of the James Limestone for the unfractured (blue) and gas-filled fractured (red) cases, in the hypothesis of randomly distributed cracks. The travel time through the fractured region of the reservoir is larger than through the unfractured zones, as expected. The difference between fractured and unfractured cases is approximately 5 milliseconds. This difference is higher than for the case of a nearly vertical set of fractures with the same fracture density of 0.07. However, the difference is relatively small to be useful for fracture characterization, since the dominant frequency of this seismic survey is relatively low.

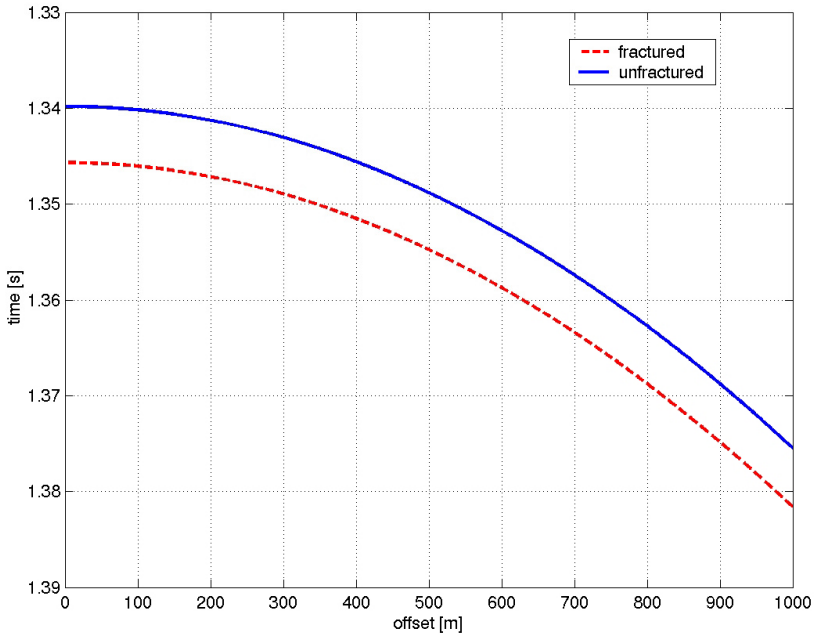

Figure 22: Expected travel time through the simulated James Limestone reservoir as a function of offset for the unfractured and fractured cases. Fractures are randomly distributed and filled with gas. Fracture density is 0.07.

We conclude that travel time methods are not very useful for fracture characterization in this case, since the James Limestone reservoir is too thin.

4.2 Interface properties

The advantage of using interface attributes, defined at the boundary between two layers, based on the contrast of their elastic properties, is that they provide localized information at the target of interest, unlike the travel time techniques. Besides, the interface properties are more appropriate than the travel time methods for thin reservoirs above the tuning thickness.

This section presents the results of the stochastic simulations for *PP reflectivity* Amplitude Variation with Offset (AVO) in the case of an isotropic distribution of cracks, and also for the PP reflectivity Amplitude Variation with Angle of Incidence and Azimuth (AVAZ) in the case of an HTI medium.

For the interface properties, we consider the boundary between the cap rock, represented by the Bexar shale, and the underlying reservoir, modeled with various distributions of fractures.

AVO gradient and Intercept

For the case of an isotropic distribution of cracks, we use Shuey's (1985) approximation for predicting the AVO gradient.

Figures 23 and 24 show the joint PDF of the *AVO Gradient* and *Intercept* of the reflected PP wave for the three different possible facies in the reservoir. The fractured facies (green) is modeled with randomly oriented fractures filled with gas and with brine. The corresponding results are presented in Figure 23 and Figure 24, respectively.

We observe a larger overlap between the different facies in the interface attributes domain than in the interval attributes domain. This is due to the larger variability in the seismic properties of the cap rock.

From Figure 23 we see that on average, the normal *PP reflectivity* from the fractured zones saturated with gas is smaller than that from the unfractured ones. The presence of the gas-filled fractures decreases the *PP reflectivity*. However, on average we should expect the smallest reflectivity from the shaliest rocks in the reservoir. As the fracture density increases, the *PP reflectivity* from the fractured zones decreases, and becomes closer to the *PP reflectivity* from the shaly limestones in the reservoir. The *AVO gradient* can help resolve this ambiguity. From the right-side panel of Figure 23, we see that on average, the *AVO gradient* for the shaly rocks is higher than that of the clean, unfractured limestones. At the same time, the *AVO Gradient* of the fractured limestones is smaller than that of the unfractured, clean limestones. Therefore, the shaliness moves the *AVO gradient* to smaller negative values as compared to the unfractured, clean limestones, while the fractures filled with gas move the *AVO gradient* to larger negative values as compared to the clean, unfractured limestones. In conclusion, using reflectivity together with *AVO gradient* can help in better discriminating the gas-filled fractured zones from the shaly zones in the reservoir.

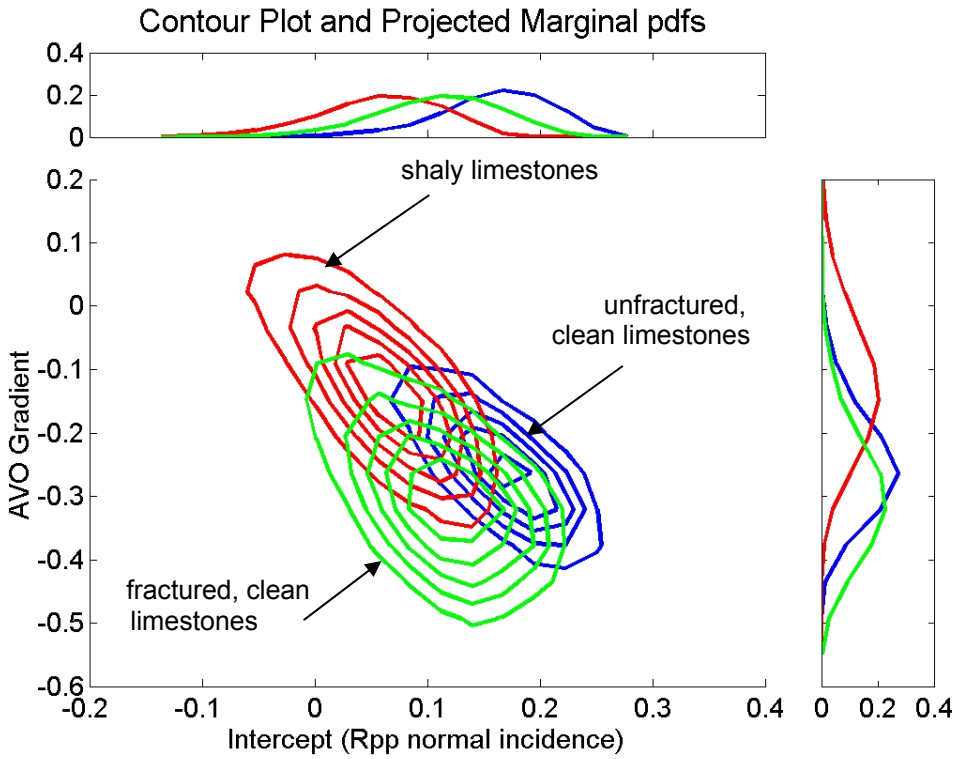

Figure 23: Joint probability distribution functions of the AVO Gradient and Intercept for the Monte Carlo simulations of the unfractured, clean limestones (blue), fractured limestones with **randomly oriented** cracks (green), and shaly rocks (red). Fractures are filled with **gas**.

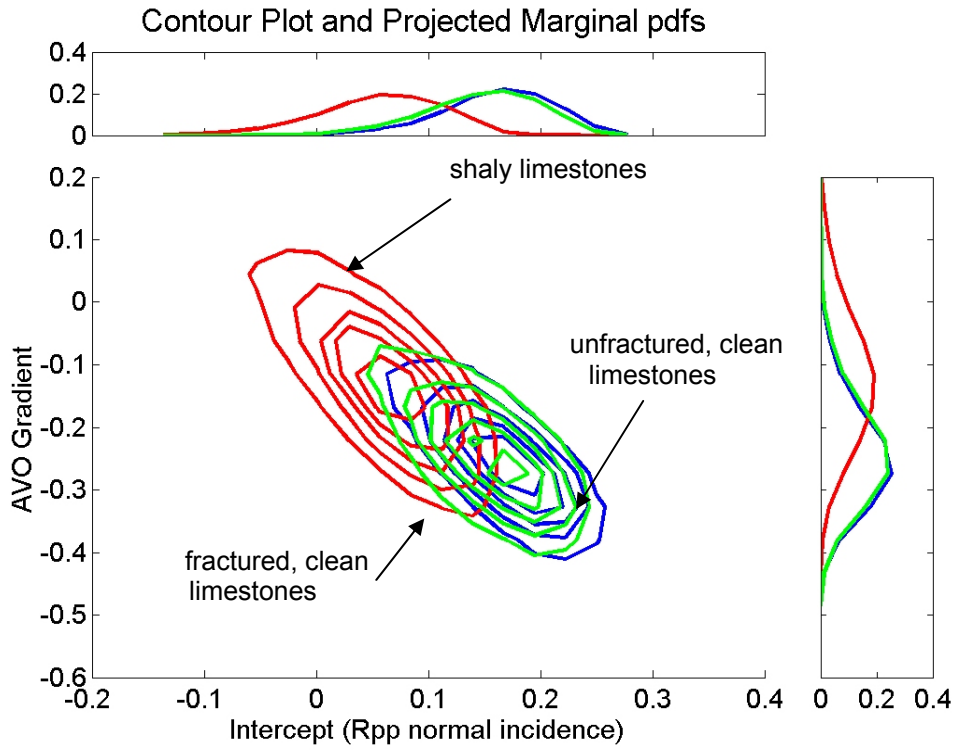

Figure 24: Joint probability distribution functions of the AVO Gradient and Intercept for the Monte Carlo simulations of the unfractured, clean limestones (blue), fractured limestones with **randomly oriented** cracks (green), and shaly rocks (red). Fractures are filled with **brine**.

From Figure 24 we see that the brine-filled fractured zones are not distinguishable from the unfractured clean limestones in the reservoir, if the fracture orientations are isotropically distributed. The assumption is that there is little fluid communication between the fluid in the fractures and the fluid in the matrix pores, during seismic excitation. This assumption is most appropriate when the matrix porosity and permeability are low, which is the case for the tight, clean limestones intervals in this reservoir.

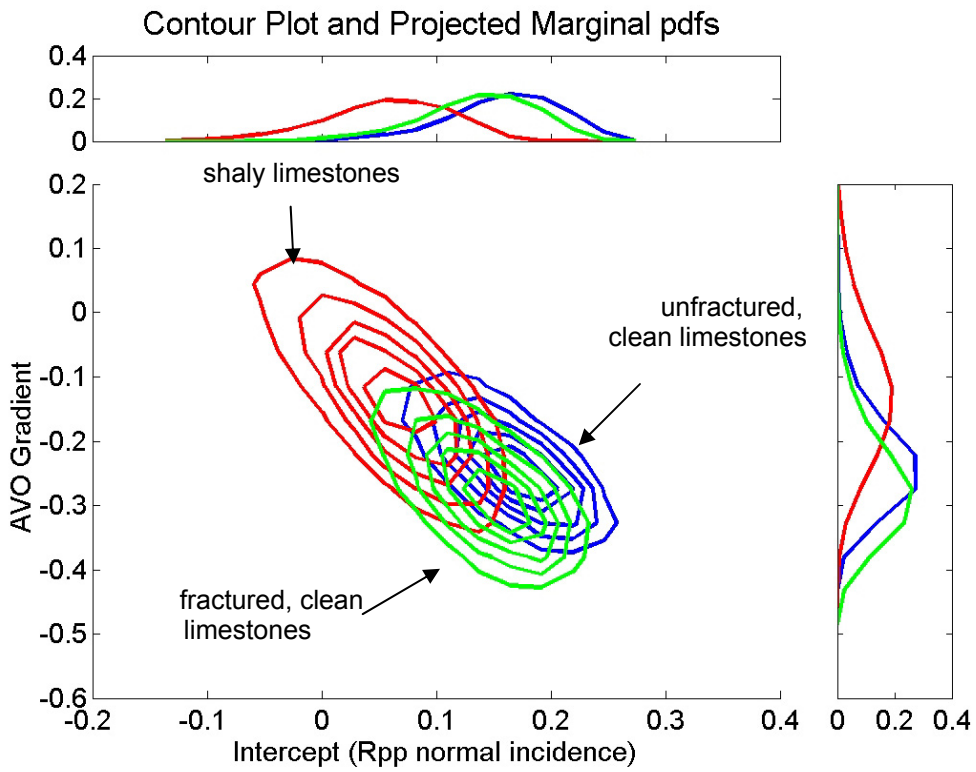

Figure 25: Joint probability distribution functions of the AVO Gradient and Intercept for the Monte Carlo simulations of the unfractured, clean limestones (blue), fractured limestones with **a vertical set of cracks** (green), and shaly rocks (red). Fractures are filled with **gas**. The azimuth is **parallel** to the crack's plane.

If we consider the case of vertical aligned fractures, the *AVO gradient* is a function of azimuth. We use Ruger's (1995, 1997) approximation to estimate the *AVO gradient* for the James Limestone reservoir modeled as an HTI medium. Figure 25 presents the *AVO gradient* parallel to fractures, while Figure 26 shows the *AVO gradient* orthogonal to fractures. The azimuthal variation of the *AVO gradient* for gas-filled fractures is insignificant.

In both cases we observe the same behavior as in the case of a random distribution of fractures filled with gas (Figure 23). The azimuthal variation of the *AVO gradient* for gas-filled fractures is small.

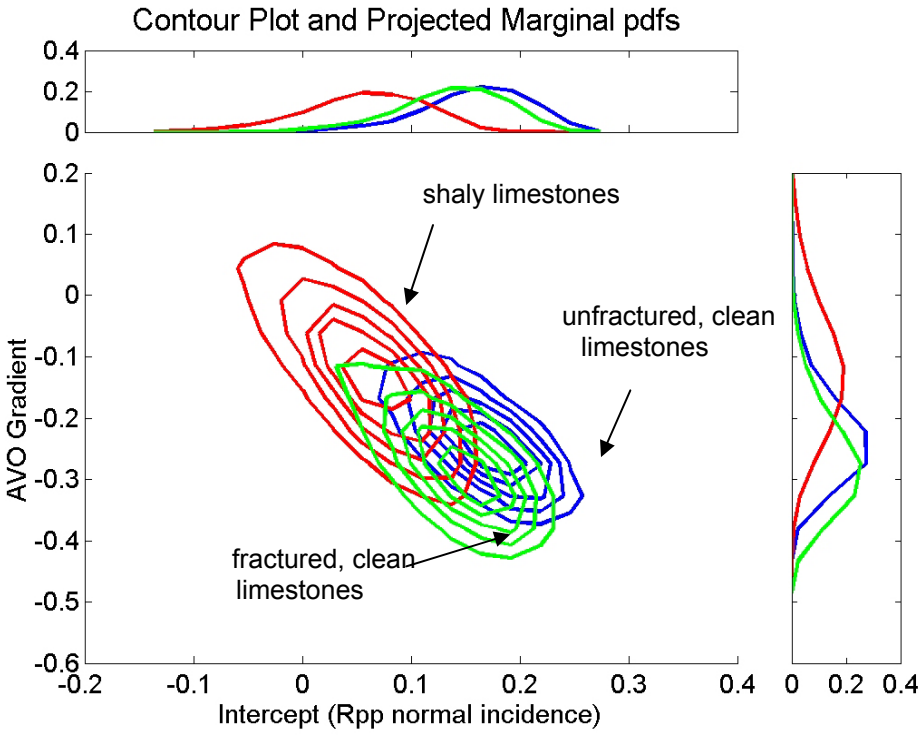

Figure 26: Joint probability distribution functions of the AVO Gradient and Intercept for the Monte Carlo simulations of the unfractured, clean limestones (blue), fractured limestones with **a vertical set of cracks** (green), and shaly rocks (red). Fractures are filled with **gas**. The azimuth is **orthogonal** to the crack's plane.

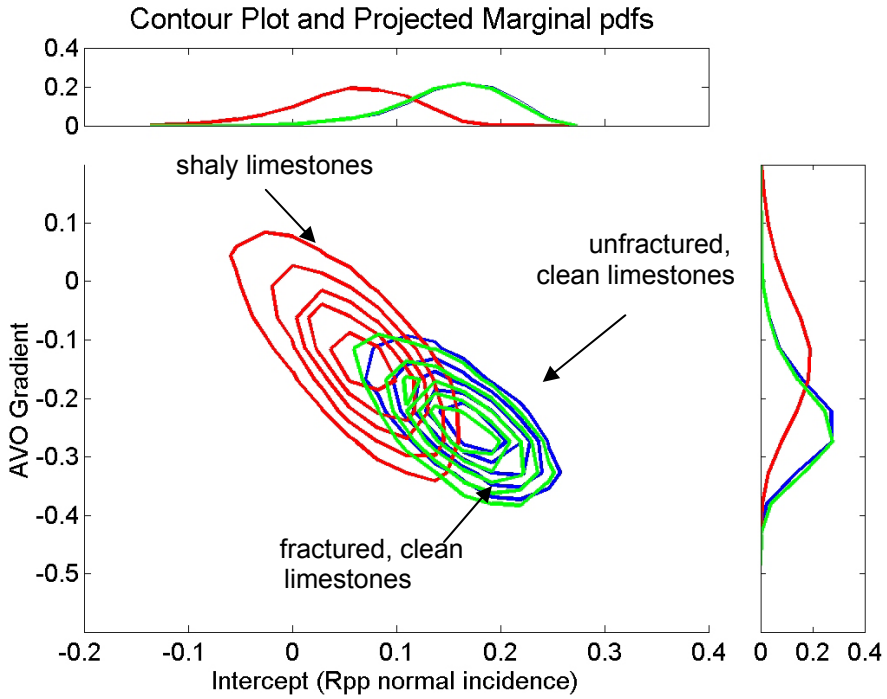

Figure 27: Joint probability distribution functions of the AVO Gradient and Intercept for the Monte Carlo simulations of the unfractured clean limestones (blue), fractured limestones with **a vertical set of cracks** (green), and shaly rocks (red). Fractures are filled with **brine**. The azimuth is **parallel** to the crack's plane.

Figures 27 and 28 show the joint PDF of the *AVO Gradient* and *Intercept* for brine-filled fractures in the directions parallel and orthogonal to fractures, respectively. We see that brine-saturated fractured zones are indistinguishable from the unfractured clean limestones.

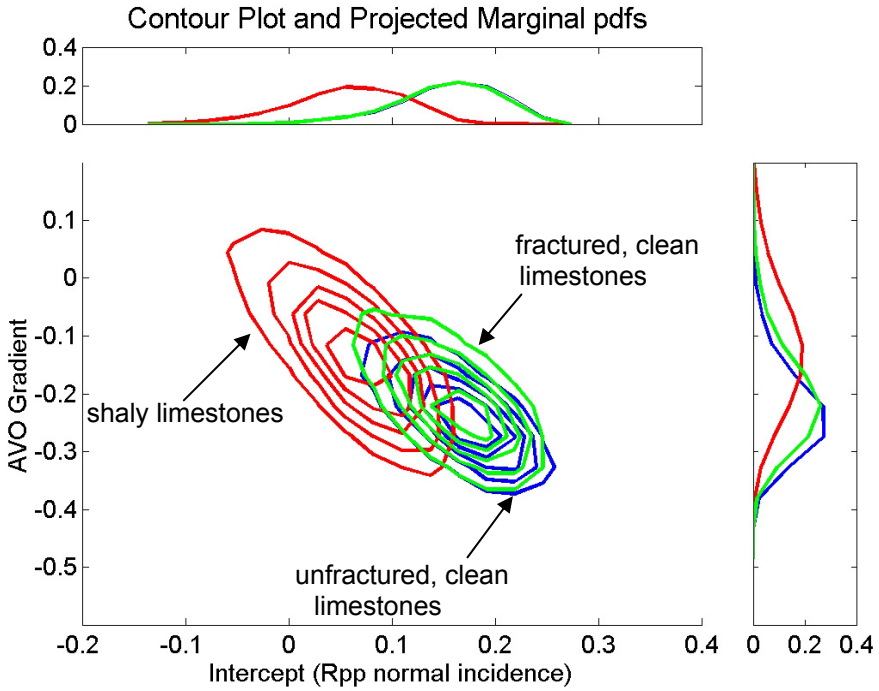

Figure 28: Joint probability distribution functions of the AVO Gradient and Intercept for the Monte Carlo simulations of the unfractured, clean limestones (blue), fractured limestones with **a vertical set of cracks** (green), and shaly rocks (red). Fractures are filled with **brine**. The azimuth is **orthogonal** to the crack's plane.

To summarize, brine-filled fractures are difficult to delineate in the *AVO Gradient – Intercept* domain, for both isotropic and anisotropic distributions of fractures. The gas-saturated fractured zones are easier to distinguish from the unfractured clean limestones. Independently of the fracture distribution, the *AVO gradient* of the gas-filled fractured zones has higher negative values than the unfractured clean limestones. The shaly limestones in the reservoir exhibit smaller negative values than the unfractured, clean limestones. Therefore, the *AVO gradient* is a useful attribute for delineating gas-saturated fractures from the shaly limestones in the reservoir. However, due to a larger variability in the seismic properties of the cap rock, there is a significant overlap between the different facies in the reservoir in the interface-attributes domain.

AVAZ modeling

For an HTI medium generated by a single set of vertical fractures, amplitude variation with incidence angle and azimuth (AVAZ) can be a useful technique for determining the main fracture orientation. AVAZ may also give us information about fracture density and type of fluid in the fractures. In the modeling we use Ruger's (1995, 1996, 1998) approximation for calculating *PP reflectivity* as a function of offset and azimuth.

Figures 29 and 30 show the statistical expected values of the *PP reflectivity* (R_{PP}) as a function of incidence angle and azimuth, for gas- and brine-saturated fractures, respectively. In both cases the matrix porosity is brine-saturated.

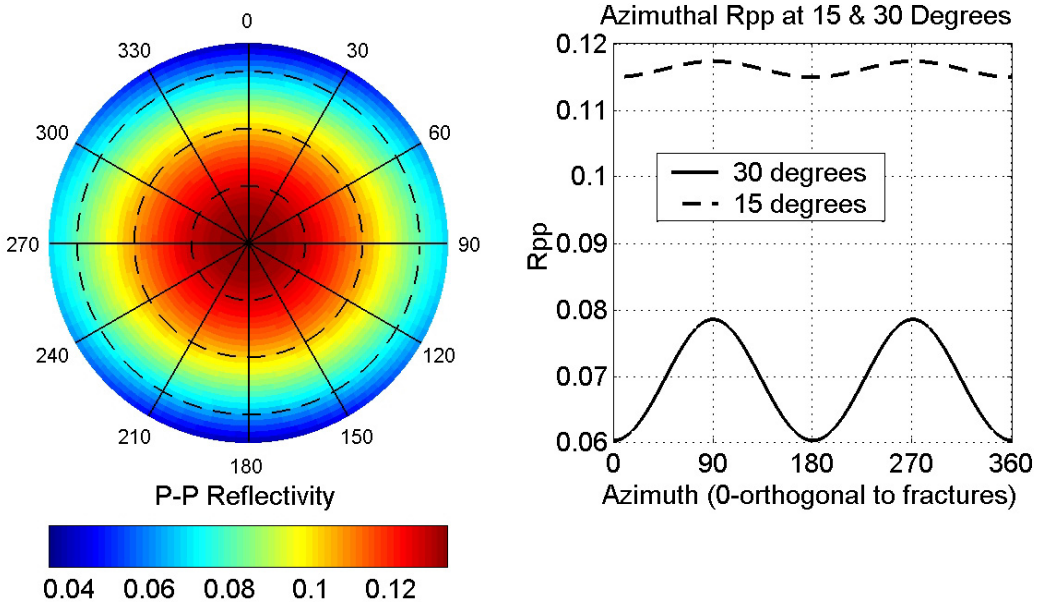

Figure 29: Expected values for the *PP reflectivity* as a function of angle of incidence and azimuth. The right side panel presents the R_{PP} amplitude variation with azimuth at 15 and 30 degree angles of incidence. Azimuth 0 is perpendicular to the fracture plane. Fractures are oriented E-W. Matrix porosity is brine-saturated, while the fractures are filled with **gas**.

The fractures are orientated E-W. The azimuth 0 corresponds to the symmetry axis of the HTI medium, orthogonal to fractures. On the right panels of Figures 29 and 30 is represented the R_{PP} as a function of azimuth for the 15 and 30 degree angles of incidence.

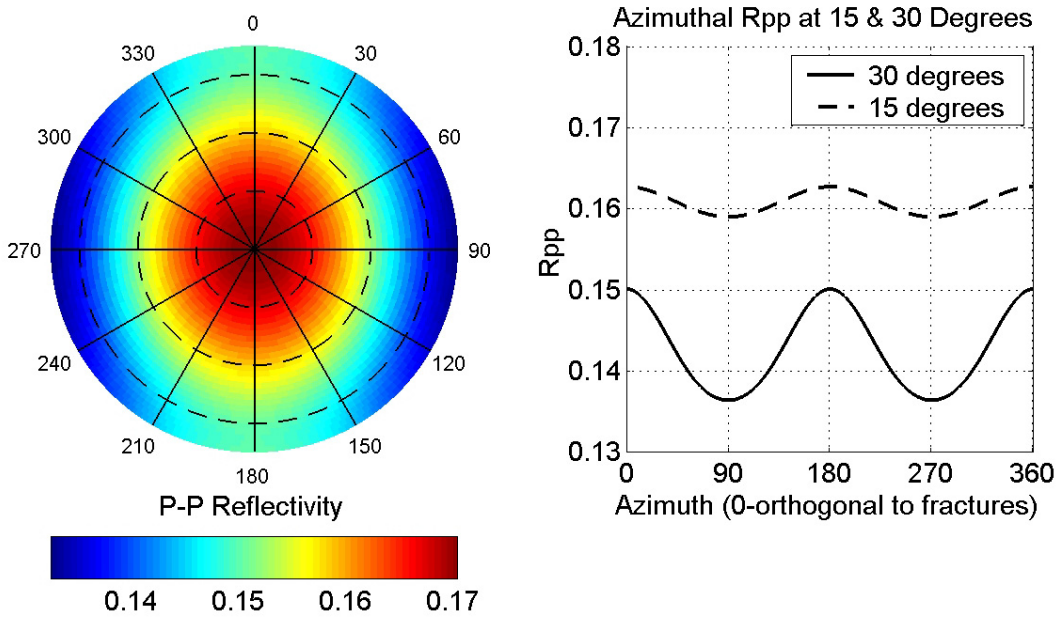

Figure 30: Expected values for the *PP reflectivity* as a function of angle of incidence and azimuth. The right side panel presents the R_{PP} amplitude variation with azimuth at 15 and 30 degree angles of incidence. Azimuth 0 is perpendicular to the fracture plane. Fractures are oriented E-W. Matrix porosity is brine saturated, while the fractures are filled with **brine**.

As expected, the azimuthal variation of *PP reflectivity* increases with angle of incidence, for both brine-filled and gas-filled fractures. The main difference between brine-saturated and gas-saturated fractures is that the polarity of the azimuthal variation is opposite. For the brine-filled fractures, the maximum R_{PP} value at a fixed angle of incidence is in the direction perpendicular to fractures, while for the gas-filled fractures the maximum R_{PP} value is in the direction parallel to fractures. This is an interesting result that can be used to differentiate between gas-filled and brine-filled fractures under the assumption that the azimuthal anisotropy is due only to the presence of a vertical set of joints.

Conclusions

The results of the rock physics analysis, together with the interpreted FMI information about fractures from one of the wells, show that fractures in the James Limestone reservoir are associated with the clean limestone intervals, which have higher velocities and smaller porosities. This association of fractures with the higher-velocity

rocks may be used directly in fracture delineation from seismic data. Even if the velocity will be drastically lowered in the most highly fractured zones, on average the velocities of the fractured regions may be larger than the velocities of the unfractured rocks, but with higher shale content. Therefore, an impedance inversion may help in delineating the zones with higher fracture probability. Within each higher-impedance region, more detailed analysis can map the zones of higher fracture density.

As the rock physics analysis of the well log-data shows, the high-velocity rocks, with the least shale content are much more likely to be fractured. This is expected, since the fractures tend to be associated with the more brittle intervals. Therefore, we consider that the reservoir may exhibit three main types of facies: 1) unfractured, clean limestones, 2) shaly limestones, and 3) fractured, clean limestones, which we have modeled with different distributions of cracks. The goal is to find the optimal combination of seismic attributes for distinguishing the gas-filled fractured zones from the shaly and unfractured limestones in the reservoir.

A geologic model for the James Limestone reservoir suggests the presence of fracture swarms associated with small faults. Between these fracture swarms, the reservoir may exhibit regularly spaced vertical joints. Therefore, in the analysis of the fractured James Limestone reservoir we model the cases of both anisotropic and isotropic distribution of fractures. The anisotropic model that we use is a good representation for approximately vertical, parallel joints that create an HTI medium. The isotropic distribution of fractures can be a good approximation for the fractured zone in the vicinity of faults, where the cracks can be oriented randomly, like in a breccia zone.

For each of the hypotheses of isotropic and anisotropic fracture distribution we stochastically model seismic interval and interface properties such as velocities, travel time, and *PP reflectivity* as a function of angle of incidence and azimuth. By using the stochastic approach we can incorporate natural variability in deterministic physical models.

The modeling shows that all of these seismic attributes may be influenced by the presence of the gas-filled fractures. However, the brine-filled fractures are difficult to distinguish, due to the smaller compressibility in comparison with that of the gas.

The interval velocities decrease with the fracture density. From the modeling we observe that in the V_P-V_S domain the gas-saturated fractures are much more easily distinguishable from the unfractured rocks than are the brine-saturated fractures, in both hypotheses of isotropic and anisotropic fracture distributions.

If the fractures are saturated with gas, modeling shows that the *P*-wave velocity is more sensitive to fractures than the *S*-wave velocity polarized orthogonal and parallel to fracture planes. As expected, the *P*-wave velocity decreases the most when the waves are propagating in the direction orthogonal to a set of aligned cracks. For large crack densities, the V_P of the gas-filled fractured zones becomes comparable to the V_P of the shaly limestones in the reservoir, which are less susceptible to fracture. The *S*-wave velocity decreases less than V_P, and its expected value remains larger than the *S*-wave velocity of the shaly rocks. Therefore, V_S is a valuable piece of information to discriminate between the gas-filled fractured zones and the shaly limestones in the reservoir.

If the fractures are brine-saturated, it is more difficult to distinguish the fractured zones from the unfractured ones. V_P and V_S are little or not at all affected by the presence of the fractures, in both the hypotheses of isotropic and anisotropic distribution of cracks.

In the case of an isotropic distribution for the fracture orientation, the *P*-wave *Impedance - Poisson's ratio* domain is an optimal combination of interval properties for delineating the gas-filled fractured zones in the reservoir. However, if the fractures are saturated with brine, it is difficult to distinguish them from the unfractured, clean limestones.

The travel time can be also influenced by the presence of fractures. However, for the James Limestone reservoir the travel time difference between the fractured and the unfractured cases is very small, due to the fact that the reservoir is too thin.

For the interface properties, the *AVO Gradient - Intercept* domain is a potentially useful combination for discriminating gas-filled fractures in the reservoir. However, due to a large variability in the seismic properties of the cap rock, the uncertainty in differentiating fractured zones from interface properties is a little higher than from interval properties, such as *P-Impedance* and *Poisson's Ratio*. As the fracture density increases, the *PP reflectivity* from the fractured zones decreases, and becomes closer to

the *PP reflectivity* from the shaly limestones in the reservoir. The *AVO gradient* can help resolve this ambiguity. Modeling shows that the shaliness moves the *AVO gradient* to smaller negative values as compared to the clean, unfractured limestones, while the fractures filled with gas move the *AVO gradient* to larger negative values as compared to the clean, unfractured limestones. Therefore, the *AVO gradient* can help in better separating the gas-filled fractured zones from the shaly zones in the reservoir.

Brine-saturated fractures are difficult to distinguish also in the *AVO Gradient - Intercept* domain.

In the hypothesis of a nearly vertical set of joints, we also model the Amplitude Variation with Angle of Incidence and Azimuth (AVAZ). The azimuthal variation depends on the fluid type. In the assumption of little fluid communication between fractures and matrix porosity during a seismic period, the gas-filled fractures and brine-filled fractures have opposite azimuthal polarity. For the brine-saturated fractures, the maximum *PP reflectivity* value, at a fixed angle of incidence, is in the direction perpendicular to fracture strike, while for the gas-saturated fractures the maximum *PP reflectivity* value is in the direction parallel to fracture planes. This result can be used to differentiate between gas-filled and brine filled-fractures for a vertical set of joints. However, if we do not have additional geological information about the orientation of the main fracture system, the different responses in the azimuthal variation of the amplitudes due to fluids bring more ambiguity in determining the fractures' strike.

In summary, rock physics fracture modeling and stochastic simulations for seismic attributes of the James Limestone reservoir provide a framework for delineating fractured zones from seismic data, and for estimating the uncertainty in fracture characterization due to natural variability.

Attachment F

Multi-Offset, Multi-Azimuth VSP Analyses

Introduction

This attachment focuses on the multi-offset, multi-azimuth vertical seismic profile (VSP) data used as a pilot study in Phase II of the project. After describing the acquisition geometry and parameters, we show some of the results of the intermediate sorting and processing steps. Finally we describe results of interpretations of observed anomalies in the seismic data that can be potential indicators of fractured zones. Different possible geological hypotheses about fracture occurrence that are consistent with the observations are laid out. More complete 3-D data can help to single out the most probable hypothesis. This phase benefited greatly by the value added by the state-of-the art VSP processing carried out by the Scott-Pickford Company and paid for by Marathon.

A Vertical Seismic Profile was acquired for us at Marathon's Henderson A#1–H well, on 21st of May, 2001. The survey was acquired using a Vibroseis source. A zero-offset VSP with the source located at 348 ft from the wellhead was acquired first. The second data set was an offset VSP acquired by moving the vibrators to a location of 3500 ft from the well, at an azimuth of 152 degrees (S-E). The third data set, also an offset VSP, was acquired at an offset of 5700 ft from the well, again at an azimuth of 152 degrees. The last offset VSP was obtained at 3200 ft offset, but at an azimuth of 230 degrees (S-W). Figure 1 presents a schematic of the VSP acquisition geometry. The VSP survey parameters are presented in Table 1.

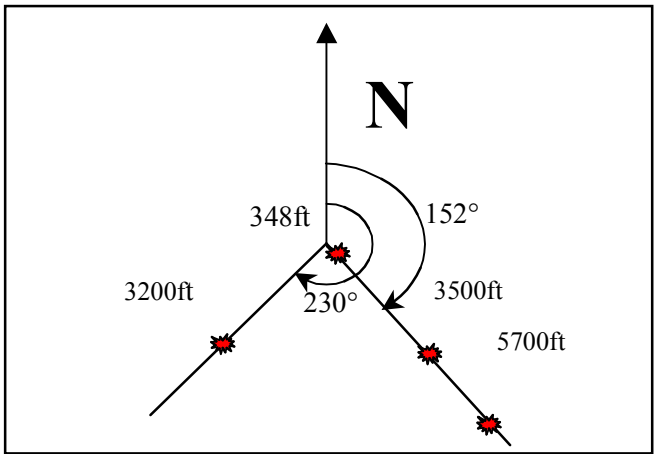

Fig 1: Schematic map view of VSP acquisition geometry. Well bore is at the intersection of the three lnes. Arrow points north. Shot points lie along the lines have azimuths 152^{o} and 230^{o}.

Table 1: VSP survey parameters

Well	HENDERSON A # 1-H
Field	Neuville
County	Shelby
State	Texas
Well Coordinate	Easting 3934143.7 Northing 784151.3
VSP log datum: KB elevation above MSL 472ft	
Elevation of Kelly Bushing (KB)	472 ft
Elevation of Ground Level (GL)	445 ft
Elevation of Seismic Reference (SRD)	0 ft
Source type	2 PLS 351 vibrators
Sweep	8-110 HZ, nonlinear, 3db/oct, 0.3 s taper
Receivers	40 ft intervals from 4900 ft to 7100 ft
Velocity from Source to Surface Sensor	6000 ft/s
Velocity from Source to SRD	6000 ft/s
Source Elevation below KB, zero-offset	27 ft
Source Distance from Wellhead, zero-offset	348 ft
Source Azimuth from North, zero-offset	0 degrees
Source Elevation below Kb, 3200ft Offset	12 ft
Source Distance from Wellhead, 3200 Offset	3200 ft
Source Azimuth from North, 3200 Offset	230 degrees
Source Elevation below Kb, 3500ft Offset	106 ft
Source Distance from Wellhead, 3500 Offset	3500 ft
Source Azimuth from North, 3500 Offset	152 degrees
Source Elevation below Kb, 5700ft Offset	106 ft
Source Distance from Wellhead, 5700 Offset	5700 ft
Source Azimuth from North, 5700 Offset	152 degrees

VSP Data

In the next few figures we show snapshots of the recorded wavefields at different azimuths and offsets followed by the results of decomposing the total wavefield into upgoing and downgoing components. Figures 2 and 3 show the different wavefields for zero offset VSP; Figures 4 and 5 show the wavefield decompositions for 3500' offset, and 152 degress azimuth. The corresponding wavefield decompositions for 5700' offset are shown in Figures 6 and 7, while Figure 8 shows data for offset of 3200' and azimuth 230 degrees. The wavefield decompositions include upgoing and downgoing components for P-to-P reflections and P-to-S mode converted waves.

The VSP data were time migrated and processed to make corridor stacks. Corridor stacks are stacks of the VSP upgoing traces taking only a corridor of a few 100 ms after the first arrivals on each trace. The corridor stack helps to eliminate multiples and can be compared with surface seismic stacks. Figure 9 shows different band-pass filter panels of the corridor stack with the James Lime top indicated on the gamma ray log. The Henderson well had no other petrophysical log (e.g. Vp, Vs, density) except the logs obtained while drilling. Sonic logs from a nearby well (Hilton) was used to do forward synthetic seismic modeling. The comparison between observed field data corridor stack (at Henderson) and the computed synthetic corridor stack (based on Hilton logs) are shown in Figure 10. There is a good match at the top James Lime. The amplitudes at the Bexar show some differences, but the base of the Massive Anhydrite shows a good correlation. The satisfactory match is promising and gives us confidence in building the background rock physics model based on logs obtained from nearby wells. VSP corridor stacks and time migrated sections for the different offsets and azimuths are shown in Figures 11, 12, and 13. Figure 14 shows time migrated panels for P-to-S converted waves.

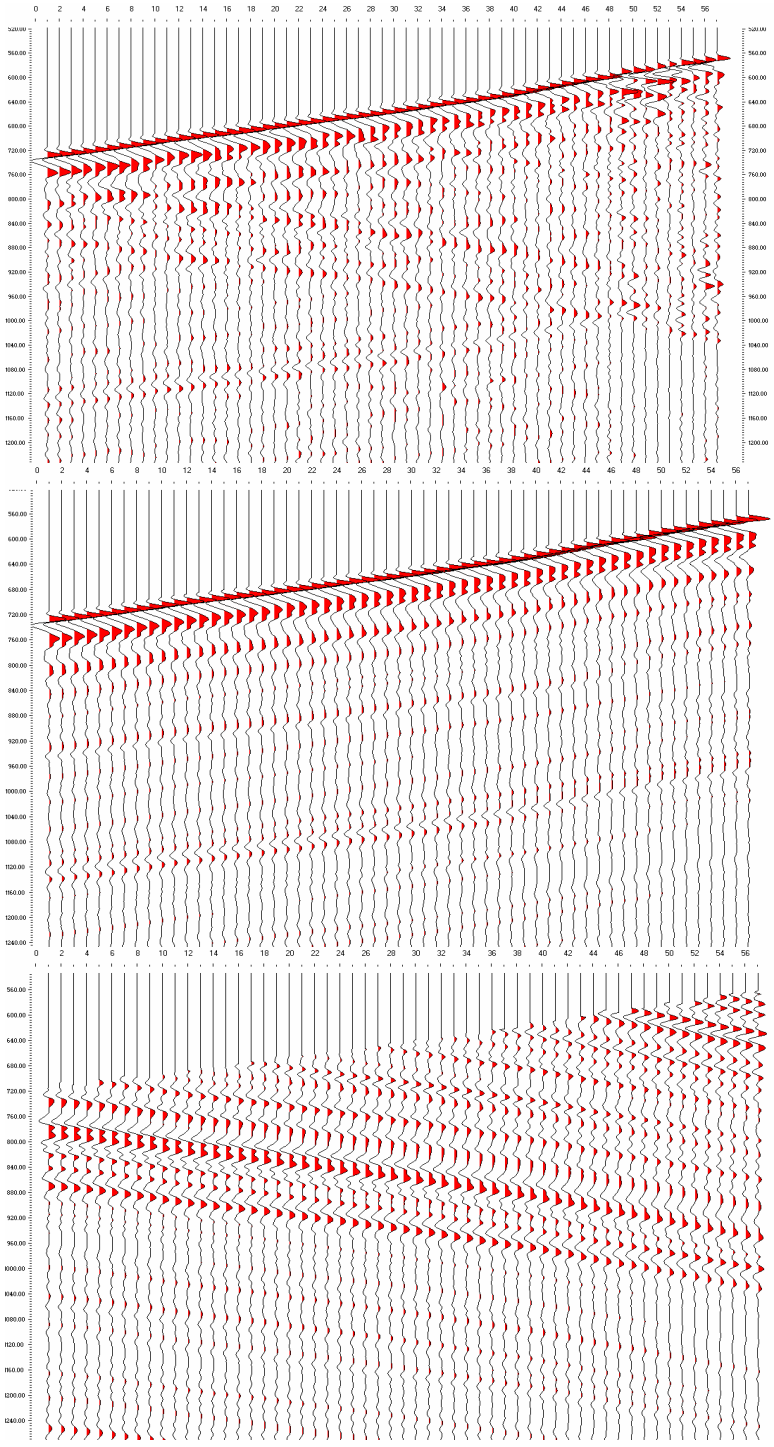

Figure 2: Zero-offset VSP. Top: complete wavefield, Center: Downgoing wavefield. Bottom: Upgoing wavefiled. Depth increases from right to left, and traveltime from top to bottom.

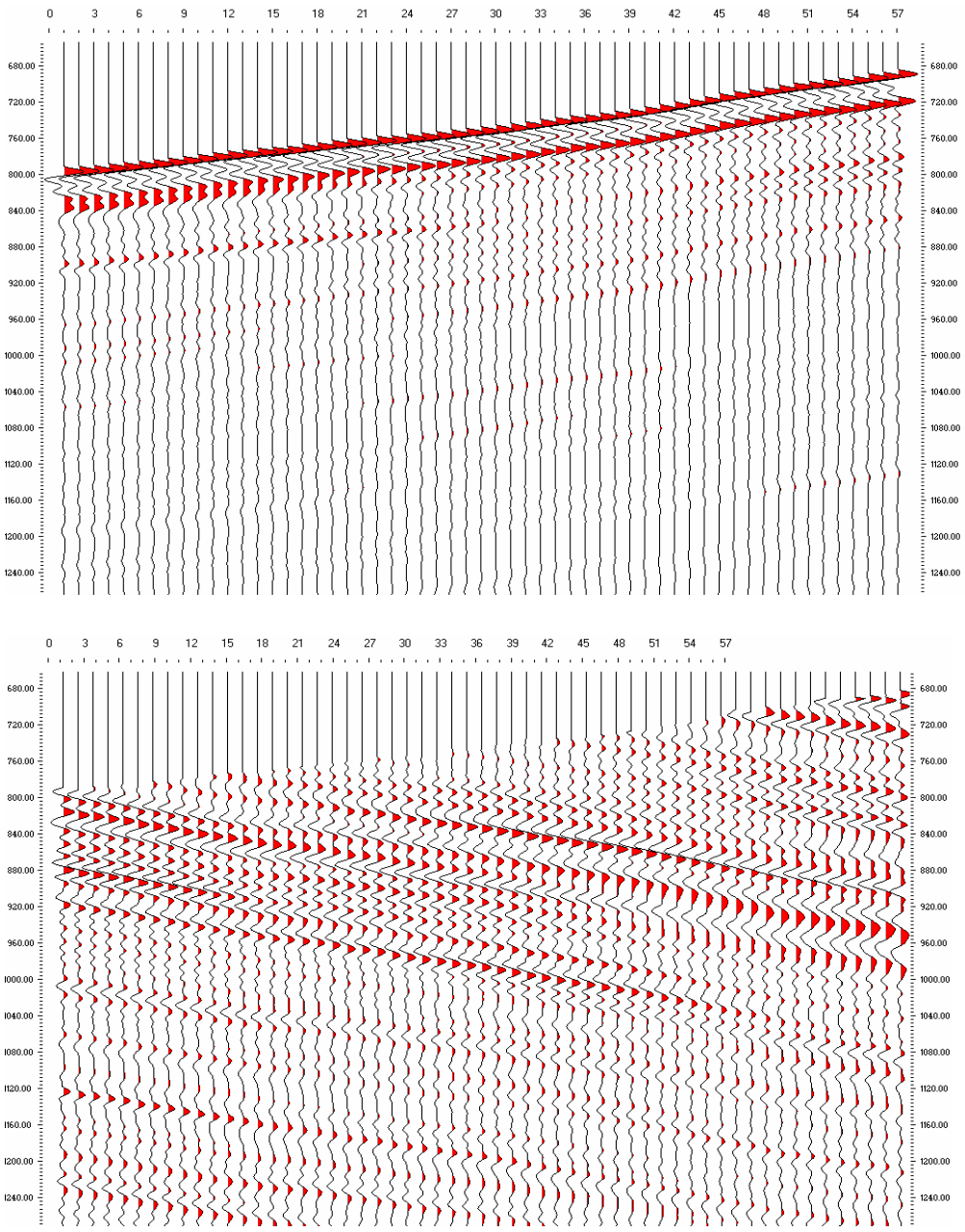

Figure 3: Zero-offset VSP. Top: Downgoing PP wavefield. Bottom: Upgoing PP.

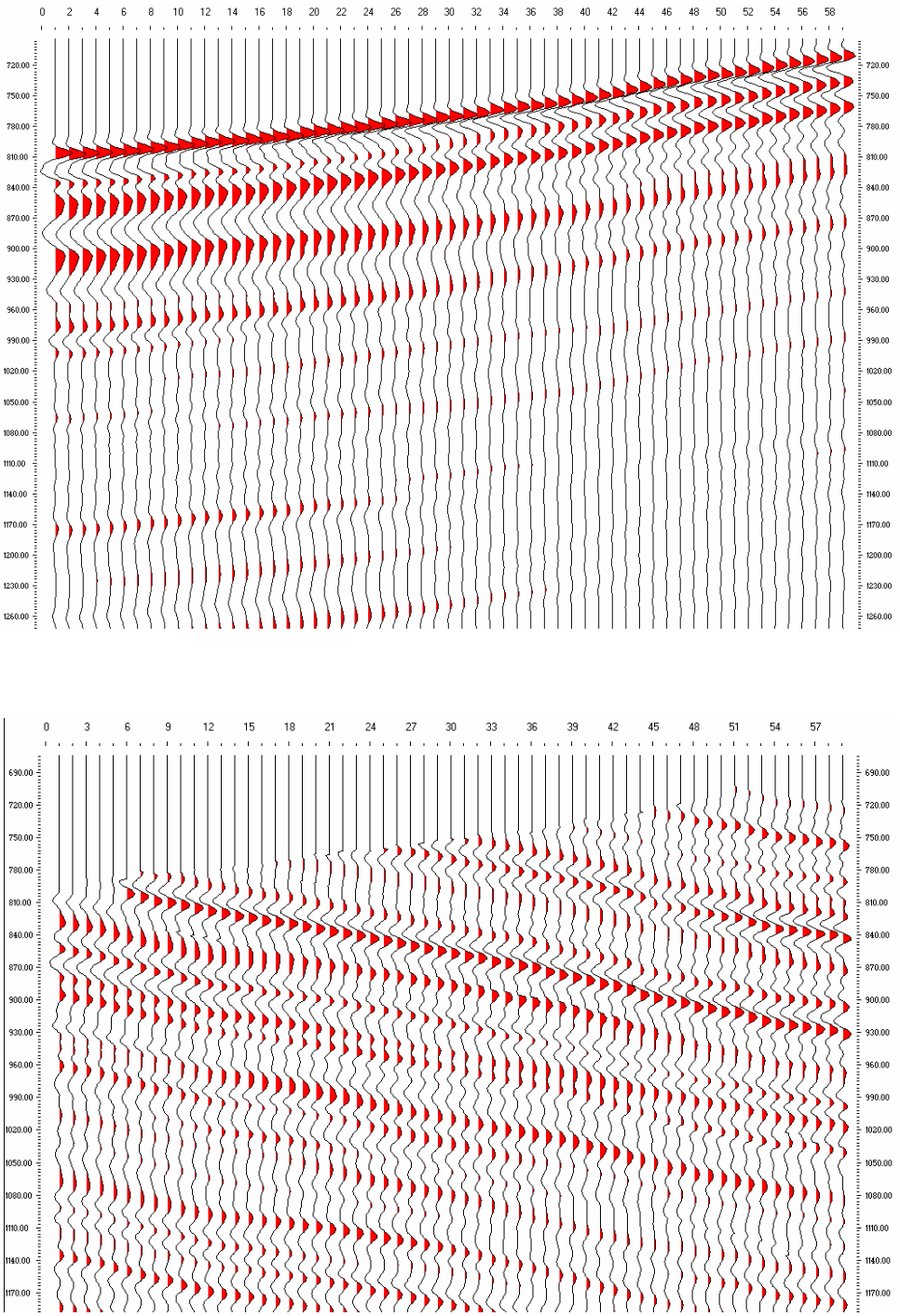

Figure 4: 3500 Offset VSP (152 degrees azimuth). Top Downgoing: PP. Bottom: Upgoing PP.

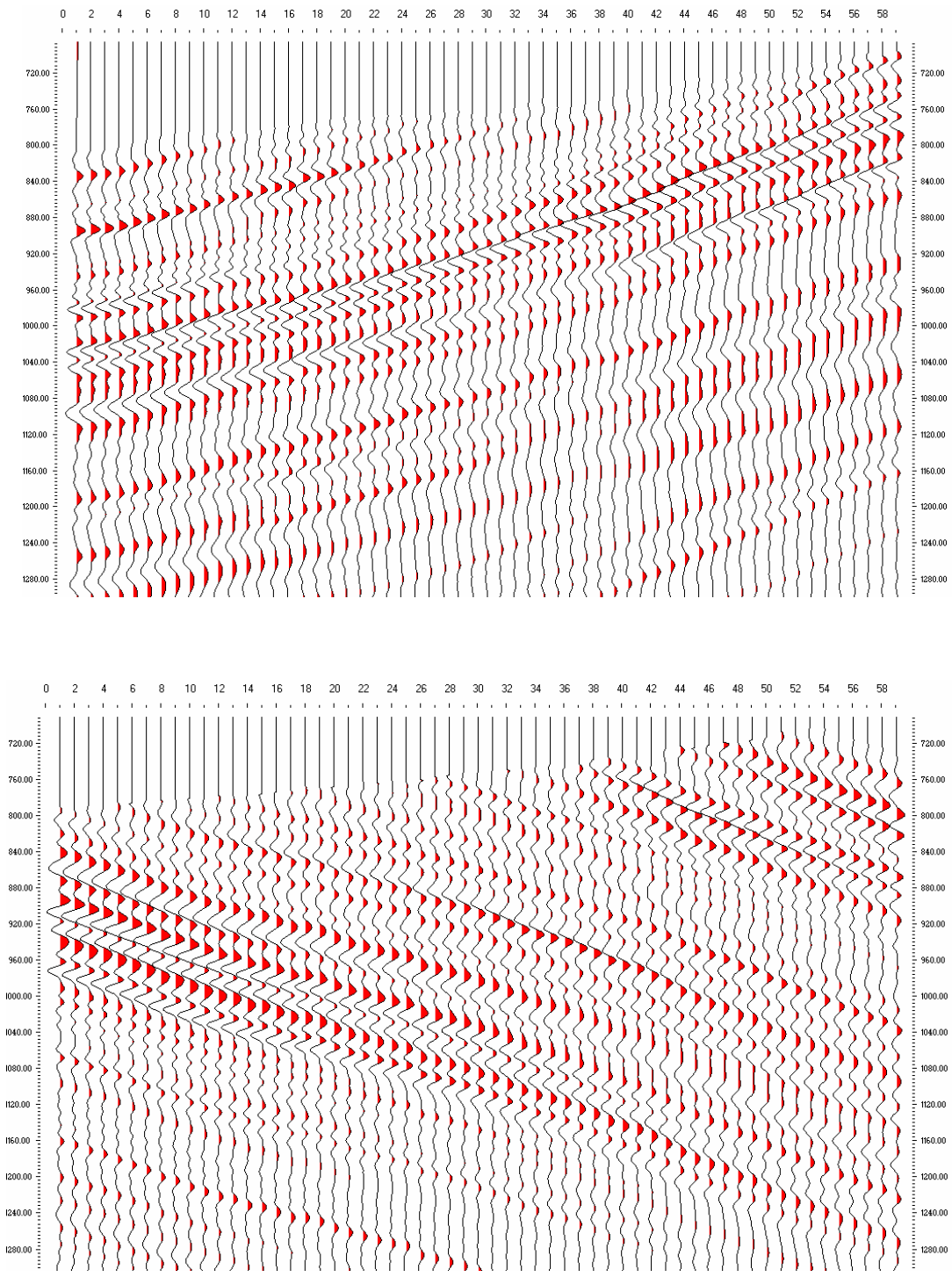

Figure 5: 3500 Offset VSP (152 degrees azimuth). Top: Downgoing PS. Bottom: Upgoing PS.

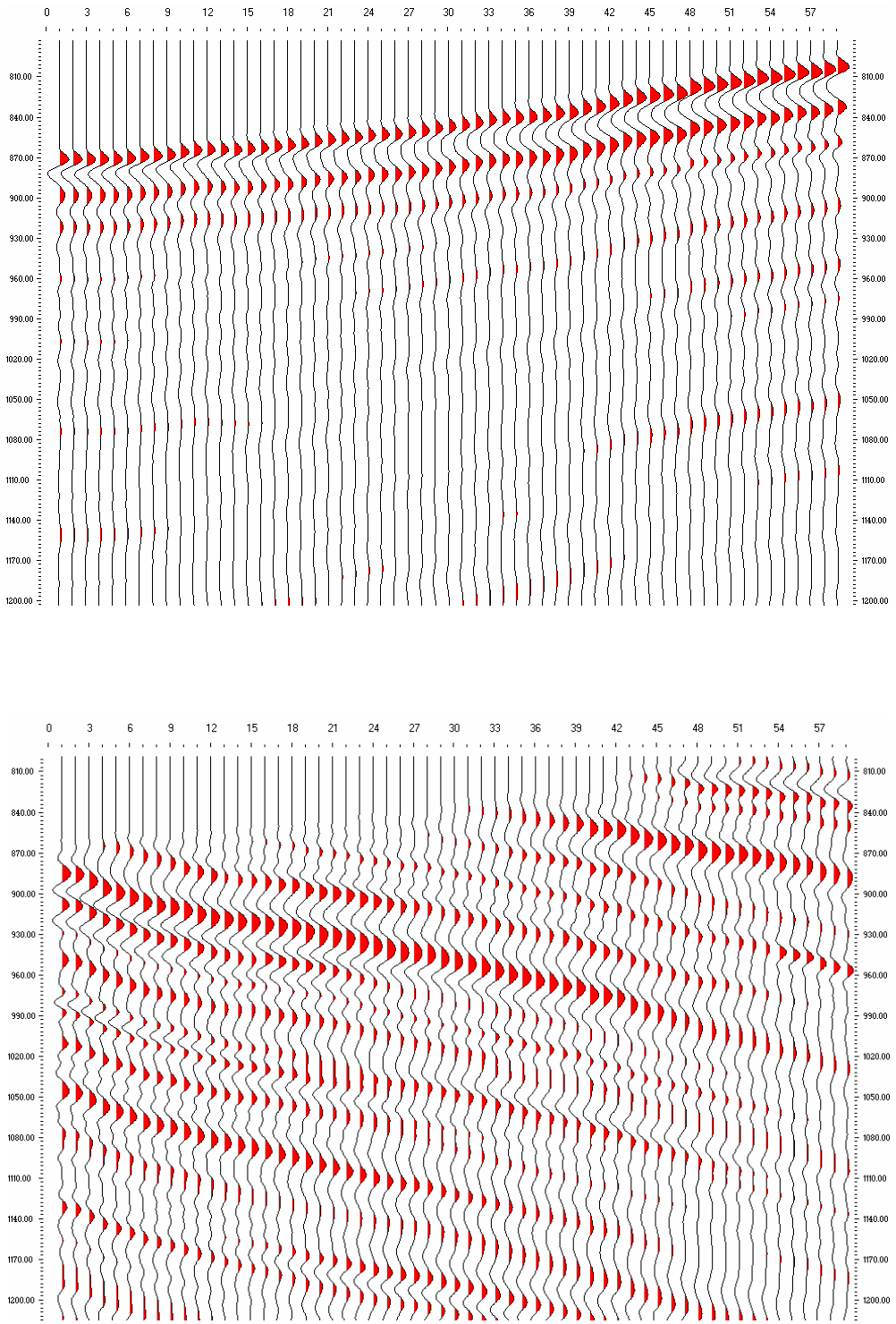

Figure 6: 5700 Offset VSP (152 degrees azimuth). Top: Downgoing PP. Bottom: Upgoing PP.

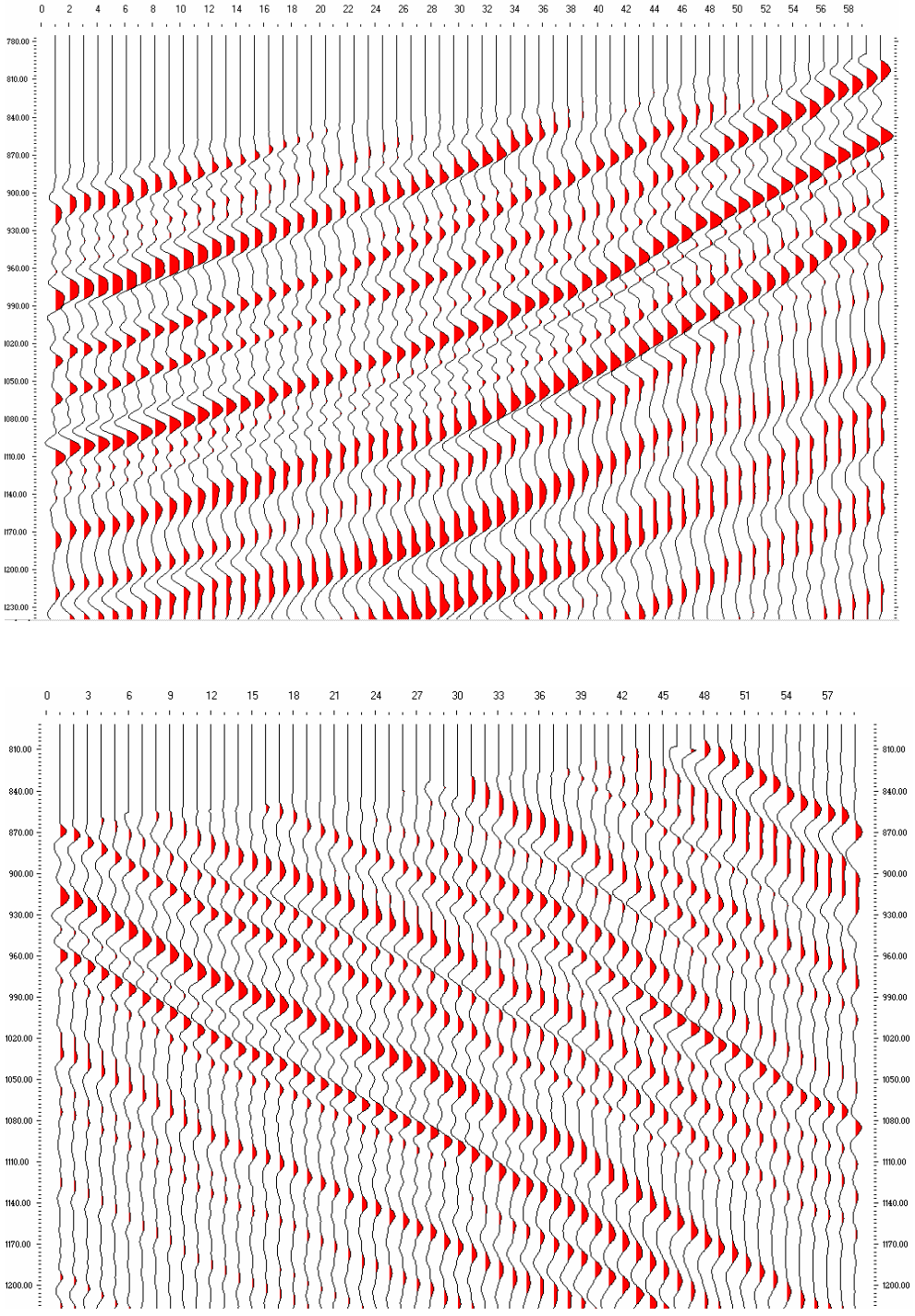

Figure 7:5700 Offset VSP (152 degrees azimuth). Top: Downgoing PS. Bottom: Upgoing PS.

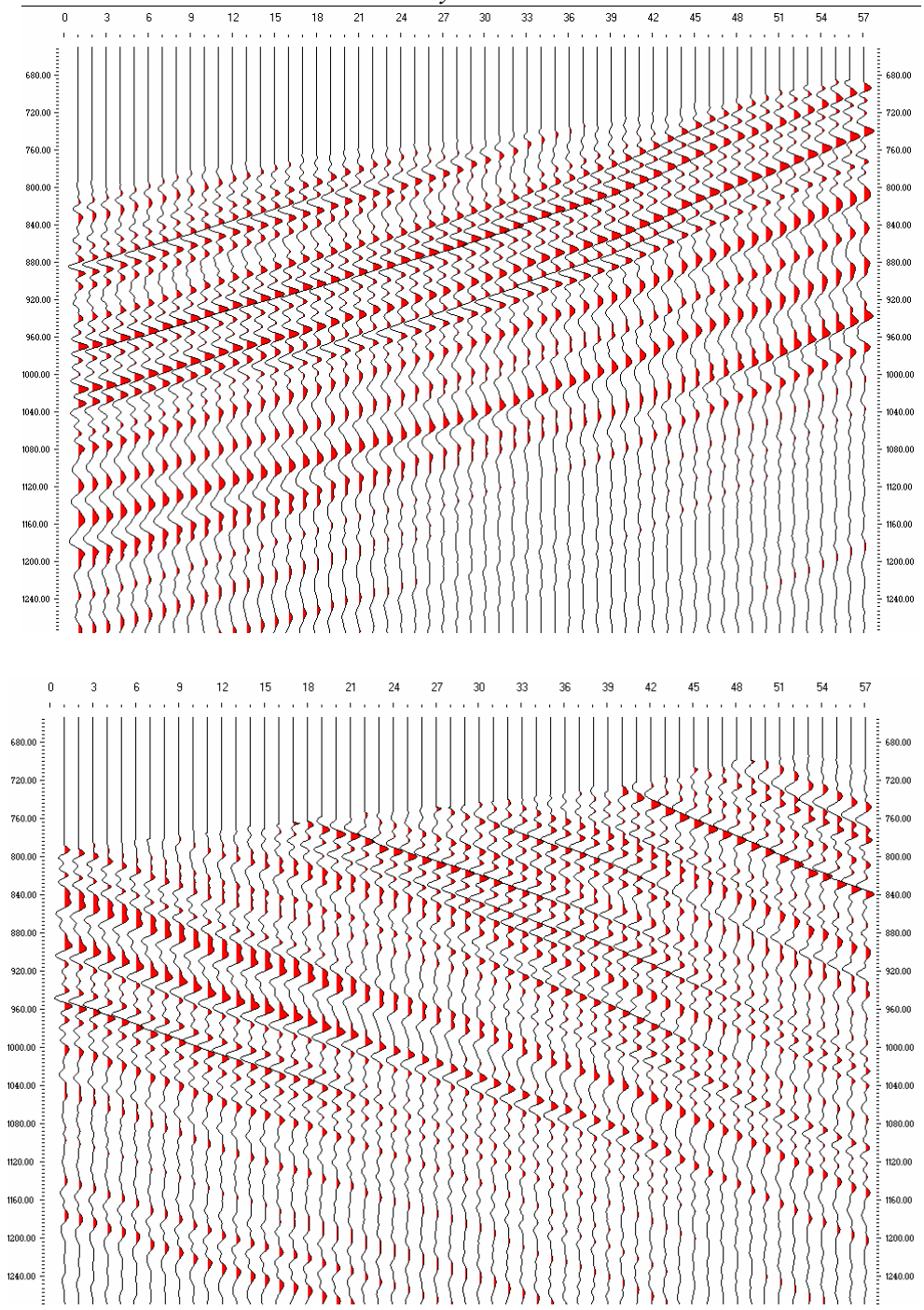

Figure 8: 3200 Offset VSP (230 degrees azimuth). Top: Downgoing PS. Bottom: Upgoing PS.

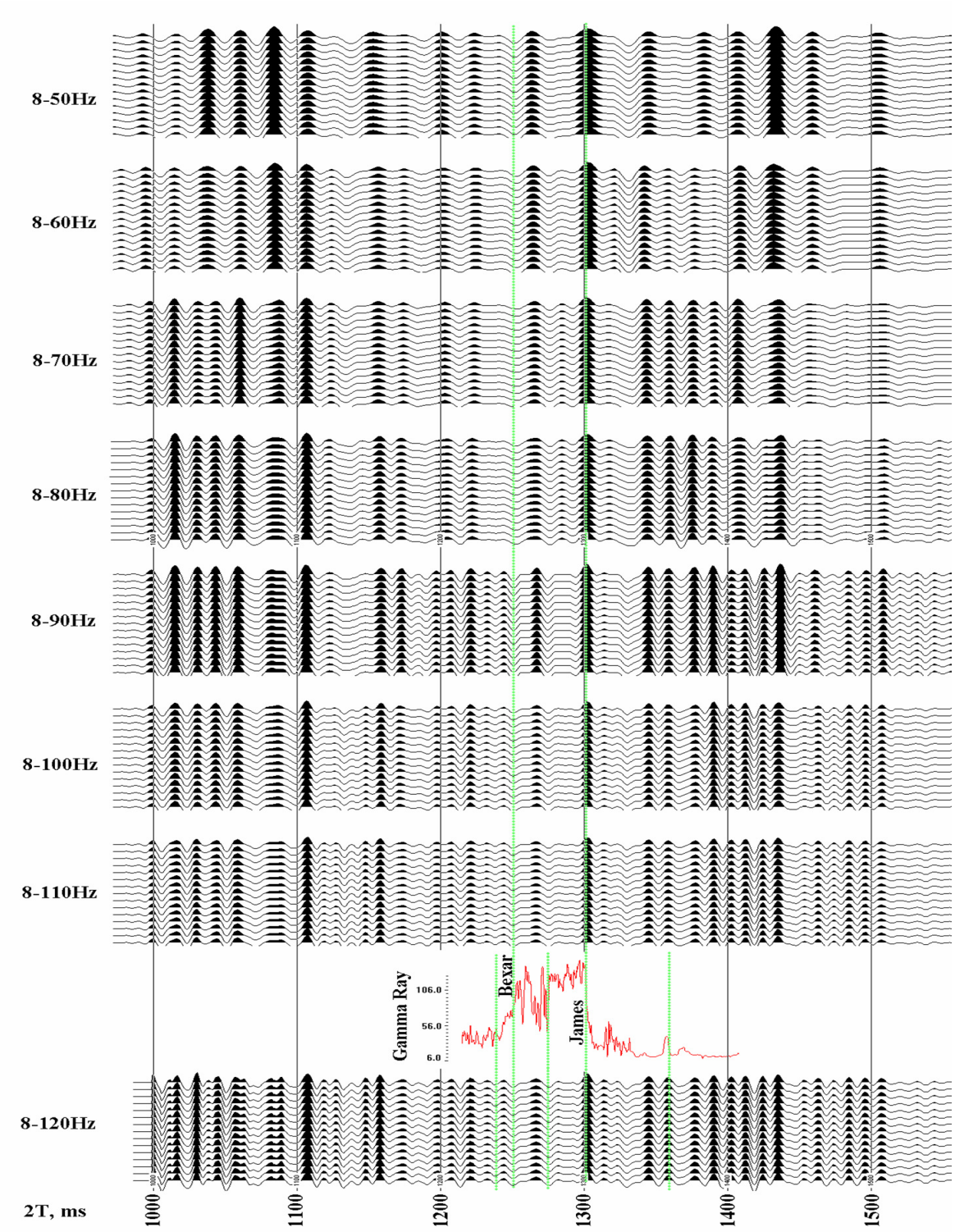

Figure 9: VSP corridor stacks with different band-pass filters.

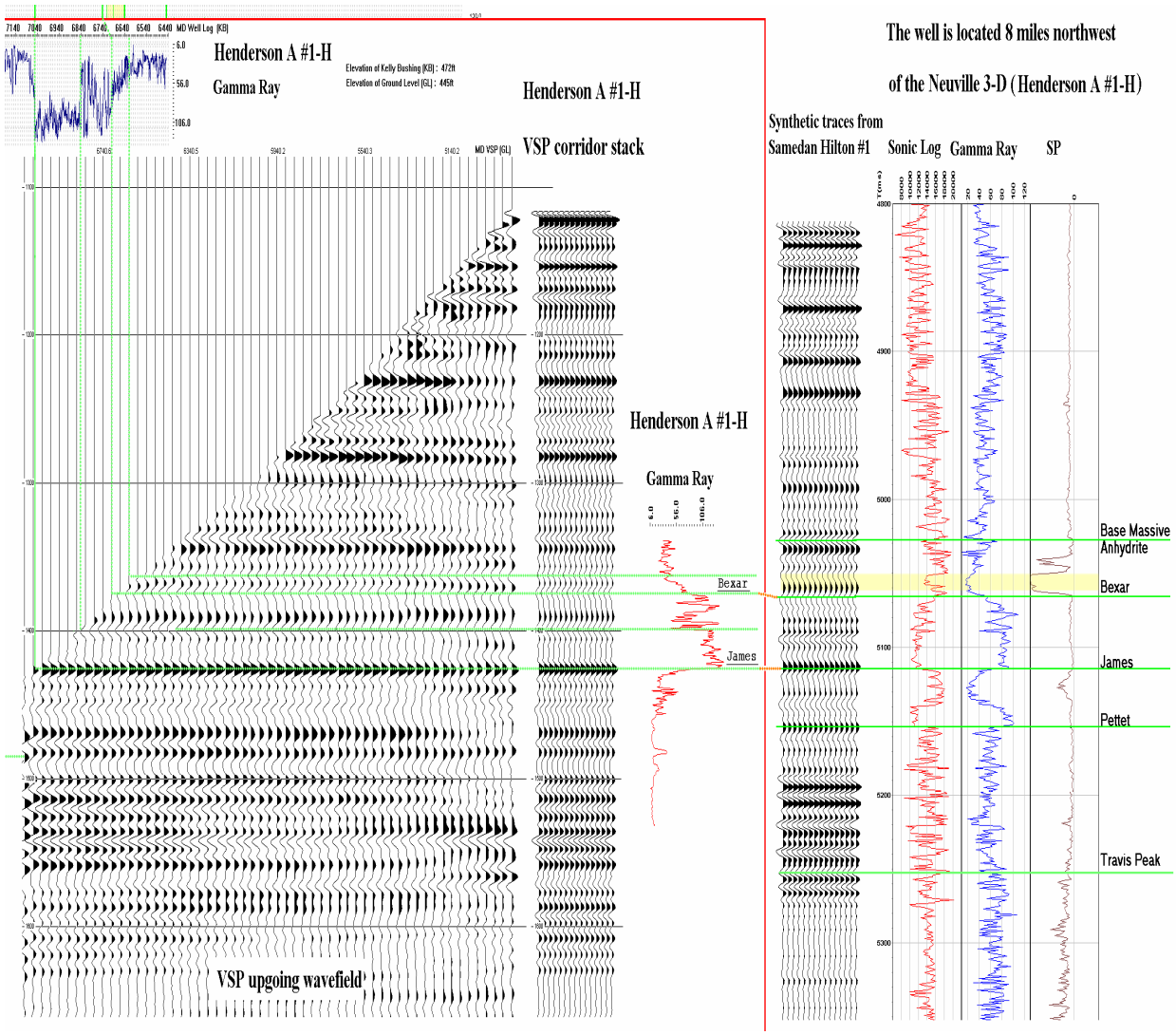

Figure 10: Correlation of Gamma Ray and sonic logs from Hilton #1 Well with VSP corridor stack and synthetic corridor stack.

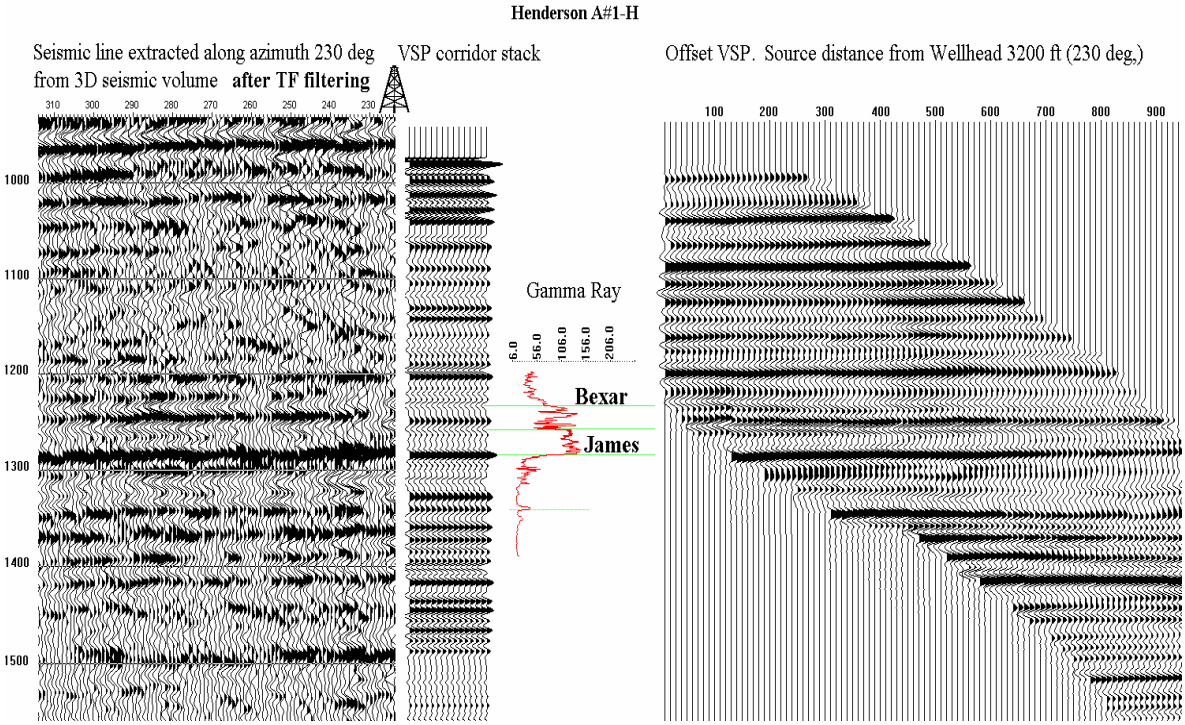

Figure 11: 3200 Offset VSP with the corridor stack and seismic line extracted along azimuth of the VSP (230 deg).

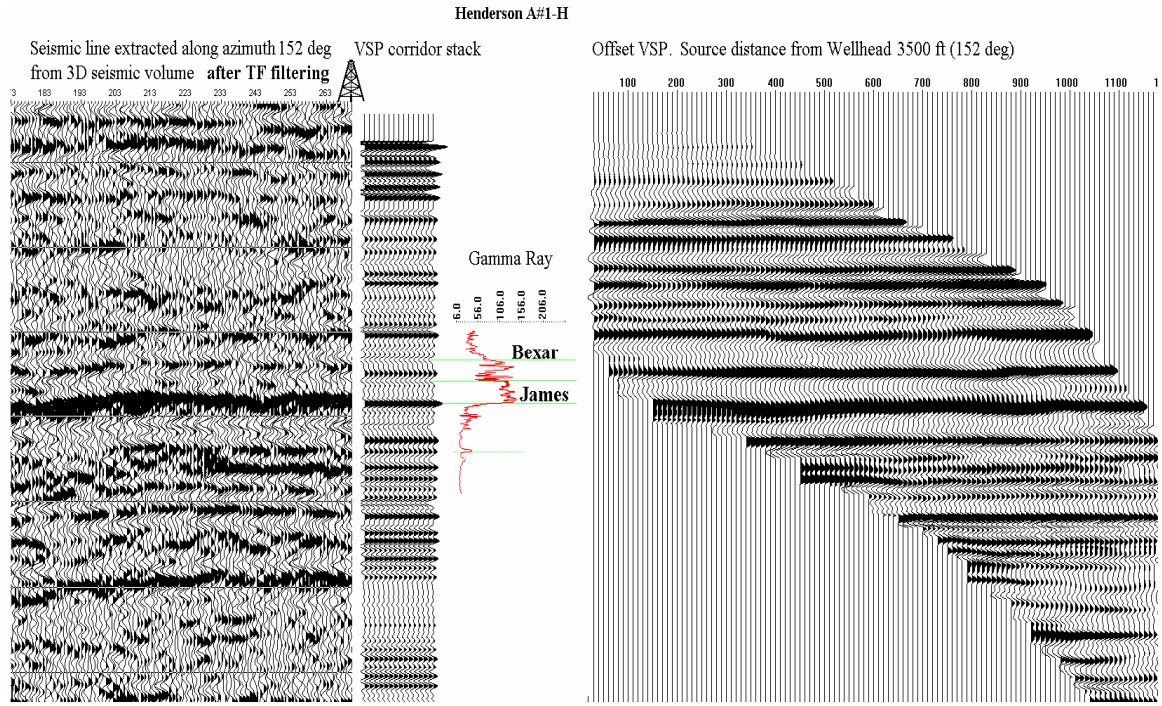

Figure 12: 3500 Offset VSP with the corridor stack and seismic line extracted along azimuth of the 3500 Offset VSP (152 deg).

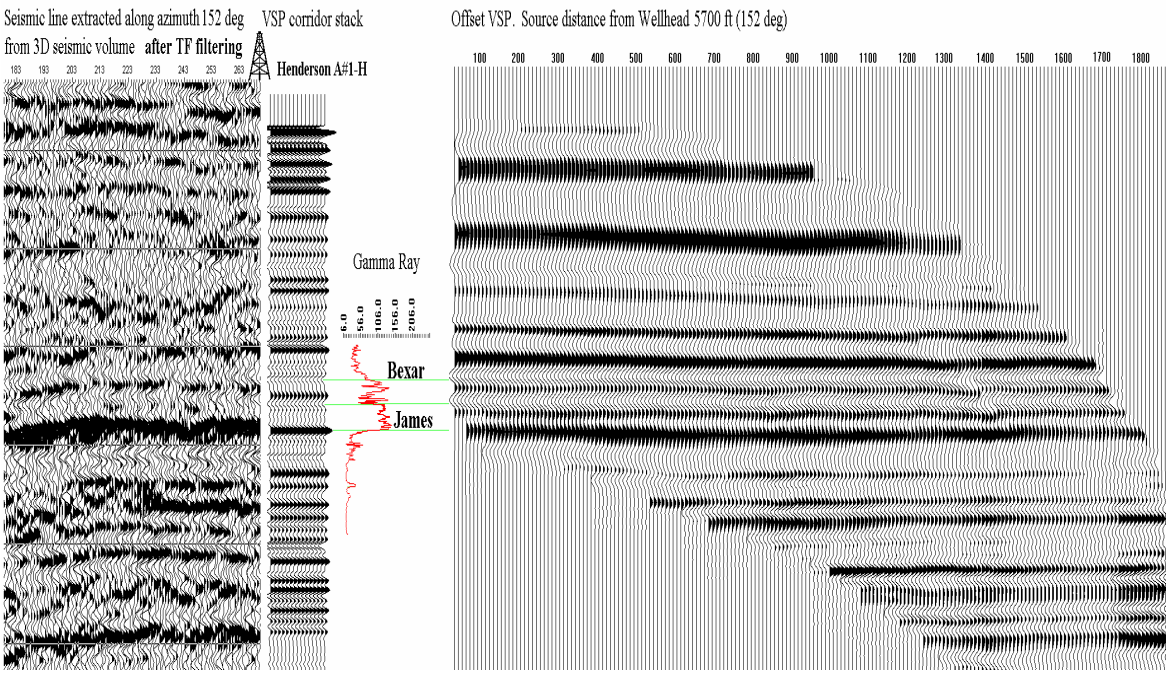

Figure 13: 5700 Offset VSP migrated section with the corridor stack and seismic line extracted along the azimuth of the 5700 offset VSP (152 deg).

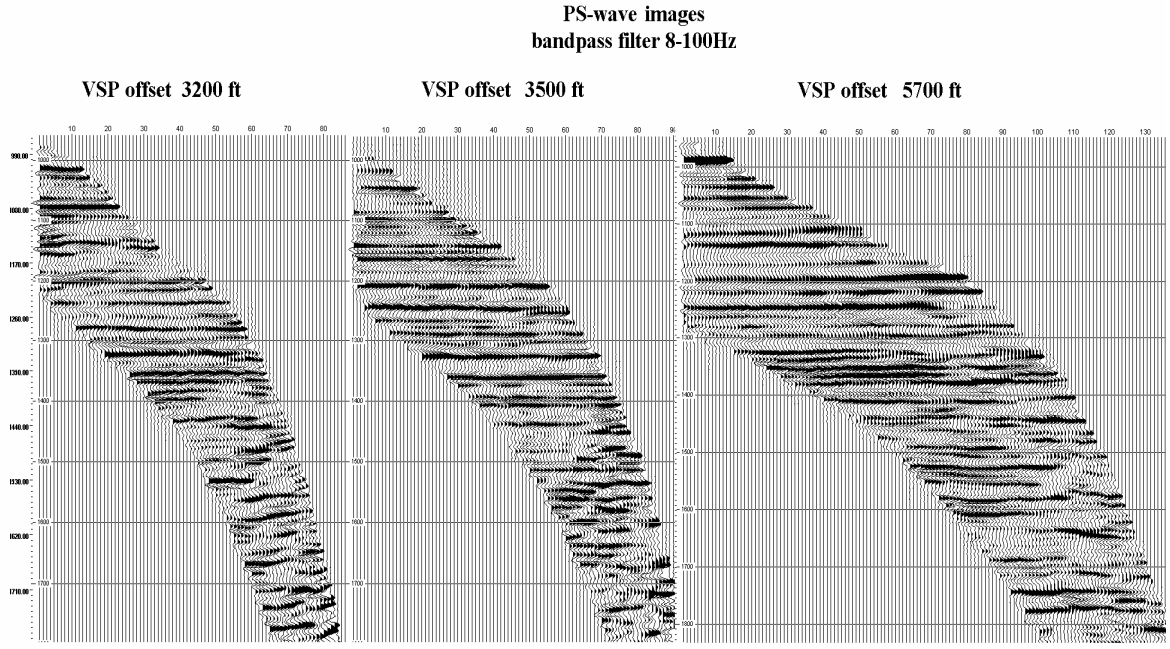

Figure 14: All Offset VSPs migrated image for PS waves.

Time to depth conversion and seismic attributes

The seismic interpretation of the VSP is based on the analysis of seismic attributes and the match to geologic markers resulting from the time to depth conversion. The time to depth conversion, required to compare the VSP results to the geologic interpretation of LWD gamma-ray data (Fig. 15), is based on the check-shot data (Figure 16). Different attributes have been calculated to help the seismic interpretation of the VSP. The attributes calculated are amplitude, instantaneous phase, instantaneous frequency, central frequency, impedance, the instantaneous amplitude (analytical signal or quadrature) and the zero-phase amplitude (the central coordinate of the Fourier transform of a wavelet window). In the following section we combine the results from the 5700-offset VSP with the geologic interpretation of LWD gamma ray data (Fig. 15), to develop a geologic model of the reservoir along the path of Henderson-1 well.

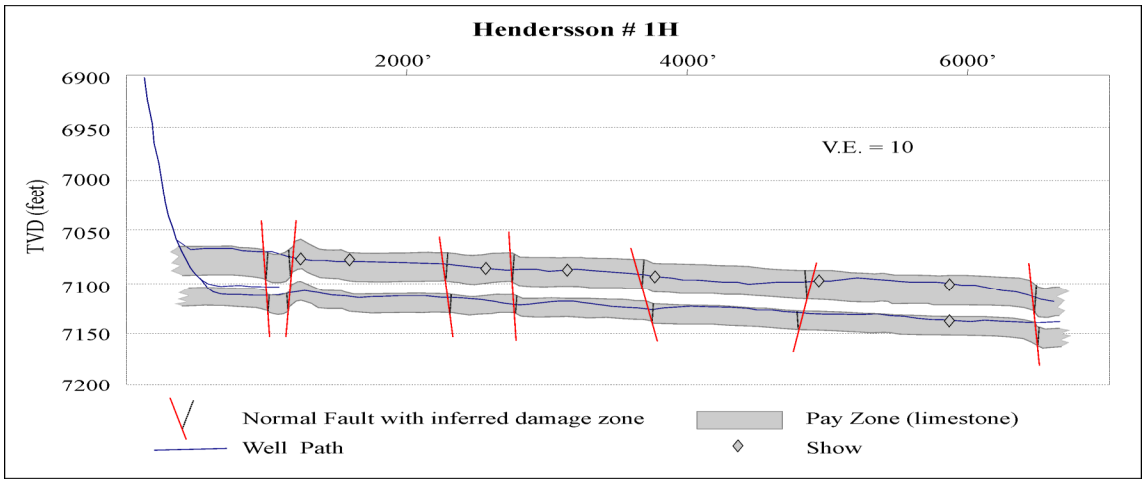

Figure 15: Geologic model of James Lime along the Henderson-1 path, based on LWD gamma ray (Courtesy of Marathon).

The check-shot allows an accurate location of top James Lime on the VSP sections (Figure 17). Top James Lime is located at 1.295 milliseconds (TWT). The interval velocity at this depth is 7000 ft/s, and since the James Lime at this locality is only about 70 ft thick (Figure 15), this limestone unit corresponds to only 20 to 30 milliseconds in the TWT seismic section. The location of top James Lime in the VSP seismic section is shown in Figure 17.

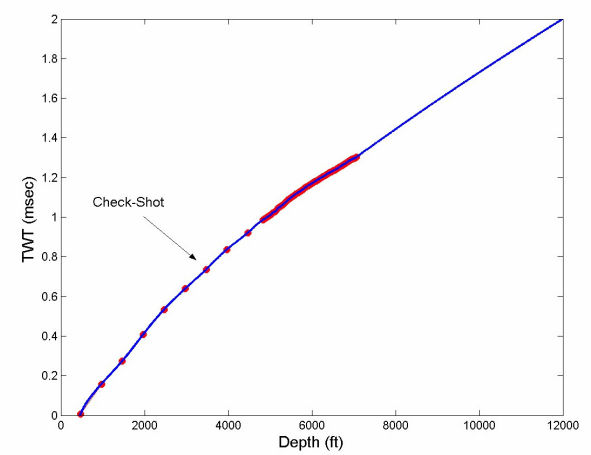

Figure 16: Time to Depth table based on Check-Shot data.

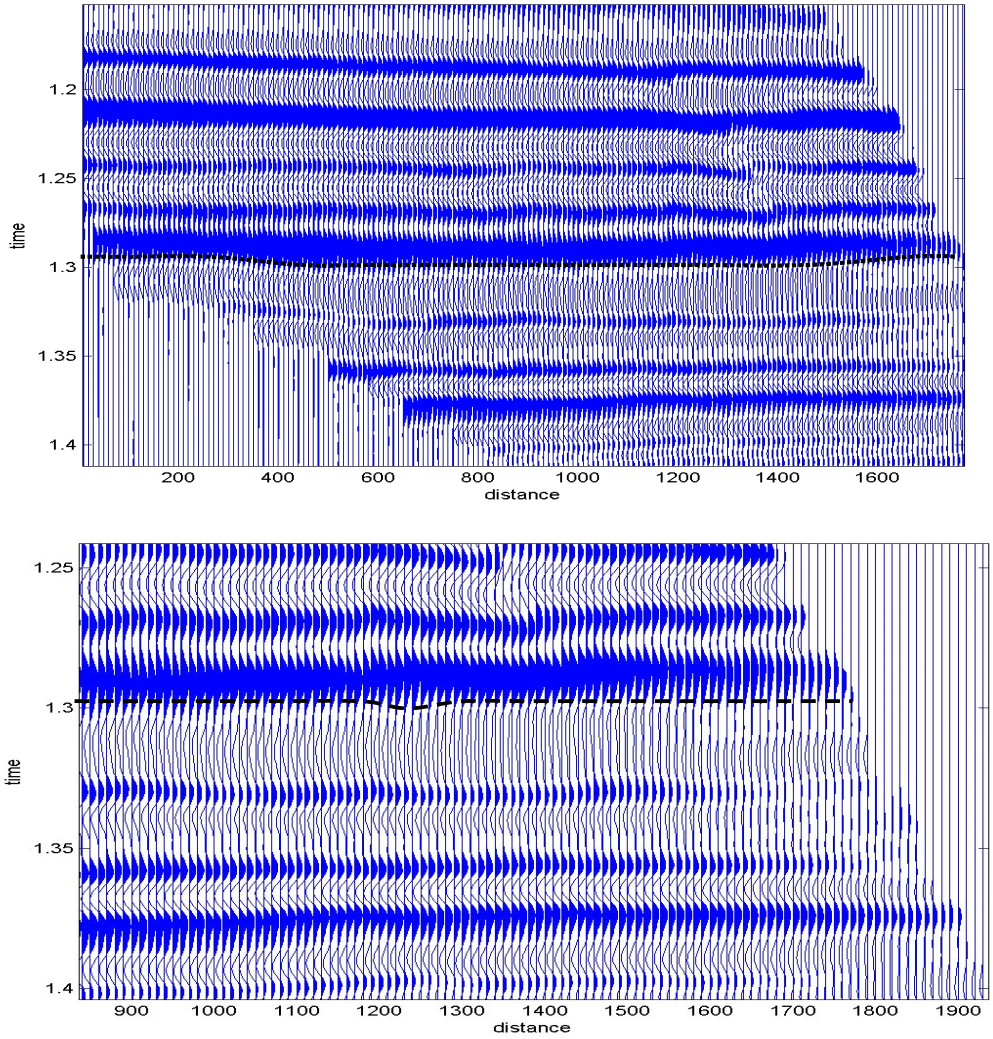

Figure 17: Seismic sections from the 5700-offset VSP, showing the location of top James Lime.

The zero-phase amplitude and instantaneous phase are the two attributes that provide a better image of the reservoir structure, and the lateral variations in reflectivity. The calculated seismic attributes are related to the amplitude, frequency or phase of the recorded signal. The instantaneous amplitude is Hilbert's transform of the wavelet. The instantaneous phase is the natural logarithm of this transform, and the instantaneous frequency is the derivative of the instantaneous phase. The attributes related to the amplitude are: the amplitude itself (Fig. 18), the pseudo-impedance (Fig. 19), the instantaneous amplitude (Fig. 20), and the zero-phase amplitude (Fig. 21). In essence, the amplitude-based attributes are equivalent and all of them carry out the same information, however the zero-phase amplitude (Fig. 21) provides an image of the reservoir with better resolution.

The VSP shows evidence of AVA (Amplitude Variation with Angle) effects superimposed on amplitude anomalies. A good example of these AVA effects occurs at the James Lime interval itself, and is particularly evident in the zero-phase amplitude section (Fig. 21). Notice that between 7050 ft and 7100 ft, there is a constant gradient of amplitude reduction from the well trajectory. The angle of incidence varies between 20° to 30° from the near to the far offset along the well path.

The frequency-based attributes, instantaneous frequency (Fig. 22) and frequency centroid (Fig. 23), do not show significant attenuation effects. The instantaneous frequency helps to outline the lateral continuity of the reflections (Fig. 22). The frequency centroid (Fig. 23) shows that the dominant frequencies in the VSP seismic section range from 40 to 70 Hertz.

The instantaneous phase (Fig. 24) provides the best image to analyze the lateral continuity of the reservoir. Since it is calculated taken the natural logarithm of the instantaneous amplitude, it enhances both the pick, the troughs and the inflection points of the wavelet, providing an image with better continuity and resolution. This image, however, does not preserve any information about the seismic properties of the horizons.

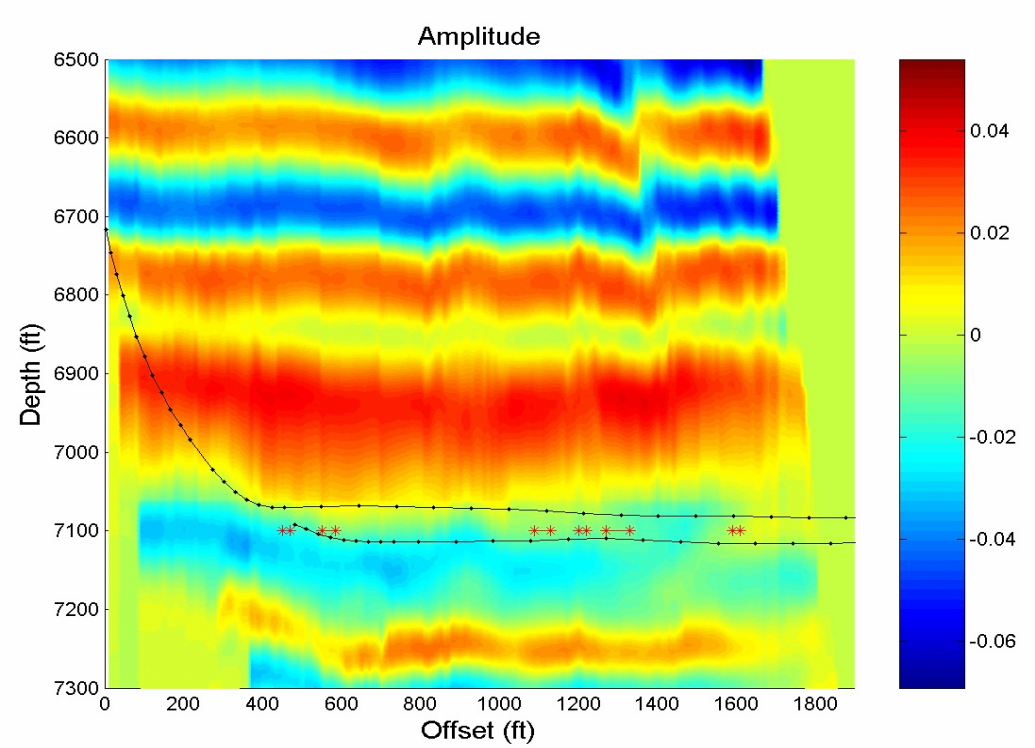

Figure 18: VSP seismic section showing the variation of amplitude along the path of Hendersson-1. The asterisks (*) indicate the location of faults according to the interpretation of the LWD gamma ray.

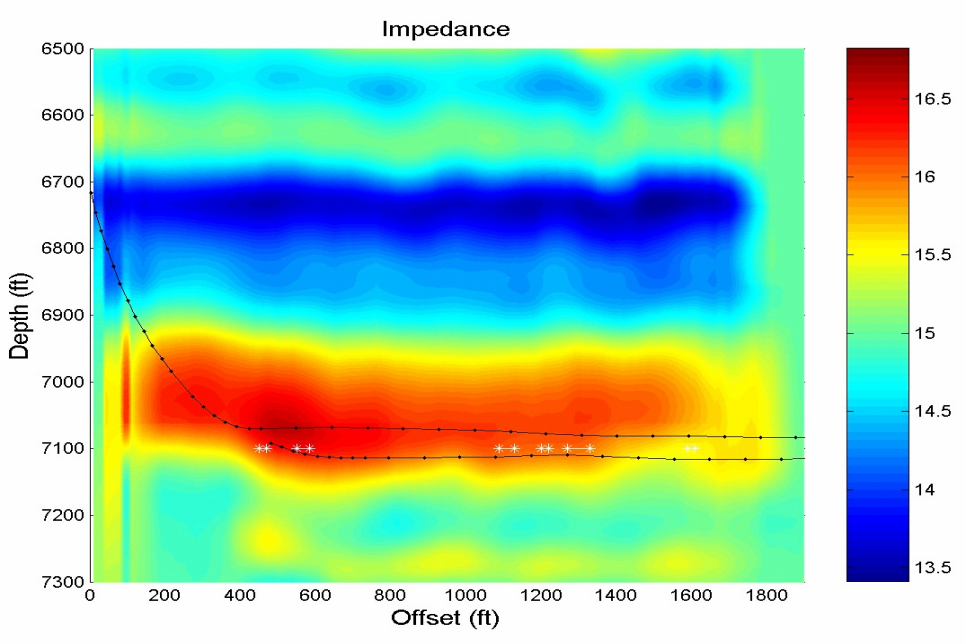

Figure 19: VSP seismic section showing the variation of pseudo-impedance along the path of Hendersson-1. The asterisks (*) indicate the location of faults according to the interpretation of the LWD gamma ray.

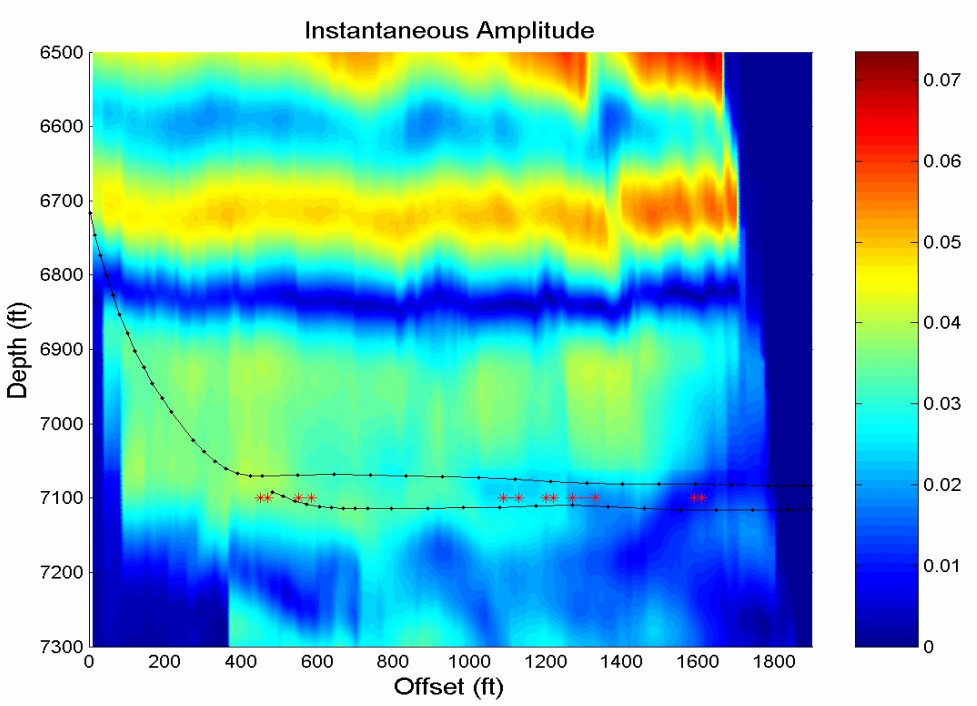

Figure 20: VSP seismic section showing the variation of instantaneous amplitude along the path of Hendersson-1. The asterisks (*) indicate the location of faults according to the interpretation of the LWD gamma ray.

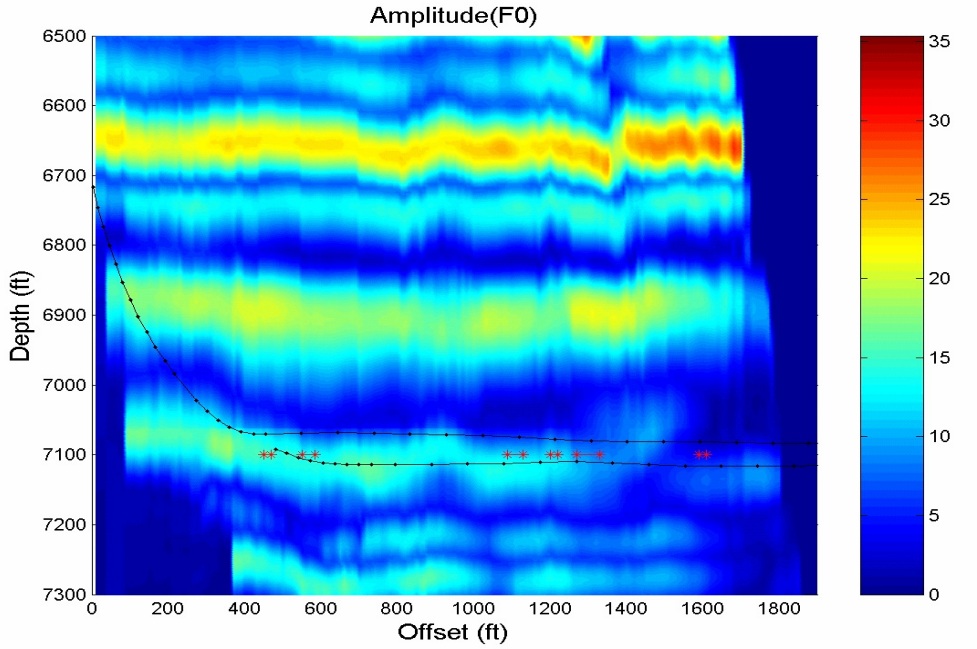

Figure 21: VSP seismic section showing the variation of zero-phase amplitude along the path of Hendersson-1. The asterisks (*) indicate the location of faults according to the interpretation of the LWD gamma ray.

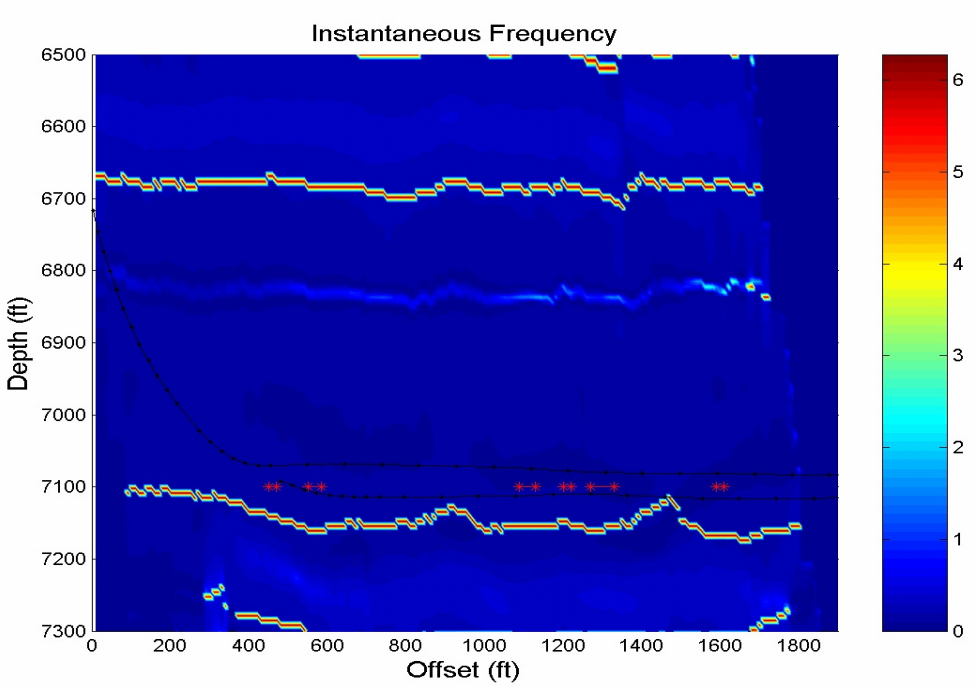

Figure 22: VSP seismic section showing the variation of zero-phase amplitude along the path of Hendersson-1. The asterisks (*) indicate the location of faults according to the interpretation of the LWD gamma ray.

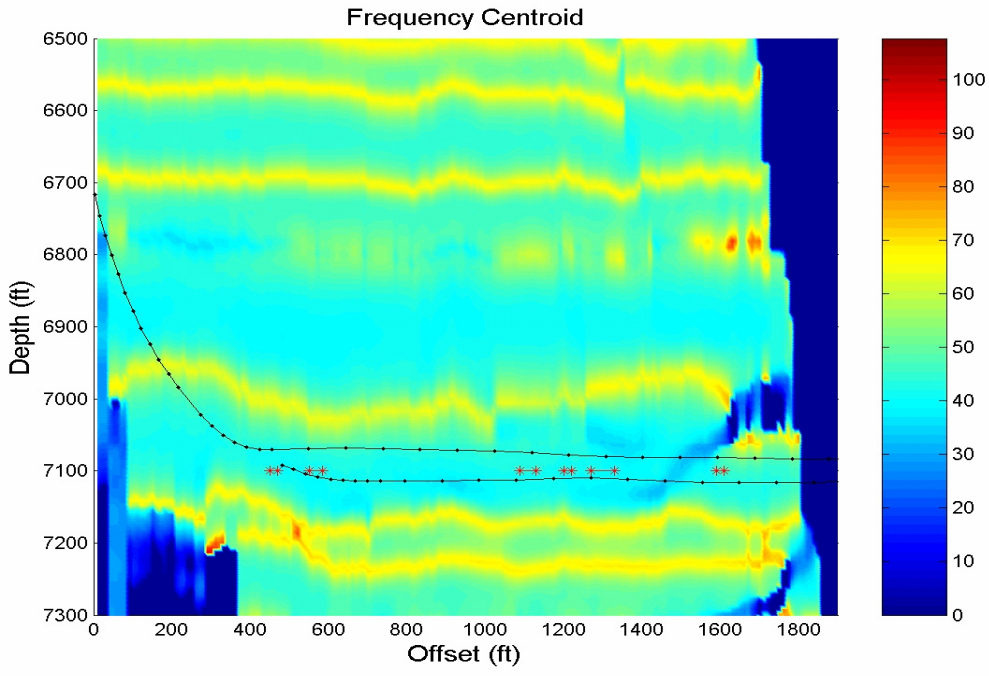

Figure 23: VSP seismic section showing the variation of zero-phase amplitude along the path of Hendersson-1. The asterisks (*) indicate the location of faults according to the interpretation of the LWD gamma ray.

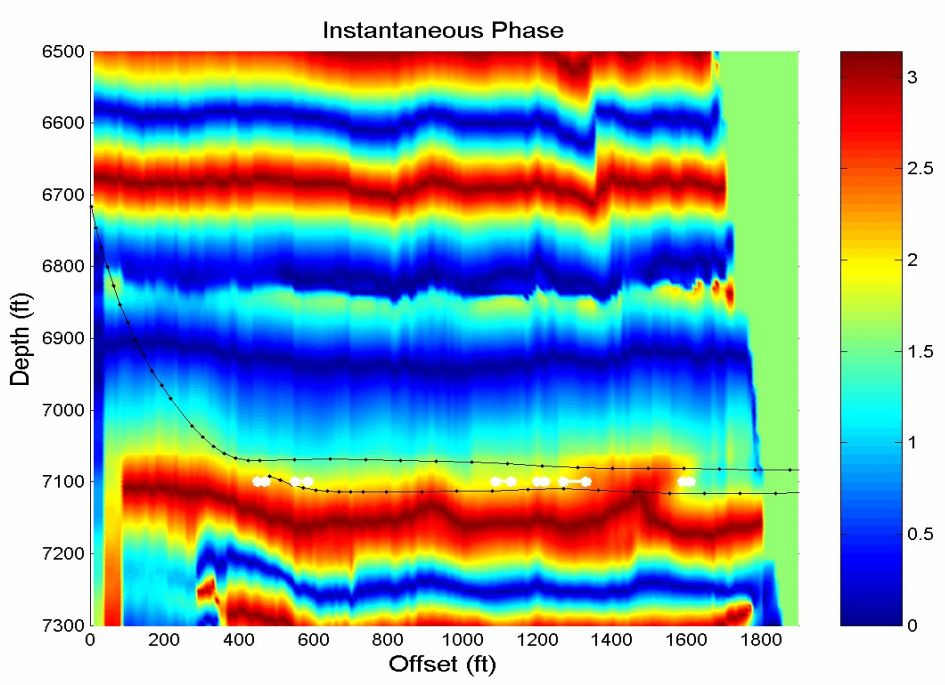

Figure 24: VSP seismic section showing the variation of zero-phase amplitude along the path of Hendersson-1. The asterisks (*) indicate the location of faults according to the interpretation of the LWD gamma ray.

VSP interpretation and Comparison with lateral boreholes

The combination of the VSP seismic sections and the geologic interpretation of the LWD gamma-ray allow us to locate small faults along the path of Hendersson-1. The gamma ray LWD log and other information collected during the drilling of Hendersson-1, such as drilling rate (DR) and calcite (CALC) content in the mudlog, was used to generate a preliminary interpretation of small faults along the well path (Figs. 25, 26 and 27). The final interpretation was superimposed on the VSP sections, as discussed above. The coincidence of offsets or amplitude anomalies with the interpreted fault locations provide an additional evidence of the presence of faults and probable fracture swarms at these locations, the final interpretation is shown in Figures 28 and 29.

Horizontal wells have demonstrated the presence of faults in the reservoir that cannot be imaged with conventional seismic techniques. Such faults are normally referred to as

subseismic faults. As explained in Attachments A and B, fracture swarms are commonly associated with subseismic faults. According to Marathon's interpretation, there are at least six normal faults along the horizontal sections of Hendersson-1. We reviewed Marathon's interpretation, especially along the section between 0 to 2000' offset, which is the interval relevant for the comparison with the VSP data.

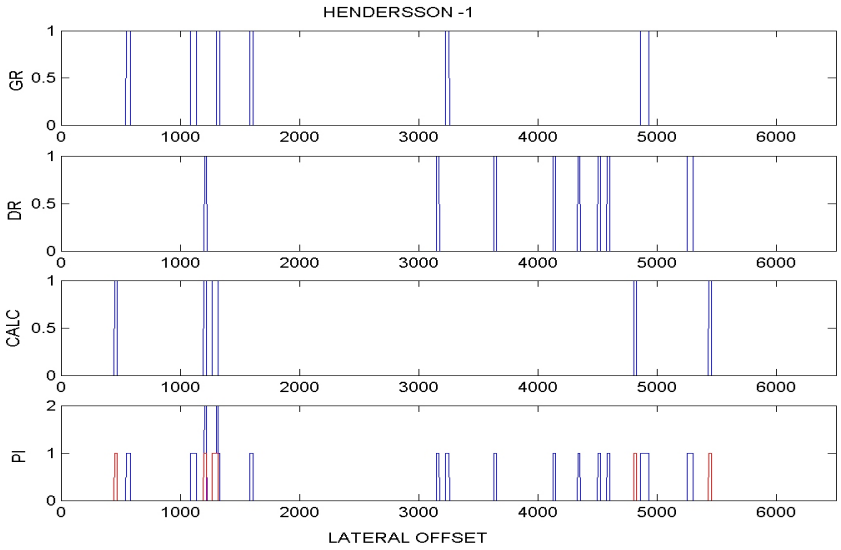

Figure 25. Location of probable faults along the upper lateral wellbore of Hendersson-1, PI stands for Probability Indicator and corresponds to the number of fault-indicators (GR, DR or CALC) overlapping over a given location, within a window of 20 feet. Calcite (CALC, and red in the lower graph) overlaps in one case with the drilling rate (DR) and in another case with the gamma ray (GR). The indicator anomalies corresponding to these two locations are considered to have a higher probability of being faults.

In order to evaluate the uncertainty related to the different faults interpreted along the lateral wellbores of Hendersson-1, we apply a systematic analysis to the main parameters that may indicate faults along the wellbore: (1) gamma ray log, (2) drilling rate, and (3) the presence of calcite. The analysis follows the methodology explained in Attachment B, basically we add both the indicator absolute value and the derivative, and apply a threshold, leaving only those points that correspond not only high values, but also to high or abrupt changes. Afterwards, we give a value of one for each fault location derived from each parameter, and sum all them together using a match window of 20 feet. As a result, if two indicators overlap they sum together; then the higher the value obtained for each position, the higher the probability of a fault located at that lateral offset (Figure 15).

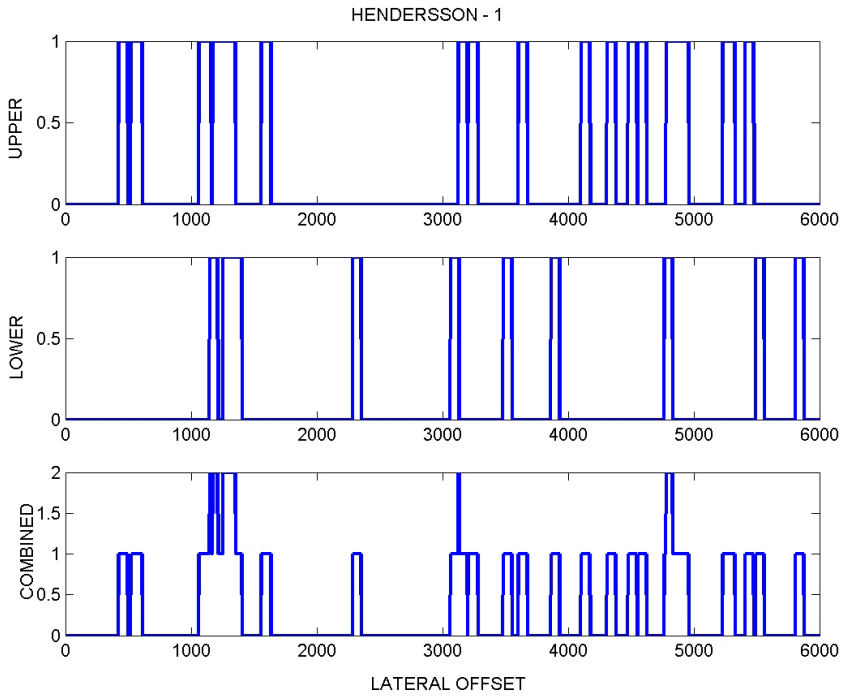

Figure 26. Location of probable faults along the upper lateral and lower wellbores of Hendersson-1, and comparison between the two (combined). The location of faults along each lateral is given by any of the indicators shown in figure 15 (GR, DR or CALC). The comparison has been done using an overlap window of 50 feet, if faults occur in both laterals within that window it is considered that the probability of a fault is higher. It can be observed that there are just four cases (about 1200, 1300, 3200 and 4800).

In addition to this, we compare the fault locations along both, the upper and lower lateral wellbores. We used again a window of 50 feet to compare the fault locations. As explained above, when the fault locations are within the window, the indicators are summed, resulting in a higher probability indicator for a fault at that particular offset (Figure 26). A plot of the final result is presented (Figure 27) in order to visualize the distribution of faults between 0 and 2000 feet lateral offset. The location of faults obtained from this analysis constitutes the most likely case that can be used to compare against the distribution of amplitude anomalies along the 152°-azimuth VSP.

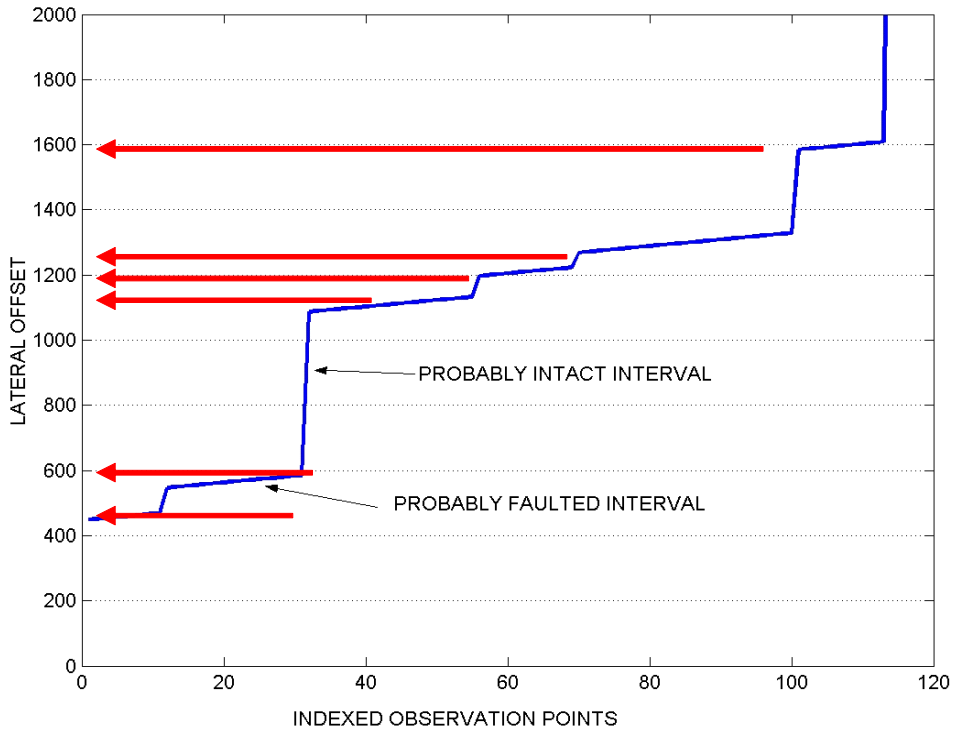

Figure 27. Visualization of the distribution of probable fault zones along the lateral section of Henderson-1, from 0 to 2000 feet offset, the subhorizontal line segments correspond to probably faulted intervals, whereas the subvertical segments correspond to probably non-faulted or intact intervals. This graph is based on the results of the combination of fault indicators (GR, DR and CALC) on both the upper and the lower lateral (lower graph of figure 26).

The comparison of the VSP data and the geologic interpretation shows that amplitude anomalies and vertical offsets observed in the VSP section coincides with fault locations. The zero-offset amplitude section provides the image with better resolution (Fig. 28), and spite of the presence of AVA effects, the largest faults predicted from the gamma ray log coincide with significant amplitude anomalies. Similarly, the instantaneous phase images (Fig. 29) clearly outlines the offset of seismic horizons, which coincide with the interpreted faults and the amplitude anomalies. These three independent lines of evidence provide enough support to the final seismic interpretation of the VSP data, shown in Figures 28 and 29. Four faults have been finally interpreted, with offsets between 40 ft and less than 10 ft, all of them associated with amplitude anomalies caused by fracture swarms.

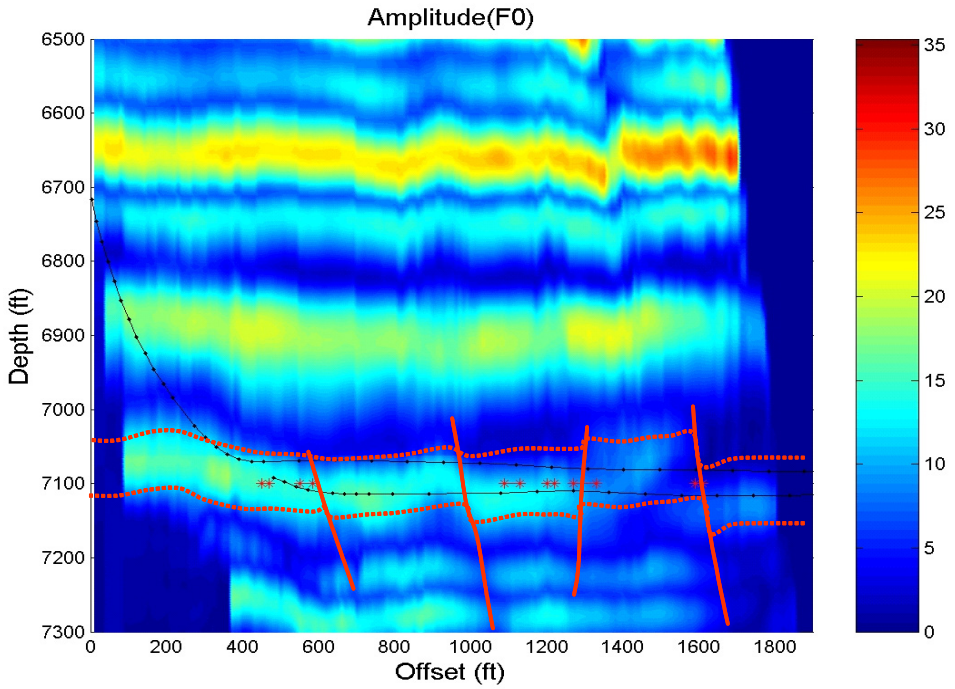

Figure 28: Interpretation of the VSP seismic section based on amplitude anomalies and the LWD gamma ray. The well path is shown in black and the asterisks (*) indicate the location of faults according to the interpretation of the LWD gamma ray.

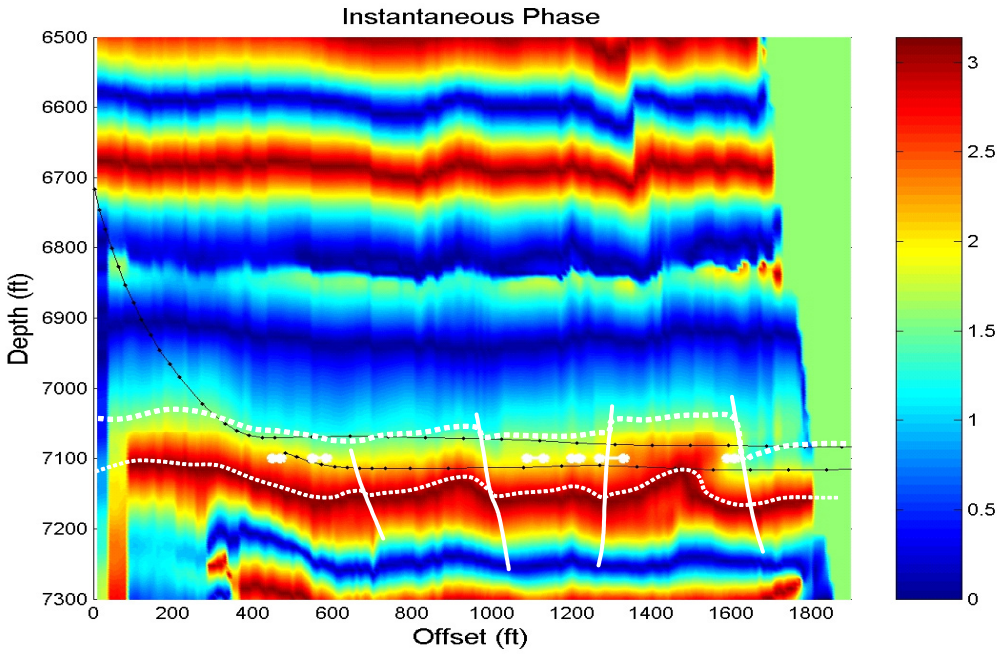

Figure 29: Interpretation of the VSP seismic section based on vertical offset of some reflectors and the LWD gamma ray. The well path is shown in black and the asterisks (*) indicate the location of faults according to the interpretation of the gamma ray.

Fracture orientation and integration with 3D seismic

The fracture orientation has been determined using 3D seismic data. The VSP data alone could not constrain the orientation of faults and fractures around Hendersson-1. As explained in attachment A, there is a large normal fault located 2 km east of Hendersson-1. That fault is trending to the WNW or ESE (113°) and dipping to the SW. We have discussed three different possible scenarios, A, B and C, for fracture/fault orientation based on the tectonic evolution of the region and the current tectonic configuration (see Attachment A). The AVAZ analysis of the 3D seismic data rules out the possibility of scenarios B and C, and leaves scenario A as the most likely. Here we discuss the implications for these probable three scenarios derived from the results of the VSP.

Scenario A (Figure 30) implies that faults are trending WNW-ESE, as the large fault located to the east. This is considered to be the most likely case, since it implies that faults are contemporaneous and generated under the same loading conditions as the large fault. Given the geometric configuration of the VSP, a fault observed in the 152°-azimuth VSP would be also seen in the 230°-azimuth VSP. However, we observe just one fault in the 230°-azimuth VSP, which implies that either most of the faults are short and do not extend to the 230°-azimuth VSP or they have different orientation. On the other hand, the fault observed in the 230°-azimuth VSP can be linked to the best-defined fault zone in the 152°-azimuth VSP.

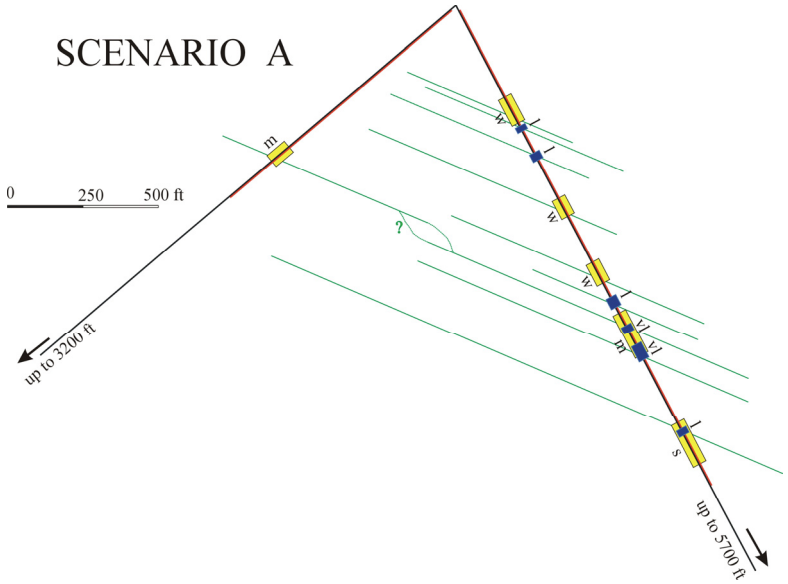

Figure 30: Scenario A. the small-scale faults are parallel to the large fault. In this case, most of the small faults along the well (azimuth 152°) should stop before the 230°-azimuth VSP. Small discrepancies in fault projection can be the result of fault linkage, as shown in the region with question mark.

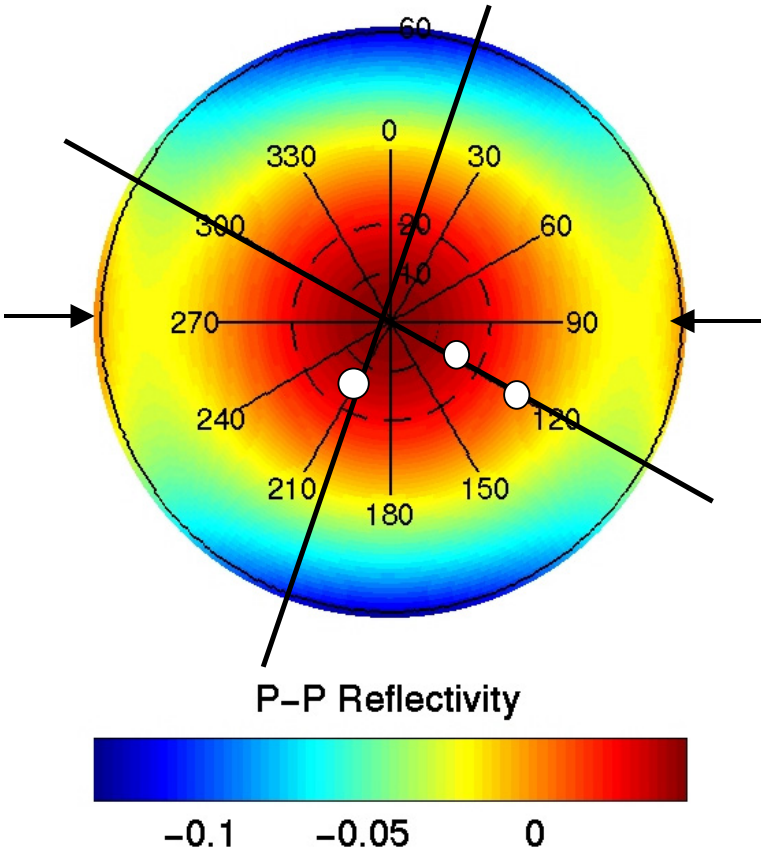

Figure 31: VSP sampling on the azimuthal variation of Rpp in the Scenario A. The small white circles represent the windows seen by the Offset VSP on the azimuth 152 (3500ft at an average of 15 degrees angle of incidence, 5700ft at an average of 30 degrees angle of incidence) and azimuth 230 (3200ft at about 15 degrees angle of incidence). Fracture orientation is represented through the arrows (E-W).

Figure 31 shows a PP reflectivity map versus azimuth and angle of incidence as modeled for an HTI medium (ATTACHMENT D). In this figure the fractures are orientated E-W. The concentric circles represent the angles of incidence. The dark lines represent the orientation of the two azimuths of the VSP with respect to fracture orientation, corresponding to scenario A. For the 3200-ft, and 3500-ft offset VSP, the estimated average angle of incidence at the top of the James Lime is about 15 degrees, while for the 5700 offset VSP the estimated average angle of incidence is about 30 degrees. The white circles represent the sampling of the VSP in the AVOZ (Amplitude variation with offset and Azimuth) domain.

Scenario B (Figure 32) corresponds to the case of faults trending ENE-WSW, similar to the faults affecting the Cenozoic section in the subsurface. In this case, faults would be perpendicular to the wellbore trajectory. This seems to be in agreement with the fact that more amplitude anomalies are observed along the 152°-azimuth VSP than along the 230°-azimuth VSP. Therefore, results obtained from the VSP provide a better support for this case than for Scenario A, considered to be the most likely.

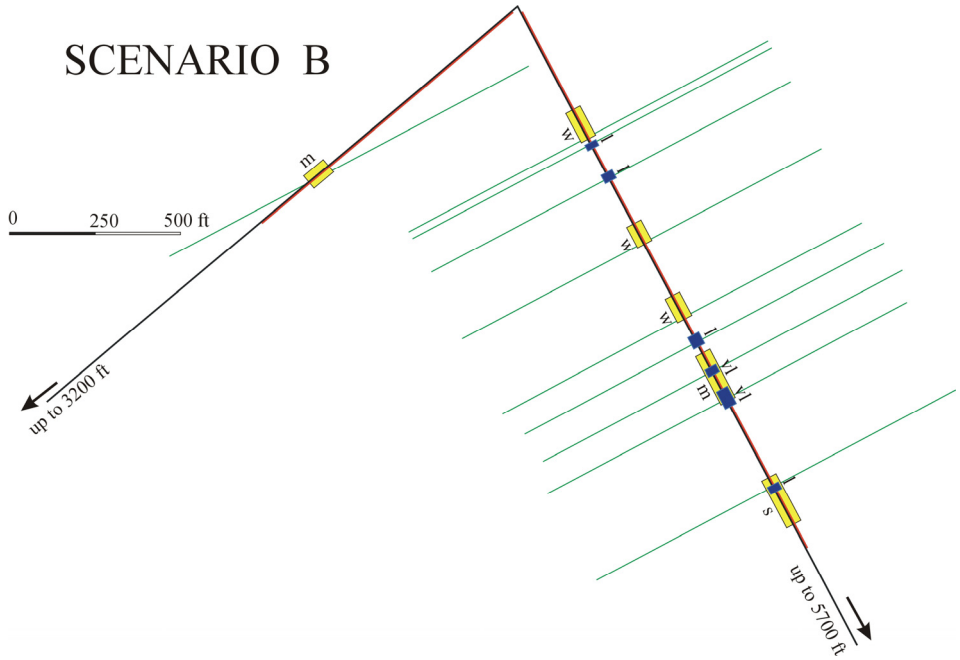

Figure 32. Scenario B. Faults parallel to the faults at surface (Cenozoic). In this case faults would be perpendicular to the 152°-Azimuth VSP and subparallel to the 230°-Azimuth VSP. Faults observed along the 152°-Azimuth VSP do not intercept the 230°-Azimuth VSP.

Figure 33 shows again the windows seen by the VSP superimposed on the map of PP reflected amplitude, but this time in the scenario B. In the figure the fractures are orientated E-W. The concentric circles represent the angles of incidence. The dark lines represent the orientation of the two azimuths of the VSP with respect to fracture orientation corresponding to scenario B. For the 3200ft and 3500ft offset VSPs, the estimated average angle of incidence at the top of James Lime is about 15 degrees, while for the 5700 offset VSP the estimated average angle of incidence is about 30 degrees. The white circles represent the sampling of the VSP in the AVOZ (Amplitude variation with offset and Azimuth) domain in scenario B. The rest of the domain is not sampled.

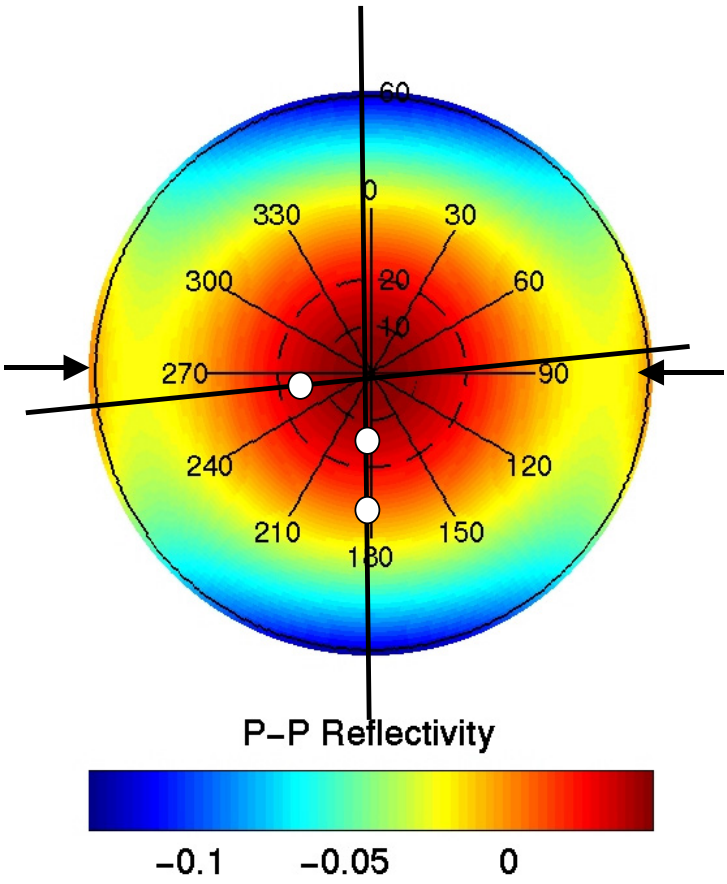

Figure 33: VSP sampling on the azimuthal variation of Rpp in the Scenario B. The small circles represent the windows seen by the Offset VSP on the azimuth 152 (3500ft at about 15 deg angle of incidence, and 5700ft –at about 30 degrees angle of incidence), and azimuth 230 (3200 ft at about 15 degrees angle of incidence). Fracture orientation is represented through the arrows.

Scenario C (Figure 34) corresponds to an alternative case, in which faults are trending NE, normal to the main fault located further east. As in the previous case, the results obtained from the VSP provide better support for this scenario than for the one considered as most likely. However, the results from the VSP cannot distinguish between scenarios B and C. Even more, scenario A cannot be ruled out, since the VSP presents good continuity for the best-defined fault and poor continuity for less well-defined, probably smaller, faults, as should be expected.

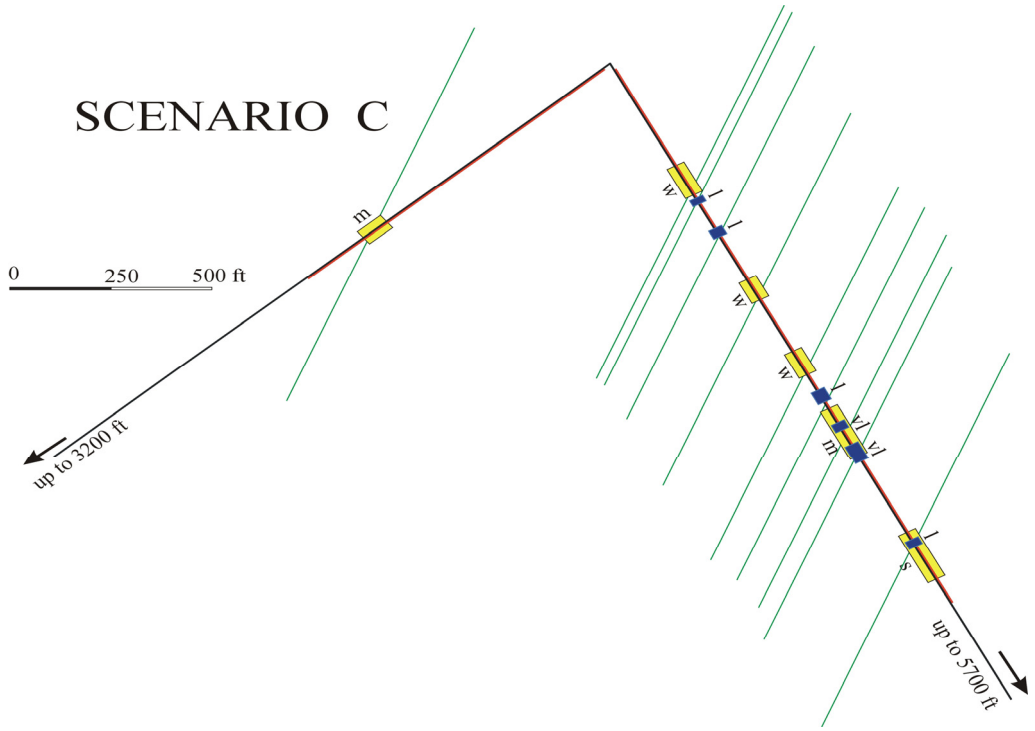

Figure 34. Scenario C. Faults oriented at 33° (NE), normal to the large fault located 2 km east. In this case faults would be oblique to both the 152°-Azimuth VSP and the 230°-Azimuth VSP, but they may not intersect both VSP directions.

Figure 35 shows again the windows seen by the VSP superimposed on the PP reflected amplitude map, but this time in the scenario C. In the figure, the fractures are orientated E-W. The concentric circles represent the angles of incidence. The dark lines represent the orientation of the two azimuths of the VSP with respect to fracture orientation corresponding to scenario C. For the 3200ft and 3500ft offset VSPs, the estimated average angle of incidence is about 15 degrees, while for the 5700 offset VSP the estimated average angle of incidence is about 30 degrees. The white circles represent the sampling of the VSP in the AVOZ (Amplitude variation with offset and Azimuth) domain. The rest of the domain is not sampled. Therefore, 3D seismic data, which provide a much better coverage, can help in differentiating between different possible geological scenarios.

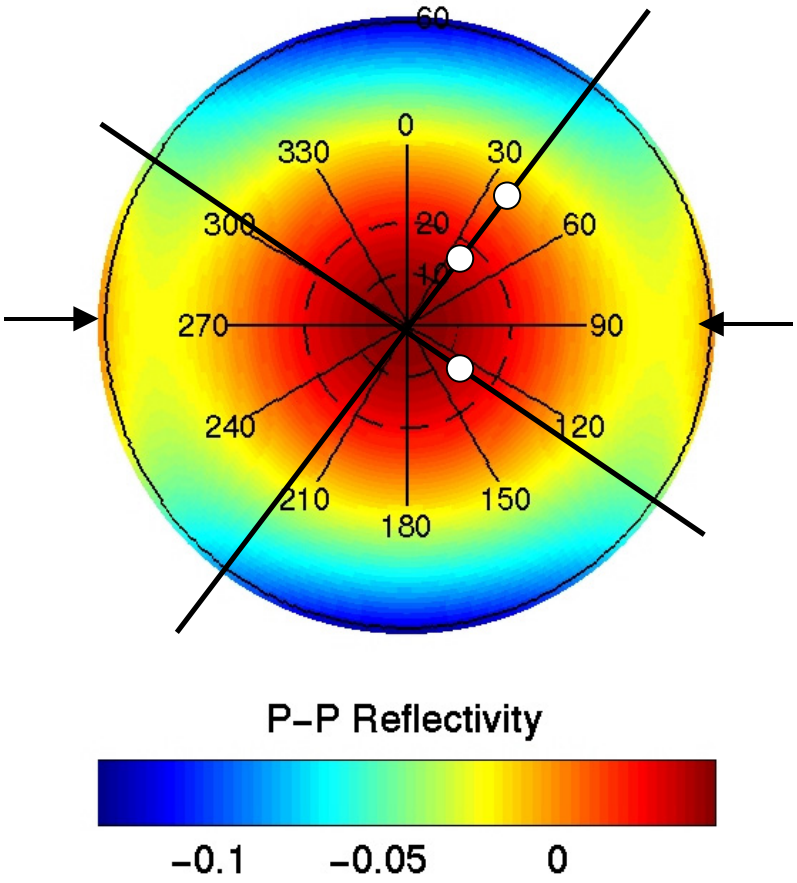

Figure 35: VSP sampling on the azimuthal variation of Rpp in the Scenario C. The small circles represent the windows seen by the Offset VSP on the azimuth 152 (3500ft, at about 15 deg angle of incidence, and 5700ft, at about 30 degrees angle of incidence), and azimuth 230 (3200 ft, at about 15 degrees angle of incidence). Fracture orientation is represented through the arrows.

Figure 36 shows the good tie between the VSP time migrated section and the corresponding seismic line extracted from the 3D seismic cube on the 152 azimuth. On this stacked migrated section we can also observe variations in amplitude on the top of James Lime. A more detailed view of the top of James Lime is presented on Figure 37.

On the bottom of the Figure 37 we interpret the faults, based on the time offsets. We notice the presence low amplitude anomalies in the hanging wall that may correspond to fractured zones.

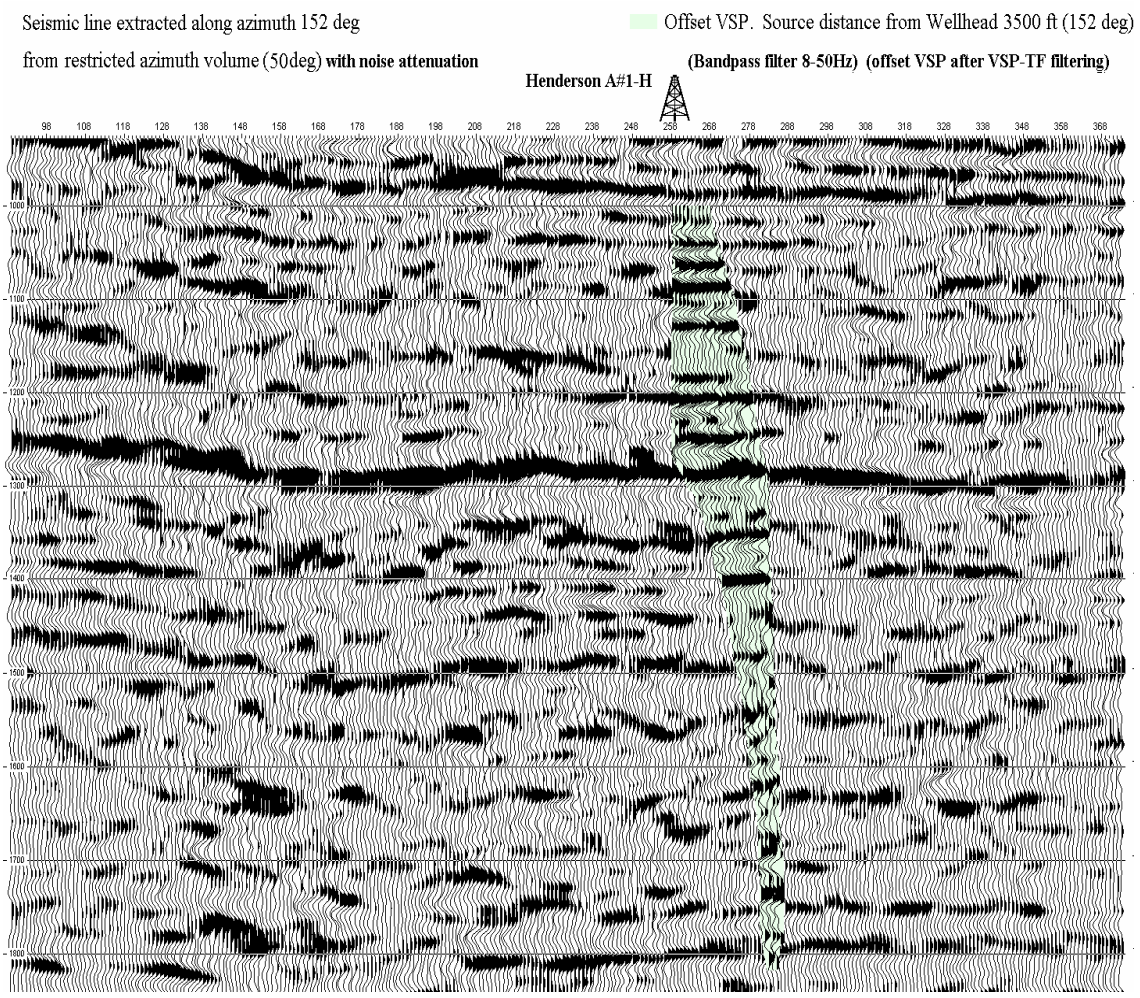

Figure 36: Tie between VSP and seismic time migrated section extracted from the 3D cube on the 152 azimuth.

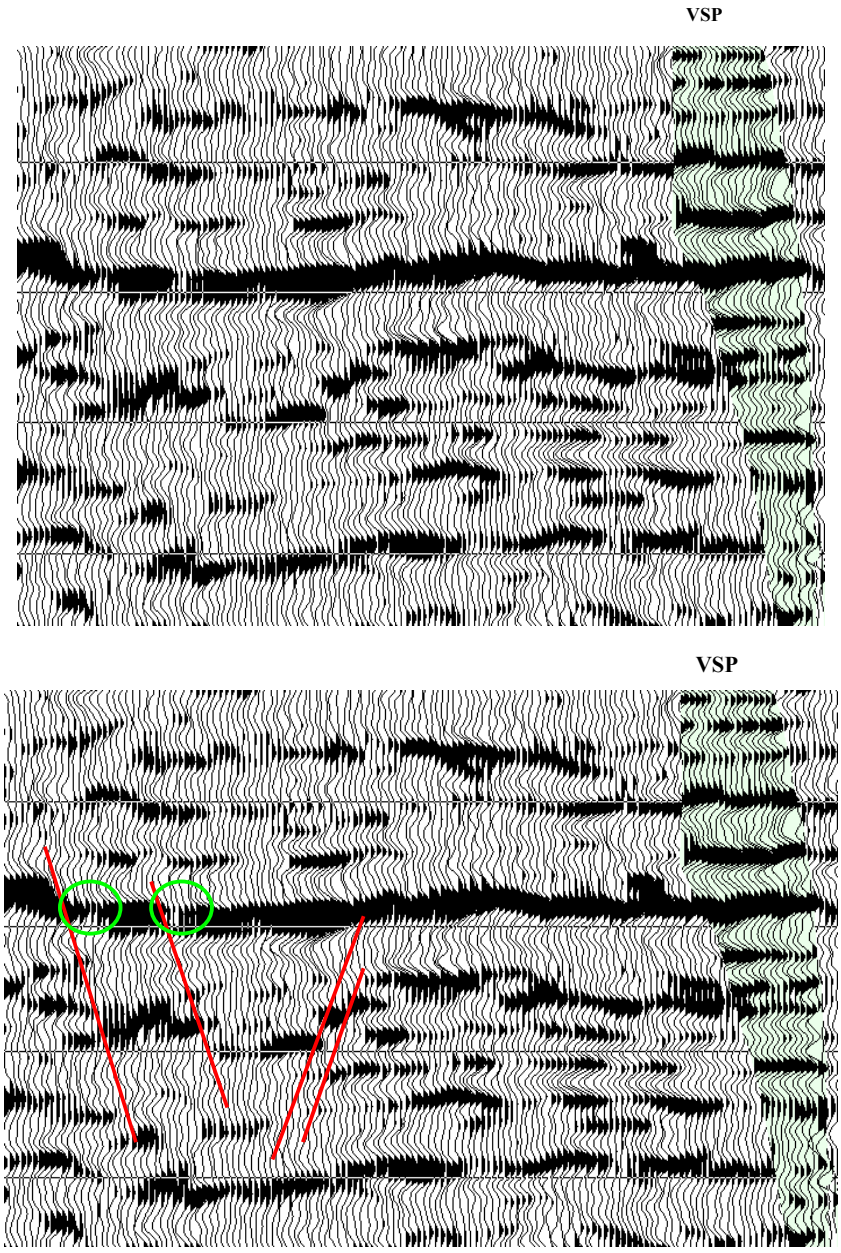

Figure 37: Seismic line extracted from the 3D seismic cube on azimuth 152. Top: without interpretation. Bottom: with interpreted faults. Near the faults we can see lowering in the amplitudes, possibly due to the fractures associated with the faults.

Figure 38 shows a semiquantitative interpretation of some of the amplitude anomalies identified on the top of James Lime from a seismic line extracted from the 3D seismic cube at azimuth 152. On the bottom of Figure 38 we present a portion of the top of James Lime from this migrated section (Figure 37), where we can notice lateral variations in Rpp amplitude associated with time offsets. The time offsets indicate presence of the faults, while the associated amplitude anomalies that occur on the

hanging walls are interpreted as signatures of fracture zones. The low amplitude anomalies are circled in red. We consider that the strongest reflections correspond to the unfractured zones (circled in blue). With this assumption we can estimate the relative decrease in the Rpp amplitude in the fractured zones, as compared with the unfractured ones. In this case the decrease in amplitude is about 60%.

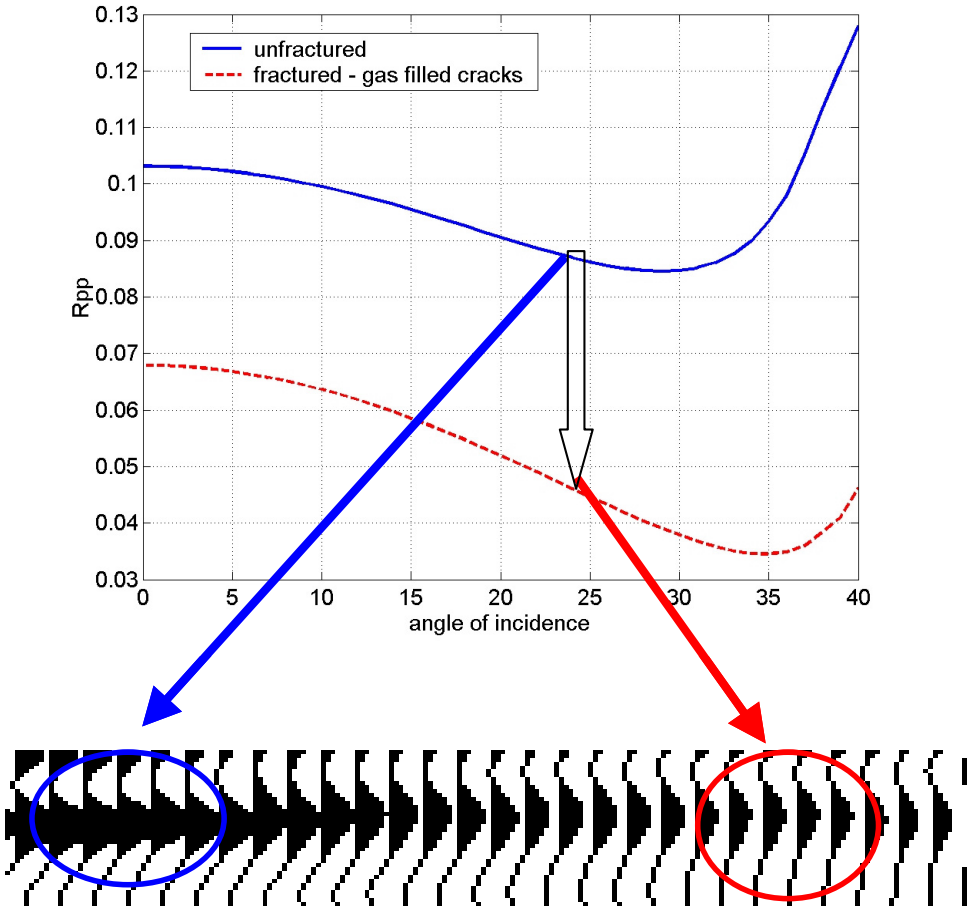

Figure 38: Semiquantitative interpretation of the Rpp amplitude anomaly on the top James Lime, 5700 Offset VSP migrated section, based on the Rock Physics fracture modeling. At this offset the angle of incidence is about 25 degrees. Blue curve represents the AVO for the unfractured reservoir, while the dashed red curve is the AVO for the fractured James Lime. From the modeling, the difference in Rpp between fractured and unfractured is approximately 45%, at 25 degrees angle of incidence. The decrease in the amplitude at the top of the James Lime from the VSP data is also about 45%, which corresponds to a fracture density of 0.04.

The AVAZ analysis of 3D seismic data indicates a dominant E-W trend in seismic anisotropy (Figure 39). Under the assumption that this anisotropy is basically induced by gas-filled fractures, this anisotropy indicates a dominant E-W fracture and fault

orientation. Even though this orientation is slightly oblique to the normal fault located to the East of Hendersson-1, still coincides with the orientation predicted from scenario A.

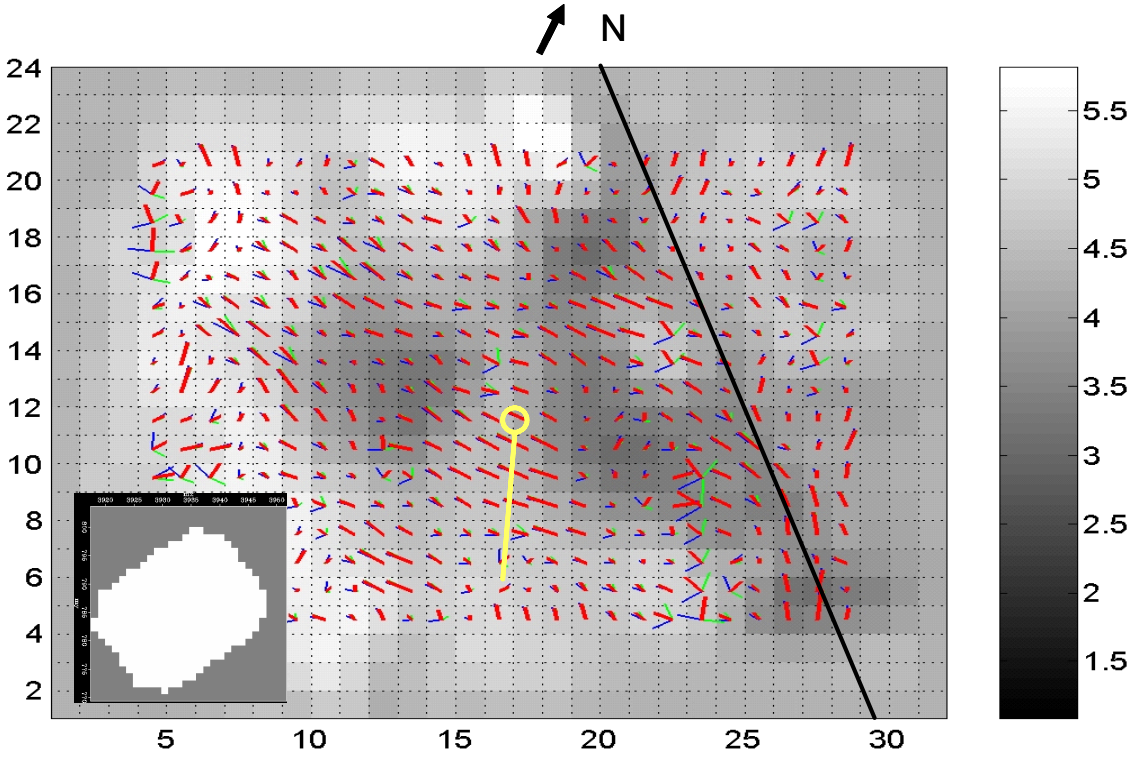

Figure 39: Amplitude anomalies and seismic anisotropy at the top of James Lime. The black line shows the location of the large normal fault, and the yellow line and spot shows the location and path of Hendersson-1.

This study shows that an accurate reservoir model requires the integration of seismic data at different scales, and diverse sources of data like geology and seismic. In this case, the VSP section allowed us to identify faults below the resolution of the 3D seismic data. The small faults interpreted from the VSP section and the LWD logs are not apparent in the 3D seismic section (Figure 38). The only indication of structural heterogeneities in this location, from the 3D seismic, is the increment in seismic anisotropy. On the other hand, the 3D seismic provides a clear picture of the spatial heterogeneity at larger scale. The variations in seismic anisotropy observed and amplitudes observed in the 3D seismic can be translated into maps of crack density, or fracture density, which could be calibrated with results from reservoir simulation.

Conclusions

Combining the seismic attribute analysis of VSP data and the geologic interpretation of LWD logs we have mapped the location of small faults along the path of Hendersson-1 well. Amplitude anomalies, enhanced using zero-offset amplitude, and small offsets visualized using instantaneous phase, coincide with fault locations interpreted from drilling breaks, changes in calcite concentration and abrupt changes in gamma ray. These two independent sources of information provide the basis for a consistent interpretation of the VSP data.

The VSP data could not constrain the orientation of faults and fractures, which has been determined from the AVAZ analysis of 3D seismic data. The results show that small fractures are sub-parallel to the large fault located East of Hendersson-1. This is the Scenario A discussed in the geologic model (ATTACHMENT A).

The small faults found along the path of Hendersson-1 are below the resolution of the 3D seismic survey, and the only indication of structural heterogeneities in the 3D seismic data is seismic anisotropy. 3D seismic provides, however, a clear picture of the spatial distribution of amplitude anomalies and seismic anisotropy, the two most important seismic attributes associated with fractures.

Attachment G

3D Seismic data: Analysis of the Azimuthal Variation of Reflectivity

Abstract

Aligned vertical fractures can produce elastic anisotropy in the shallow crust that can be observed in seismic data, such as amplitude variation with angle of incidence and azimuth (AVAZ). AVAZ can be a useful technique that can give information about the fracture orientation, fracture density, and sometimes the type of fluid in the fractures.

In this attachment, we present the analysis of the *PP* reflectivity from a 3D seismic data set acquired over a fractured carbonate reservoir in East Texas, with the final goal of determining the orientations of the fractures and the relative intensity of fracturing.

We compare the results of the rock physics fracture modeling for AVAZ, based on the well-log data, with the seismic observations. Fracture modeling shows that the polarity of the azimuthal variation of the reflectivity changes with the fluid and fracture compressibility. Therefore, rock physics modeling is a key link between the observed seismic amplitude variation with azimuth (observable parameter) and the actual fracture parameters, such as fracture strike and density. Based on the results of the rock physics modeling, we derive the mean fracture orientations from the seismic data using a bootstrap method. By using this technique, we quantify the uncertainty in fracture orientation due to the possible measurement errors.

We find a good agreement between the fracture orientation derived from the azimuthal variation of the seismic amplitudes at far offsets and the fracture orientation derived from the FMI logs from the nearby wells. There is also a good agreement between the mean fracture strikes from the azimuthal variation in the seismic amplitude

and the present regional stress field. The mean fracture strike is approximately parallel to the maximum horizontal stress in the region.

From the seismic data, we also derive the map of the azimuthal anisotropy for the *PP* reflectivity at the top of the reservoir. The degree of anisotropy represents a measure of the relative degree of fracturing, if the cracks are gas-saturated.

In this attachment, we also emphasize the impact of the acquisition footprint on the seismic amplitudes. For this 3D seismic survey the fold is not uniform and it creates artificial stripes of low and high amplitudes that vary with both offset and azimuth. This footprint can mask the actual signatures of fractures. Therefore, to interpret the variations of the reflectivity with offset and azimuth in terms of fracture distribution, we first need to suppress this footprint. In this attachment, we show how increasing the bin size of the regular grid used for analyzing the seismic data gradually diminishes the acquisition footprint. However, this comes at the expense of the spatial resolution.

Introduction

Most of the seismic field studies for fracture detection have as targets, vertical and open joints (Grimm and Lynn, 1997, Teng, 1998; Grimm et al, 1999; Perez et al, 1999; Lynn et al., 1999). A single set of vertical, parallel fractures embedded in an isotropic background can be described using a transversely isotropic model with a horizontal axis of symmetry (HTI).

Earlier research on HTI media was focused on the propagation of shear-waves, due to their sensitivity to the direction and the amount of fracturing. More recently, *P*-wave methods for fracture detection have attracted considerable interest. *P*-wave methods offer several advantages, such as decreased cost and increased data quality. Moreover, *P*-wave data are sensitive to fluids, unlike the *S*-wave data that contain information mainly about the rock frame.

One of the *P*-wave methods for fractures developed in the recent years is the Amplitude Variation with Offset (AVO). For aligned, vertical fractures the *P*-wave AVO response is azimuthally dependent. The azimuthal variations in the *P*-wave reflections have been observed in field data by different authors, such as Lynn, (1996), Mallick et al.

(1998), Teng (1998), Perez et al. (1999), Shen et al. (2002). One important advantage of this method is that it can provide localized information at the interface of interest, unlike the travel time methods, which describe the cumulative effect over larger scales. Also, if the reservoir is thin, travel time techniques are not very useful for fracture characterization, as we showed in Attachment E.

The reservoir in our study area is approximately 7000 ft deep, and has an average thickness of 200 ft. The formation is a microcrystalline fractured limestone, with matrix permeability between 0.001 and 0.1 mD (Marathon Oil Co., Internal Report). However, the presence of fractures may significantly increase the permeability. Therefore, precise localization of fractured zones has a crucial impact on reservoir management.

The area of study is situated in a normal faulting regime. The maximum horizontal stress in the region is oriented E-W. In such regime, the strike of the faults is expected to be approximately parallel to the maximum horizontal stress. A geological model based on the logs from a horizontal well suggests that the fractures are controlled by subseismic normal faults (Meeder, personal communication). These small faults can generate narrow zones with high fracture density, where the cracks are more or less randomly oriented, as in brecciated zones. Between these fracture swarms, there may be vertical joints, more uniformly distributed. The rock physics fracture modeling predicts low *PP* reflectivity values associated with the fracture swarms (Sava et al., 2002), as we present in Attachment E. These low reflectivity zones may be identified in the seismic data.

In this attachment, we present the analysis of the *PP* reflectivit*y* from a 3D seismic data set acquired over this reservoir. The focus is on the Amplitude Variation with Azimuth (AVAZ) in the hypothesis of a single set of vertical aligned fractures. AVAZ involves partial stacking the data on different ranges of azimuth. There is a tradeoff between the azimuthal resolution, which requires small ranges of azimuths, and the signal-to-noise ratio, which requires larger fold, and implicitly larger azimuth ranges. However, we can increase the fold either by considering larger azimuth bins (which diminishes the azimuthal resolution), or by considering larger spatial bins (which lowers the spatial resolution).

The acquisition footprint of the survey significantly impacts the reflectivity. The fold is not uniform and creates artificial stripes of low and high amplitudes that vary with both offset and azimuth. This footprint can mask the actual signatures of fractures. In this attachment, we investigate the influence of increasing the spatial bin size on reducing the survey footprint, such that the amplitude variations can be interpreted in terms of fracture distribution.

We also present the results of the rock physics fracture modeling for AVAZ, based on the well-log data, and we compare them with the seismic observations. The fracture modeling shows that the interpretation of the azimuthal variation of the *PP* reflectivity depends on both the compressibility of the fractures and of the fluids filling the fractures.

Based on the results of the rock physics fracture modeling, We derive the mean fracture orientations at the top of the reservoir from the azimuthal variation of the seismic amplitudes at far offsets. We use a bootstrap method that takes into account the possible measurement errors.

We also present the distribution of the azimuthal anisotropy of the *PP* reflectivity at the top of the reservoir derived from the seismic data. As the rock physics fracture modeling shows, the degree of reflectivity anisotropy may be a measure of the relative degree of fracturing, in the case of uniformly saturated fractures.

3D Seismic survey and the acquisition footprint

A 3D seismic data set was acquired over a fractured carbonate reservoir in East Texas. The source and receiver locations are presented in Figure 1. In Figure 1, as well as in all of the other figures showing the seismic data, the actual survey is rotated 34 degrees East with respect to North, for the purpose of display.

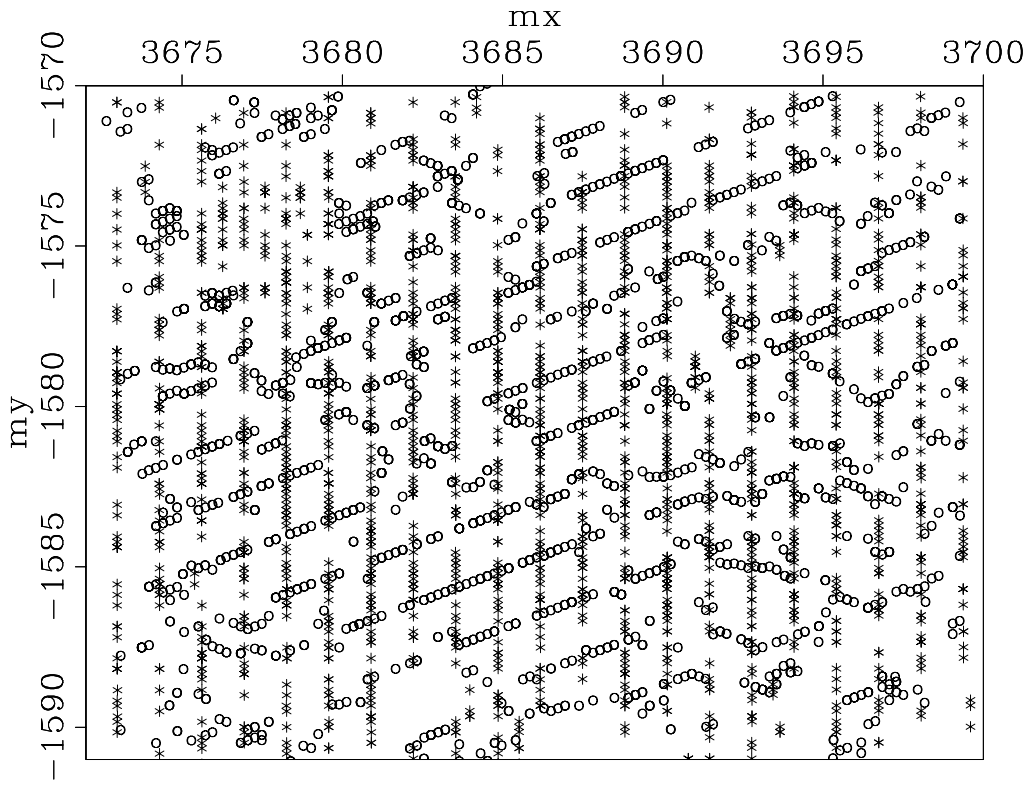

Figure 1: Map view with the source (open circles) and receiver (stars) locations. The survey is rotated 34 degrees East with respect to North.

From this acquisition geometry we can get a map of mid-point locations. Figure 2 presents a sub-sample of the mid-point positions.

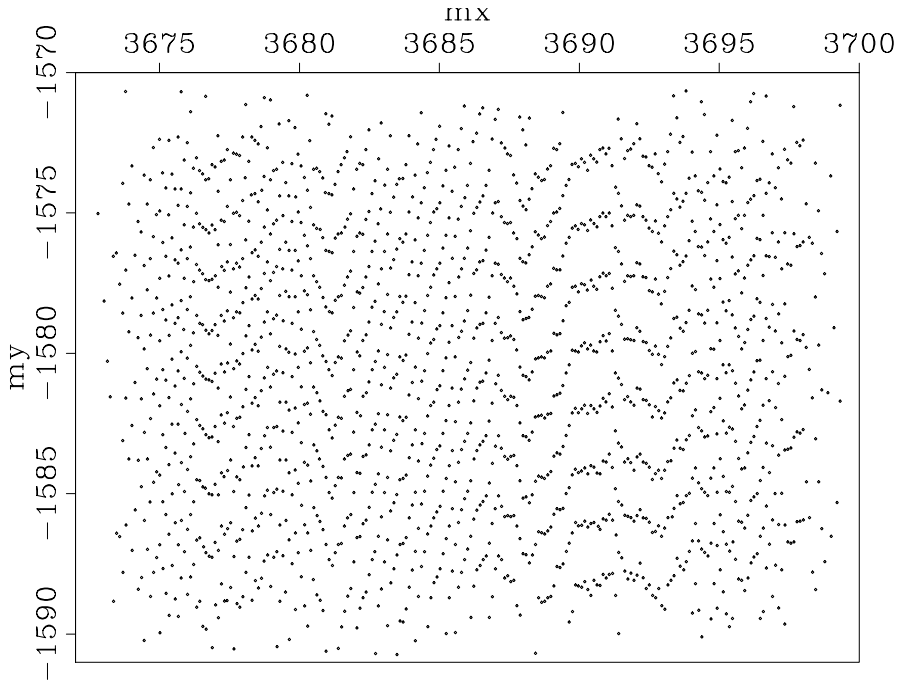

Figure 2: Map view with a sub-sample of the midpoint locations. The survey is rotated 34 degrees East with respect to North.

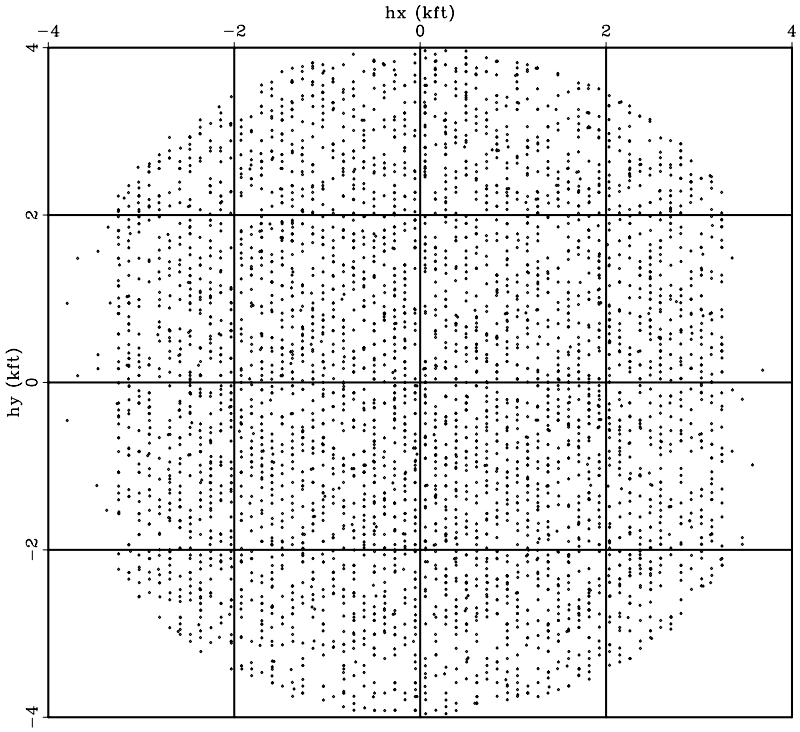

Figure 3: Scatter-plot with the x and y components of the offset vector for every 200th trace of the data set. The survey is rotated 34 degrees East with respect to North.

Figure 3 shows a scatter-plot with the x and y components of the offset vector, for every 200th trace of the data set. The plot shows a wide azimuth acquisition, with a relatively uniform distribution, displaying no obvious preferential orientation of the acquisition with respect to azimuth.

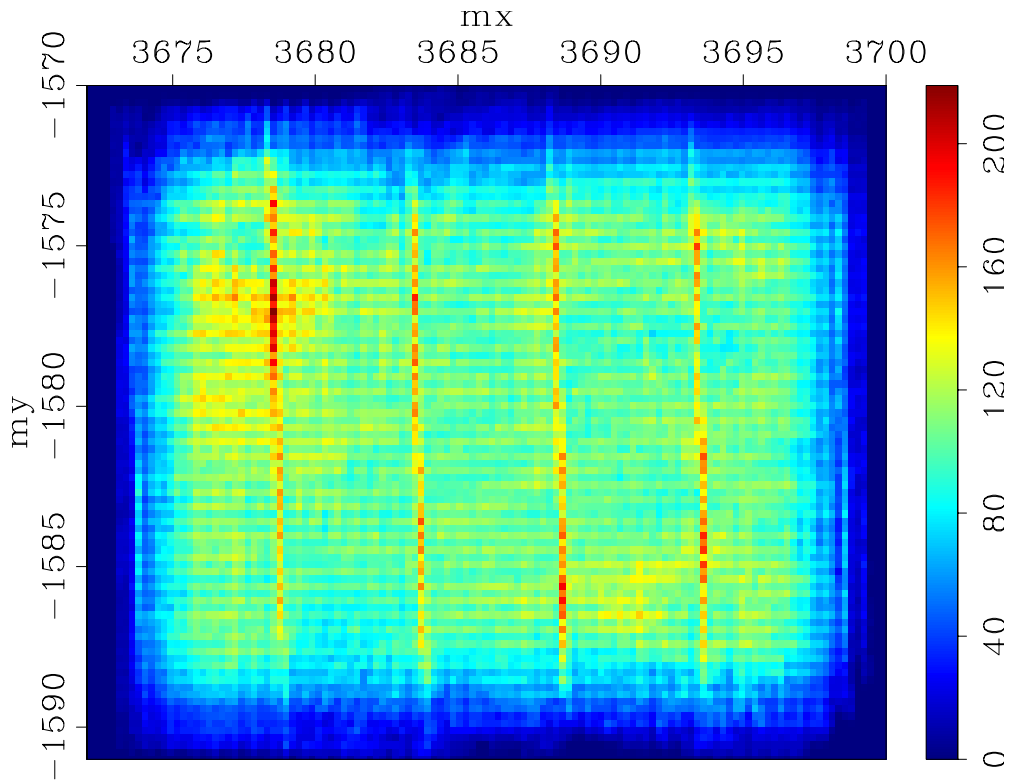

Figure 4: Map view with the fold for the stack data (**200ft bin size**).

Analysis of the reflectivity variations with offset and azimuth requires seismic data arranged on a regular grid. We first choose a small bin size equal to 200 ft. The corresponding fold map for the stack data of all azimuths and offsets is presented in Figure 4. We can see alternating parallel stripes of low and high fold along some of the receiver lines. This pattern can be misleading, especially when analyzing amplitude data.

Figures 5 and 6 show the impact of the acquisition footprint on the *PP* reflectivity maps for two different azimuth ranges of 60 degrees each, one centered about azimuth 0º, the other centered about azimuth 60º. The data are stacked for all offsets, between 0 and 8000 ft. The top panels of Figures 5 and 6 show the amplitude maps at 1.2 seconds, while on the bottom panels we present the amplitude maps at 1.3 seconds, corresponding to the top of the reservoir. The corresponding fold maps are presented on the top-right

panels in each figure, while the acquisition geometry for the survey is presented on the bottom-right panels. The left panels of both figures show the amplitude maps un-normalized by the fold, while the middle panels show the amplitude maps normalized by the fold.

By comparing Figures 5 and 6 we can see that the pattern of low and high seismic amplitude values varies with the azimuth, as the fold pattern changes. Normalizing the amplitude values by fold does not completely suppress the acquisition footprint.

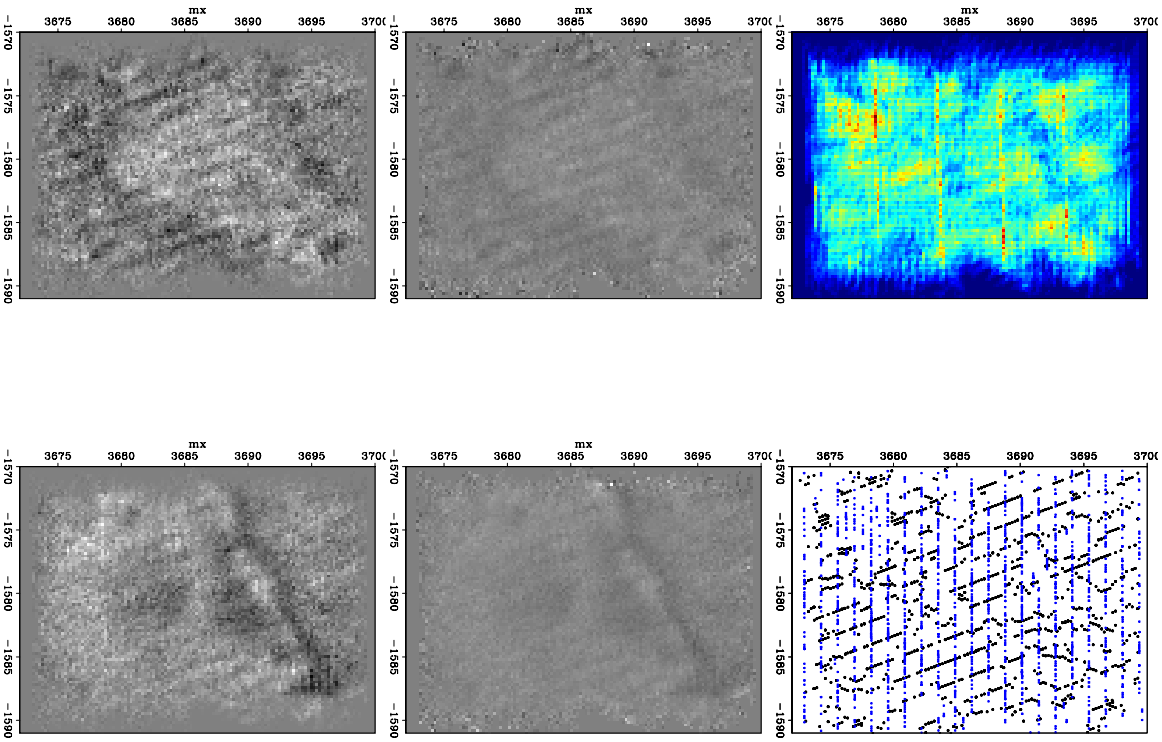

Figure 5: Amplitude maps for two time slices at 1.2 seconds (top) and 1.3 seconds (bottom) for an azimuth bin of 60 degrees, **centered about azimuth 0º**.Left panels show the un-normalized reflectivity maps. Centered panels show the corresponding reflectivity maps normalized by fold. Top right panel shows the fold map for the chosen azimuth range. Bottom right panel shows the acquisition geometry.

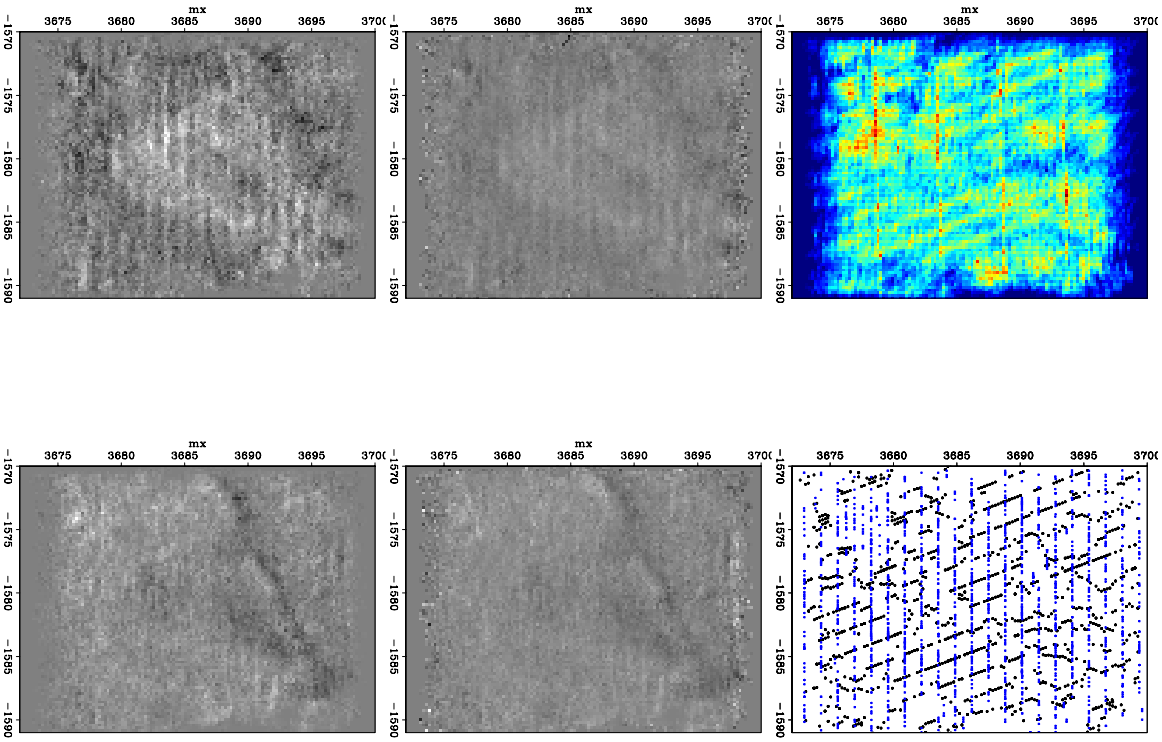

Figure 6: Amplitude maps for two time slices at 1.2 seconds (top) and 1.3 seconds (bottom) for an azimuth bin of 60 degrees, **centered about azimuth 60º**.Left panels show the un-normalized reflectivity maps. Centered panels show the corresponding reflectivity maps normalized by fold. Top right panel shows the fold map for the chosen azimuth range. Bottom right panel shows the acquisition geometry.

The structural geological model suggests the presence of fracture swarms in the proximity of the normal subseismic faults (Meeder, personal communication). Rock physics modeling shows decreased amplitudes associated with the gas-filled fractured zones in the reservoir (Sava et al, 2002). Therefore, we should expect to observe low *PP* reflectivity values on the 3D seismic data set, aligned with the possible subseismic faults. However, the acquisition footprint artificially creates alternating alignments of high and low amplitudes due to the alternating high and low folds along the sources and receiver lines (Figures 5 and 6). Therefore, to interpret the variations in reflectivity with offset and azimuth in terms of fracture distribution, we first need to eliminate this footprint.

To reduce the acquisition footprint, we choose to keep the azimuthal bins constant and change the spatial bin sizes. The next section shows how increasing the bin size reduces the acquisition footprint of the survey.

3D Seismic data processing for reflectivity analysis

In this section, we present the main processing steps of the 3D seismic data. The goal is to eliminate the survey footprint, such that the amplitude variations with offset and azimuth may be interpreted in terms of fracture orientation and relative degree of fracturing.

The data had refraction statics applied, and they were NMO corrected by Marathon Oil. Co. We initially binned the data into small bins of 200 ft size, as presented in the figures from the preceding section.

For a reliable azimuthal analysis of the *PP* reflectivity, we partially stack the data on relatively small azimuthal ranges of 20 degrees. In the ideal case of full coverage for all azimuth ranges, we get nine reflectivity values at each spatial bin location, corresponding to the 9 different azimuthal ranges. However, for small bin sizes, the azimuthal coverage is very low. We can increase the fold at each grid location by increasing the spatial bin size, while keeping the azimuthal ranges constant. There is a tradeoff between the spatial resolution, which requires small bin sizes, and the signal-to-noise ratio, which requires larger bin sizes. Ideally, we want to obtain the smallest grid size for which we get a more uniform distribution of the fold over the survey for each azimuthal range, and also a larger signal-to-noise ratio at each bin location.

Alternatively, for a fixed bin size we can increase the fold by increasing the azimuthal range. For 60º azimuthal bins, we expect a larger fold and consequently a larger signal to noise ratio than for smaller azimuthal bins of 20º. However, in this case we considerably diminish the resolution in the azimuthal variation of the *PP* reflectivity, and implicitly we reduce from our ability to determine accurately the fracture orientations.

Figure 7 shows a conceptual sketch of the competing effects between the spatial and azimuthal resolutions, and the fold. The curves represent schematic lines of constant fold, and emphasize the fact that we can obtain approximately the same fold by either increasing the spatial bin size and decreasing the azimuthal range (consequently decreasing the spatial resolution, while increasing the azimuthal resolution), or alternatively, by increasing the azimuthal range and decreasing the spatial bin size

(consequently decreasing the azimuthal resolution, while increasing the spatial resolution). The fold increases with both azimuthal range and spatial bin size.

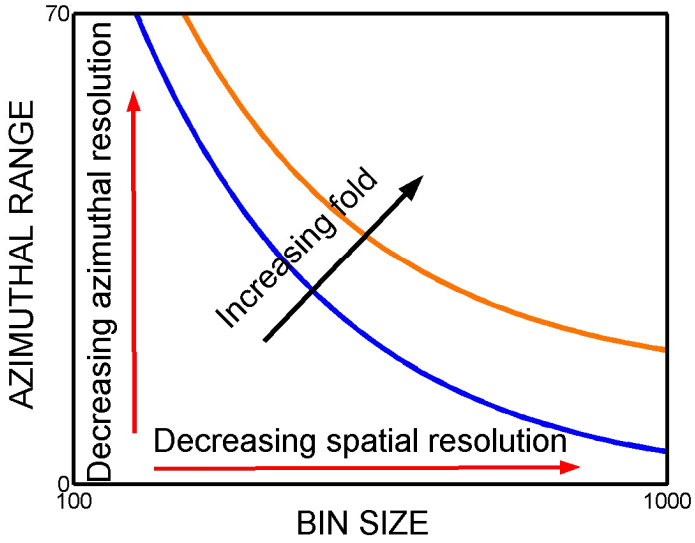

Figure 7: Conceptual variation of the fold with the azimuthal bin size and the spatial bin size. We can keep the fold approximately constant either by increasing the bin size and decreasing the azimuthal range (consequently decreasing the spatial resolution, while increasing the azimuthal resolution), or by decreasing the bin size and increasing the azimuth range (consequently increasing the spatial resolution, while decreasing the azimuthal resolution). The fold increases with both azimuthal and spatial bin sizes.

In this section, we present the analysis of the fold, and the corresponding amplitude maps, with increasing spatial bin sizes, at fixed azimuthal range. The goal is to determine the optimal grid dimension for which the acquisition pattern is significantly reduced.

At fixed spatial bin size, the fold varies with azimuth, as well as offset. For each of the spatial bin sizes considered, we partially stack the data for the near-offsets (0 –3000 ft) and for the far-offsets (4000-8000 ft). For each of the near- and far-offset stacks, we additionally sort the data and partially stack them on 9 different azimuth ranges of 20 degrees each.

Figure 8 shows the seismic amplitudes and the corresponding fold maps for the far-offset stack (top panels), and for the near-offset stack (bottom panels), at a time slice corresponding to the top of the reservoir. The size of the spatial bins is 200 ft. The azimuthal range is 20 degrees, centered about azimuth 20º. The left panels present the un-normalized amplitude maps, while the middle panels present the amplitude maps

normalized by the fold. We can observe a strong acquisition pattern on both near- and far-offset stacks for this azimuthal range.

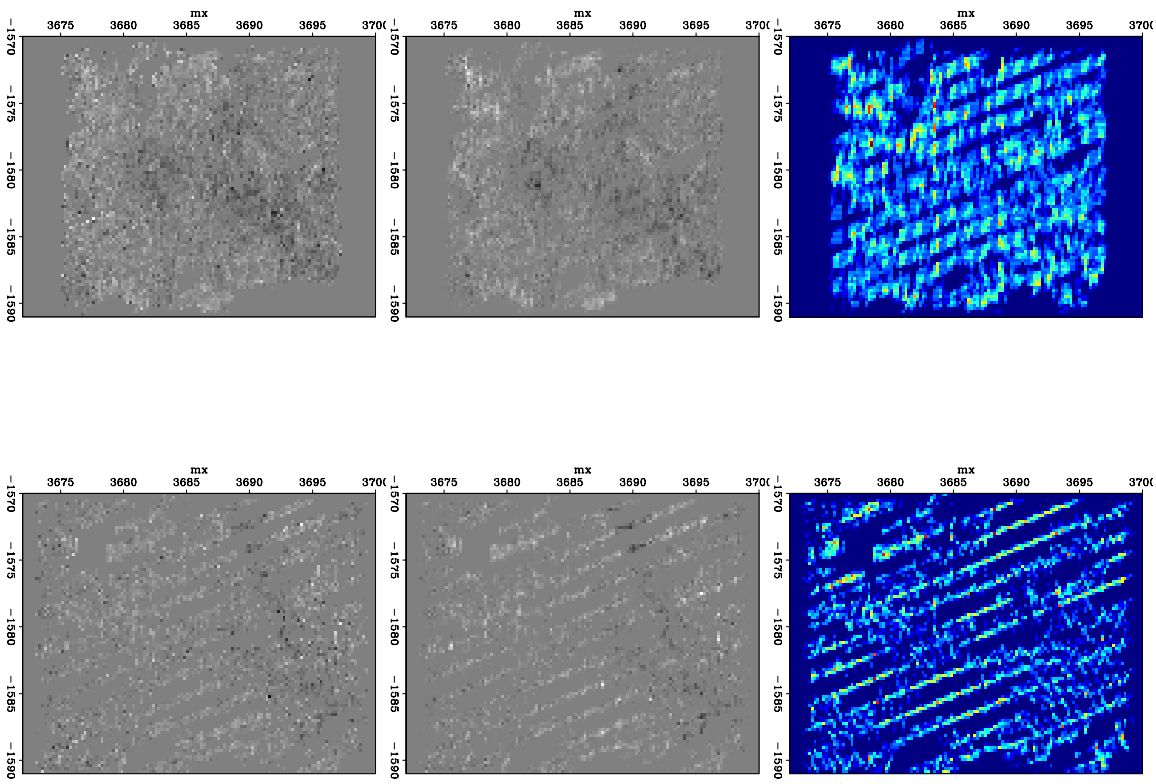

Figure 8: **200 ft bin size**. Amplitude maps for a time slice at 1.3 seconds for the far -offset stacks (top panels) and the near-offset stacks (bottom panels) with their corresponding fold maps (right panels). Left panels: amplitudes un-normalized by fold. Middle panels: amplitudes normalized by fold. Azimuth centered about 20º.

Figure 9 is similar with Figure 8, but corresponds to another azimuth range, centered at azimuth 80º. Comparing Figures 8 and 9, we can see that the fold maps change with the azimuth for both far and near offsets, as expected. The seismic amplitude maps also change with the azimuth.

For a small bin size of 200 ft, the azimuthal coverage is very low. For the specified ranges of azimuth and offsets, there are numerous bins that do not have any data. Furthermore, even for the bins that have data, the fold is very small, and therefore the signal-to-noise ratio is not satisfactory to confidently interpret any seismic amplitude variations.

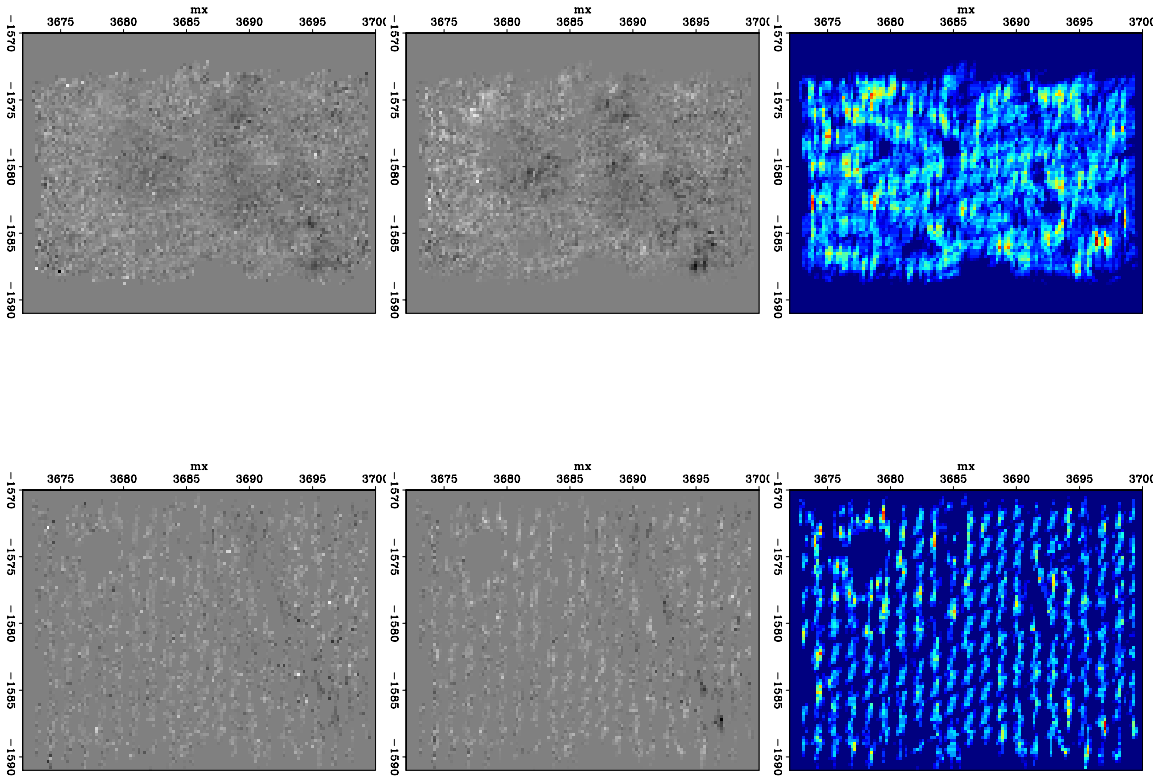

Figure 9: **200 ft bin size**. Amplitude maps for a time slice at 1.3 seconds for the far - offset stacks (top panels) and the near-offset stacks (bottom panels) with their corresponding fold maps (right panels). Left panels: amplitude un-normalized by fold. Middle panels: amplitude normalized by fold. Azimuth centered about 80º.

Next, we double the grid size, and repeat the analysis of the fold for the same ranges of azimuths and offsets. Figure 10 shows the fold map for all of the azimuths and offsets taken together, using bins of 400 ft. The acquisition footprint is not yet eliminated, although the fold increases, as compared to the case of 200 ft bin size (Figure 4).

However, from Figure 11 we can see that, for a grid size of 400 ft, the azimuthal coverage is still low. There are many bins that do not have any data for the specified ranges of azimuths and offsets. The acquisition footprint is still visible on the fold maps for the near- and far-offset stacks, corresponding to the range of azimuth centered about 80º.

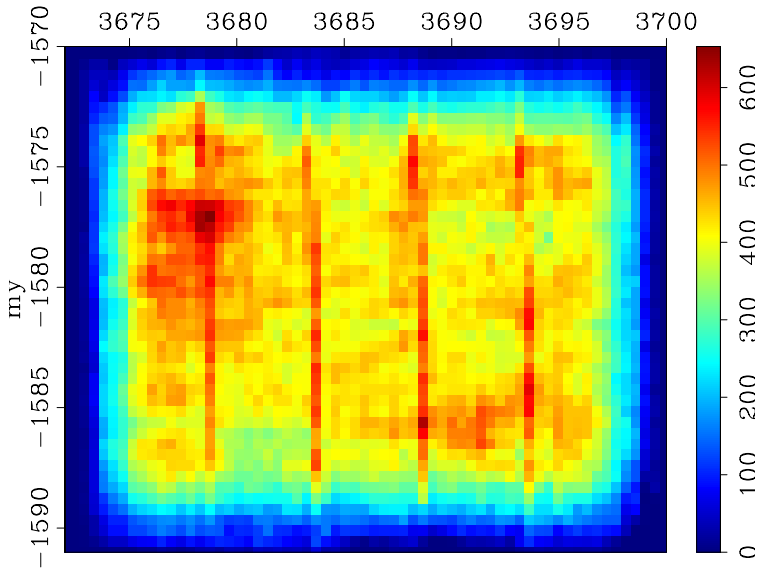

Figure 10: Map view with the fold for the stack data (**400 ft bin size**).

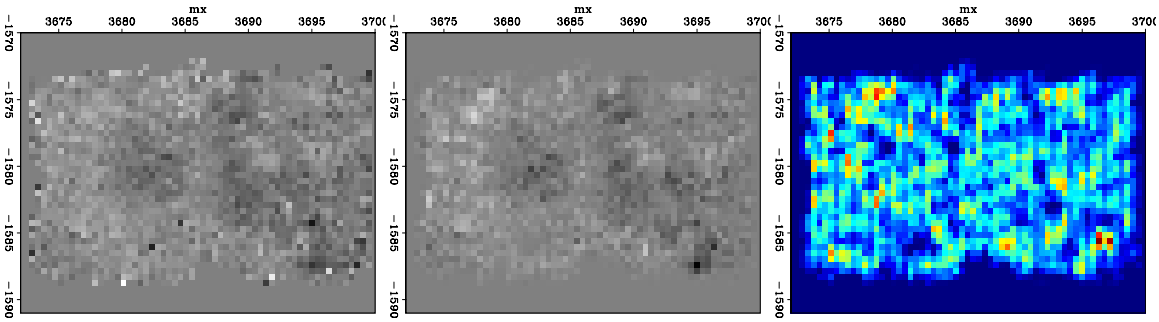

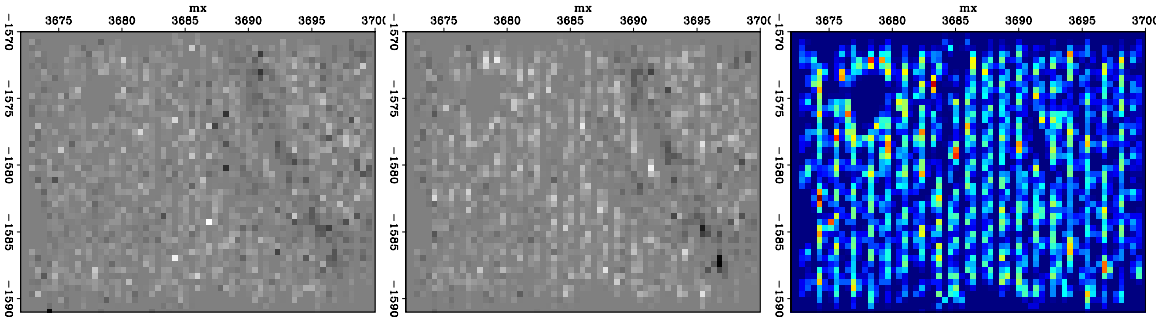

Figure 11: **400 ft bin size**. Amplitude maps for a time slice at 1.3 seconds for the far - offset stacks (top panels) and the near-offset stacks (bottom panels) with their corresponding fold maps (right panels). Left panels: amplitude un-normalized by fold. Middle panels: amplitude normalized by fold. Azimuth centered about 80º.

Figure 12 shows the fold map corresponding to superbins of 800 ft, for all offsets and azimuths. We can still observe the acquisition footprint at this large superbin size. However, as Figure 13 shows, the fold map for the far-offset stack corresponding to an azimuthal range of 20 degrees, centered about 80º, becomes more uniform than those corresponding to the smaller bin sizes. Therefore, we determine that, for a reliable azimuthal analysis of the reflectivity from this 3D seismic survey, the superbin size should be at least 800 ft, to get a satisfactory fold for the specified offset and azimuths ranges, for most of the grid points.

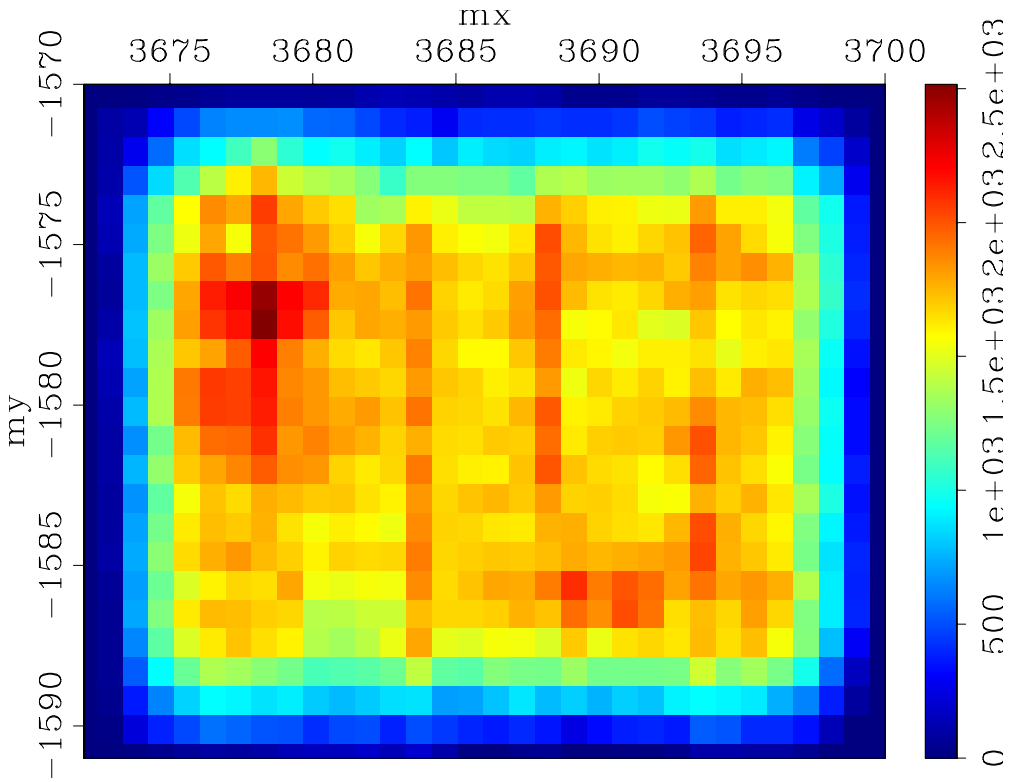

Figure 12: Map view with the fold for the stack data (**800 ft bin size**).

For completeness, we also consider superbins of 1600 ft. The corresponding fold map for all azimuths and offsets is presented in Figure 14. The fold map shows a much more uniform distribution over the survey. The acquisition footprint is eliminated at this superbin size. However, by using bins of 1600 ft size, we lose significantly on the spatial resolution.

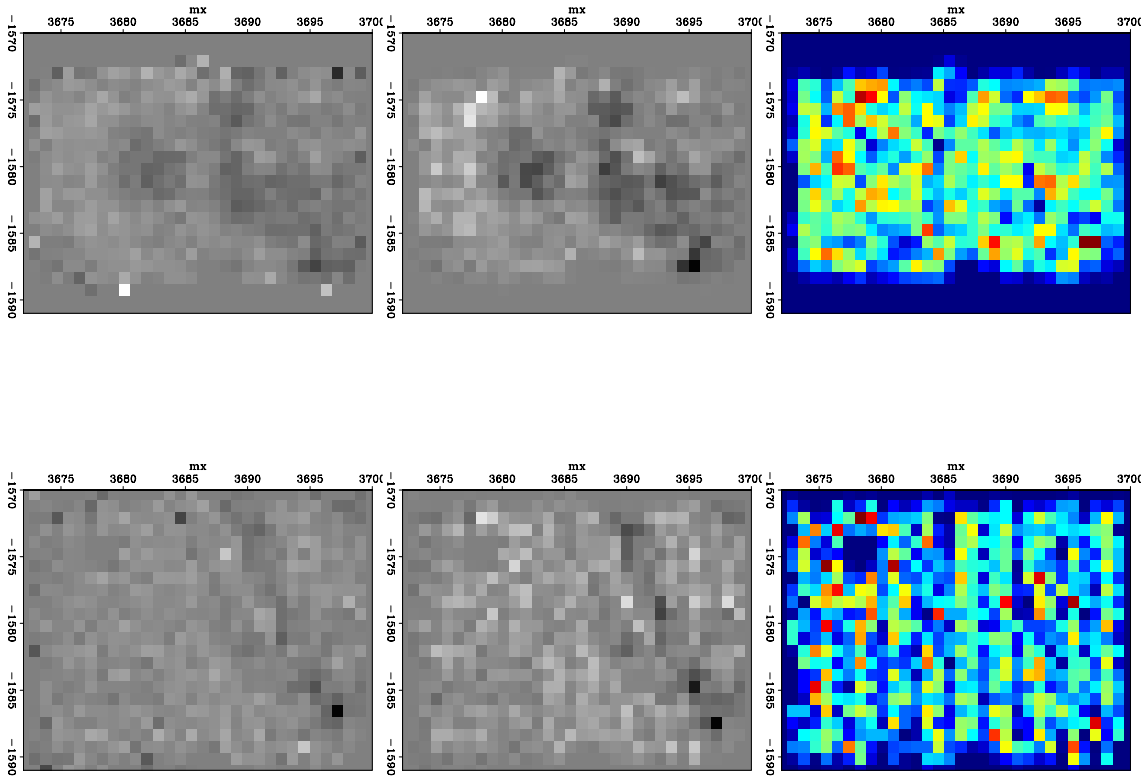

Figure 13: **800 ft bin size**. Amplitude maps for a time slice at 1.3 seconds for the far-offset stacks (top panels) and the near-offset stacks (bottom panels) with their corresponding fold maps (right panels). Left panels: amplitude un-normalized by fold. Middle panels: amplitude normalized by fold. Azimuth centered about 80º.

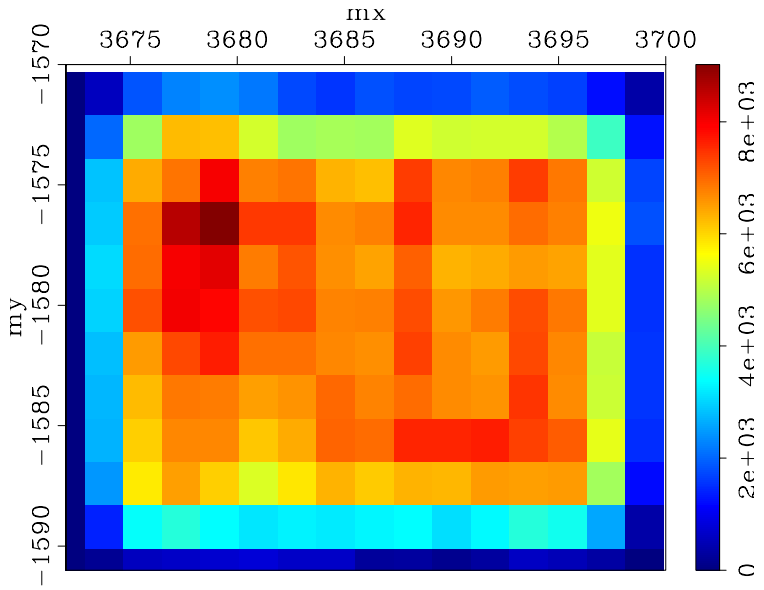

Figure 14: Map view with the fold for the stack data (**1600 ft bin sizes**).

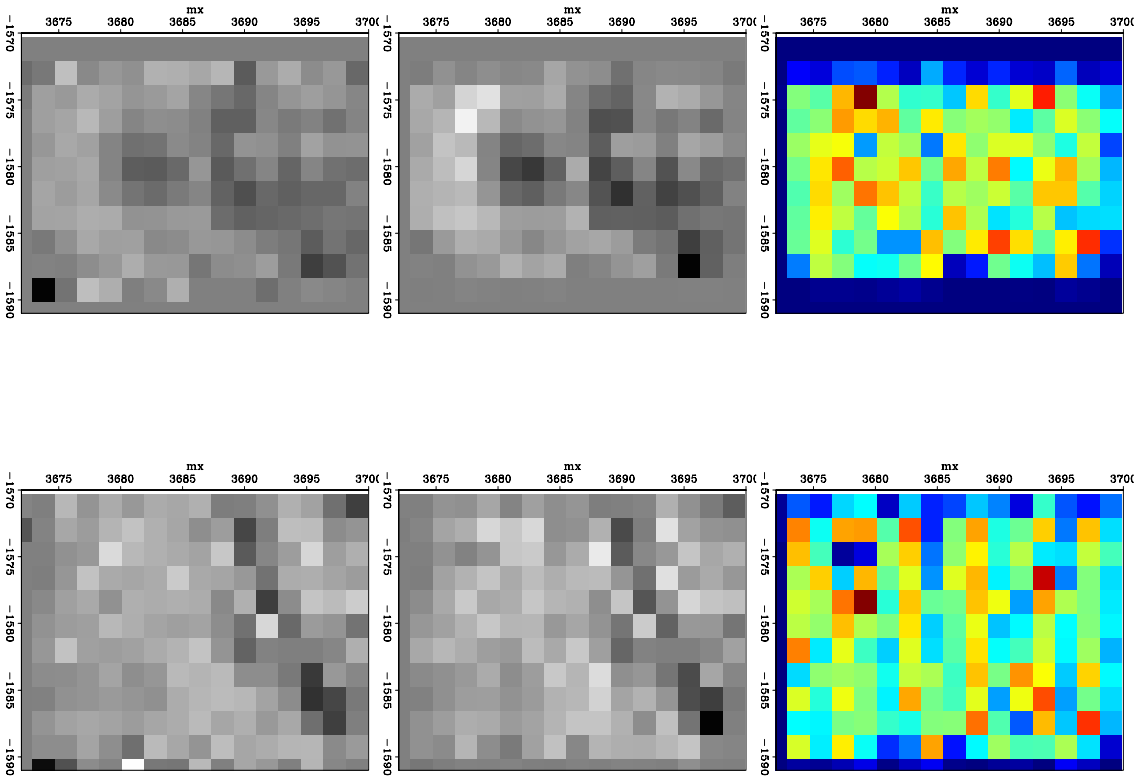

Figure 15: **1600 ft bin size**. Amplitude maps for a time slice at 1.3 seconds for the far -offset stacks (top panels) and the near-offset stacks (bottom panels) with their corresponding fold maps (right panels). Left panels: amplitude un-normalized by fold. Middle panels: amplitude normalized by fold. Azimuth centered about 80º.

Figure 16 shows the amplitude maps at the top of the reservoir for the far-offset stack, summed over all of the azimuths, for each of the bin sizes considered. We observe the significant loss in spatial resolution due to increasing spatial bin size.

In conclusion, by increasing the spatial bin size, we reduce the influence of the acquisition footprint, and we also increase the signal-to-noise ratio, by increasing the fold at each superbin. However, the spatial resolution is diminished, as we can see in Figure 16, and therefore the ability to precisely localize possible fracture swarms is also reduced.

From the analysis presented in this section, we consider that for this 3D seismic survey, the superbin size should be at least 800 ft at 20º azimuthal ranges to make a reliable interpretation of the *PP* reflectivity variation with offset and azimuth.

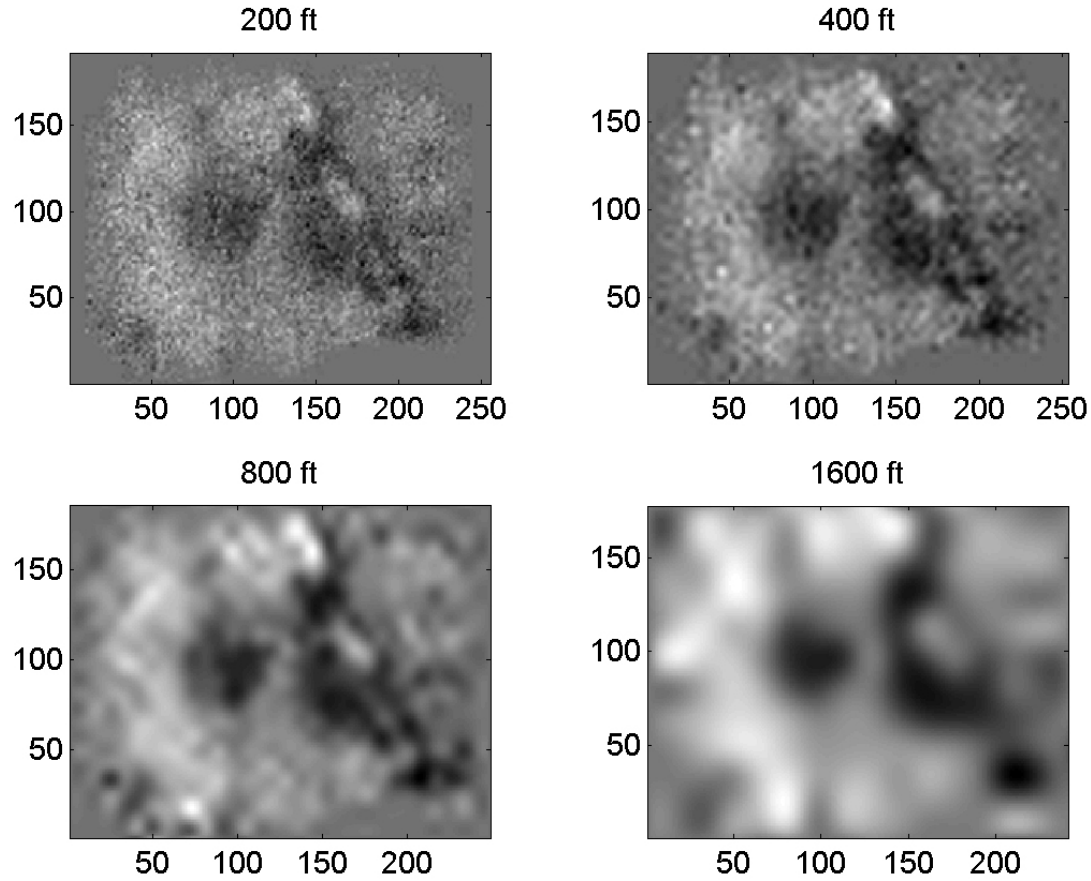

Figure 16: Interpolated amplitude maps for the far-offset stack and all azimuths corresponding to the four different spatial bin sizes considered. Top left panel: 200 ft. Top right panel: 400 ft. Bottom left panel: 800 ft. Bottom right panel: 1600 ft. We can see how the increasing bin size reduces the spatial resolution.

Bootstrap analysis of the PP reflectivity variation with azimuth

In this section, we present the method we use to analyze the *PP* reflectivity variation with azimuth for fracture characterization.

As previously discussed, the smallest superbin size we should use for the seismic amplitude analysis is 800 ft, when we consider azimuthal bins of 20 degrees.

Figure 17 presents the seismic amplitude values at the top of the reservoir as a function of azimuth, for both the far- and the near-offset stacks, corresponding to two randomly chosen superbin locations, each of 800 ft size. The top panel of Figure 17 shows very little azimuthal variation for both near- and far-offset stacks.

However, the azimuthal variation may be significant at other location, as we can observe on the bottom panel of Figure 17. As expected, the azimuthal variation of the seismic amplitudes is stronger for the far-offset stack than for the near-offset stack, as predicted by fracture modeling (Sava et al, 2002), as we also show in Attachment E

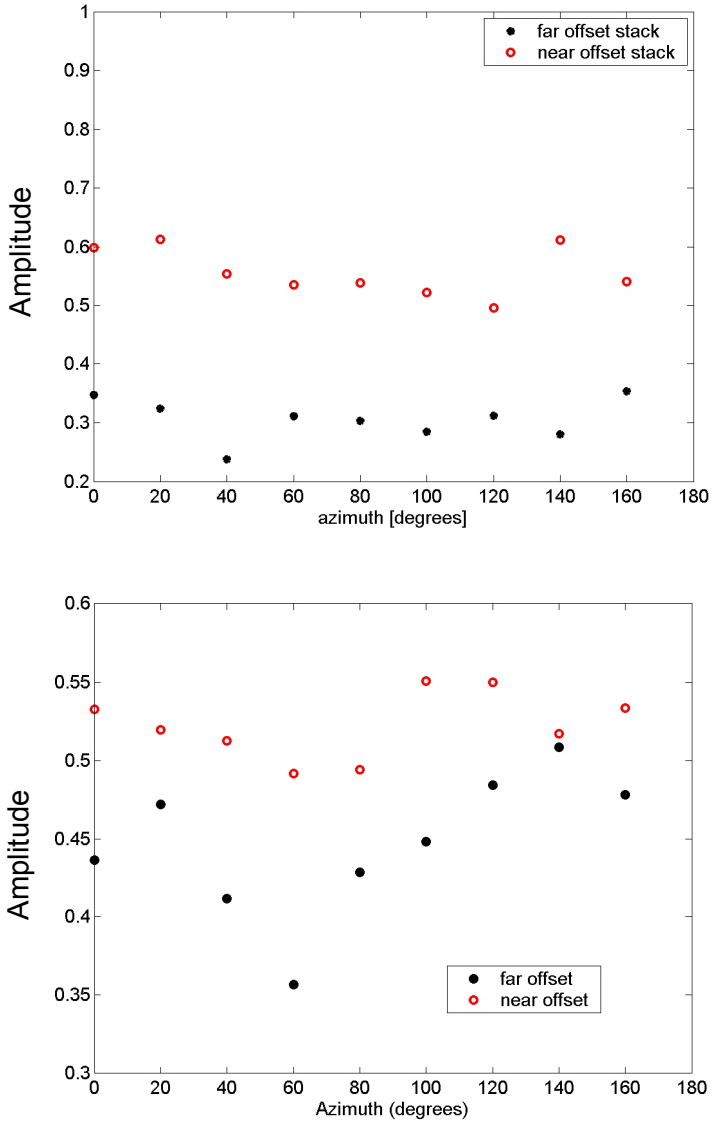

Figure 17: Amplitude for the far- and near-offset stacks as a function of azimuth at two different superbin locations.

For a fixed angle of incidence, the azimuthal variation of the relfectivity due to the presence of a single set of aligned fractures can be approximated by a cosine function (Teng, 1998). The parameters of this cosine function are its mean value, the amplitude of

the oscillation, and the phase. The mean value of the cosine function is influenced by the degree of fracturing, and the fluid type in the fractures. The amplitude of the cosine function is commonly interpreted as a measure of the fracture density, while the phase of the cosine function gives information about the fracture orientation.

To determine the parameters of the least-squares cosine fit to the observed azimuthal variation at each superbin, we use a bootstrap method (Efron and Tibshirani, 1998; Teng, 1998). The idea is that the measurements for the 9 different azimuthal ranges of 20 degrees can be treated as 9 random samples out of an infinite number of measurements we could have made. The errors in the reflectivity values are considered to be Gaussian. Therefore, each data value belongs to a normal distribution with the mean equal to the measured value, and the standard deviation evaluated as a percentage of the mean amplitude at the top of the reservoir, to represent the measurement uncertainty. Then, we draw a value independently from each of the 9 individual normal distributions. These 9 different values, corresponding to the 9 different azimuthal ranges of 20 degrees each, represent one realization. Next, we fit a cosine curve to these 9 values using the least-square method. This cosine curve represents one bootstrap realization for estimating the true model. We repeat the procedure many times and obtain hundreds of cosine functions that would fit the observations affected by errors. Therefore, from this large number of realizations we can derive the corresponding distributions for the cosine parameters, which represent a measure of uncertainty due to measurement errors. Figure 18 presents 100 realizations for the least-square cosine fits to the data corresponding to the far-offset stack presented at the bottom of the Figure 17.

However, the interpretation of the fracture parameters based on the cosine fitting alone is not enough. Rock physics modeling shows that the azimuthal variation of amplitudes depends strongly on the model we consider. Therefore, rock physics fracture modeling is the crucial link between the observed seismic data and the actual parameters of fractures.

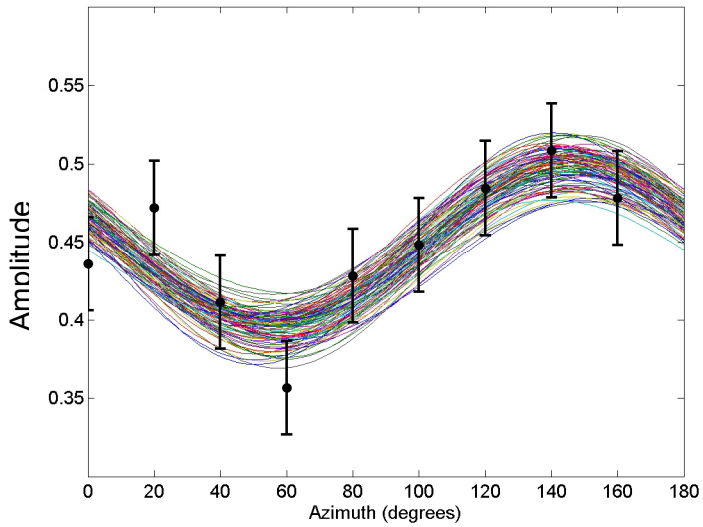

Figure 18: Amplitude variation with azimuth at a fixed superbin, and the 100 cosine fits obtained using a bootstrap method, taking into account the measurement errors represented by the error bars.

In the next section we present the results of the rock physics fracture modeling for the *PP* reflectivity variation with azimuth for the James Limestone reservoir.

Rock physics fracture modeling of the PP reflectivity

In this section, we present the results of the *PP* reflectivity modeling, based on the well-log data from a nearby field. More details and results are given in Attachment E. The carbonate reservoir is modeled with a single set of vertical fractures. The cap rock, represented by a shaly formation, is considered unfractured. The seismic properties (V_P, V_S, and *density*) for the cap rocks and the reservoir rocks are derived from the well-log data, by upscaling, as we describe in more detail in the Attachment E.

For an HTI medium generated by a single set of vertical fractures, the amplitude variation with angle of incidence and azimuth (AVAZ) can help in determining the fracture's strike. AVAZ can also give information about the degree of fracturing and the type of fluid in the fractures.

In this analysis, we use Hudson's (1981) penny-shaped crack model to derive the elastic properties of the fractured reservoir. Then we use the approximation by Vavrycuk

and Psencik (1998) to calculate the *PP* reflectivity variation with angle of incidence and azimuth at the interface between the reservoir, modeled with a vertical set of fractures, and the cap rock, represented by a shaly formation.

Figures 19 and 20 show the mean values of the *PP* reflectivity from the top of the reservoir, as a function of the incidence angle and azimuth, for the gas- and brine-filled fractures, respectively (Sava et al, 2002). In both cases the matrix porosity is brine saturated.

As expected, the azimuthal variation of the *PP* reflectivity (R_{PP}) increases with angle of incidence, for both brine-filled and gas-filled fractures. From the bottom panel of Figure 17, we observe that the *PP* reflectivity derived from the 3D seismic survey at this randomly chosen spatial bin shows qualitatively the same result as the one predicted by the rock physics fracture modeling. The modeling results are displayed on the whole 360º range for the azimuth (Figures 19 and 20, right panels), while the seismic derived amplitudes are displayed on a 180º range, due to symmetry considerations.

The modeling shows that there is a change in the polarity of the azimuthal variation of the *PP* reflectivity (R_{PP}) between 100% brine-filled fractures and 100% gas-filled fractures, as we also presented in Attachment E. For the brine-filled fractures, the maximum R_{PP} value at a fixed angle of incidence is in the direction perpendicular to fractures, while for the fractures saturated with gas the maximum R_{PP} value is in the direction parallel to fractures. This result can be used to differentiate between gas-filled and brine-filled fractures, assuming that the azimuthal anisotropy is due only to the presence of a vertical set of joints. On the other hand, this fact introduces an additional ambiguity, when considering only the azimuthal variation of the amplitude. If we do not have information about the fluid type we cannot say, for example, if the fractures are oriented E-W or N-S, based on the azimuthal variation of the seismic amplitudes alone.

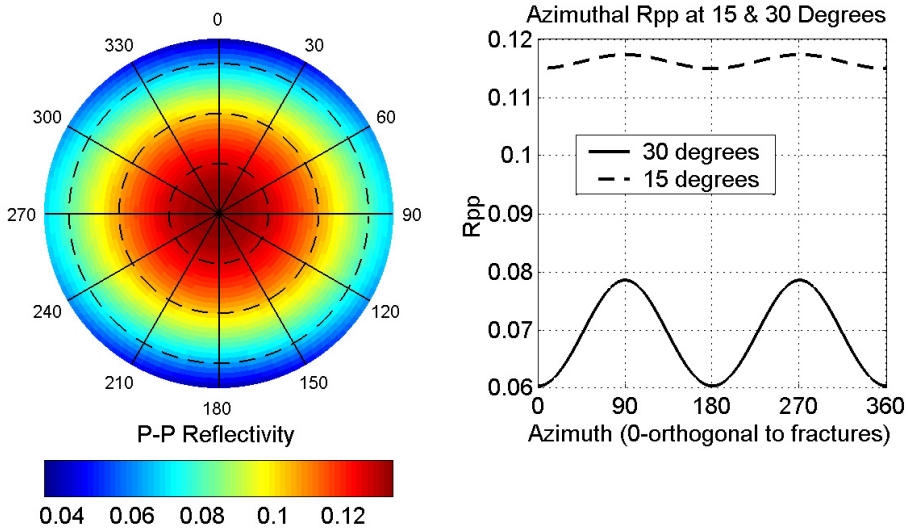

Figure 19: Expected values for the *PP* reflectivity as a function of angle of incidence and azimuth. The right side panel presents the R_{PP} amplitude variation with azimuth at 15º and 30º angles of incidence. Azimuth 0º is perpendicular to the fracture plane. Fractures are oriented E-W. Matrix porosity is brine saturated, while the fractures are 100% filled with **gas**. Aspect ratio of the fractures is 0.01.

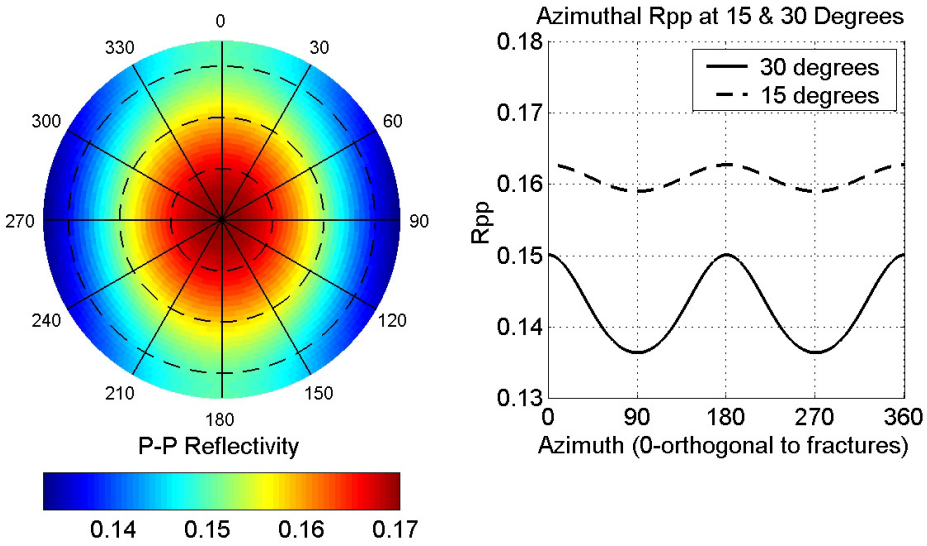

Figure 20: Expected values for the *PP* reflectivity as a function of angle of incidence and azimuth. The right side panel presents the R_{PP} amplitude variation with azimuth at 15º and 30º angle of incidence. Azimuth 0º is perpendicular to the fracture plane. Fractures are oriented E-W. Matrix porosity is brine saturated, while the fractures are filled with **brine**. Aspect ratio of the fractures is 0.01.

In practical situations the fractures may be partially saturated with gas. We investigate the azimuthal variation of the *PP* reflectivity with gas saturation. To determine the bulk modulus for the mixture of fluids, we consider both the fine-scale mixing of brine and gas, by using Reuss (1929) average, and also the patchy saturation, approximated by the Voigt average. We expect the patchy saturation to be more relevant for field studies, since the gas tends to segregate gravitationally from the brine.

Figure 21 presents the reflectivity variation with azimuth, at fixed angle of incidence, equal to 30º, for different gas saturations. The fracture density as defined in Hudson's model is 0.1, while the aspect ratio of the ellipsoidal cracks is 0.01. The different curves correspond to different gas-saturation levels (from 100% to 0%). The left panel corresponds to the fine-scale mixing of the gas and the brine, while the right panel corresponds to the large-scale mixing of the two fluids (patchy saturation). Azimuth 0º corresponds to the direction orthogonal to fractures. In the direction parallel to fractures (azimuth 90º), the *PP* reflectivity does not change significantly with the fluid type, as expected.

However, in the direction orthogonal to fractures, the *PP* reflectivity varies significantly. Also, the polarity of the azimuthal variation changes with gas saturation. The type of fluid-mixing law has also a significant influence on the amplitude variation. In the case of patchy saturation (right panel), the azimuthal polarity changes at a brine saturation of only 20%. Therefore, for fractures saturated 80% with gas and 20% with brine in a patchy manner, the polarity of the azimuthal variation becomes identical to that of the 100% brine saturated fractures. Also, we observe that in this example, for a gas saturation of 90%, the azimuthal variation is very small. Therefore, the modeling suggests that for some gas saturations, the azimuthal variation of the *PP* reflectivity may not be very useful to predict the main fracture orientation. In the case of the fine-scale mixing of gas and brine, the gas-saturation level at which the azimuthal polarity of the *PP* reflectivity becomes identical to that of the 100% brine filled fractures is around 30%.

The compressibility of the cracks also influences the azimuthal variation of the *PP* reflectivity. For a higher compressibility (aspect ratio of 0.001), the azimuthal variation of the *PP* reflectivity has the same polarity, independently of the gas concentration

(Figure 22). The *PP* reflectivity is has a maximum value in the direction orthogonal to the fracture plane. In this case, the azimuthal variation increases slightly with increasing brine saturation.

In conclusion, rock physics modeling enables us to understand the relations between the azimuthal variation of seismic amplitudes and physical parameters, such as fracture orientation, fluid content and compressibility of the fractures. Observing a certain azimuthal variation of the reflectivity in the seismic data does not determine fracture orientation and density. Rock physics of fractures shows that the variation of the *PP* reflectivity with azimuth depends significantly on the model considered. Therefore, careful analysis should be performed before interpreting the seismic observations.

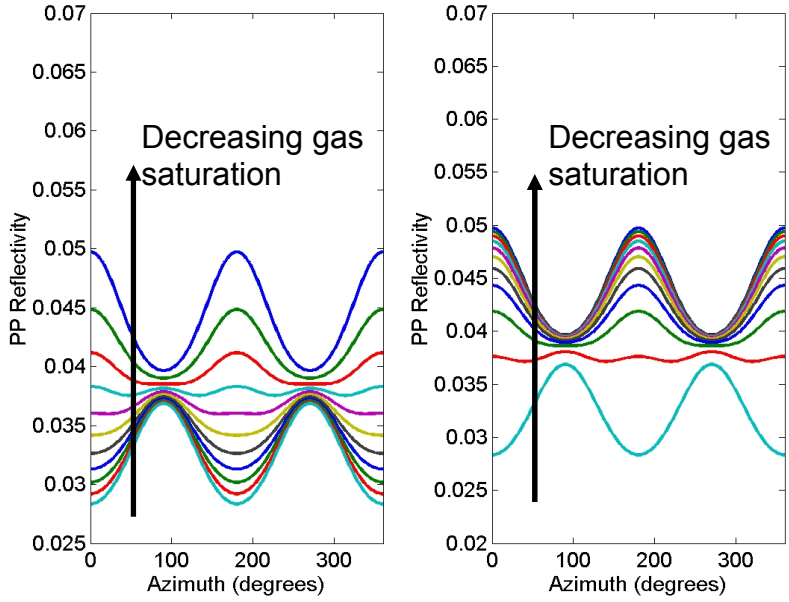

Figure 21: *PP* reflectivity as a function of azimuth at a 30º degrees angle of incidence. Different curves correspond to different gas-saturation levels (from 100% to 0%). Left panel corresponds to fine-scale mixing of gas and brine. Right panel correspond to patchy saturation. The arrow indicates decreasing gas saturation. **Aspect ratio** of the fractures is **0.01**. Azimuth 0º is orthogonal to fractures.

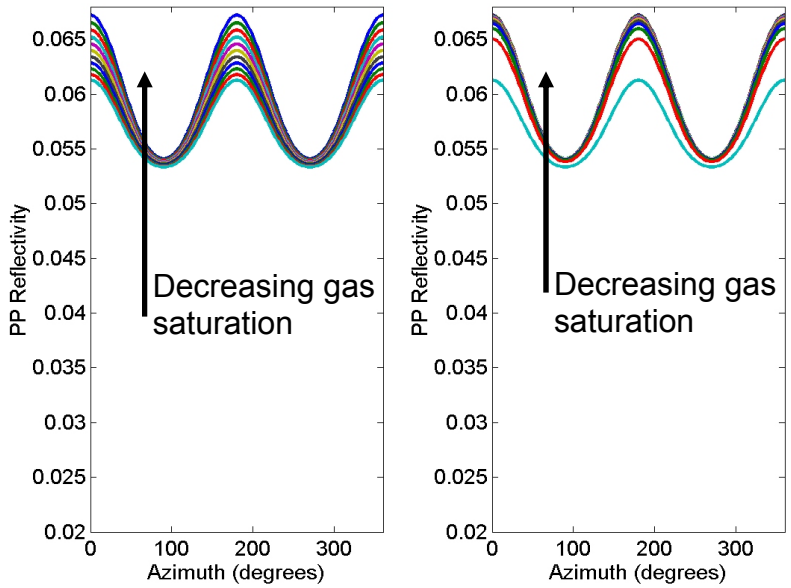

Figure 22: *PP* reflectivity as a function of azimuth at a 30º angle of incidence. Different curves correspond to different gas-saturation levels (from 100% to 0%). Left panel corresponds to fine-scale mixing of gas and brine. Right panel correspond to patchy saturation. The arrow indicates decreasing gas saturation. **Aspect ratio** of the fractures is **0.001**. Azimuth 0º is orthogonal to fractures.

Fracture distribution from the azimuthal variation of the PP reflectivity

In this section, we present the results of the azimuthal analysis of the *PP* reflectivity from the 3D seismic survey presented in previous sections. The goal is to determine the fracture orientations and the anisotropy of the azimuthal variation in the amplitudes at the top of the fractured carbonate reservoir. Since the geological structure is very flat, the top of the reservoir corresponds to a time slice at 1.3 seconds.

The fracture orientation at each bin location is derived from the azimuthal analysis of *PP* reflectivity at far-offset stacks (4000-8000 ft) using the bootstrap method. Therefore, we obtain not only a map with the mean fracture orientations, but also the associated standard deviations, due to measurement errors. These standard deviations correspond to a measurement error in the seismic amplitudes equal to 10% of the mean amplitude at the top of the reservoir.

As the rock physics modeling shows, the fracture strike may correspond to the azimuth for which we obtain either a minimum or a maximum of the amplitude, depending on the compressibility of the fluid and of the fractures.

Based on the modeling results for the carbonate reservoir, we determine the fracture strike such that it corresponds to the azimuth for which we get a minimum in the azimuthal variation of the reflectivity. This criterion corresponds primarily to two situations: either the fractures are highly compressible, independently of the type of fluids that saturate them (Figure 22), or the fractures are less compressible and partially saturated with 90% or less of gas, in a patchy manner (Figure 21, right panel).

Figure 23 presents the mean fracture orientations at each superbin locations. The bin size in this case is 1600 ft. The orientations of the red segments represent the mean fracture strikes, while those of the green and blue segments are the corresponding standard deviations from the mean orientation. The results for fracture orientation are superimposed on the map of the stack amplitudes on all offsets and azimuths, at a time slice of 1.3 seconds. The length of the red segments is proportional to the mean difference between the maximum and minimum values in the azimuthal variation of the reflectivity. The lengths of the blue and the green segments represent the standard deviations of this mean amplitude difference.

From Figure 23 we can observe that for some bin locations, the standard deviation of the mean orientation of the fractures is large, especially at the edges of the survey. However, for most of the superbins we obtain relatively small standard deviations, showing that the seismic data, with their associated measurement errors, constrain the fracture orientations reasonably well.

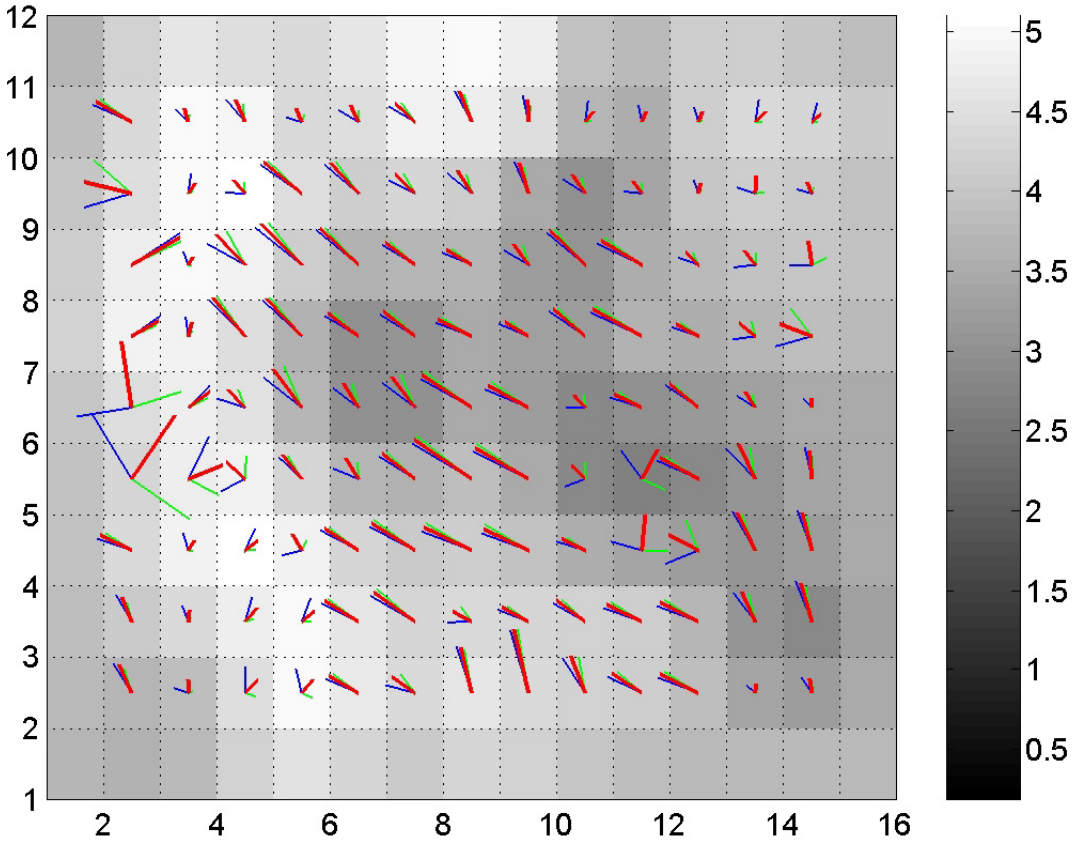

Figure 23: Fracture orientation at time slice of 1.3 seconds, corresponding to the top of James Limestone reservoir. The red segments represent the mean fracture strikes, while the blue and green segments represent the standard deviations from the mean orientation. The length of the red segments is proportional to the mean of the difference between the maximum and minimum amplitudes at each bin location (reflectivity anisotropy). The lengths of the blue and green segments give the standard deviations from this mean difference in the amplitudes. The fracture strikes are superimposed on the stack amplitude map for the time slice. The superbin size is 1600 ft.

However, as we can see in Figure 23, the superbin size is very large, equal to 1600 ft. Thus, this map only gives average trends for fracture orientation. To obtain a more detailed interpretation we have to use smaller bin sizes. Therefore, we also consider the case of a superbin size of 800 ft. This dimension is the smallest we should use to avoid the artifacts introduced by the acquisition footprint, as we showed earlier.

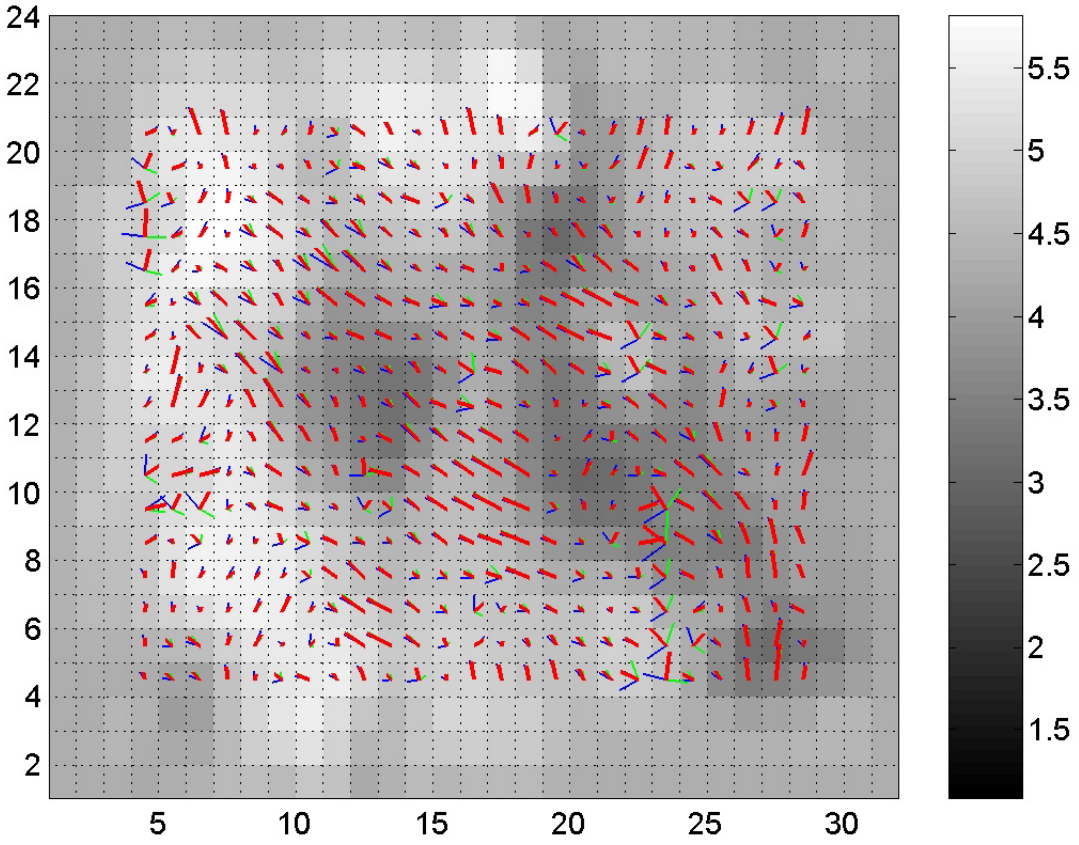

Figure 24: Fracture orientation at time slice of 1.3 seconds, corresponding to the top of James Limestone reservoir. The red segments represent the mean fracture strikes, while the blue and green segments represent the standard deviations from the mean orientation. The length of the red segments is proportional to the mean of the difference between the maximum and minimum amplitudes at each bin location (reflectivity anisotropy). The lengths of the blue and green segments give the standard deviations from this mean difference in the amplitudes. The fracture strikes are superimposed on the stack amplitude map for the same time slice. The superbin size is 800 ft.

Figure 24 gives the same representation for the fracture orientation as Figure 23. However, in this case the superbin size is 800 ft, enabling us to obtain a more detailed interpretation of the fracture orientation at the top of the reservoir. We again observe some bins that show large standard deviations of the fracture strike determined from the azimuthal variation in the seismic amplitudes at far offsets. Most of the superbins display relatively small standard deviations, suggesting that the azimuthal variation in seismic amplitudes at far offset can be used to constrain the fracture orientation for this survey.

The distributions of the mean fracture orientations in the rotated coordinate system for both the 1600 ft and 800 ft bin size cases are presented in Figure 25. From the two rose diagrams, we observe that the mean fracture strikes derived from the amplitude variation with azimuth at far offsets does not change significantly with the bin size. The trends observed at smaller scale (800 ft bin size) are preserved also at larger scale (1600 ft).

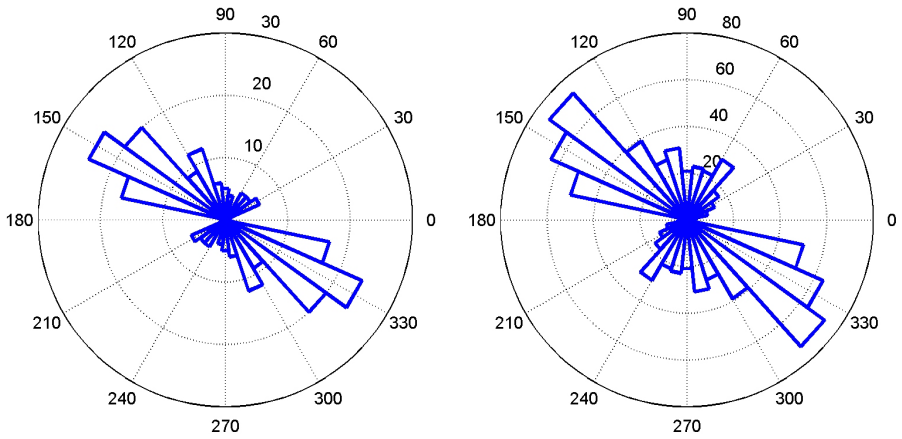

Figure 25: Rose diagrams for the fracture strike in the rotated coordinate system for 1600 ft bin size (left) and 800 ft bin size (right). This coordinate system is rotated 34º East with respect to the geographic North.

If we represent the fracture orientation in the original system of coordinates of the survey, we observe an E-W trend for the fracture strikes in this field.

The FMI log data show the existence of open, nearly vertical fractures with dips around 89 degrees, whose orientations are W10N-E10S. There is a relatively small spread of the mean fracture strike around this main orientation. We find a very good agreement between the fracture orientation derived from azimuthal analysis of the seismic amplitudes and the FMI measurements from the well, as we can see in Figure 27.

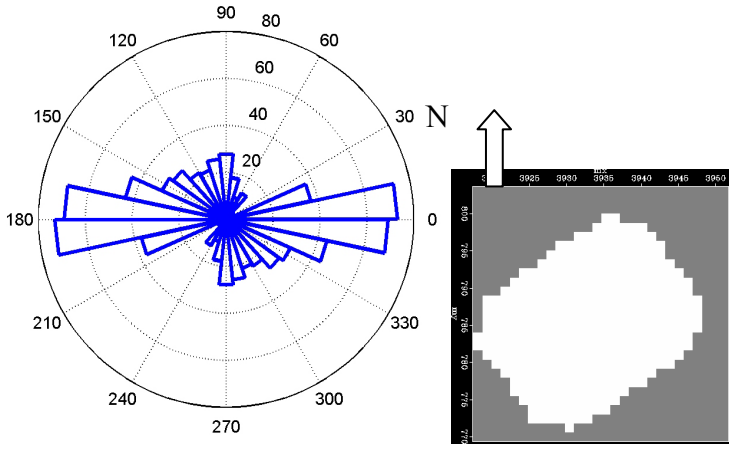

Figure 26: Left: Rose diagram for the fracture strike from azimuthal variation of PP reflectivity at far offsets in the original system of coordinates of the survey. In the rose diagram, 90 degrees azimuth corresponds to the geographical North . Right: Schematic representation of the seismic survey area.

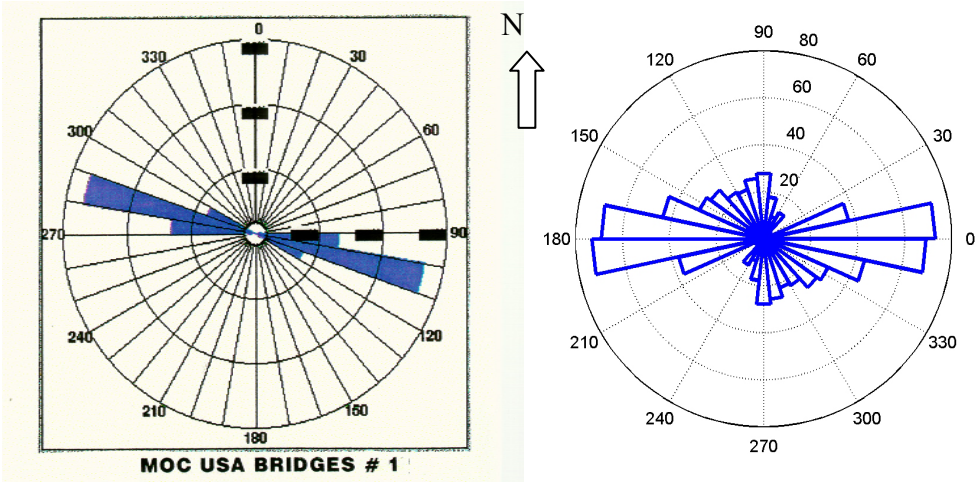

Figure 27: Comparison between the distributions of fracture strikes interpreted from a FMI log in James Limestone reservoir from a well in a nearby field (left) and the fracture strike interpreted from the azimuthal analysis of the seismic amplitudes at far offsets at the top of the James Limestone reservoir (right). Geographic North is the same for both rose diagrams. The observed fractures in the FMI log have dips of 89 degrees.

If we plot the mean fracture orientation from the distribution that we get from the azimuthal analysis of the *PP* reflectivity on the map with the regional stress field we observe again a good agreement. The mean fracture strike is almost parallel to the maximum horizontal stress (Figure 28).

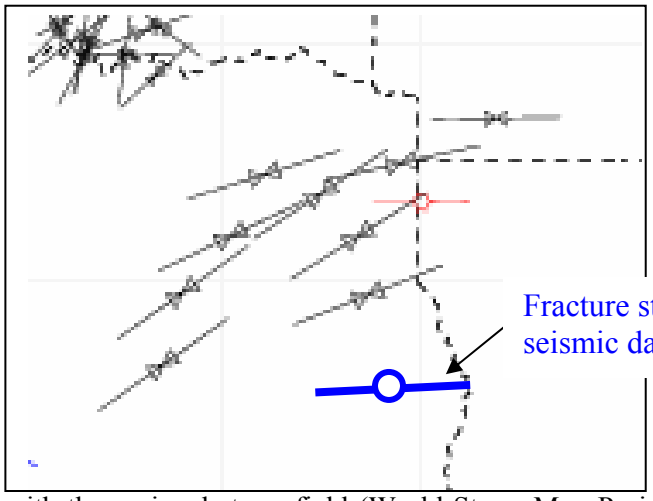

Figure 28: Map with the regional stress field (World Stress Map Project, data collected originally by Zoback). Superimposed is the fracture strike obtained from the azimuthal analysis of the PP reflectivity at far offsets (blue).

We also derive the relative anisotropy observed in the azimuthal variation of the seismic amplitudes at far offsets. Figure 29 presents a map at the top of the reservoir with the mean values for the relative anisotropy of the azimuthal variation in the seismic amplitudes. The relative anisotropy is defined as:

$$R_{anis} = \frac{\left| R_{\max} - R_{\min} \right|}{\left| R_{\min} \right|} \qquad (1)$$

The modeling shows that the difference between the maximum and minimum values of the amplitude from the azimuthal variation at far offsets is a function not only of the crack density, but also of the compressibility of the fractures and of the fluids that saturate them. In the hypothesis of little variability in the fracture compressibility and of uniformly saturated fractures, the map presented in Figure 29 can be interpreted as a relative degree of fracturing at the top of the reservoir.

We can observe a relatively higher anisotropy in the proximity of an interpreted fault that penetrates the carbonate reservoir. This fault is schematically represented in Figure 28. This may be due to a relatively higher fracture density of nearly vertical fractures in the proximity of the fault. The anisotropy anomaly is slightly asymmetric with respect to the fault. Larger values of the relative reflectivity anisotropy are encountered in the hanging wall, as some outcrop observations for analogs show (Florez, 2002). However,

we can also observe a zone of higher azimuthal anisotropy in the seismic amplitudes away from the fault. This zone may also correspond to larger fracture densities associated with possible subseismic faults. This reflectivity anisotropy is used in the integration methodology to constrain the fracture density distribution at the top of the reservoir.

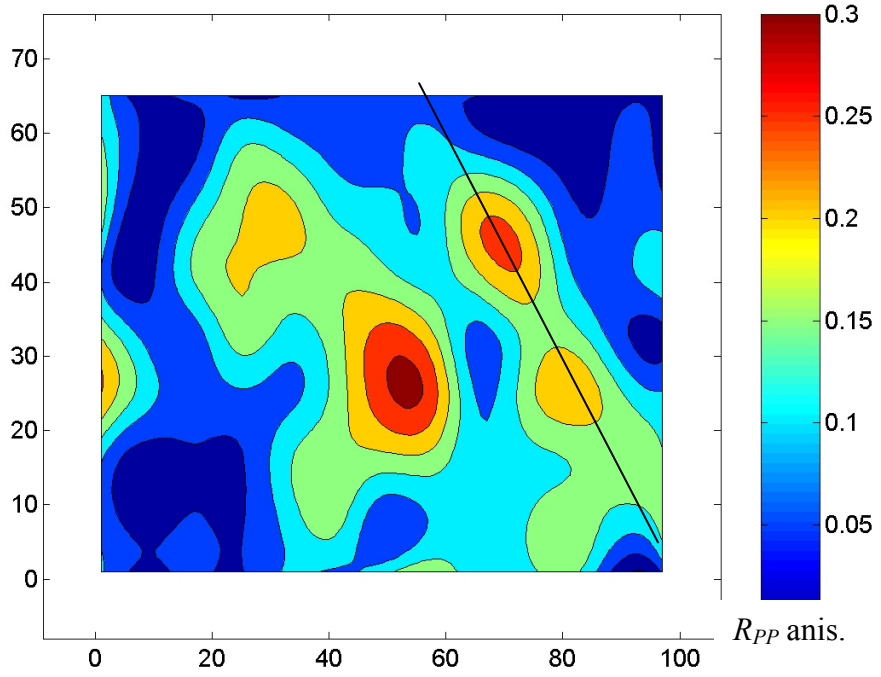

Figure 29: Map with the mean relative azimuthal anisotropy in reflectivity at the top of the reservoir.

In conclusion, we find an excellent agreement between the fracture orientation derived from the azimuthal variation of seismic amplitudes at far offsets and the fracture orientation derived from the FMI logs from the nearby wells. Furthermore, the mean fracture orientation derived from the seismic data is parallel to the maximum horizontal stress in the region, as expected in a normal faulting environment.

The distribution of the azimuthal anisotropy in the *PP* reflectivity derived from the seismic data at the top of the reservoir may be interpreted as a relative degree of fracturing, assuming little variability in the fracture compressibility for the zone of interest, and uniform saturation for the fractures.

Conclusions

In this attachment, we present the analysis of the *PP* reflectivity from a 3D seismic data set acquired over a fractured carbonate reservoir in eastern Texas, for determining the fracture orientations and the azimuthal anisotropy in reflectivity at the top of the reservoir.

In the first part of this attachment, we show the impact of the 3D seismic acquisition footprint on analyzing the variation of the reflectivity with both offset and azimuth. The acquisition footprint of this survey affects significantly the seismic amplitudes, as we observe on the reflectivity time slices. The fold is not uniform, and it creates artificial stripes of low and high reflectivity that can mask the actual signatures of fractures.

Azimuthal analysis of the *PP* reflectivity involves partial stacking of the data on different ranges of azimuth. There is a tradeoff between the azimuthal resolution, which requires small ranges of azimuth, and the signal-to-noise ratio that requires larger fold, and implicitly larger azimuthal bins. For a fixed azimuthal range we can increase the fold by increasing the bin size, at the expense of reducing the spatial resolution.

In this attachment, we show how increasing the spatial bin size can diminish the strong acquisition footprint, while increasing the fold and implicitly the signal-to-noise ratio at each superbin location. The azimuthal range for stacking the reflectivity is kept constant, equal to 20 degrees. Based on the analysis, we determine that for this 3D seismic survey, the superbin size should be at least 800 ft, at 20º azimuthal range, to make a reliable interpretation of the reflectivity variation with offset and azimuth.

Once we observe an azimuthal variation in the seismic amplitudes, the challenge is to interpret it in terms of fracture density, orientation, and fluid saturation. Rock physics fracture modeling enables us to link the observed seismic attributes to the actual parameters of fractures. Therefore, in the second part of this attachment we present more modeling results of the amplitude variation with incidence angle and azimuth (AVAZ) for the fractured carbonate reservoir. The rock physics fracture modeling shows that the interpretation of the azimuthal variation of the *PP* reflectivity in terms of fracture orientation and relative degree of fracturing requires careful rock physics modeling and additional geological constraints. The polarity of the azimuthal variation of the

reflectivity changes with both gas saturation and the compressibility of the cracks. Therefore, the fracture strike can be given by the azimuth corresponding to either a maximum or a minimum in the azimuthal variation of the reflectivity. This result that may be used to differentiate between gas-filled and brine-filled fractures, assuming that the azimuthal anisotropy is due only to the presence of a vertical set of joints whose orientation is determined from other sources of information. On the other hand, this fact introduces an additional ambiguity when we want to determine the fracture orientation from the AVAZ alone. If we do not have information about the fluid that saturates the fractures, in some situations we may not be able to determine the fracture strike.

Based on the rock physics analysis, we consider that the fracture strike at the top of the James Limestone reservoir is given by the minimum in the azimuthal variation of the reflectivity. This criterion corresponds to the cases for which either the fractures are highly compressible, independently of the type of fluids that saturate them, or the fractures are less compressible and partially saturated with 90% or less of gas, in a patchy manner. Under these hypotheses, we derive a map with the fracture orientation and the associated azimuthal anisotropy in the reflectivity at the top of the reservoir. Using a bootstrap method, we also estimate the uncertainty in the fracture orientation and the azimuthal anisotropy in the reflectivity due to measurement errors. We find an excellent agreement between the mean fracture orientations derived from the azimuthal variation of the seismic amplitudes at far offsets and the fracture orientations derived from the FMI logs from a nearby well. There is also a very good agreement between the mean fractures' strike from AVAZ and the present regional stress field. The mean fracture orientations are approximately parallel to the maximum horizontal stress in the region.

The distribution of the azimuthal anisotropy in the *PP* reflectivity at the top of the reservoir may be interpreted as a distribution of the relative degree of fracturing, assuming little variability in the fracture compressibility for the zone of interest, and uniform saturation for the fractures. We observe a relatively higher anisotropy in the proximity of an interpreted fault that penetrates the James Limestone reservoir. This may be due to higher fracture densities in the proximity of the interpreted fault. The anisotropy anomaly is slightly asymmetric, with higher values of the anisotropy in the

hanging wall of the fault. This interpretation is in agreement with field observations, and with the geological model for the reservoir. However, we can also observe a zone of higher azimuthal anisotropy in the seismic amplitudes away from the fault. This zone may also correspond to larger fracture densities, perhaps associated with subseismic faults.

Fracture characterization from AVAZ requires careful rock physics modeling and additional geological and geomechanical information on fracture compressibility and fluids distribution. However, in the absence of such information, using multiple seismic attributes can also help reduce the uncertainty in the interpretation of fracture orientation and density. For example, using the azimuthal variation in the reflectivity together with the seismic amplitude values either at the near- or far-offsets can better constrain the fracture distribution.

The Attachment H presents the methodology for integrating quantitatively the geological information about fracture density with seismic data, including the azimuthal reflectivity anisotropy, to reduce the uncertainty in fracture characterization.

Attachment H

Quantitative Integration for Fracture Characterization

Abstract

Subsurface property estimation in the geosciences is always subject to uncertainty. This is mainly due to measurement errors, to limited measurement resolution, to incomplete understanding of the physical and geological phenomena, to natural variability of the target rock properties, etc. Each geoscience discipline brings different information, often complementary, but sometimes contradictory, about the subsurface heterogeneities. Therefore, integrating different types of geological and geophysical information can better constrain the predictions on the subsurface properties.

In this attachment, we design a methodology for quantitative integration of geological and seismic data, using statistical rock physics. Rock physics theories provide a link between geology and seismics, while the statistical approach allows for quantitative integration of the various types of information.

Every geophysical measurement is designed to increase our knowledge of the subsurface properties we want to estimate. For example, in fracture characterization the goal is to update the prior geological information about the crack density and orientation by acquiring seismic data. We formulate the integration methodology in the framework of an inverse problem. We use the language of probability theory and Bayesian statistics to combine quantitatively the different types of information from geology, well-log, seismic measurements, and rock physics theories, to better constrain the fracture distribution in the subsurface. The probabilistic approach also allows for estimating the

associated uncertainty, and therefore, the method can have an impact on risk and decision analysis in reservoir development.

In this attachment, we illustrate the quantitative integration methodology with fracture characterization of a carbonate reservoir in eastern Texas. The main objective is to constrain the prior information about fracture density, from the geologic interpretation, with reflectivity attributes derived from the 3D seismic data set (Attachment G), using rock physics theories on fractures. We also present a method for estimating prior uncertainties on the fracture density, using geological constraints.

Introduction

Estimating the subsurface properties from geophysical measurements represents an inverse problem always subject to uncertainty. Among the contributing factors to this uncertainty are the measurement errors, the limited measurement resolution, the imperfect dependence between the measurements and the rock properties, etc. The information provided by seismic data about the subsurface fracture distribution is influenced by many factors, such as the type and number of seismic attributes, sensitivity of these attributes to the fracture properties, natural variability of the target rocks, and accuracy of the derived seismic attributes.

However, we often have prior, independent information about the spatial distribution for the variable of interest from the geological interpretation. In some cases, the prior information can play an important role in constraining the geophysical data, to reduce the uncertainty of our estimations.

This attachment presents a way to integrate quantitatively the geological and seismic observations using stochastic rock-physics modeling. The approach is based on the framework of an inverse problem, as formulated by Tarantola (1987), using the language of probability theory. The probabilistic approach allows us to integrate quantitatively the various types of information and also to estimate the uncertainty in our predictions (Tarantola, 1987; Houck, 1999; Takahashi et al., 1999). Therefore, this method can have a significant impact on risk and decision analysis for reservoir management.

The first part of this attachment presents the general methodology of integrating prior geological information with seismic data, using rock physics theories (Mavko et. al, 1998). This method can be applied not only to fracture characterization, but also to estimating other subsurface rock properties. However, the illustrative examples are related to fracture density estimation.

In any Bayesian (Bayes, 1783; Box and Tiao, 1992; Jaynes, 2003) analysis, we start by quantifying the *state of knowledge* about the variable of interest before acquiring new data, through the so-called *a priori* probability density function (PDF). In this attachment we also present a method to derive the *a priori* PDF for the fracture density, based on a set of constraints imposed by the geological interpretation and theoretical considerations.

Finally, we show an example of integrating prior geological information about fracture density and various reflectivity attributes from a 3D seismic dataset acquired over a fractured carbonate reservoir in eastern Texas.

Methodology

The methodology presented in this section is based on Tarantola's (1987) approach to solving inverse problems, by using Bayesian analysis. The inverse problem can be divided into the following steps:

- Decide on a minimal set of model parameters which represent the model space ($\mathcal{M}$),
- Define the physical laws that relate the model parameters to the observable, or data parameters,
- Use measurements of the observable parameters, which constitute the data space ($\mathcal{D}$), to infer the actual values of the model parameters.

In fracture characterization, the model parameters are represented by the fracture density, fracture orientation, fracture compressibility, and type of fluids saturating the fractures. The physical laws that relate the model parameters to elastic properties that can be measured seismically are given by rock-physics fracture models, such as those of Hudson (1981) or Schoenberg (1980).

In this section, we present in more detail the three different components of the inverse problem for fracture characterization: the prior information on the model parameters, the

theoretical relations between the model and the observable parameters, and the experimental data. Finally, we present the method of combining all these pieces of information to obtain the updated, or posterior state of information on the model parameters.

A priori PDF on the model parameters

As already mentioned, we often have some prior information on the model parameters, independent of the site-specific geophysical measurements. The general way of expressing mathematically the state of information over a parameter set is through a probability density function (Feynman et al., 1963; Tarantola, 1987). In estimation problems, the PDF provides us with a complete quantitative description of how likely is each of the parameter values.

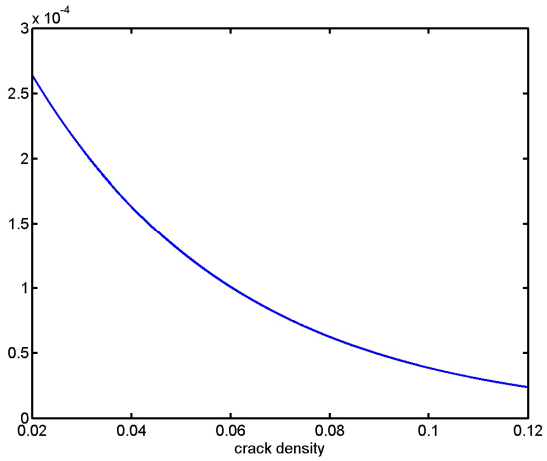

Figure 1: Probability density function for crack density. The PDF is assumed to be a truncated exponential on the interval 0.02 to 0.12, with mean 0.04. The small values are more probable than the large values.

For example, Figure 1 presents an *a priori* probability density function for the crack density (e) as defined in Hudson's (1981) model. The prior information often comes from geological observations in outcrops, from laboratory measurements, and also from previous field studies. In the example from Figure 1, the PDF is assumed to be exponential over the crack density interval from 0.02 to 0.12, with a mean equal to 0.04.

This PDF suggests that the smaller values of the crack density are more probable than the higher values..

In the case of a multi-dimensional parameter set, including for example, the fracture density, orientation, and compressibility of the fractures and of the saturating fluid, we can describe the prior information using the joint PDF over these variables. In the simple case of independence among the variables, the joint PDF is given by the product of the individual marginal PDFs for each of the variables. Following Tarantola's (1987) notation, $\rho_M(\mathbf{m})$ represents the probability density function for the prior information on the model parameters, where **m** is a vector representing the parameter set of the model space ($\mathcal{M}$).

In the example from Figure 1, the prior PDF of the crack density can be denoted as $\rho_M(e)$. In this case, the model parameter is the crack density, *e*.

The prior information about the model parameters is by definition statistically independent of the measurements, and represents an important component of any Bayesian analysis (Bayes, 1783). In this attachment , we also present a way of estimating the prior PDF based on constraints imposed by geological and theoretical information.

Experimental data

The geophysical measurements, in our case the seismic data, are affected by errors. Thus, the most general way of expressing the uncertainty about the observed data is through probability density functions, often with a Gaussian distribution.

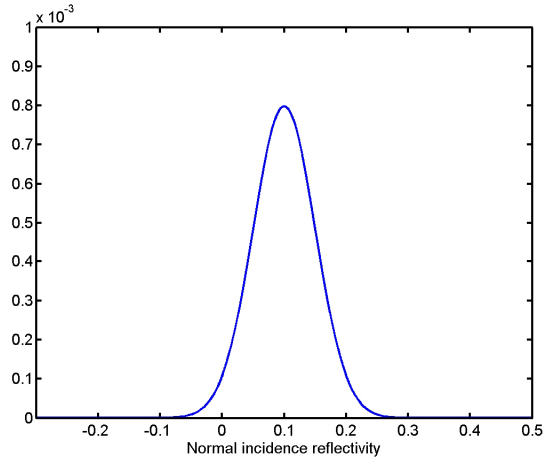

Figure 2: Probability density function for seismic reflectivity. The PDF is assumed Gaussian, with the mean centered about the observed value. The variance is a measure of the uncertainty about the observed value.

For example, Figure 2 presents a Gaussian PDF associated with a measurement of near-offset seismic reflectivity. The mean of the Gaussian represents the observed reflectivity, while the variance represents our degree of belief in that particular measured value.

The data space ($\mathcal{D}$) usually includes different types of measurements, for example, the near- and the far-offset seismic reflectivity. we generically denote the joint PDF over the data space as $\rho_{\mathbf{D}}(\mathbf{d})$. Therefore, for multiple types of data, we can represent the measurement errors by a multivariate Gaussian, as follows:

$$\rho_D(\mathbf{d}) = Gaussian(\mathbf{d}, \mathbf{d}_{obs}, \boldsymbol{C}_D), \tag{1}$$

In Equation 1, $\mathbf{d}$ is the vector with the data variables (such as the near- and the far-offset reflectivity), $\mathbf{d}_{obs}$ is the vector with the observed values, which contains the means of the multivariate Gaussian function, and $\boldsymbol{C}_D$ is the covariance matrix over the data space. If the data are assumed independent, the covariance matrix is diagonal with the variances of the individual data types.

In the example from Figure 2, the PDF expressing the uncertainty of the near-offset reflectivity value can be written as:

$$\rho_D(R_N) = Gaussian(R_N, R_{Nobs}, s^2) = \frac{1}{\sqrt{2\pi}s} \exp\left[-\frac{(R_N - R_{Nobs})^2}{2s^2} \right] \tag{2}$$

In this case, the data is represented by the near-offset reflectivity, R_N. The mean of the Gaussian function is the observed value of reflectivity $R_{Nobs,}$ while the variance, s^2, is assumed to represent the uncertainty about the observed value.

Theoretical relation between model parameters and experimental data

Probability density functions can be used to express not only the *a priori* information on the model parameters and the measurement uncertainty in the data, but also the physical correlations between these model parameters and the measurable, or data parameters. The joint PDF between the model parameters and the measurable seismic attributes describes the uncertainty of the relation between them. This uncertainty can be caused by various factors, including the approximations in the physical theory, as Tarantola (1987) describes, which are difficult to estimate. However, the uncertainty due to the natural variability of the target rock properties may be a more significant source of uncertainty. In this case we can incorporate the natural variability of the rock properties into deterministic rock-physics theories, using stochastic simulations (Mavko and Mukerji, 1998; Mukerji et. al, 2001).

Figure 3 gives an example for the joint PDF between the model parameter (crack density), and the data parameter (azimuthal reflectivity anisotropy), in the assumption of aligned vertical fractures. The physical law from which we generate the joint PDF in Figure 3 is given by Hudson's (1981) theory, which relates the fracture density to the elastic properties of the fractured media. Using the elastic properties for the fractured rocks we estimate the seismic reflectivity anisotropy based on the Ruger's (1997) equations, in the hypothesis of a vertical set of fractures (more details in Attachment G). The *Monte Carlo* simulations for deriving the theoretical joint PDF between the model parameters and the observable data will be presented in the following sections; more details are given in Attachment E.

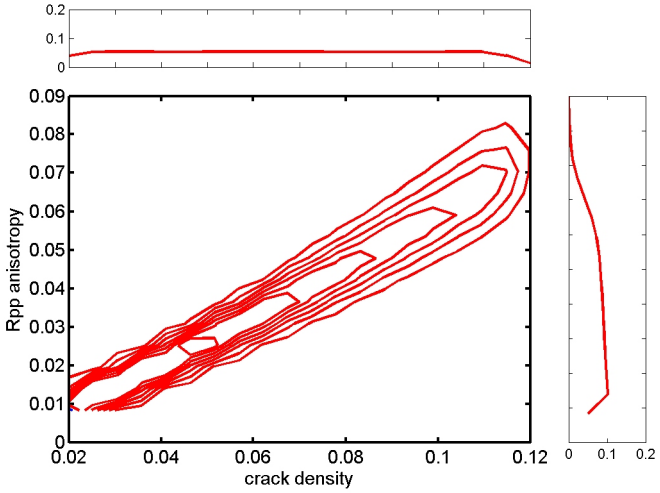

Figure 3: Joint PDF of crack density and azimuthal reflectivity anisotropy, showing uncertainty in the relation between model parameters and observable parameters due to natural variability of the rock properties.

The joint PDF that describes the theoretical relation between the model parameters and the data is symbolically represented as $\Theta(\mathbf{m},\mathbf{d})$.

In the example from Figure 3, the theoretical joint PDF can be written as $\Theta(e,A)$, where e is the crack density and A is the azimuthal reflectivity anisotropy.

Combining *a priori*, experimental and theoretical information

To summarize, any geophysical inverse problem has three different components: 1) the prior information on the model parameters, which often comes from geology, 2) the results of some experiments, often represented by the seismic data, and 3) the theoretical relation between the model parameters and the experimental data, which in fracture characterization is given by rock-physics theories. Therefore, the general question we should ask in solving an inverse problem is the following (Tarantola, 1987): Given a certain amount of prior information on the model parameters, and given an uncertain physical law relating the observable parameters to the model parameters, how should we modify the *a priori* information, given the uncertain results of some measurements?

In this framework, the inverse problem is solved by integrating quantitatively the prior, experimental, and theoretical information.

If we combine the prior PDF for the model parameters with the information on the data, we can define the prior joint PDF $\rho(\mathbf{m}, \mathbf{d})$ in the space $\mathcal{M} \times \mathcal{D}$. Since the *a priori* information on the model parameters is by definition statistically independent from the data, the joint PDF of the model parameters and the observable data is given by the product between the PDF for the model parameters $\rho_M(\mathbf{m})$ and the PDF for the data $\rho_D(\mathbf{d})$:

$$\rho(\mathbf{m}, \mathbf{d}) = \rho_M(\mathbf{m})\, \rho_D(\mathbf{d}) \tag{3}$$

The joint probability density $\rho(\mathbf{m}, \mathbf{d})$, defined on the $\mathcal{M} \times \mathcal{D}$ space, represents the prior geological information on the model parameters, **m,** and the information from the geophysical data, **d**.

On the other hand, we also have the theoretical PDF, $\Theta(\mathbf{m}, \mathbf{d})$, which represents the state of information on the physical correlations between the model parameters, **m,** and the data, **d**, which are given by the rock physics theories.

The solution to the inverse problem is obtained by combining these two states of information to produce the *a posteriori* state of information on the model parameters and the data, as follows (Tarantola, 1987):

$$\sigma(\mathbf{m}, \mathbf{d}) \sim \frac{1}{\mu} \rho(\mathbf{m}, \mathbf{d})\, \Theta(\mathbf{m}, \mathbf{d}), \tag{4}$$

where $\sigma(\mathbf{m}, \mathbf{d})$ represents the *a posteriori* state of information on the model parameters and the data, defined also in the $\mathcal{M} \times \mathcal{D}$ space. The *a posteriori* distribution is obtained by dividing the product of the two different states of information, $\rho(\mathbf{m}, \mathbf{d})$ and $\Theta(\mathbf{m}, \mathbf{d})$, as described above, by the non-informative PDF, also known as the homogeneous probability, μ (Tarantola, 1987). Although no coherent inverse theory can be set without the introduction of the homogeneous probability, it does not play an important role, and numerical inverse results do not critically depend on the particular form of μ (Tarantola, 1987).

The posterior PDF for the model parameters is obtained by integrating the *a posteriori* joint PDF for the model parameters and the observable parameters, $\sigma(\mathbf{m}, \mathbf{d})$, over the data dimension:

$$\sigma_M(\mathbf{m}) = \int \sigma(\mathbf{m}, \mathbf{d})\, d\mathbf{d}. \quad (5)$$

The *a posteriori* distribution on the model parameters, $\sigma_M(\mathbf{m})$, represents the updated state of information after integrating quantitatively the prior information, the measured data affected by errors, and the theoretical relations between the model parameters and data. From the posterior distribution on the model parameters, $\sigma_M(\mathbf{m})$, we can obtain any type of information, such as the expected values and the median values. More importantly, we can obtain the probability that the model parameters will satisfy various criteria, such as the probability that fracture density is greater than certain thresholds.

In fracture characterization, the model parameters, represented by the vector **m**, may include the fracture density, the fracture orientation, compressibility of the fractures and of the saturating fluid, etc., while the data may be represented by the near- and the far-offset reflectivity, the azimuthal reflectivity anisotropy, etc.

Figure 4 illustrates graphically how we can determine the *a posteriori* PDF, $\sigma(\mathbf{m}, \mathbf{d})$, and its marginal distribution on the model parameters, $\sigma_M(\mathbf{m})$, from $\rho(\mathbf{m}, \mathbf{d})$ and $\Theta(\mathbf{m}, \mathbf{d})$. In this example, the model parameter is the crack density (e), as defined in Hudson's (1981) model, while the data is the azimuthal reflectivity anisotropy (A). The geological hypothesis is that there is a single set of aligned vertical fractures.

The upper panel presents $\rho(e, A)$, the prior joint PDF for the crack density and the azimuthal reflectivity anisotropy, with the corresponding marginal PDFs for the model parameter, $\rho_M(e)$, and for the data, $\rho_D(A)$.

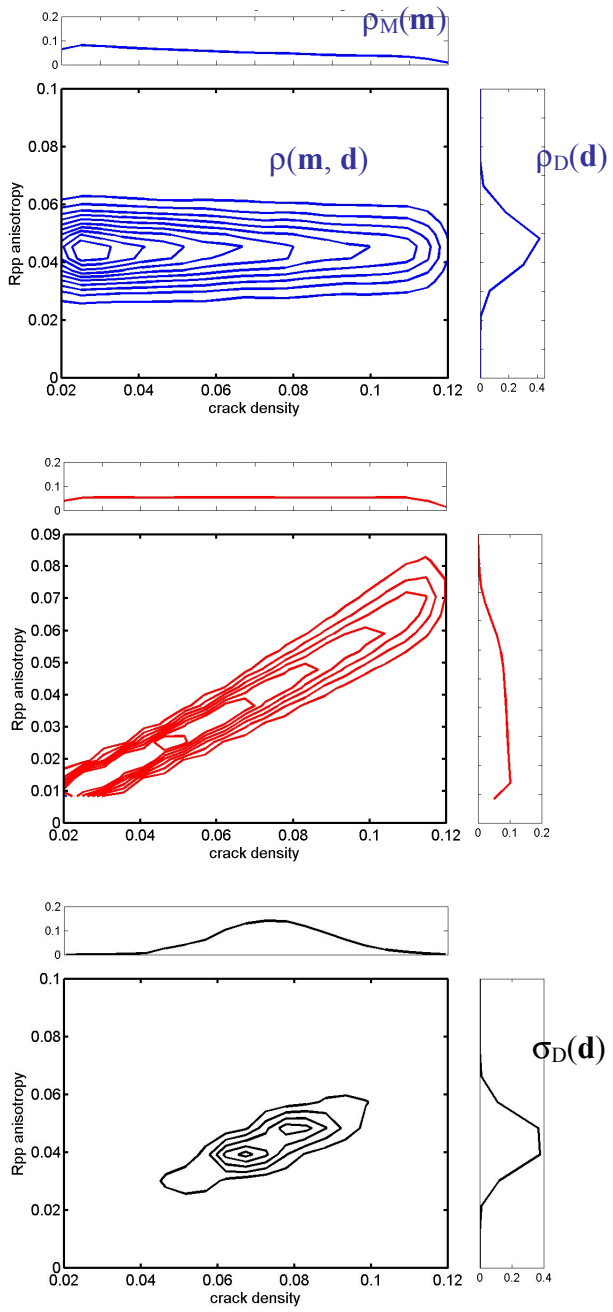

Figure 4: *Upper panel*: Joint PDF of the *a priori* information on the model parameter (crack density) and the information on the observable parameters (reflectivity anisotropy). *Middle panel*: Theoretical Joint PDF between crack density and reflectivity anisotropy derived using Hudson's model for randomly oriented fractures. *Lower panel*: *A posteriori* PDF for the model and data, computed by combining the information in the joint prior PDF and theoretical PDF presented in the upper and middle panels.

The theoretical joint PDF, $\Theta(e, A)$, presented in the middle panel of Figure 4, represents the physical correlation between the crack density and the azimuthal reflectivity anisotropy. In this example the theoretical joint PDF is derived using stochastic simulations and deterministic rock-physics fracture modeling, assuming a single set of aligned fractures. The uncertainty in the relation between the crack density and the reflectivity anisotropy is due to the natural variability of the unfractured rock properties (V_P, V_S, and *density*) of the reservoir and cap rocks, derived from the well-log data. However, the uncertainty due to imperfections and approximations in the physical model is not considered.

The lower panel of Figure 4 presents the *a posteriori* joint PDF, $\sigma(e, A)$, for the crack density (e) and the azimuthal reflectivity anisotropy (A). This *a posteriori* PDF is obtained by multiplying the prior joint PDF and the theoretical PDF, using Equation 4. The homogenous probability is considered constant. To obtained the updated distribution of crack density $\sigma_M(e)$, shown in black on the top of the lower panel in Figure 5, we integrate the *a posteriori* joint PDF $\sigma(e, A)$ over the reflectivity anisotropy (A), as in Equation 5. The *a posteriori* distribution, $\sigma_M(e)$, represents the updated measure of uncertainty about the fracture density after conditioning the prior independent information from geological interpretation with the observed azimuthal reflectivity anisotropy. Based on this posterior PDF, presented at the top of the lower panel, we can obtain any central estimators, such as expected values or median values, as well as the probability that the model parameters satisfy certain criteria.

Independent data information

Bayesian analysis (Bayes, 1783) provides mathematical rules for changing our existing knowledge in the light of new evidence. In other words, it allows scientists to combine new data with their existing knowledge or expertise, for better constrained inferences.

Bayes' rule is based on the concept of conditional probability and it allows us to update our information about the model parameters **m**, given the data, **d**. Specifically, our posterior knowledge, expressed in terms of a conditional probability, $P(\mathbf{m} \mid \mathbf{d})$, is

proportional to the prior information, $\rho(\mathbf{m})$, multiplied by the likelihood function, $P(\mathbf{d}\,|\mathbf{m})$, (Box and Tiao, 1992). The *a posteriori* distribution presented in the preceding section, $\sigma_M(\mathbf{m})$, may be interpreted as a conditional probability, $P(\mathbf{m} \mid \mathbf{d})$,.about the model parameters, **m**, given the observed data, **d**.

If we have different types of data, $\mathbf{d_1}$, $\mathbf{d_2}$,…, $\mathbf{d_n}$, statistically independent of one-another, we can derive many posterior distributions on the model parameters, $P(\mathbf{m} \mid \mathbf{d_1})$, $P(\mathbf{m} \mid \mathbf{d_2})$,…, $P(\mathbf{m} \mid \mathbf{d_n})$, by separately conditioning the prior information on the different datasets. The question is how to combine quantitatively the different posterior distributions into one result, which contains the information from all datasets. This problem reduces to combining the different conditional probability density functions, $P(\mathbf{m} \mid \mathbf{d_1})$, $P(\mathbf{m} \mid \mathbf{d_2})$,…, $P(\mathbf{m} \mid \mathbf{d_n})$, into a single conditional probability model, $P(\mathbf{m} \mid \mathbf{d_1}, \mathbf{d_2},\ldots, \mathbf{d_n})$.

From the definition of the conditional probability we obtain the following expression:

$$P(\mathbf{m} \mid \mathbf{d_1}, \mathbf{d_2},\ldots, \mathbf{d_n}) = \frac{P(\mathbf{m},\mathbf{d_1},\mathbf{d_2},...,\mathbf{d_n})}{P(\mathbf{d_1},\mathbf{d_2},...,\mathbf{d_n})}. \tag{6}$$

The numerator from the Equation 6 can be written, using the general multiplication law (Ross, 2001), as follows:

$$P(\mathbf{m},\mathbf{d_1},\mathbf{d_2},...,\mathbf{d_n}) = P(\mathbf{m})P(\mathbf{d_1} \mid \mathbf{m})P(\mathbf{d_2} \mid \mathbf{m}, \mathbf{d_1})\ldots P(\mathbf{d_n} \mid \mathbf{m},\mathbf{d_1},\ldots,\mathbf{d_{n-1}}). \tag{7}$$

In Equation 7, $P(\mathbf{m})$ is the *a priori* information on the model parameters, $\rho(\mathbf{m})$, from the preceding sections. Using again the general multiplication law, the denominator from Equation 6 can be written as follows:

$$P(\mathbf{d_1},\mathbf{d_2},...,\mathbf{d_n}) = P(\mathbf{d_1})P(\mathbf{d_2}\,|\mathbf{d_1})\ldots P(\mathbf{d_n}\,|\mathbf{d_1},\ldots,\mathbf{d_{n-1}}). \tag{8}$$

Since the data $\mathbf{d_1}$, $\mathbf{d_2}$,…, $\mathbf{d_n}$ are independent, we can write the following relations:

$$P(\mathbf{d_i} \mid \mathbf{m}, \mathbf{d_1}, \mathbf{d_2},\ldots, \mathbf{d_{i-1}}) = P(\mathbf{d_i} \mid \mathbf{m}), \quad (\forall)\ \mathbf{i} = \mathbf{1}, \mathbf{2},\ldots,\mathbf{n}, \tag{9}$$

and also:

$$P(\mathbf{d_i} \mid \mathbf{d_1}, \mathbf{d_2},\ldots, \mathbf{d_{i-1}}) = P(\mathbf{d_i}), \quad (\forall)\ \mathbf{i} = \mathbf{1}, \mathbf{2},\ldots,\mathbf{n}. \tag{10}$$

Therefore, Equation 6 can be rewritten as follows:

$$P(\mathbf{m} \mid \mathbf{d_1}, \mathbf{d_2},\ldots, \mathbf{d_n}) \frac{P(\mathbf{m})P(\mathbf{d_1} \mid \mathbf{m})P(\mathbf{d_2} \mid \mathbf{m})\ldots P(\mathbf{d_n} \mid \mathbf{m})}{P(\mathbf{d_1})P(\mathbf{d_2})\ldots P(\mathbf{d_n})} = P(\mathbf{m})\prod_{i=1}^{n}\frac{P(\mathbf{d_i} \mid \mathbf{m})}{P(\mathbf{d_i})}. \tag{11}$$

At the same time, Bayes' rule gives the following expressions:

$$P(\mathbf{d_i} \mid \mathbf{m}) = \frac{P(\mathbf{m} \mid \mathbf{d_i})P(\mathbf{d_i})}{P(\mathbf{m})} \qquad (\forall)\ \mathbf{i} = \mathbf{1}, \mathbf{2},\ldots,\mathbf{n}. \tag{12}$$

If we use Bayes' rule from Equation 12 in Equation 11, we obtain the following result:

$$P(\mathbf{m} \mid \mathbf{d_1}, \mathbf{d_2},\ldots, \mathbf{d_n}) = \frac{P(\mathbf{m} \mid \mathbf{d_1})P(\mathbf{m} \mid \mathbf{d_2})\ldots P(\mathbf{m} \mid \mathbf{d_n})}{[P(\mathbf{m})]^{n-1}} = P(\mathbf{m})\prod_{i=1}^{n}\frac{P(\mathbf{m} \mid \mathbf{d_i})}{P(\mathbf{m})}. \tag{13}$$

Equation 13 allows us to integrate quantitatively the different conditional probability density functions, $P(\mathbf{m} \mid \mathbf{d_1})$, $P(\mathbf{m} \mid \mathbf{d_2}),\ldots,P(\mathbf{m} \mid \mathbf{d_n})$, derived by independently using each of the statistically independent data, $\mathbf{d_1}, \mathbf{d_2},\ldots, \mathbf{d_n}$, into one single conditional probability model, $P(\mathbf{m} \mid \mathbf{d_1}, \mathbf{d_2},\ldots, \mathbf{d_n})$. In other words, if we derive different posterior distributions for the model parameters, based on different types of independent data by using the methodology presented in the preceding sections, we can combine all of these posterior probabilities into a single posterior probability model, conditioned on all of the data, $\mathbf{d_1}$, $\mathbf{d_2},\ldots, \mathbf{d_n}$, by simply multiplying the individual posterior distributions.

Next section presents a summary with the practical steps for the quantitative data integration applied to fracture characterization.

Summary for the methodology of integration

We present the following practical steps for integrating the prior information about fracture distribution, obtained from the geological interpretation, with the well-log and seismic measurements, using stochastic rock physics modeling within a Bayesian framework:

1) Model parameters

We first decide which model parameters are needed to answer the question under consideration. The model parameters may include the fracture density, orientation and compressibility, the type of fluid in the fractures, the connectivity of the fractures, etc. In some practical problems, we may be interested only in some of these parameters.

2) Geological hypotheses

Next we evaluate the possible geological hypotheses for the fracture model parameters, based on the site-specific outcrop observations, if available, or outcrop analogs, as well as on the well-log information. Another valuable source of information for fracture distribution is the geological structure of the reservoir, which can be obtained from the interpretation of seismic data.

3) Rock-physics modeling and stochastic simulations: Theoretical PDF

We perform rock-physics forward modeling and stochastic simulations based on the well-log data available, under the chosen geological hypotheses. The goals of this step are, first, to choose the most informative seismic attributes with respect to the model parameters (Takahashi, 2000), and second, to derive the physical relations between the model parameters and the chosen seismic attributes. We use rock-physics fracture modeling and stochastic simulations to incorporate the natural variability of the background rock properties. Thus, we run *Monte Carlo* simulations on the input parameters of the deterministic fracture models. One physical theory often used is Hudson's (1981) model. The input parameters in Hudson's penny-shaped crack model are the crack density, the aspect ratio of the ellipsoidal cracks, the elastic properties of the fluid saturating the cracks, and the V_P, V_S and *density* of the unfractured background rocks, derived from the well-logs. For the crack density, we use a uniform distribution, assuming maximum uncertainty over the interval of variation for the crack density. For the aspect ratio of the penny-shaped cracks, defined as the ratio between the aperture and the radius of the crack, we use a uniform distribution, on a logarithmic scale. For the elastic properties of the fluid, we can use deterministic values, when the fluid saturating the fractures is known, or we can use a uniform distribution spanning the possible values for the bulk modulus and density at reservoir conditions. For the unfractured matrix

properties (V_P, V_S, *density*), we use the correlated PDF for V_P, V_S, and *density* derived from the well-log data. If no addition information indicates otherwise, these properties are considered representative and stationary over the area of study. By using *Monte Carlo* simulations, we obtain many realizations of sets of fracture parameters and seismic attributes that span the intrinsic natural variability. Based on these realizations, we can estimate the theoretical joint PDF $\Theta(\mathbf{m}, \mathbf{d})$, which describes the physical relations between the fracture parameters and the seismic attributes. This PDF represents a measure of uncertainty about the relation between the model parameters and the observable data, with its inherent non-uniqueness and non-linearity, due to natural variability of the target rock properties. If the correlated distributions of V_P, V_S and *density* for the reservoir and cap rocks are assumed representative and stationary over the area of study, the theoretical PDF, which describes the relations between the fracture parameters and seismic attributes, may also be assumed stationary and representative for the area of study. However, this theoretical joint PDF is site specific.

4) Prior PDF for fracture parameters

Based on the structural-geology model of the reservoir we estimate the *a priori* PDF $\rho_M(\mathbf{m})$, for fracture parameters at each grid point of the target. More details and an example are given below.

5) Seismic data

Seismic measurements are affected by errors. Thus, we need to estimate the uncertainty associated with the observed seismic attributes and describe it using a PDF, $\rho_D(\mathbf{d})$.

6) Combining the prior information on fracture parameters with seismic data

Next we derive the joint PDF, $\rho(\mathbf{m}, \mathbf{d})$, for the fracture parameters and the data at each grid point, assuming that the prior information about the fracture parameters and the actual seismic data are statistically independent.

7) Posterior PDF for fracture parameters: integration of geology and seismic data

Finally, we compute the *a posteriori* PDF, $\sigma(\mathbf{m}, \mathbf{d})$, over the fracture parameters and data by combining the theoretical PDF, $\Theta(\mathbf{m}, \mathbf{d})$, which is considered stationary, with the prior PDF for the model parameters and observable data, $\rho(\mathbf{m}, \mathbf{d})$, which varies with

location. Then we integrate the *a posteriori* PDF, $\sigma(\mathbf{m}, \mathbf{d})$, over the seismic attributes space to obtain the updated distribution of fracture parameters $\sigma_M(\mathbf{m})$. This *a posteriori* PDF for the fracture parameters represents the solution to the inverse problem, and it gives a measure of uncertainty about the fracture parameters after integrating prior geological information with seismic data.

From this *a posteriori* PDF for the fracture parameters, we can derive any statistical information, such as any central estimators, like expected or median values. More importantly, we can compute the probability that a certain model will satisfy any criteria, for example, the probability that the fracture density exceeds certain thresholds.

Figure 5 presents a flow-chart for integration.

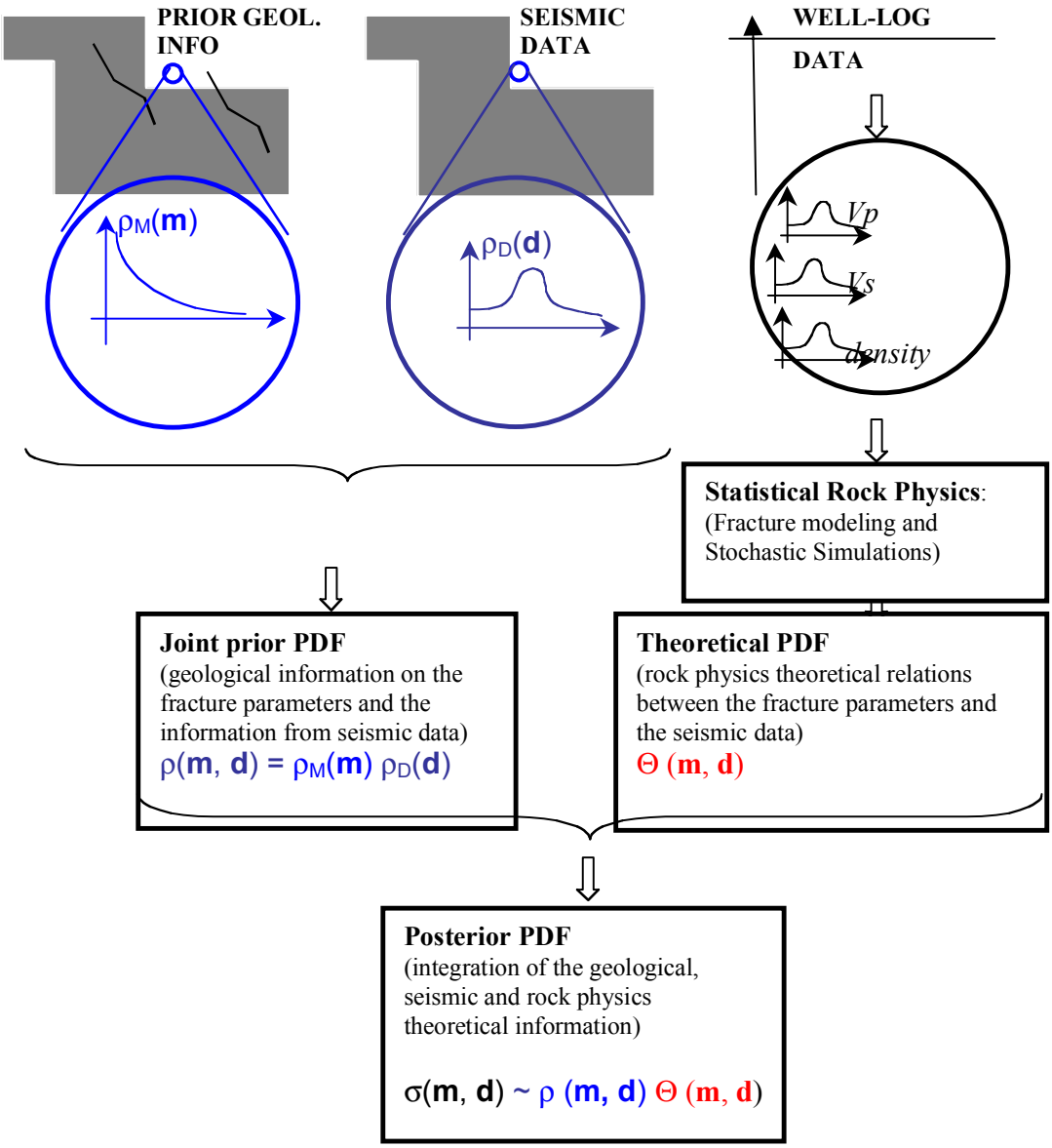

Figure 5: Flow-chart with the methodology of integration.

In the next section, we present a method of estimating the prior PDF for the fracture parameters by using geological and theoretical constraints.

The *a priori* PDF for fracture density

The prior distribution of the variable of interest is an important ingredient in any Bayesian analysis (Bayes, 1783), and it may sometimes play an important role in determining the final results. Even if the prior information is vague, using it helps in formulating well-posed inverse problems.

Traditionally, all probabilities were treated as frequencies. Here, the word "frequency" is used in the sense of the number of times an event occurs. However, Bayesian theory does not define a probability as a frequency of occurrence of an event, but as a reasonable degree of belief (Laplace, 1814). In other words, the probability is viewed as a measure of the uncertainty about a particular parameter, and it represents the *state of knowledge* about that parameter. Therefore, probability is related to the state of uncertainty, and not (only) to the outcome of repeated experiments. This view of the probability is much more useful in most of the practical applications in science and engineering.

However, assigning the prior probability is one of the most controversial areas in Bayesian probability. Yet, to a Bayesian, it is the most natural of things. No one would think of trying to solve any problem without using all of his prior experiences. There are different ways of assigning prior probabilities (Jaynes, 1983), but one of the most used is based on the Maximum Entropy Principle, as defined by Jaynes (1983), which has its foundation on Shannon's (1948) information theory.

In information theory, uncertainty is quantified by a parameter called "information entropy", *H(X)*. *H(X)* is a statistical parameter that quantifies the state of knowledge for parameter *X*, and it can be calculated from the PDF of *X*, *P(X)*, using the following formula:

$$H(X) = -\sum_i P(x_i)\log[P(x_i)]. \qquad (14)$$

This quantity is a measure of the amount of ignorance in the probability distribution of the variable *X* (Shannon, 1948; Takahashi, 2000).

Jaynes' Maximum Entropy Principle states that from all of the probability distribution functions consistent with a given set of constraints, we should choose the one that maximizes the uncertainty, as defined by Shannon (1948).

In the discreet case, it can be shown that if nothing is known, except that the probability distribution should be normalized, the maximum entropy principle reduces to the uniform prior. This is Laplace's *principle of insufficient reason* (Laplace, 1814). However, the maximum entropy is more general, because it allows one to assign probabilities that are maximally uninformative, while still incorporating the known information. The term "uninformative" may sound negative, but its meaning is related to defining PDFs that do not convey unintentional biases. Therefore, the principle of maximum entropy represents a useful tool for assigning probabilities based only on the information that one actually possesses.

Therefore, to estimate prior probabilities for fracture density, we should first quantify the geological constraints at each spatial location. Then, we can determine the maximum entropy PDF at that location by maximizing Shannon's entropy, consistent with the local constraints. This is a classical problem of optimization under constraints, for which we can use the method of Lagrange multipliers.

One of the constraints we can put on fracture density from both practical and theoretical considerations is related to its range of variability. Fracture density should not be smaller than 0, because negative fracture density has no physical meaning. At the same time, fracture density has also an upper bound, beyond which the rock loses its strength. If no other constraints are specified from geology, then the maximum entropy PDF is given by a uniform distribution over the interval between 0 and the theoretical upper bound of fracture density (e^{up}), as follows:

$$P(e) = \begin{cases} \dfrac{1}{e^{up}}, & e \in \left[0 \quad e^{up}\right] \\ 0, & else \end{cases}. \tag{15}$$

If from the geological interpretation we additionally obtain the local mean value of fracture density (*m)*, then the maximum entropy PDF is given by a truncated exponential as follows:

$$P(e) = \begin{cases} ce^{-ke}, & e \in \left[0 \;\; e^{up}\right] \\ 0, & else \end{cases}. \tag{16}$$

The constants *c* and *k* in the above formula are determined from the conditions that the *p(e)* is a PDF and therefore integrates to 1, and that the expected value of this PDF is equal to the known mean value *m*. These conditions are expressed as follows:

$$c\int_0^{e^{up}} \exp(-ke) = 1, \quad and \quad c\int_0^{e^{up}} e\ \exp(-ke) = m\,. \tag{17}$$

The probability density function for fracture density, defined as an exponential distribution, is in good agreement with the outcrop observations, which suggest exponential or log-normal distributions for fracture density (Snow, 1968; Priest and Hudson, 1976; Sen and Kazi, 1984; La Pointe and Hudson, 1985; Rouleau and Gale, 1985; Bouroz, 1990; Villaescusa and Brown, 1990; Narr and Suppee, 1991; Rives et. al, 1992). We derive the same conclusion also from the field data on shear-wave anisotropy, collected by different authors and summarized by Crampin (1994). Assuming that the shear-wave anisotropy is caused by the alignment of fractures, the computed crack density exhibits an approximately exponential, or log-normal distribution, as we discuss in Attachment D (Figures 1 and 3).

The Maximum Entropy Principle is a very useful tool to define prior probabilities for Bayesian analysis that are consistent with a given set of constraints imposed by the geological interpretation.

Real data example

In this section, we illustrate the integration of prior geological information on fractures with reflectivity attributes from a 3D seismic data set acquired over a fractured carbonate reservoir in eastern Texas. More information on the reservoir and the seismic data are presented in Attachments E and G.

The goal is to update the information on the fracture density, as described in Hudson's (1981, 1997) model, by integrating the prior information with seismic data. Thus, the model parameter is the crack density, while the observable, or data parameters

are the reflectivity attributes. We assume that the fractures are gas-saturated, and the objective is to delineate the zones of higher fracture density at the top of the reservoir.

Based on the geological information about the reservoir, we consider two geological hypotheses. The first hypothesis is that the fractures are vertical, aligned, and fairly regularly spaced, such that they generate an anisotropic medium. The fracture orientation in this hypothesis was already determined from the Amplitude Variation with Azimuth at far offsets, using a bootstrap method presented in Attachment G . Therefore, the fracture orientation is not a model parameter, since it was already determined from the seismic data.

The second hypothesis is that the fractures occur in swarms associated with possible subseismic faults, and are more-or-less randomly oriented, such as in brecciated zones. In this hypothesis, the fracture orientation is not a model parameter either, since the assumption is that the fractures are randomly oriented.

Available information

In this section we present the seismic attributes extracted from the 3D seismic data set presented in Attachment G , which we use for constraining the prior information on fracture density. We also show an example of estimating the prior information about the fracture density, based on a geological interpretation.

Seismic data

The seismic data used is represented by the amplitude of the seismic waves at the top of the fractured gas reservoir. The distribution of the near-offset (0 –3000 ft) reflectivity is shown in Figure 6, while the distribution for the far-offset (4000 ft – 8000 ft) reflectivity is shown in Figure 7. We use large superbins of 1600 ft to eliminate the strong impact of the acquisition footprint on the seismic amplitudes, as we present in Attachment G.

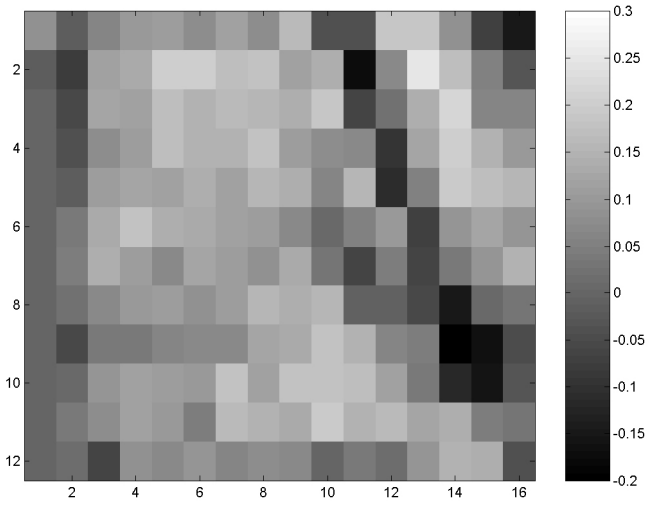

Figure 6: Map with the near-offset stack of the seismic amplitudes at the top of the reservoir for large superbins (1600 ft).

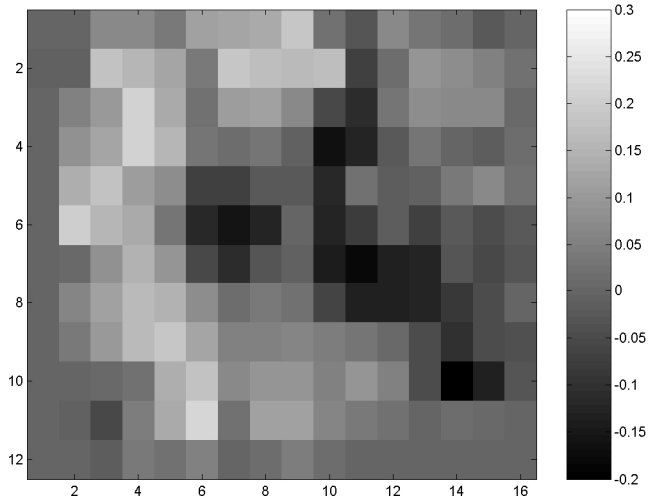

Figure 7: Map with the far-offset stack of the seismic amplitudes at the top of the reservoir for large superbins (1600 ft).

Figure 8 shows the difference between the near- and far-offset reflectivity, stacked over all azimuths, at a time slice corresponding to the top of the reservoir.

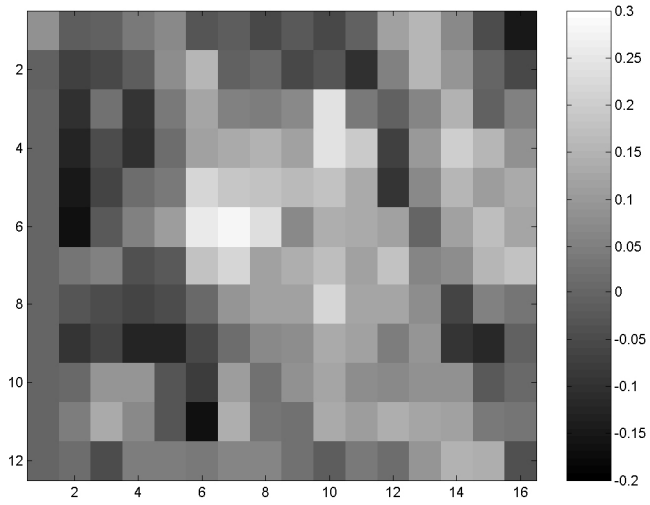

Figure 8: Map with the difference between the near- and the far-offset amplitude stacks over all azimuths at the top of the reservoir for large superbins (1600 ft).

In the hypothesis of a nearly vertical set of fractures, as the FMI data from a nearby well suggests, the reflectivity at far offsets varies with azimuth. At a fixed angle of incidence, the variation of the reflectivity with azimuth can be approximated by a cosine function (Teng, 1998). We use a least-square cosine fitting procedure to describe the observed azimuthal variation of the reflectivity at far offsets, as presented in the Attachment G. We take into account the measurement errors associated with the reflectivity, by using a bootstrap method to derive the uncertainty in the parameters describing the sinusoidal variation with azimuth: the mean value of the reflectivity, the amplitude of the oscillation, and the phase. More details on the procedure are given in Attachment G.

We define the azimuthal anisotropy of reflectivity to be the amplitude of the oscillation. This amplitude is given by the absolute difference between the maximum and the minimum values in the azimuthal variation of the reflectivity at far offsets, as follows:

$$A = |R_{max} - R_{min}|. \tag{18}$$

Rock-physics modeling shows that, at a fixed angle of incidence, this amplitude increases with increasing crack density, as we show later in this attachment .

Figure 9 shows the distribution for the mean values of the azimuthal reflectivity anisotropy at the top of the reservoir, determined in Attachment G.

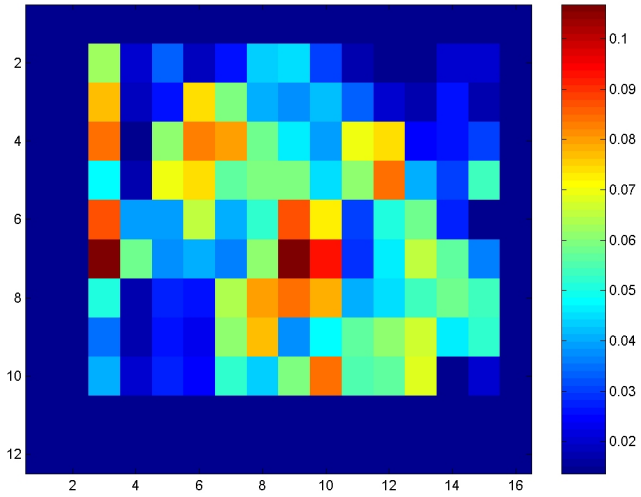

Figure 9: Map with the mean values of the azimuthal reflectivity anisotropy (*A*) at far offsets at the top of the reservoir. Superbin size is 1600 ft.

Figure 10 shows the distribution of the standard deviation associated with the mean values of the azimuthal reflectivity anisotropy from Figure 9, determined by using a bootstrap method (Attachment G).

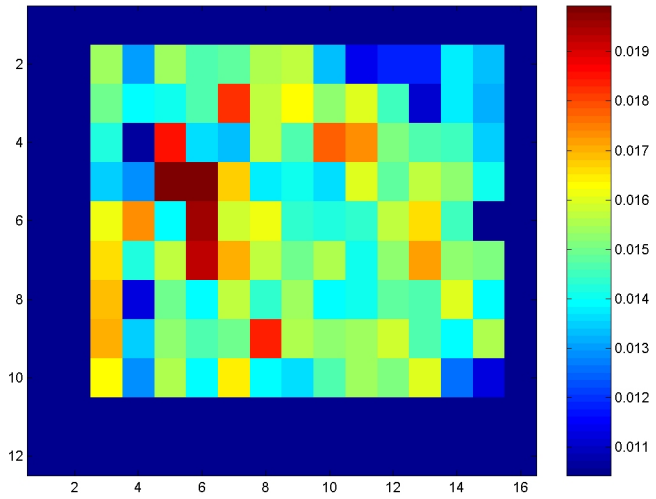

Figure 10: Map with the standard deviation for the azimuthal reflectivity anisotropy (*A*) at far offsets at the top of the reservoir. Superbin size is 1600 ft.

As the geological model for this carbonate reservoir suggests, we consider two hypotheses: a vertical set of fractures, and a random distribution for fracture orientations.

In the hypothesis of randomly oriented fractures, the data space consists of the near- and the far-offset reflectivity, presented in Figures 6 and 7, respectively.

Using Tarantola's (1987) formulation, we can express the uncertainty about the data using a probability density function over the data space. In this example, we assume the PDF to be a correlated bivariate normal distribution, as follows:

$$\rho_D(R_N, R_F) = \text{Gaussian}\ (R_N, R_F, R_{Nobs}, s^2, R_{Fobs}, s^2, r), \tag{19}$$

where R_N represents the near-offset reflectivity and R_F is the far-offset reflectivity. R_{Nobs} and R_{Fobs} are the observed data values, which represent the means of the Gaussian bivariate function. The standard deviation, s, of the near- and the far-offset reflectivity is assumed the same over the entire survey, equal to a percentage of the mean value of reflectivity at the top of the reservoir. In Equation 19, r represents the correlation coefficient between the near- and the far-offset reflectivity. This correlation coefficient is estimated from the data to be 0.6.

For the case of a vertical set of fractures, the data space is represented by the azimuthal anisotropy of reflectivity at far offsets, presented in Figure 9, together with the difference between the near- and the far-offset reflectivity, stacked over all azimuths, presented in Figure 8. In this case, the probability density function over the data space is assumed as follows:

$$\rho_D(A, G) = \text{Gaussian}\ (A, A_{obs}, s_A^2)\ \text{Gaussian}\ (G, G_{obs}, s_G^2), \tag{20}$$

where A is the azimuthal anisotropy of reflectivity at far offsets. A_{obs} are the observed values from Figure 9, which are considered to be the means of the Gaussian function, with the standard deviation s_A presented in Figure 10. G represents the difference between the near- and far offset reflectivity. G_{obs} are the observed values, presented in Figure 8, which are considered to be the mean of the Gaussian function, while s_G is the standard deviation of the difference between the near- and far-offset reflectivity. Equation 20 implies that the variables A and G are independent. This assumption may be justified, since the data shows a very small correlation coefficient between these variables. In this

case the joint PDF over the data space is given by the product between the two marginal distributions. The standard deviation squared, s_G^2, of the variable *G*, corresponds to the variance of the difference between the near- and far-offset reflectivity, and it is given as follows:

$$s_G^2 = Var\,(G) = Var(R_N - R_F) = Var(R_N) + Var(R_F) - 2Cov(R_N, R_F) = 2s^2 - 2r/s^2, \quad (21)$$

where *s* represents the standard deviation of the near- and far-offset reflectivity, and *r* represents the correlation coefficient between the near- and far-offset reflectivity, estimated from the data.

Prior geological information

Rocks undergoing fracturing exhibit increased fracture density with increased strain (Nelson, 1985). Therefore, large fracture densities are usually associated with the presence of faults. Fracture density increases in the proximity of faults, and it decreases away from them. Outcrop studies show that the decrease of the fracture density with increasing distance from a fault may follow an exponential law (Davatzes, 2003).

Figure 11 presents a map with the distribution of the mean values of fracture density at the top of the fractured reservoir. This spatial distribution is based on the geological interpretation of a fault from seismic data (Figure 12). In the proximity of the fault, the expected crack density is larger than away from the fault. Outcrop observations can help in calibrating the initial distribution of the mean values for fracture density in relation to the fault observed from seismic data. However, the fracture density values from outcrops should be transformed to the corresponding reservoir stresses.

In this example, we assume a smooth exponential decay for the mean fracture density with increasing distance from the fault, as we can observe in Figure 11. The expected fracture density in the proximity of the fault is assumed to be 0.07. This value corresponds to an upper value for the crack density of a reservoir at 2 km depth, based on the shear-wave data collected by Crampin (1994), as we discuss in Attachment D (Figure 6).

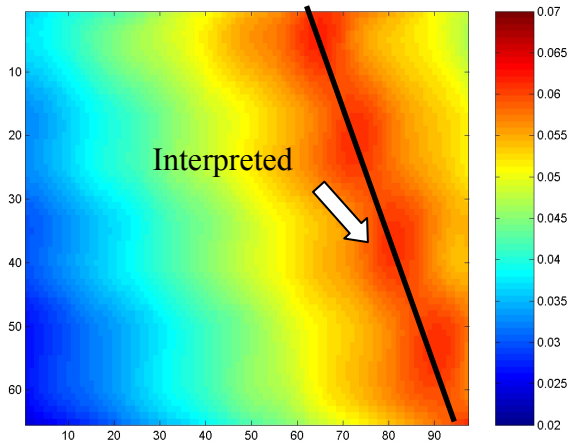

Figure 11: Map with the interpolated *a priori* spatial distribution of the mean value of fracture density at the top of the reservoir, based on the geological interpretation of a fault.

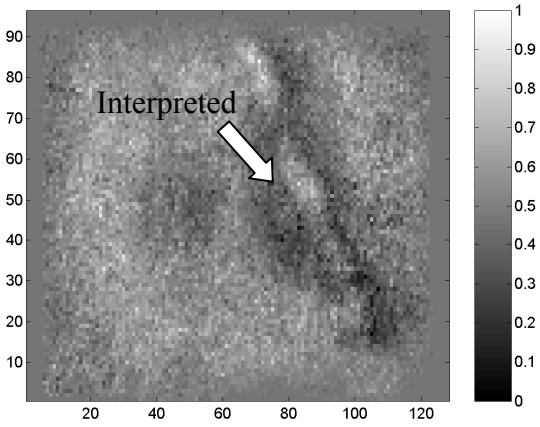

Figure 12: Amplitude map at the top of a fractured carbonate reservoir, with the interpreted fault. Bin size is 200 ft.

Of course, there is a large uncertainty about these mean values of fracture density presented in Figure 11, which is quantified through the local *a priori* probability density functions. We estimate the local prior PDF for fracture density at each grid point, using the Maximum Entropy Principle, presented in the preceding section. At each spatial location, the *a priori* PDF for fracture density is given by a truncated exponential over the interval 0.02 to 0.12, with the expectation given by the local mean values from Figure 11.

Therefore, the prior PDF on the model parameter, represented by the crack density e, is expressed as follows:

$$\rho_M(e) = \begin{cases} ce^{-ke}, & e \in [0.02 \;\; 0.12] \\ 0, & else \end{cases} . \qquad (22)$$

In Equation 22, e represents the crack density as described in Hudson's (1981) penny-shaped crack model. The lower value of the interval for which the PDF is defined corresponds to a small degree of fracturing, while the upper value of 0.12 is slightly larger than the limit of validity for the Hudson's model, and it corresponds to a high degree of fracturing for the reservoir conditions.

The constants c and k from Equation 22 are to be determined at each special location, such that the function in Equation 22 satisfies the condition of a PDF (its integral is 1), and such that its expectation is equal to the local mean, derived from the geological interpretation, presented in Figure 11.

Theoretical PDF: Rock-physics stochastic modeling

Rock-physics theories (Mavko et al., 1998) provide the link between the fracture parameters and the seismic data.

This section presents the rock-physics fracture modeling and stochastic simulations to describe the theoretical relations between the fracture parameters and the *PP* reflectivity attributes, taking into account the natural variability of the target rock properties.

We use Hudson's (1981, 1997) penny-shaped crack model to predict the elastic properties of the fractured media. We also use Vavrycuk's and Psencik's (1998) approximation for weak contrast and weak anisotropy to compute the reflectivity variation with incidence angle and azimuth from the top of the reservoir, in the case of a vertical set of fractures. We use the Zoeppritz (1919) equations in the case of randomly oriented fractures.

For example, in the hypothesis of a vertical set of aligned fractures, we can write generically the relation between the fracture parameters and the elastic properties of the fractured media:

$$[C^{bot}, den^{bot}] = g(V_p^{bot}, V_S^{bot}, density^{bot}, e, \alpha, K_{fl}) , \qquad (23)$$

where C^{bot} and den^{bot} represent the elastic stiffness matrix and the density of the fractured reservoir rocks, modeled with a single set of aligned cracks. The input parameters in

Hudson's model are the *P*-wave velocity, the *S*-wave velocity, and the density (V_P^{bot}, V_S^{bot}, $density^{bot}$) of the unfractured isotropic rocks, the crack density (e), the aspect ratio of the cracks (α), and the bulk modulus (K_{fl}) of the fluids saturating the fractures.

After we derive the elastic properties of the fractured media, we use the approximation from Vavrycuk and Psencik (1998) to compute the reflectivity at the interface between the reservoir, modeled with a set of vertical fractures, and the cap rocks. The relation between the fracture parameters and the reflectivity attributes can be written as follows:

$$\begin{aligned}[R_N, R_F, A,] &= f(C^{top}, den^{top}, C^{bot}, den^{bot}) = \\ &= f(\ g(V_p^{bot}, V_S^{bot}, density^{bot}, e, \alpha, K_{fl}),\quad V_P^{top}, V_S^{top},\ den^{top})\end{aligned}. \tag{24}$$

In Equation 24, the function f represents symbolically the approximation for the reflectivity variation with incidence angle and azimuth, at the interface between the reservoir and the cap rocks. C^{top} and den^{top} are the elastic stiffness matrix and the density of the cap rocks. If the cap rocks are isotropic, the elastic properties can be fully described by the *P*- and *S*-wave velocities (V_P^{top}, V_S^{top}). The function g represents Hudson's theory, symbolically shown in Equation 23. R_N, R_F and A represent the reflectivity attributes: the near- and far-offset reflectivity, as well as the azimuthal anisotropy of reflectivity at far offsets (Equation 18).

Theoretically, given a set of elastic parameters corresponding to the cap and the reservoir rocks, we can predict uniquely the near- and far-offset reflectivity, as well as the amplitude of the sinusoidal variation of the reflectivity at far offset as a function of azimuth. However, the relations between the fracture parameters and the reflectivity attributes are uncertain, because of approximations in the theory, and, more importantly, because the subsurface rock properties are naturally variable. When deriving the relations between the fracture parameters and the reflectivity attributes, we ignore the uncertainties due to theoretical approximations, and we account for the uncertainty due to natural variability of the target rocks. Therefore, we run *Monte Carlo* simulations on the input parameters in Hudson's model (1981). As already mentioned, the input parameters are the crack density (e), aspect ratio (α) of the ellipsoidal cracks, defined as the ratio

between the small and the long semiaxes, the bulk modulus of the saturating fluid (K_{fl}), and the V_P^{bot}, V_S^{bot} and $density^{bot}$ of the unfractured background rocks.

To estimate the theoretical PDF, which describes the uncertain relations between the fracture parameters and the observable parameters due to natural variability, we use a uniform distribution for fracture density, between 0.02 and 0.12. This represents a relevant interval for the fracture density. The lowest value of the interval corresponds to practically intact rocks, while the upper value corresponds to a relatively large degree of fracturing, especially for a reservoir at approximately 2 km depth, as we discuss in Attachment D (Figure 6). For the aspect ratio of the penny-shaped cracks we also use a uniform distribution, on a logarithmic scale (from 0.001 to 0.1).

For the unfractured matrix properties (V_P, V_S, *density*), we derive the distributions from the well-log data. Figure 13 presents in the upper panels the histograms for the V_P^{bot} V_S^{bot}, and $density^{bot}$ of the clean limestones in the reservoir, obtained from the well-log data from a nearby well. The lower panels in the same figure present the probability distribution functions (PDF) of the *P*-wave velocity, *S*-wave velocity and density derived from the histograms.

The V_P, V_S, and *density* properties derived from the well logs for both reservoir and cap rocks are upscaled to seismic wavelengths. The upscaling is performed on the well data using Backus (1962) averages for the bulk and shear moduli, and volumetric averages for density (Mukerji, 1995).

The distributions for the seismic properties (V_P, V_S, and *density*) for both reservoir and cap rocks are assumed representative and stationary over the area of study.

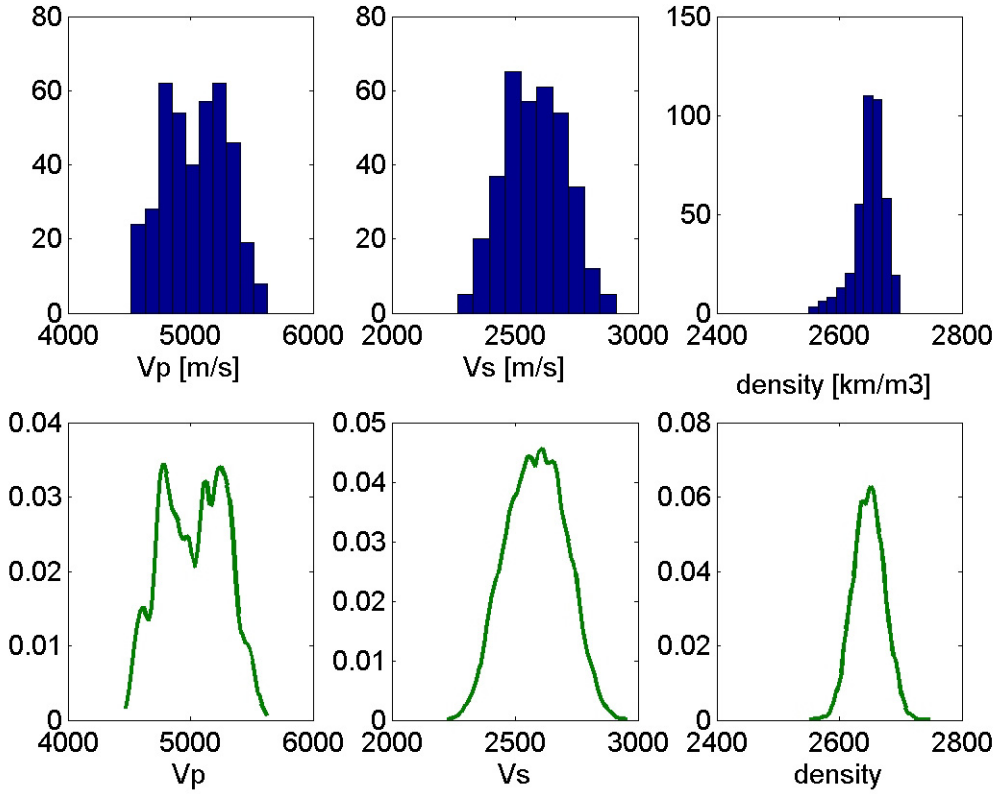

Figure 13: Upper panels: V_P V_S and density histograms derived from the well logs for the unfractured background rock properties. Lower panels: Corresponding probability density functions (PDFs).

The *Monte Carlo* procedure consists of randomly drawing correlated sets of V_P^{bot}, V_S^{bot}, and $density^{bot}$ from the distributions derived from the well logs for the unfractured background rock properties, and also from the assumed distributions for the crack density (e) and the aspect ratio (α) of the ellipsoidal cracks. We assume fractures to be saturated with gas. For each realization of a set of V_P^{bot}, V_S^{bot}, and $density^{bot}$, together with the crack density and the aspect ratio of the cracks, we compute the elastic properties for the fractured medium, using Hudson's model. If we repeat this procedure many times, we obtain a large number of realizations of elastic properties for the modeled fractured medium, which spans the intrinsic natural variability of the target rock properties.

For each realization, we again randomly draw a correlated set of V_P^{top}, V_S^{top}, and $density^{top}$ from the distribution corresponding to the cap rocks. Then, we compute the reflectivity at 0 and 40 degrees, stacked over all azimuths, corresponding to the near-

offset reflectivity (R_N) and the far-offset reflectivity (R_F). We also compute the difference between the near- and far-offset reflectivity (R_N-R_F), as well as azimuthal anisotropy of reflectivity at 40 degrees (A), using equations from Vavrycuk and Psencik (1998).

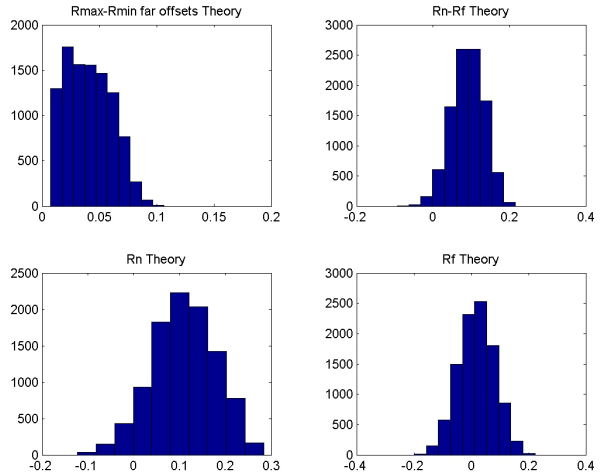

Figure 14: Histograms for the modeled reflectivity attributes. Top-left panel: Azimuthal anisotropy of reflectivity (A), evaluated at a 40 degree angle of incidence. Top-right panel: difference between the near- and far-offset reflectivity ($R_N - R_F$). Bottom-left panel: Near-offset reflectivity (R_N) Bottom-right panel: Far-offset reflectivity (R_F).

Figure 14 presents the histograms for the four different reflectivity attributes (R_N, R_F, R_N-R_F, and A) theoretically modeled, using the procedure described above. For comparison, Figure 15 presents the histograms for the same reflectivity attributes obtained from the seismic data. In both figures, the top-left panel presents the histogram for the azimuthal anisotropy in reflectivity at far offsets. We can observe that the theoretical and data-derived distributions are very similar. This suggests that the range of the crack density used in the modeling is relevant for this reservoir. The distributions for the near- and far-offset reflectivity presented on the bottom panels of both Figure 14 and 15 also agree reasonably well.

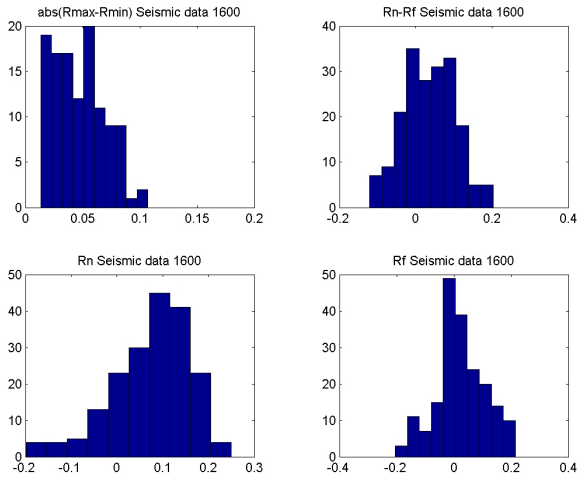

Figure 15: Histograms for the seismic reflectivity attributes derived from the real data. Top-left panel: Azimuthal anisotropy in reflectivity (A), evaluated at a 40 degrees angle of incidence Top-right panel: difference between the near- and far-offset reflectivity ($R_N - R_F$). Bottom-left panel: Near-offset reflectivity (R_N) Bottom-right panel: Far-offset reflectivity (R_F).

Figure 16 presents a 3D scatter-plot for the *Monte Carlo* realizations for sets of crack density, corresponding azimuthal anisotropy of reflectivity (A) at far offsets, and the difference between the near- and far-offset reflectivity ($R_N - R_F$).

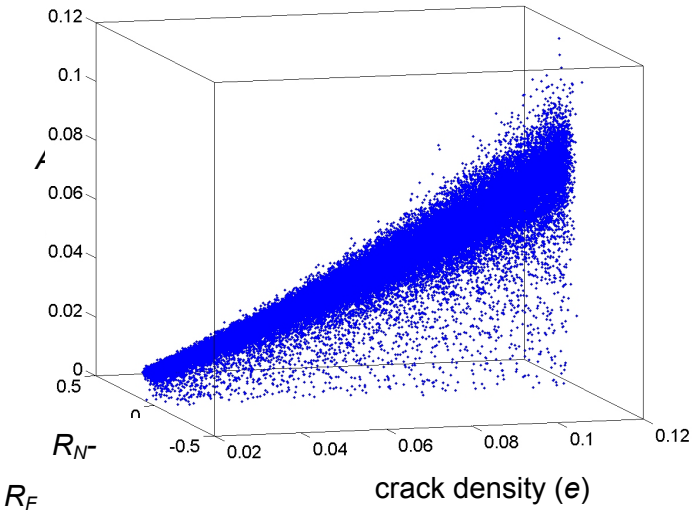

Figure 16: 3D scatter-plot for the 50,000 Monte Carlo realizations of sets of crack density (e), corresponding azimuthal anisotropy of reflectivity (A) at far offsets, and difference between the near- and the far-offset reflectivity ($R_N - R_F$).

From Figure 16, we can observe, as expected, that the azimuthal anisotropy in reflectivity at a fixed angle of incidence increases with crack density. Figure 17 presents the same scatter-plot for the *Monte Carlo* realizations as Figure 16, but projected in the plane of crack density and the difference between the near and the far reflectivity (R_N-R_F). We can observe that the rock-physics fracture modeling predicts that the difference between the near- and far-offset reflectivity increases with crack density. This observation is in accordance with the modeling results presented in Attachment E, where we show that the gas-filled fractured zones move the *AVO* gradient to larger negative values as compared to the *AVO* gradient of the unfractured rocks.

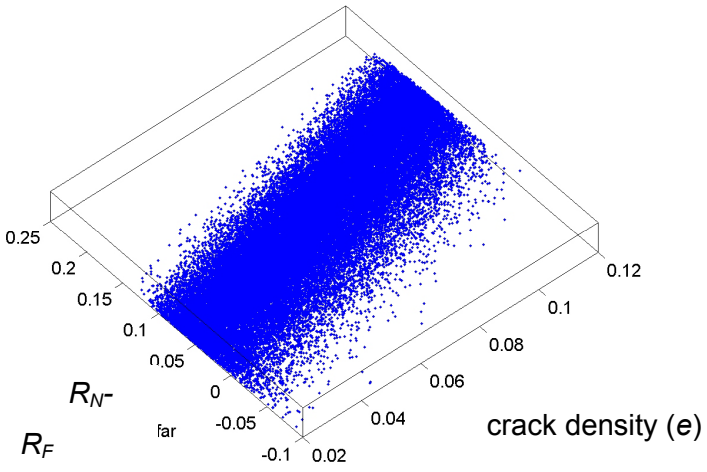

Figure 17: Scatter-plot for the 50,000 Monte Carlo realizations of sets of crack density (e) and the corresponding difference between the near- and the far-offset reflectivity ($R_N - R_F$).

Based on these 50,000 realizations of sets of crack density and reflectivity attributes, we derive the theoretical joint PDF, presented in Figure 18 as slices at constant A values. This theoretical PDF describes the relations between the fracture density and the observable data, represented by the reflectivity attributes, assuming a single set of vertical fractures. We denote this theoretical PDF as $\Theta(e, A, G)$, where G is given by the difference between the near- and far-offset reflectivity $(R_N$-$R_F)$.

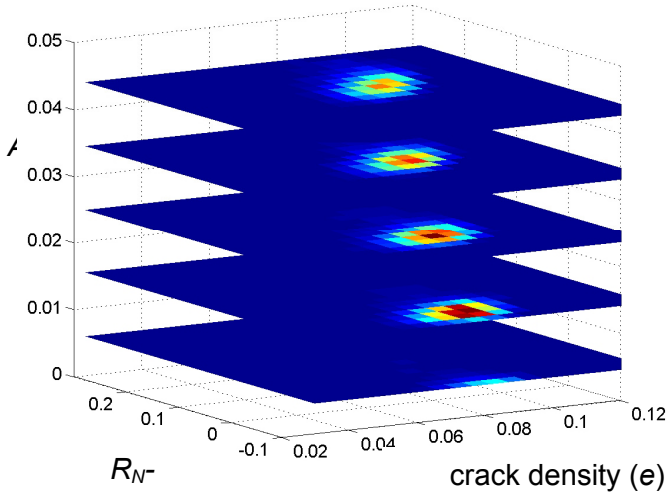

Figure 18: Theoretical Joint PDF based on the 50,000 Monte Carlo realizations of sets of crack density (e), corresponding azimuthal reflectivity anisotropy (A), and difference between the near- and the far-offset reflectivity ($R_N - R_F$). The PDF is presented as slices at constant A values.

We also consider the case of isotropic distribution of fracture orientations, corresponding to the highly fractured, brecciated zones. In this case, we use Hudson's (1981) model for isotropic distribution of the crack normals, and also Zoeppritz (1919) equations to derive the observable parameters, represented by the near- and far-offset reflectivity.

For both the isotropic and anisotropic fracture distributions, we assume the fractures to be saturated with gas.

In the next section, we present the results of integrating the prior information about fracture density with the reflectivity attributes from the 3D seismic data set, for hypotheses of both isotropic and anisotropic distribution of fractures.

A posteriori fracture density distribution

To obtain the updated distribution of fracture density at each spatial location, we need to combine the prior information, the reflectivity attributes affected by errors, and the theoretical information about the relations between the crack density and the seismic attributes, as presented in the previous sections.

We first obtain the updated fracture density distribution in the geological hypothesis of a vertical set of aligned fractures.

Figure 19 presents a map with *a posteriori* spatial distribution of the posterior expected values for fracture density at the top of the reservoir, conditioned only on the azimuthal anisotropy of reflectivity at far offsets (*A*).

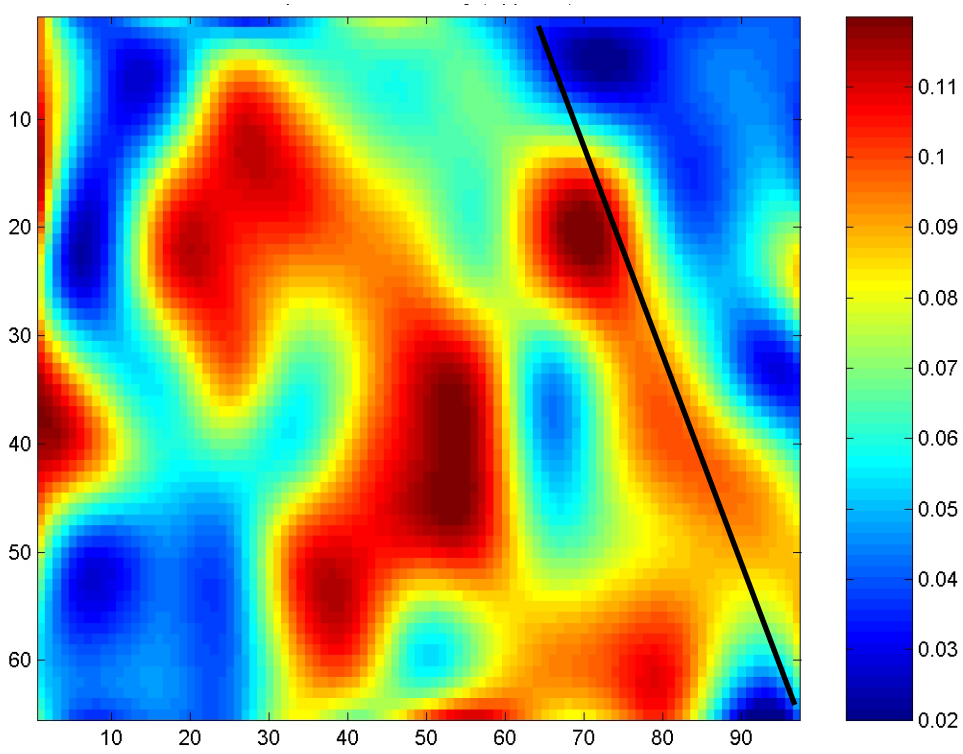

Figure 19: Map of the expected values for crack density derived from the *a posteriori* distribution, obtained by constraining the *a priori* information with the azimuthal anisotropy of reflectivity at far offsets (*A*), in the hypothesis of a vertical set of aligned fractures.

We observe a relatively higher fracture density in the proximity of the fault that penetrates the carbonate reservoir, sketched in Figure 19. We can also observe the asymmetric distribution of the expected crack density with respect to the fault, with higher values of fracture density in the hanging wall. This result is in agreement with outcrop observations that suggest higher fracture density in the proximity of the fault, especially in the hanging wall (Florez, 2003). We can also observe zones of higher fracture density away from the fault. These zones may also correspond to possible subseismic faults. Also, the expected posterior values for the crack density are

significantly larger than the prior values, presented in Figure 11, which were calibrated using Crampin's (1994) collection of field data (Attachment D) The stochastic rock physics modeling predicts a large correlation coefficient between the crack density and the azimuthal anisotropy in reflectivity, equal to 0.96. Therefore, the theory predicts that the azimuthal anisotropy in reflectivity is very constraining, such that the prior distribution for fracture density does not play a crucial role in the final results, in this case.

However, if we consider larger uncertainty in the data, the impact of the prior information is more significant. For example, Figure 20 presents a map with *a posteriori* distribution of the expected values for fracture density at the top of the reservoir, conditioned on the azimuthal anisotropy of reflectivity at far offsets (*A*), whose standard deviations of the measurement uncertainty are one order of magnitude larger than the ones derived from the bootstrap procedure.

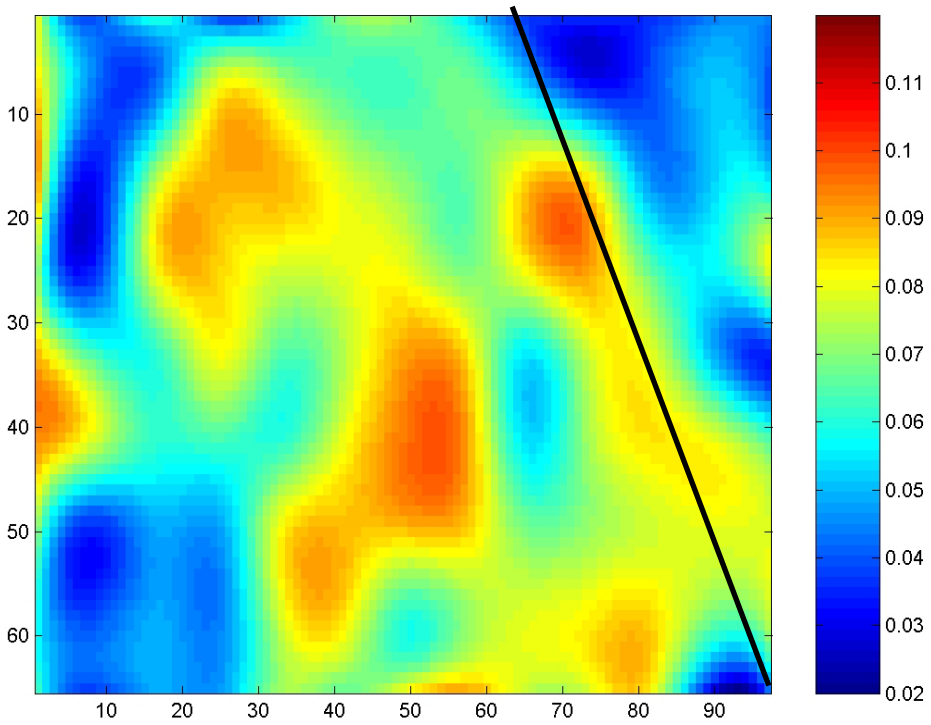

Figure 20: Map of the expected values for crack density derived from the *a posteriori* distribution, obtained by constraining the *a priori* information with the azimuthal anisotropy of reflectivity at far offsets (*A*), in the hypothesis of a vertical set of aligned fractures. Standard deviations of the measurement uncertainty are one order of magnitude larger than those in Figure 10.

We can observe that, when the measurement uncertainty is significantly larger, the prior information has a bigger impact on the posterior distribution of the crack density.

The expected posterior values of crack density from Figure 20 are significantly closer to the prior values, than the ones from Figure 19.

Next we obtain the distribution for the posterior expected values of fracture density at the top of the reservoir, conditioned on the difference between the near- and far-offset reflectivity ($G = R_N - R_F$), presented in Figure 21.

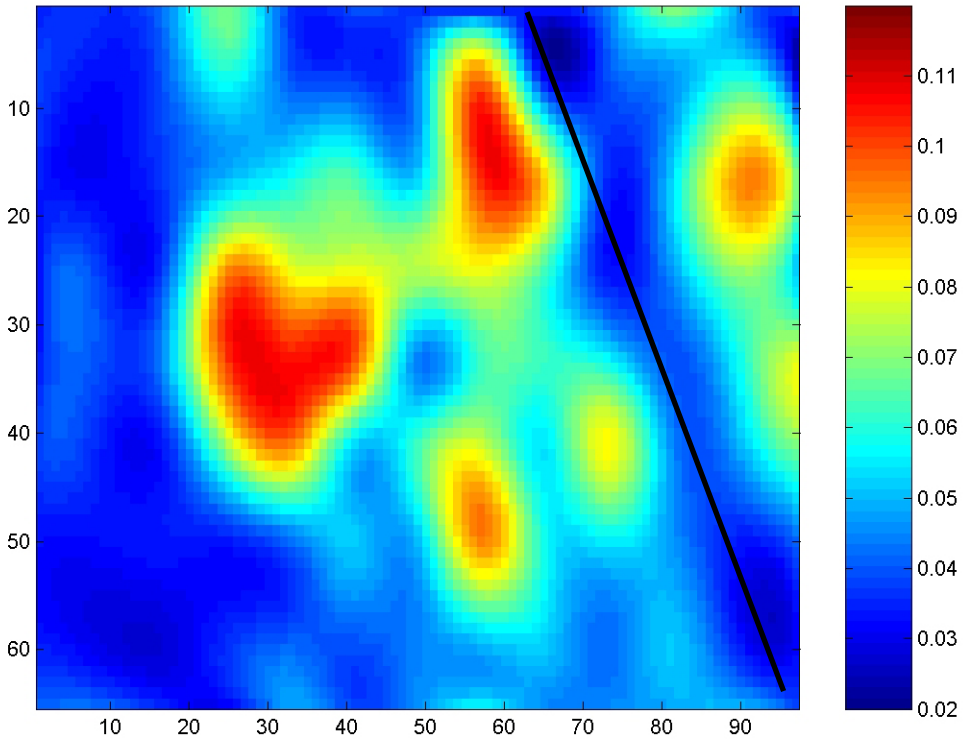

Figure 21: Map of the expected values for crack density derived from the *a posteriori* distribution, obtained by constraining the *a priori* information with the difference between the near- and far-offset reflectivity (*G*), in the hypothesis of a vertical set of aligned fractures.

From Figure 21 we observe that, by conditioning on the difference between the near- and the far-offset reflectivity, the expected values for fracture density along the fault are small. This is because along the fault the difference between the near- and far-offset reflectivity is small (Figure 8), and the rock-physics modeling predicts lower fracture density for smaller differences between the near- and far-offset reflectivity, as we can see in Figure 17. This result apparently contradicts the geological hypothesis of larger fracture densities along the fault. One explanation may be that the fault acts as a scattering feature for the seismic waves, generating small amplitudes for the near-offsets,

such that the difference between the near- and the far-offset reflectivity is itself small. On the other hand, the theoretical relations between the fracture properties and the seismic amplitudes derived through rock-physics fracture modeling and stochastic simulations correspond to effective medium theory, and they do not account for phenomena such as scattering.

However, we can still observe relatively higher fracture density in the proximity of the fault, especially in the hanging wall, as well as away from the fault (Figure 21). On average, the expected crack-density values obtained by combining the prior information with the difference between the near- and far-offset reflectivity (*G*) are smaller than the expected values for crack density obtained by combining the prior information with the azimuthal anisotropy of reflectivity at far offsets (*A*). This is because the stochastic rock physics modeling predicts a smaller correlation coefficient between the crack density and *G* (0.63), than between the crack density and *A* (0.96). Therefore, the impact of the prior crack density distribution on the posterior distribution obtained by conditioning on *G* is more significant than on the posterior distribution obtained by conditioning on *A*.

We also obtain the updated distribution of the expected values for fracture density at the top of the reservoir using jointly both reflectivity attributes: the azimuthal anisotropy of reflectivity at far offsets (*A*), and the difference between the near- and far-offset reflectivity (*G*).

Figure 22 presents the posterior expected values of fracture density jointly conditioned on both attributes. We can see that the distribution of the expected values for the crack density at the top of the reservoir conditioned on both attributes *A* and *G* is dominated by the reflectivity anisotropy (*A*) at far offsets. This is because the rock-physics fracture modeling and stochastic simulations predict higher correlation between the crack density and *A* than between the crack density and *G*.

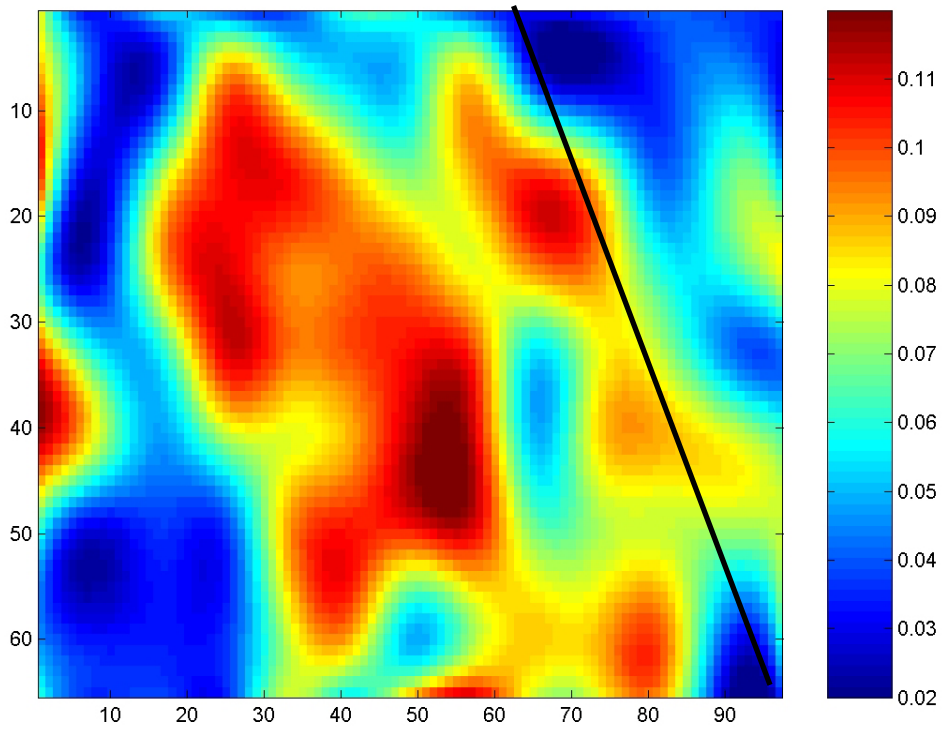

Figure 22: Map of the expected values for crack density derived from the *a posteriori* distribution, obtained by jointly constraining the *a priori* information with both the azimuthal anisotropy of reflectivity at far offsets (A) and the difference between the near- and far-offset reflectivity ($G=R_N-R_F$), in the hypothesis of a vertical set of aligned fractures.

However, if we consider the measurement uncertainty in the reflectivity anisotropy (A) to be one order of magnitude larger, then the posterior distribution for the expected values of crack density, conditioned both on A and G in Figure 23, is significantly different from the distribution in Figure 22. In this case, the impact of the prior information is more important. The values of fracture density are smaller, closer to the prior values of crack density.

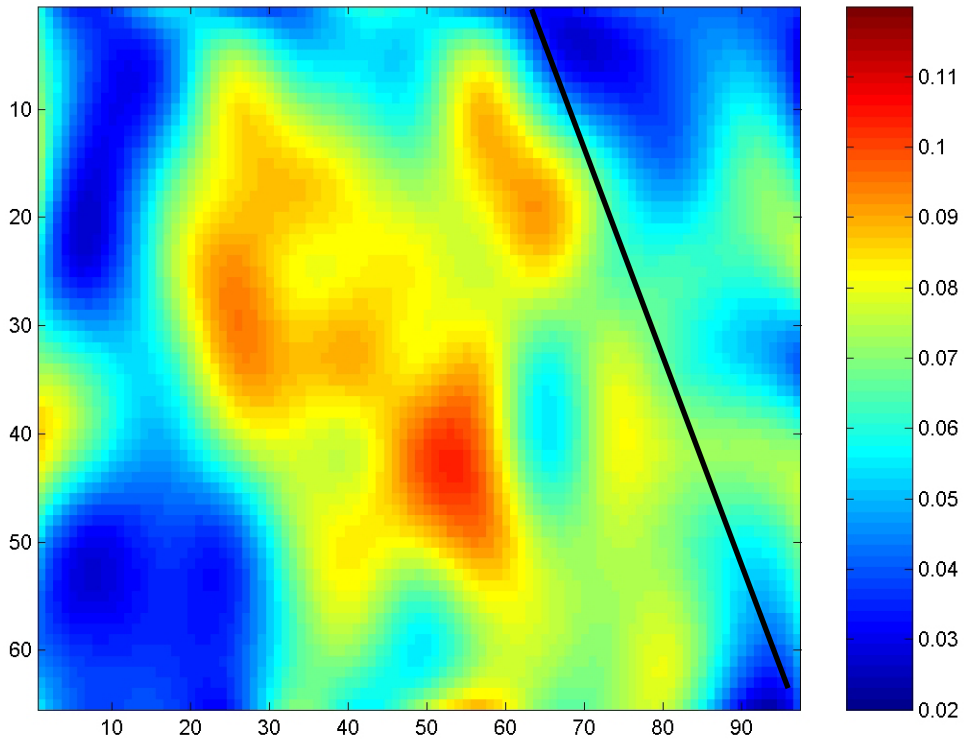

Figure 23: Map of the expected values for crack density derived from the *a posteriori* distribution, obtained by jointly constraining the *a priori* information with both the azimuthal anisotropy of reflectivity at far offsets (*A*) and the difference between the near- and far-offset reflectivity ($G=R_N-R_F$), in the hypothesis of a vertical set of aligned fractures. Standard deviations of the measurement uncertainty are one order of magnitude larger than those in Figure 10.

At each spatial location, we obtain not only the expected value of crack density, but the posterior probability density function (PDF). Figure 24 shows the prior PDF (red) for the crack density at a randomly chosen location, and also the *a posteriori* PDF after conditioning separately on *A* (black) and *G* (green), as well as the *a posteriori* PDF after jointly conditioning on *A* and *G* (blue).

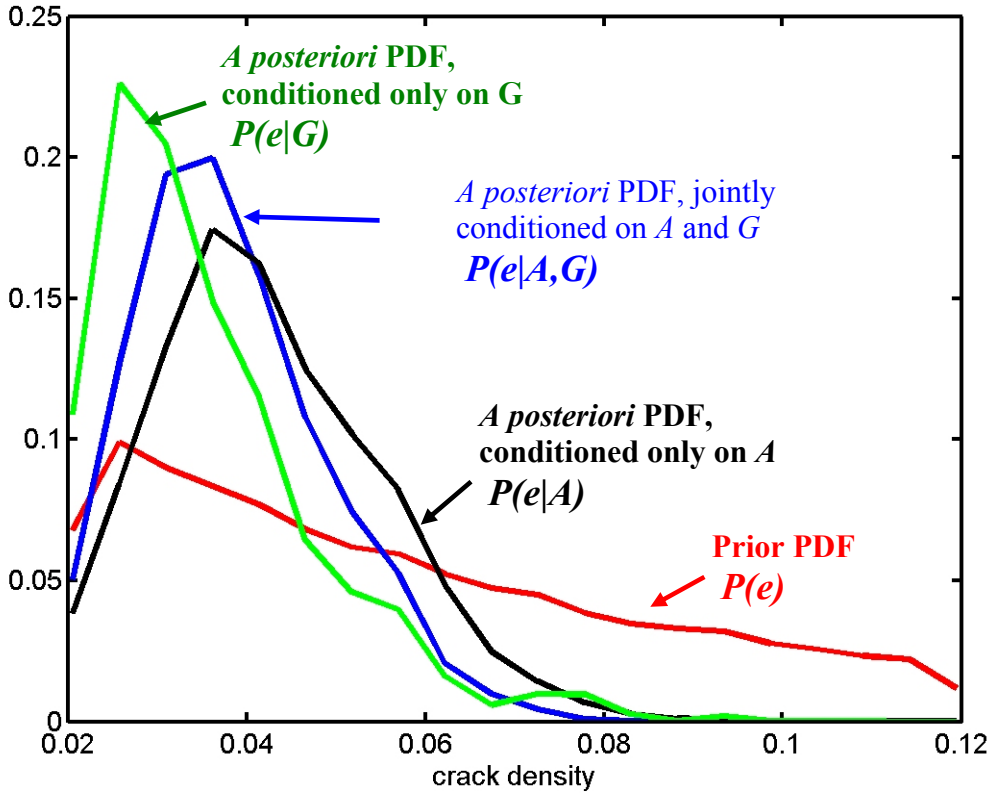

Figure 24: Probability density function for crack density at a randomly chosen location at the top of the reservoir. Red: *A priori* PDF for fracture density. Black: *A posteriori* distribution, conditioned only on the azimuthal anisotropy of reflectivity (*A*) at far offsets Green: *A posteriori* distribution for crack density conditioned only on the difference between the near- and the far-offset reflectivity (*G*). Blue: *A posteriori* distribution for crack density jointly conditioned on *A* and *G*.

The *a posteriori* distribution of crack density represents the updated measure of uncertainty after we combine the prior, the experimental and the theoretical information available. The standard deviation of the *a posteriori* distribution is a good measure for uncertainty when the posterior distribution is Gaussian. For example, Figure 25 presents the standard deviation about the expected values for fracture density from Figure 22, evaluated from the posterior PDF at each spatial location.

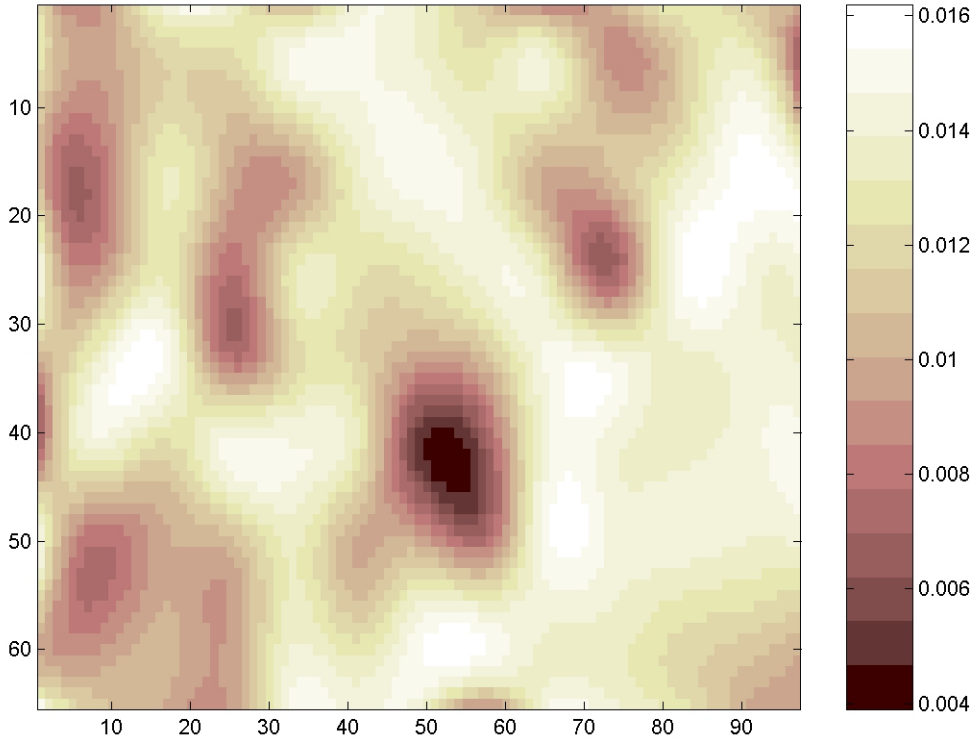

Figure 25: Map of the standard deviation about the expected values for crack density from Figure 5.21, derived from the *a posteriori* distribution obtained by jointly constraining the *a priori* information with both the azimuthal anisotropy of reflectivity at far offsets (A) and the difference between the near- and far-offset reflectivity ($G=R_N-R_F$), in the hypothesis of a vertical set of aligned fractures.

However, a more general way of expressing the uncertainty about the fracture density is through probability maps. At each grid point we can determine the probability that the fracture density exceeds a certain threshold. The probability that the fracture density exceeds a value of 0.09 is calculated at each grid point from the posterior PDF, as follows:

$$P(e > 0.09) = 1 - \int_{-\infty}^{0.09} \sigma_M(e)\, de \ . \tag{25}$$

For example, Figures 26 shows the probability map for crack density exceeding a value of 0.09, based on jointly conditioning the prior PDF on the azimuthal reflectivity anisotropy (A) and the difference between the near- and the far-offset reflectivity (G).

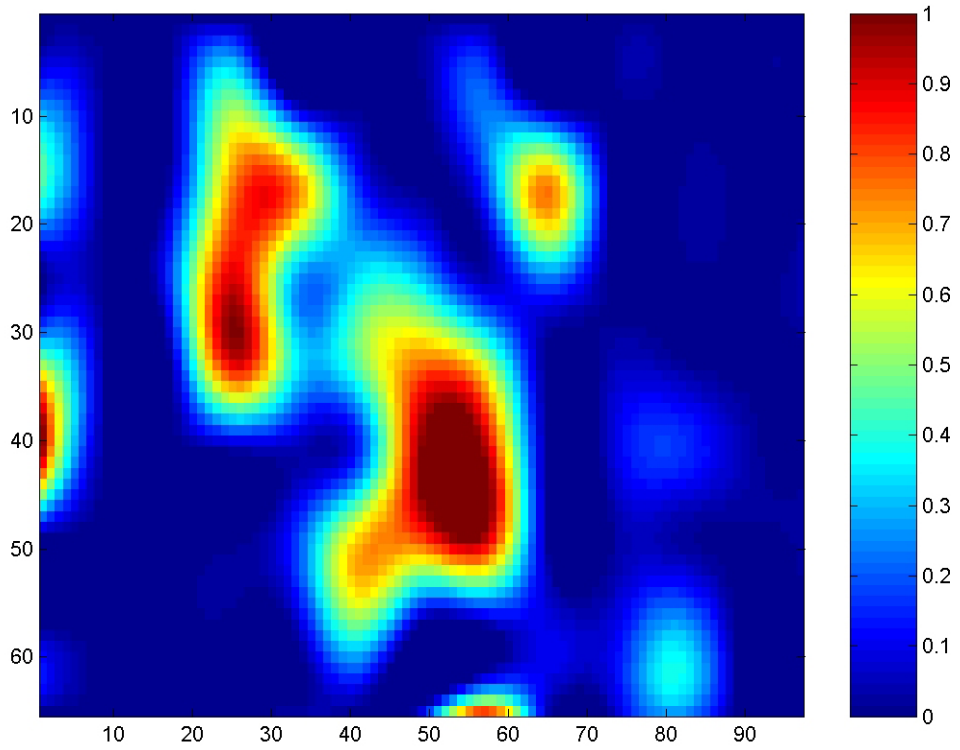

Figure 26: Probability map for fracture density exceeding a value of 0.09, obtained by jointly conditioning on the azimuthal reflectivity anisotropy (*A*) at far offsets and the difference between the near- and far-offset reflectivity (*G*). Geological hypothesis: a vertical set of aligned fractures.

From Figure 26 we can see that the probability of the fracture density exceeding a value of 0.09 is relatively small, except in two zones. Therefore, in the hypothesis of a vertical set of aligned fractures, the areas of higher probability of fractures are the ones highlighted in red on the probability map from Figure 26.

Figure 27 presents the same probability map as in Figure 26, but in this case the measurement uncertainty in the reflectivity anisotropy (*A*) is one order of magnitude larger. We can see that in this case, the probability that the fracture density exceeds the value of 0.09 is much lower, since the impact of the prior information, which indicates smaller fracture density values, is more significant.

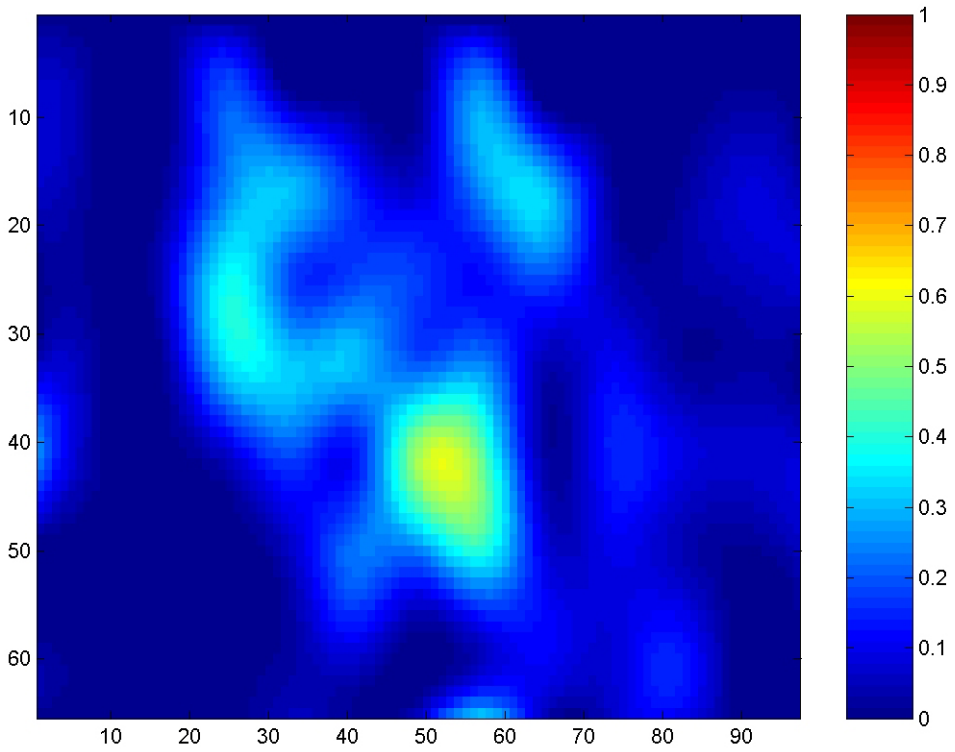

Figure 27: Probability map for fracture density exceeding a value of 0.09, obtained by jointly conditioning on the azimuthal reflectivity anisotropy (*A*) at far offsets and the difference between the near- and far-offset reflectivity (*G*). Geological hypothesis: a vertical set of aligned fractures. Standard deviations of the measurement uncertainty are one order of magnitude larger than those in Figure 10.

We can also obtain at each spatial location, the probability that the fracture density is smaller than a certain threshold. For example, Crampin (1994) suggests that a fracture density of 0.04 corresponds to a relatively small degree of fracturing. Therefore, it is important to evaluate at each location the probability that the fracture density is smaller than this value. In this way we can estimate the risk of drilling a new well in a zone of small fracture density.

Figure 28 shows a probability map for fracture density being smaller than 0.04, after combining the prior information with the azimuthal anisotropy in the reflectivity at far offsets, and the difference between the near- and far-offset reflectivity. The highlighted zones in red from Figure 28, correspond to the areas where the probability that the fracture density is smaller than 0.04 is high. If the permeability of the reservoir is

dominated by the open fractures, then these areas should be avoided for drilling production wells.

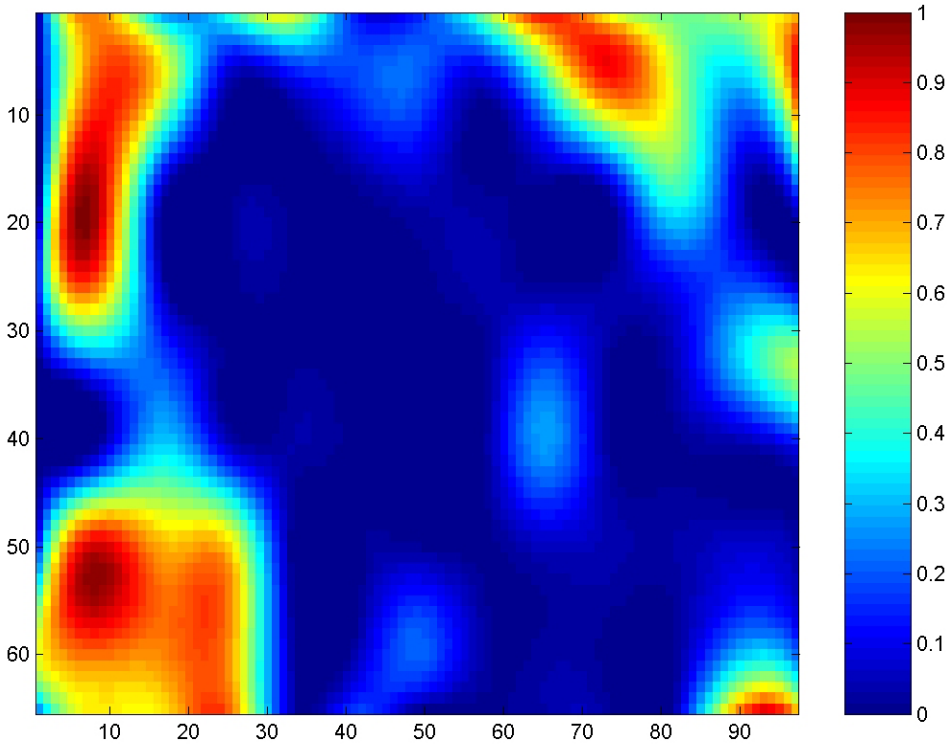

Figure 28: Probability map for fracture density being smaller than a value of 0.04, obtained by jointly conditioning on the azimuthal reflectivity anisotropy (A) at far offsets and the difference between the near- and far-offset reflectivity (G). Geological hypothesis: a vertical set of aligned fractures.

We also consider the geological hypothesis of randomly oriented fractures, which may correspond to brecciated zones in the proximity of possible subseismic faults. In this case, we combine the prior information about fracture density from geological interpretation with the near- and the far-offset reflectivity attributes.

Figure 29 presents a map with the expected values of crack density after conditioning the prior information on the far-offset reflectivity (R_F).

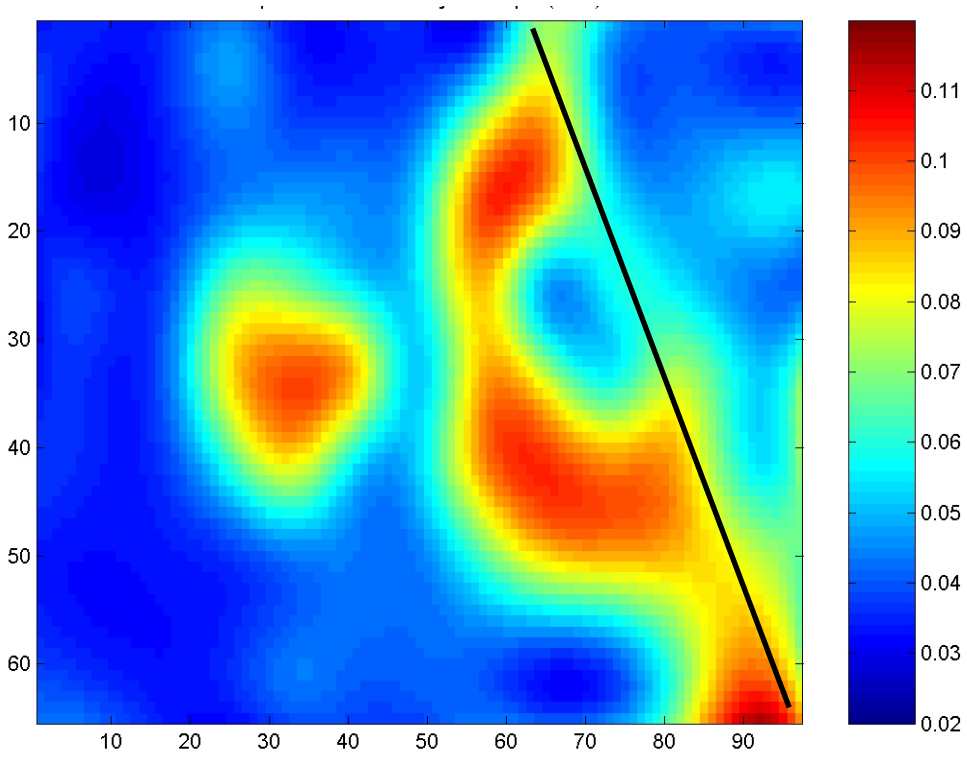

Figure 29: Map of the expected values for crack density derived from the *a posteriori* distribution obtained by constraining the *a priori* information with the far-offset reflectivity (R_F), in the hypothesis of randomly oriented fractures.

We can observe relatively larger crack density values in the hanging wall of the fault, schematically represented in Figure 29, as well as away from the fault.

Figure 30 presents a map with the expected values of crack density after conditioning the prior information on the near-offset reflectivity (R_N). In the vicinity of the fault, we observe a very good agreement between the geological hypothesis of higher fracture densities associated with the interpreted fault, and the actual near-offset reflectivity data. The seismic amplitudes are significantly smaller along the fault, implying that the assumed randomly oriented cracks have higher density in this area. However, there may be other phenomena associated with the interpreted fault, such as scattering, which are not accounted for by the theory used in this case.

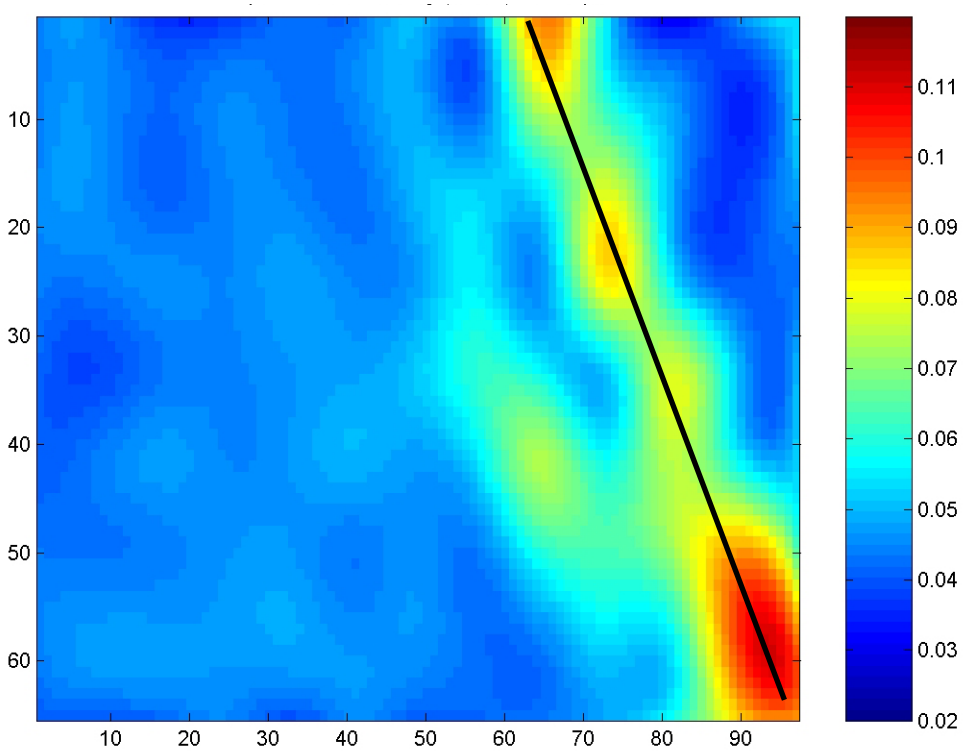

Figure 30: Map of the expected values for crack density derived from the *a posteriori* distribution, obtained by constraining the *a priori* information with the near-offset reflectivity (R_N), in the hypothesis of randomly oriented fractures.

If we assume independence between the near- and far-offset reflectivity, we can derive the updated distribution of the crack density conditioned on both the near- and far-offset reflectivity, by simply multiplying each of the individual posterior probability density functions (PDF), as presented earlier. Equation 26 is derived from Equation 13, showing that the *a posteriori* PDF conditioned on R_N and R_F, $\sigma_M(e|R_N,R_F)$, is proportional to the *a posteriori* PDF conditioned on R_N, $\sigma_M(e|R_N)$ multiplied by the *a posteriori* PDF conditioned on R_F, $\sigma_M(e|R_F)$. In Equation 26, $\rho_M(e)$ represents the prior PDF for fracture density.

$$\sigma_M(e|R_N,R_F) = \frac{1}{\rho_M(e)} \sigma_M(e|R_N)\sigma_M(e|R_F) \tag{26}$$

Figure 31 presents a map with the expected values of the crack density computed from the *a posteriori* PDF, $\sigma_M(e|R_N,R_F)$, assuming independence between the variables R_N and R_F (Equation 26).

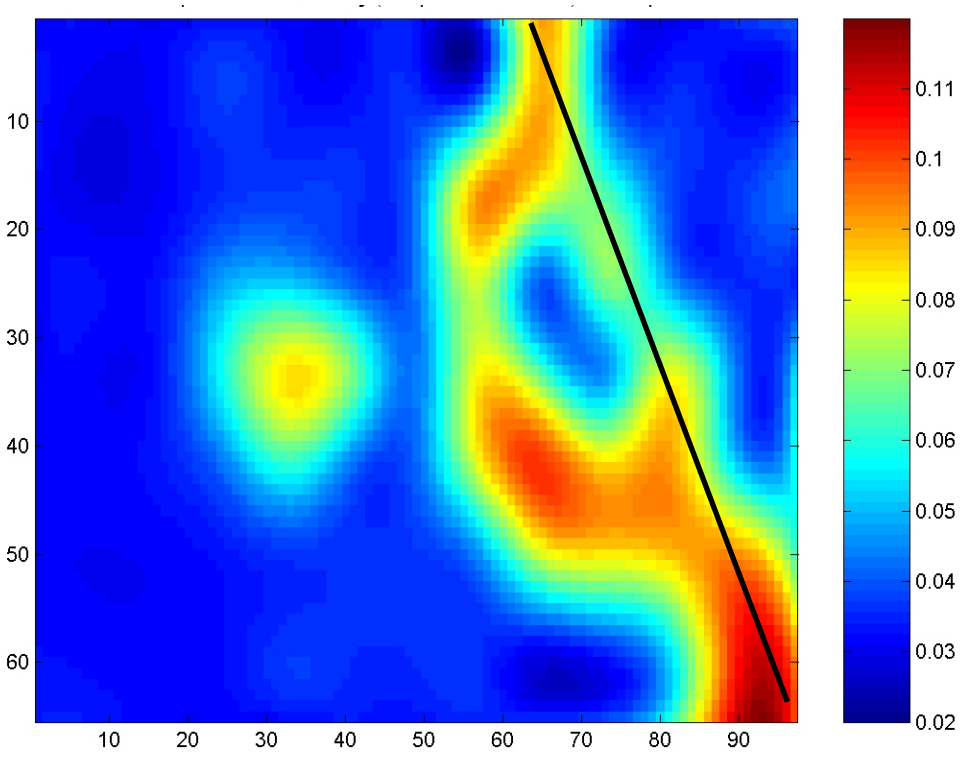

Figure 31: Map of the expected values for crack density derived from the *a posteriori* distribution, assuming independence between the near- and far-offset reflectivity (Equation 26). Geological hypothesis: randomly oriented fractures.

If we jointly condition the prior information about fracture density on both the near- and the far-offset reflectivity, without assuming independence, we obtain a different distribution for the expected values of crack density at the top of the reservoir, presented in Figure 32. In this case, the correlations between the near- and the far-offset reflectivity are taken into account, by using the general framework of the methodology presented earlier.

By comparing Figures 31 and 32, we can observe that, assuming independence in this case leads to a different distribution for the expected crack density than is derived by jointly conditioning on the near- and far-offset reflectivity. The correlation coefficient between the near- and far-offset reflectivity calculated by rock-physics stochastic simulations is 0.86. This value shows a significant correlation between the variables, and that is why the assumption of independence does not hold in this case. Therefore, if the

variables that we condition on are not independent, deriving the *a posteriori* PDF for the model parameters using Equation 26 may be misleading.

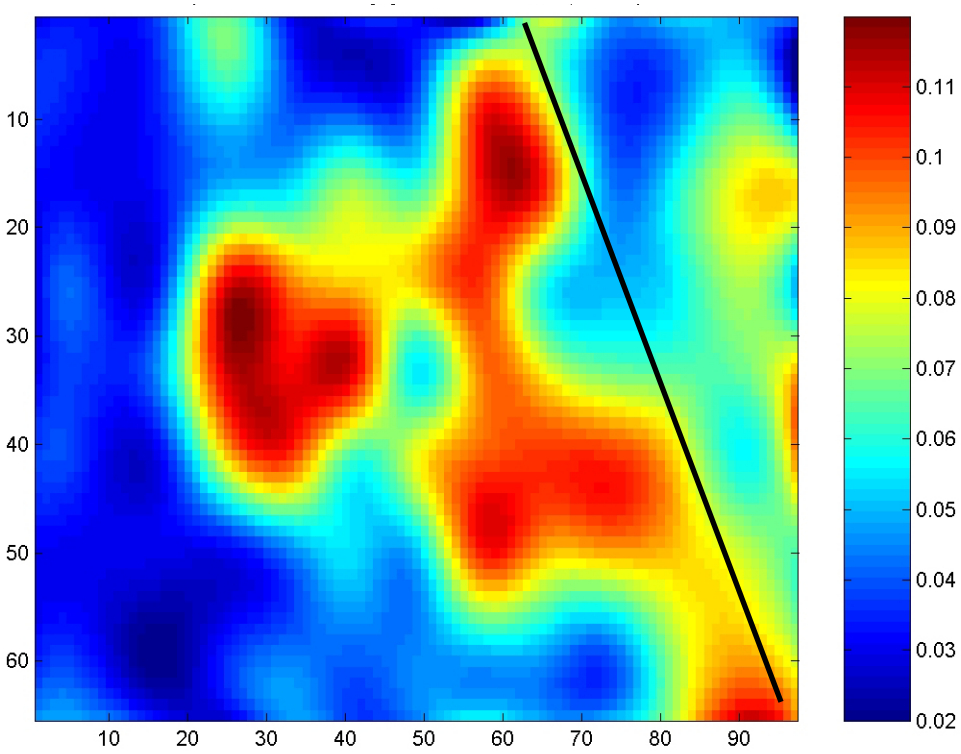

Figure 32 Map of the expected values for crack density derived from the *a posteriori* distribution obtained by jointly constraining the *a priori* information with both the near- and far-offset reflectivity, in the hypothesis of randomly oriented fractures.

We also use the difference between the near- and far-offset reflectivity, ($G=R_N-R_F$), to obtain the updated crack density distribution. Figure 33 presents the map with the expected values of crack density after conditioning the prior information on the difference between the near- and far-offset reflectivity (G).

For the geological hypotheses of a single set of vertical fractures and of randomly oriented cracks, the distributions of the expected fracture density at the top of the reservoir, obtained by combining the prior information with the difference between the near- and far-offset reflectivity stacked over all azimuths, are very similar, as we can see from Figures 21 and 33.

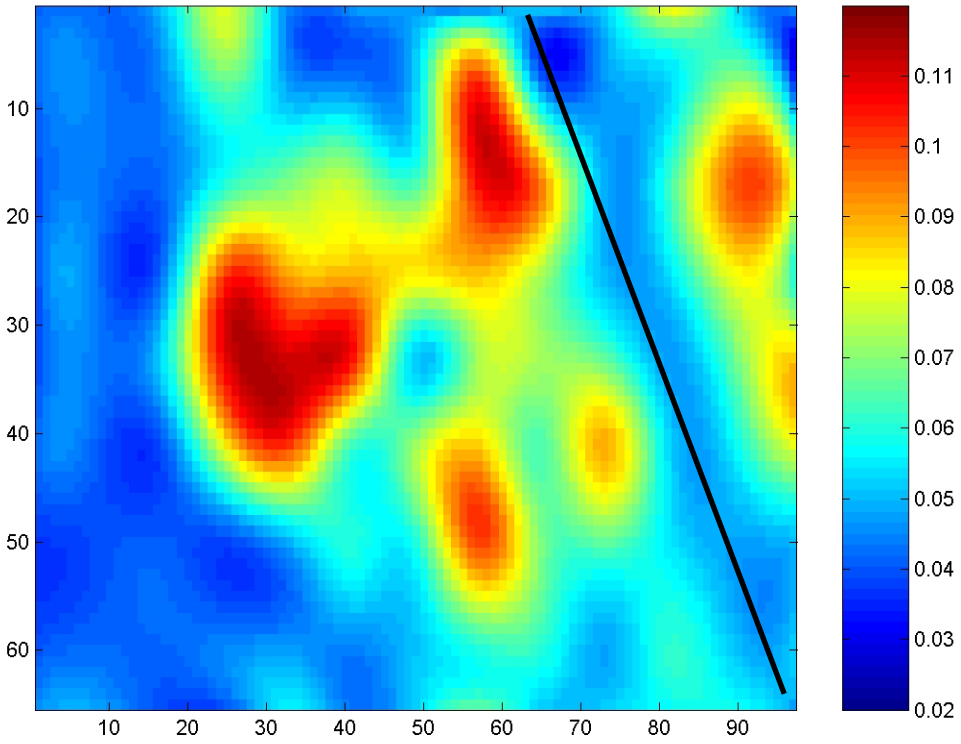

Figure 33: Map of the expected values for crack density derived from the *a posteriori* distribution obtained by constraining the *a priori* information with the difference between the near- and far-offset reflectivity (*G*), in the hypothesis of randomly oriented fractures.

Next, we obtain the updated distribution of fracture density at the top of the reservoir by jointly conditioning the prior PDF on both the far-offset reflectivity (R_F) and the difference between the near- and far-offset reflectivity (*G*). Figure 34 presents the map with the expected values of fracture density jointly conditioned on both reflectivity attributes (R_F and *G)*.

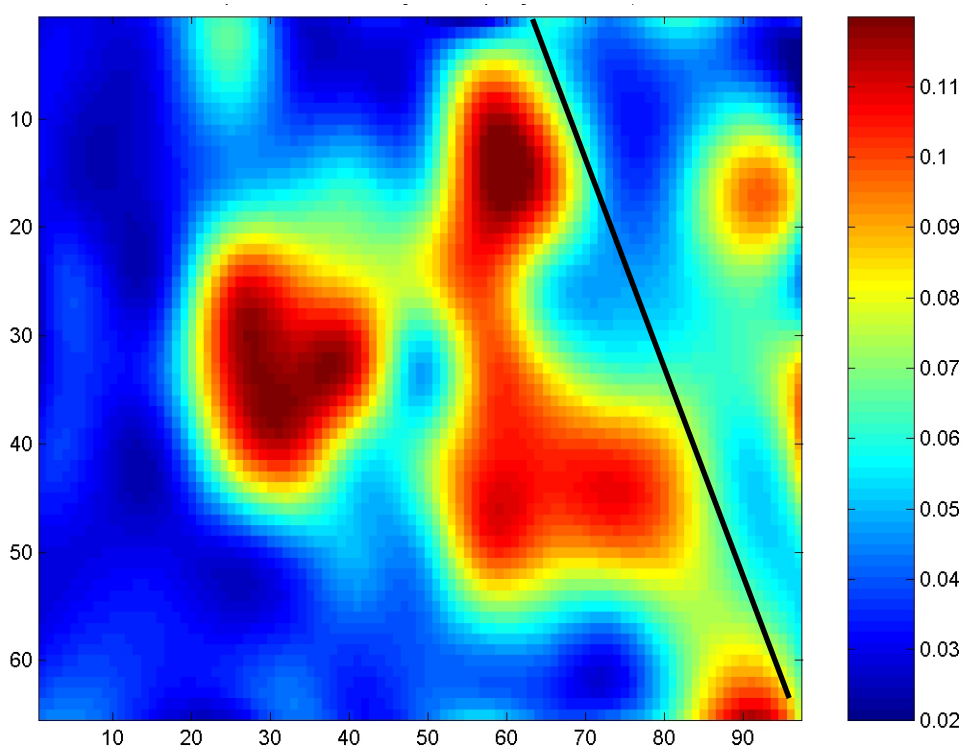

Figure 34: Map of the expected values for crack density derived from the *a posteriori* distribution obtained by jointly constraining the *a priori* information with both the far-offset reflectivity (R_F) and the difference between the near- and far-offset reflectivity (G), in the hypothesis of randomly oriented fractures.

By comparing Figures 32 and 34, we can observe that the distributions for the posterior expected fracture densities obtained by jointly conditioning on R_N and R_F (Figure 32) are practically identical to those obtained by jointly conditioning on R_F and the difference R_N-R_F (Figure 34). This result is expected, suggesting that data manipulation does not bring new information. The two different pieces of information used in both cases are the near- and far-offset reflectivity.

However, data manipulation may play a role in obtaining independent variables, such that we can use the independence assumption to derive the *a posteriori* PDF on the fracture parameters. For example, Figure 35 presents the updated distribution for the expected values of fracture density derived by assuming independence between G and R_F, by using the Equation 13, as follows:

$$\sigma_M(e|G,R_F) = \frac{1}{\rho_M(e)}\sigma_M(e|G)\sigma_M(e|R_F). \quad (27)$$

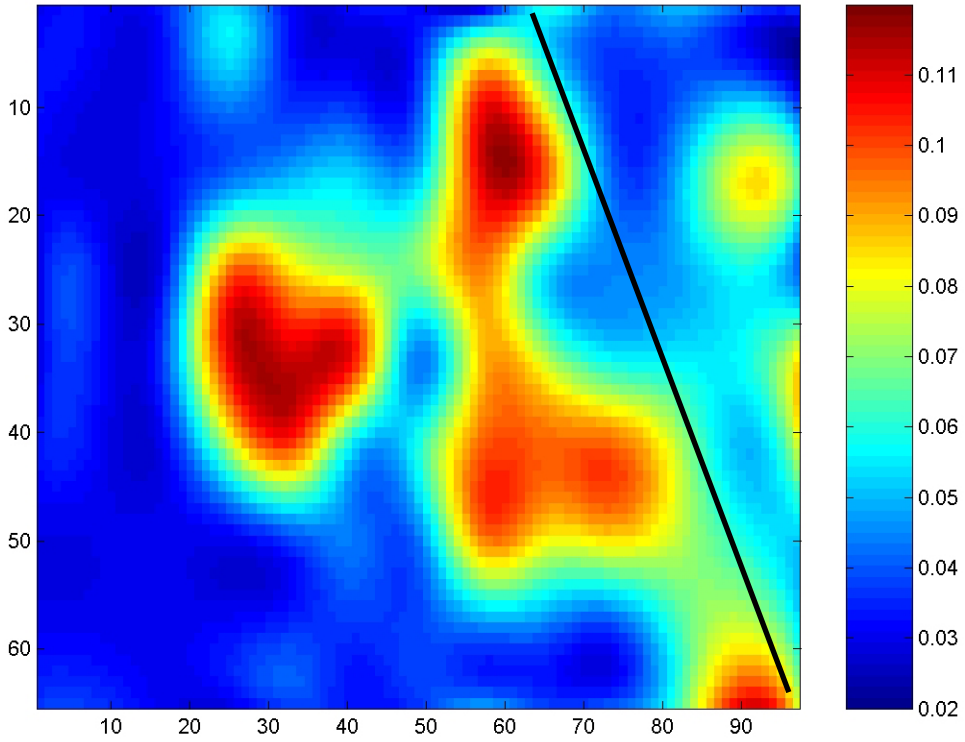

Figure 35: Map of the expected values for crack density derived from the *a posteriori* distribution by assuming independence between the far-offset reflectivity (R_F) and the difference between the near- and far-offset reflectivity (G), using Equation 27. Geological hypothesis: randomly oriented fractures.

In this case, the map of the expected values for fracture density at the top of the reservoir, derived by assuming independence between R_F and G (Figure 35), is very similar to the map obtained by jointly conditioning the prior PDF of fracture density on R_F and G (Figure 34). This suggests that the variables R_F and G (R_N-R_F) can be considered independent. Their correlation coefficient calculated based on the rock physics modeling and stochastic simulations has a small negative value of -0.18. This is why the distribution for the expected values of the crack density derived based on R_F and G by assuming independence is almost the same as the distribution for the expected crack-density values jointly conditioned on the G and R_F.

For both geological hypotheses of isotropic and anisotropic distribution of cracks, the prior information about the fracture distribution for this reservoir does not play a crucial

role in the final results of the integration. This is because the rock-physics fracture modeling predicts that the seismic data is very constraining compared to the prior uncertainty about the fracture density. However, the prior information can sometimes have a significant impact on the posterior distribution of the model parameters. This happens when the uncertainty in the data and/or in the theoretical PDF, due to natural variability of the rock properties, are comparable with the prior uncertainty on the model parameters.

To conclude, in this section we show examples of integrating the prior information about fracture density with seismic-reflectivity attributes from a 3D seismic data for a fractured carbonate reservoir, under two geological hypotheses. The first hypothesis is that the fractures are vertical, aligned and more-or-less regularly spaced, such that they generate an azimuthally anisotropic medium. The second hypothesis is that the fractures occur in swarms associated with possible subseismic faults, and they are more randomly oriented, such as in brecciated areas.

Under both geological hypotheses we highlight the zones of higher fracture density at the top of the reservoir by conditioning the prior PDF of fracture density on different reflectivity attributes. The final result is represented by the *a posteriori* PDF of the fracture density at each spatial location. The posterior PDF of fracture density provides us with a complete measure of uncertainty after integrating the available geological, theoretical, and seismic information.

Conclusions

This attachment presents a way of integrating prior geological information with seismic data for improved subsurface property estimation, using statistical rock-physics within the framework of an inverse problem, as defined by Tarantola (1987). We illustrate the method with fracture characterization. The rock-physics theories provide the link between the fracture parameters and the seismic data, while the statistical approach allows us to integrate quantitatively all the various types of information derived from geology, theory, well-log and seismic measurements.

The most general way to express mathematically the state of knowledge about the fracture parameters is through probability density functions. The language of Probability Theory allows us to account for the measurement errors and for the uncertainty in the relation between the fracture parameters and the seismic data due to natural variability of the target rock properties. This approach enables us to also estimate the uncertainty about our predictions, and to quantify the value of each type of information in reducing this uncertainty. Therefore, this method can have a significant impact on risk and decision analysis.

The methodology for quantitative data integration provides a new framework for estimating the subsurface rock properties and the uncertainty of our estimations, emphasizing the key importance of the rock physics theories in linking geological observations and seismic measurements. In this approach we use stochastic simulations together with deterministic rock-physics theories to estimate the uncertainty between the fracture parameters and seismic data due to natural variability of the rock properties. The well-log data represents an essential piece of information for calibrating the seismic properties of the target rocks. The natural variability of the rock properties is derived from the well-logs. Therefore more logged wells can help in better estimating the variability of the target rock properties.

To summarize, there are three different types of information that we need to integrate quantitatively: 1) the prior information on the fracture parameters, which often comes from geology, 2) the results of some experiments, often represented by the seismic data, and 3) the theoretical relation between the fracture parameters and the experimental data, which is given by the rock-physics theories, and calibrated using well-log data. The solution to the integration methodology is obtained by combining the prior, the experimental, and the theoretical information, to derive the *a posteriori* state of knowledge (Tarantola, 1987) of the fracture parameters. The *a posteriori* probability density function represents the updated measure of uncertainty about the fracture parameters after conditioning the prior information with the observed seismic data.

An important component of the integration methodology is the prior information on the fracture parameters. This attachment also presents a method to estimate the prior

uncertainty about the fracture parameters, using a probability density function derived from the maximum entropy principle (Jaynes, 1983). This principle allows us to assign probabilities that are maximally uninformative, while still incorporating the information that one actually possesses. Therefore, we can estimate the *a priori* PDF based on a set of constraints imposed by geological interpretation.

In this attachment we emphasize not only the theoretical approach of combining prior geological information with seismic data, but we also present the practical steps of the methodology for quantitative data integration, giving an example from a fractured carbonate reservoir of gas in eastern Texas.

Based on the geological information about the reservoir, we consider two geological hypotheses. The first hypothesis is that the fractures are vertical and aligned, such that they generate an anisotropic medium. The second hypothesis is that the fractures occur in swarms associated with possible subseismic faults, and they are more or less randomly oriented, such as in brecciated zones.

In the example presented in this attachment, the model parameter is the fracture density. The prior distribution for the expected values of fracture density at the top of the reservoir is derived based on the interpretation of a major fault, resolved by the seismic data. The uncertainty about the prior values of fracture density is estimated using the Maximum Entropy Principle.

The observable data parameters used in this example are represented by various reflectivity attributes, such as the near- and the far-offset reflectivity, and also the azimuthal anisotropy of reflectivity at far offsets. The uncertainty in the reflectivity data is assumed to be Gaussian.

The theoretical relations between the fracture parameters and the observable data are derived using rock physics modeling and stochastic simulations, in both geological hypotheses of isotropic and anisotropic fracture distributions. The theoretical PDFs represent the uncertainty in the relation between the fracture density and seismic attributes due to natural variability, and it is assumed representative for the entire study area.

Finally, we combine the prior information, the reflectivity attributes and the theoretical information to obtain the *a posteriori* distribution of fracture density at each spatial location. From the *a posteriori* PDF on the fracture density we can compute the posterior expected values. The integration methodology relatively higher fracture density values in the proximity of the fault. However, we also highlight zones of higher fracture density away from the fault, possibly associated with smaller, subseismic faults, which may not have been predicted otherwise.

The *a posteriori* PDF derived at each spatial location represents a complete measure of uncertainty, from which we can derive, for example, the probability that the fracture density is smaller than certain thresholds. In this way we can assess the risk of drilling a new well in an area with low fracture density. These probability maps can serve as a decision-making guideline for reservoir management.

Attachment I

References

Alford, R.M., 1986, Shear data in the presence of azimuthal anisotropy: Dilley, Texas, 56th Ann. Int. SEG Meeting, Houston, Expanded Abstracts, 476-479.

Anselmetti, F.S. and Eberly, G.Pl., Sonic velocity in carbonate sediments and rocks, Cabonate Seismology, ed. Palaz, I. and Marfurt, K.J., SEG.

Aster, A. C., Shearer, P. M., 1991, High frequency borehole sismograms recorded in the San Jacinto fault zone, Southern California, Bull. Seism. Soc. Am., 81, 1057-1080.

Avseth, P., Mukerji, T., and Mavko, G., 2005, Quantitative seismic interpretation, Cambridge University Press, in press.

Anderson, E. M., 1951, Dynamics of Faulting and Dyke Formation with application to Britain. 206p.

Antonellini and Cruikshank, 1992, Geometry of faults and joints in Entrada Sandstone, Arches National Park, Utah: Stanford Rock Fracture Project Field Guide.

Aydin, A., 1973, Field study and theoretical analysis of some small faults in Montana, Wyoming, and Utah. M. Sc. Thesis: Stanford University.

Backus, G., 1962, Long-wave elastic anisotropy produced by horizontal layering, J. Geophys, Res., 76, 4427-4440.

Bakulin, A., Grechka, V. Tsvankin, I., 2000, Estimation of fracture parameters from reflection seismic data – Part I: HTI model due to a single fracture set, Geophysics, 65, 1788-1802.

Bai, T., and D.D. Pollard, 2000, Fracture spacing in layered rocks: a new explanation base on the stress transition, Journal of Structural Geology, 29, p.43-57.

Bai, T. and D. Pollard, 2000, Fracture spacing in layered rocks; a new explanation based on the stress transition, Journal of Structural Geology, vol.22, no.1, pp.43-57.

Barton, C.A., Zoback, M.D., and Moos, D., 1995, Fluid flow along potentially active faults in crystalline rock: Geology, v. 23, p. 683-686.

Batzle, M., Wang, Z., 1992, Seismic properties of pore fluids, Geophysics, Vol. 57, No. 11, 1396-1408.

Bayes, T., 1783, An essay towards solving a problem in the doctrine of chances, Phil. Trans. Roy. Soc., 53, 370-418.

Booth, D.C, Crampin, S., Evans, R., Roberts, G., 1985, Shear -wave polarizations near the North Anatolian Fault-I Evidence for anisotropy induced shear-wave splitting, Geophys. J. R. astr. Soc., 83, 61-73

Booth, D. C.,Crampin, S., Lovell, J.H., Chiu, J.-M., 1990, Temporal changes in shear wave splitting during an earthquake swarm in Arkansas, J. Geophys. Res., 95, 11151-11164.

Box, G. E. P., Tiao, G. C., 1992, Bayesian Inference in Statistical Analysis, (edited by Wiley- Interscience).

Buchbinder, G. G, 1985, Shear wave splitting and anisotropy in the Charlevoix seismic zone, Quebec, Geophys. Res. Lett., 12, 425-428.

Buchbinder, G. G., 1990, Shear wave splitting and anisotropy from the aftershocks of the Nahanni, Northwest Territories, earthquakes, J. Geophys. Res., 95, 4777-4785.

Bush, I., Crampin, S., 1991, Paris Basin VSPs: case history establishing combinations of matrix-and crack-anisotropy modeling shear wave-fields near point singularities, Geophys. J. Int., 107, 433-447

Castagna, J.P., Batzle, M.L.,and Kan,T.K., 1993, Rock-Physics- the link between the rock properties and AVO response, Offset-Dependent Reflectivity-Theory and Practice of AVO Analysis, eds. Castagna J.P. and Backus, M.M., SEG, Tulsa.

Cliet, C., Brodov, L, Tikhonov, A., Marin, D. Michon, D., 1991, Anisotropy survey for reservoir definition, Geophys. J. Int, 107, 417-427.

Cooke, M. L., P. N. Mollema, D. Pollard and A. Aydin, 2000, Interlayer slip and joint localization in the East Kaibab Monocline, Utah: field evidence and results from numerical modeling, in: J. W. Cosgrove, and M. S. Ameen, Forced Folds and Fractures. Geological Society, London, Special Publications, v. 169, 23-49.

Crampin, S., 1994, The fracture criticality of crustal rocks, Geophys. J. Internat., 118, 428-438.

Crawforth, F.C., 1951, The James Lime and its relationship to the Cow Creek and Dierks limestones, Gulf Coast Association Geological Society, First Annual Meeting, 171-181.

Daley, T. M., McEvilly, T. V., 1990, Shear-wave anisotropy in the Parkfield Varian Well VSP, Bull. Seism. Soc. Am., 80, 857-869.

Davatzes N., 2003, Ph.D. Dissertation, Stanford University

Davatzes, N. and A. Aydin, 2003, The formation of conjugate normal fault systems in folded sandstone by sequential jointing and shearing, Waterpocket monocline, Utah, Journal of Geophysical Research, vol. 108, no. B10, p.2478, doi: 10.1029/2002JB002289.

Deutsch, C., and A. Journel, 1998, GSLIB Geostatistical software library and user's guide, second edition, Oxford University Press, New York. pp. 369.

Diegel, F.A., J.F. Karlo, D.C. Schuster, R.C. Shoup, and P.R. Tauvers, 1995, Cenozoic structural evolution and tectono-stratigraphic framework of the northern Gulf coast continental margin, in M. P. A. Jackson, D.G. Roberts, and S. Snelson, eds, Salt tectonics: a global perspective: AAPG Memoir 65, 109-151.

Du, X., 1990, On shear-wave splitting in the Los Angeles Basin, Pure and Applied Geophys., 134,175-194.

Dula, W. F., Jr., 1991, Geometric models of listric normal faults and rollover folds, AAPG Bulletin, v. 75, no. 10, 1609-1625.

Efron B., Tibshirani, R., 1998, An introduction to the bootstrap: Chapman and Hall/CRC.

Ewing, T., R. Budnik, J. Garrison, A. Goldstein, D. Henry, A. Jackson, S. Lovell, W. Muehlberger, R. Nicholas, S. ruppel, M. Sandstrom and C. Woodruff, 1990, Tectonic Map of Texas, Bureau of Economic Geology, The University of Texas at Austin.

Ewing, T., 1991, The tectonic framework of Texas, Bureau of Economic Geology, University of Texas at Austin, 36 pp.

Ferril, D., A. Morris, J. Stamatakos and D. Sims, 2000, Crossing conjugate normal faults, AAPG Bulletin, vol. 84 no. 10, pp. 1543-1559.

Feynman, R., Leighton, R., and Sands, M.,1963, The Feynman lectures on physics: Wesley, Reading, MA.

Flodin, E., and A. Aydin, 2004, Evolution of a strike-slip fault network, Valley of Fire, southern Nevada, Geological Association of America Bulletin, January/February, v. 116, no. 1-2, p. 42-59.

Florez, J. M., Mavko, G., 2002, Evolution of conjugate normal faults in sedimentary sequences with high brittleness/ductility contrast, Stanford Rock Physics and Borehole Geophysics Project (SRB) report, Stanford University Vol. 84, paper F2.

Flórez, J-M., A. Aydin, G. Mavko, M. Antonellini and A. Ayaviri, 2003, Faults and fractures systems in a fold and thrust-belt: an example from Bolivia, Proceedings of the Stanford Rock Physics and Borehole Project Workshop.

Friedman, M., and D.M. Wiltschko, 1992, An approach to exploration for naturally fractured reservoirs –a generic approach with examples from the Austin Chalk. In J. W. Schmoker, E.B. Coalson and C.A. Brown, eds, Geological Studies Relevant to Horizontal Drilling: Examples from Western North America, Rocky Mountain Association of Geology, Denver, Colorado, 143-153.

Florez, J.M., 2000, Fracture distribution in a fault-cored anticline. Stanford Rock Fracture Project, v.11, P-E-1.

Gassmann, F., 1951, On the elasticity of porous media: Vier. Der Natur. Gesllschft in Zurich, 96, 1-23.

GledhillK.R., 1991, Evidence for shallow and pervasive seismic anisotropy in the Wellington Region, New Zealand, J. Geophys. Res., 96, 21505-21516.

Goovaerts, P., 1997, Geostatistics for natural resources evaluation, Oxford University Press, New York, pp. 483.

Graham-Wall, B., R. Girbacea, A. Mesoniesi, A. Aydin, Evolution of fluid pathways through fracture controlled in carbonates of the Albanides fold-thrust belt, submitted for publication at the AAPG Bulletin.

Graham, G., Crampin, S. Fernandez, L. M., 1991, Observations of the shear-wave polarizations from rockbursts in a South African gold field and analysis of acceleration and velocity recordings, Geophys. J. Int., 107, 661-672.

Graham, G., Crampin, S. 1993 Shear-wave splitting from regional earthquakes in Turkey, Can. J. expl. Geophys., 29, 371-379.

Grechka , V. and Tsavankin, I., 1998, 3-D description of normal moveout in anisotropic inhomogeneous media, Geophysics, 63, 1079-1092.

Greenhalgh, S. A., Wright, C., Goleby, B., Soleman, S., 1990, Seismic anisotropy in granulite facies rocks of the Arunta Block, Central Australia, Geophys. Res. Lett. ,17, 1513-1516

Grimm R.E. and Lynn, H.B., 1997, Effects of acquisition geometry, large scale structure and regional anisotropy on AVOA: an example from the Wind River Basin, 67th Ann. Internat. Mtg. Soc. Expl. Geophys., Exp. Abstracts, 1997-2000.

Grimm, E.R., Lynn, H. B., Bates, C. R., Phillips, D. R., Simon K. M., Beckham, W. E., 1999, Detection and analysis of naturally fractured gas reservoirs: Multiazimuth seismic surveys in the Wind River basin, Wyoming, Geophysics, 64, 1277-1292.

Gutierrez, M. A., A. Nur, 2001, 3-D seismic interpretation of tectonic wrenching and faulting in La Cira-Infantas, The Leading Edge (Tulsa, OK), vol.20, no.7, 752-760.

Heffner, K. J., and T. G. Bevan, 1990, Scaling relationships in natural fractures, data, theory and applications. SPE 20981. Proceedings of Europec 90, The Hague, Netherlands.

Helgeson, D E, A. Aydin, 1991, Characteristics of joint propagation across layer interfacies in sedimentary rocks, Journal of Structural Geology, vol.13, no.8, 897-911.

Holmes, G.M., Crampin, S., Young R.P., 1993, Preliminary analysis of sher-wave splitting in granite at the Underground Research Laboratory, Manitoba, Can. J. Expl. Geophys, 29, 140-152.

Horsfield, 1980, Contemporaneous movement along crossing conjugate normal faults: Journal of Structural Geology, v.2, no. 3, 305-310.

Houck, R., 1999, Estimating uncertainty in interpreting seismic indicators: The Leading Edge, 18, 3, 320-325.

Hsu, C-J.,Schoenberg M., 1993, Elastic waves through a simulated fractured medium, Geophysics, 58, 964-977.

Hubbert, M. K., 1951, Mechanical basis for certain familiar geologic structures, Bulletin of the Geological Society of America, Vol. 62, 355-372.

Hubbert, M. K., and Rubey, W., 1959, Role of fluid pressure in mechanics of overthrust faulting, Bulletin of the Geological Society of America, Vol. 70, 115-166.

Hudson, J. A., 1980, Overall properties of a cracked solid, Math. Proc. Camb. Phil. Soc., 88, p. 371-384.

Hudson, J. A., 1981, Wave speeds and attenuation of elastic waves in material containing cracks: Geophys. J. Roy. Astr. Soc., 64, p. 133-150.

Hudson, J. A., 1990, Overall elastic properties of isotropic materials with arbitrary distribution of circular cracks, Geophys. J. Int., 102, p. 465-469.

Hudson, J. A., 1994, Overall properties of anisotropic materials containing cracks, Geophys. J. Int., 116, p. 279-282.

Hudson, J.A., Liu, E., and Crampin, S., 1996, The mechanical properties of materials with interconnected cracks and pores, Geophys. J. International, 124, 105-112.

Hudson, J.A., 1997, The mean transmission properties of a fault with imperfect facial contact, Geophys. J. Int, 129, 720 –726.

Hudson, J.A., Liu, E., 1999, Effective elastic properties of heavily faulted structures, Geophysics, 64, 479-485.

Innanaccone G., Deschamps, A. 1989 Evidence of shear-wave anisotropy in the upper crust of central Italy, Bulletin of seism Soc Am., 79 1905-1912.

Jackson, M. P. A., 1982, Fault tectonics of the East Texas Basin, The university of Texas at Austin, Bureau of Economic Geology, Geological Circular 82-4, 31 pp.

Jaynes, E. T., 2003, Theory of Probability: The logic of science, Cambridge Univ. Press.

Jaynes, E. T., 1983, Papers on Probability, Statistics and Statistical Physics, Rosenkrantz, R. D. ed.

Jev, B.I., C. Kaars-Sijpesteijn, M. Peters, N. Watts and T. Wilkie, 1993, Akaso Field, Nigeria use of integrated 3-D seismic, fault slicing, clay smearing, and RFT pressure data on fault trapping and dynamic leakage: AAPG Bulletin, v. 77 no. 8, 1389-1404.

Kaneshima, S., Ando, M. Crampin, S., 1987, Shear wave splitting above small earthquakes in the Kinki District of Japan, Phys. Earth. Planet Inter., 45, 45-58.

Kaneshima, S., Ito, H. Sugihara, M. 1988, Shear wave polarization anisotropy observed in a rift zone in Japan, Tectonophysics, 157, 281-300.

Kaneshima, S., Ando, M., 1989, An analysis of split shear-waves observed above crustal and uppermost mantle earthquakes beneath Shikoku, Japan, implications in effective depth extent of seismic anisotropy, J. Geophys. Res., 94, 14077-14092.

Kattenhorn, S., A. Aydin and D. Pollard, 2000, Joints at high angles to normal fault strike; an explanation using 3-D numerical models of fault-perturbed stress fields, Journal of Structural Geology, vol.22, no.1, 1-23.

Koledoye, A B., A. Aydin, and E. May, 2000, Three-dimensional visualization of normal fault segmentation and its implication for fault growth, The Leading Edge (Tulsa, OK), vol.19, no.7, 692-701.

Krystinik, Lee F, 2000, Predicting fractures 5 km down; integrated reservoir characterization to site horizontal wells, UPR/DOE Rock Island 4-H well, AAPG Bulletin, vol.84, no.7, pp.1063.

Kuwakhara, Y. Ito, H., Kiguchi, T., 1991, Comparison between natural fractures and fracture parameters derived from VSP, Geophys. J. Int., 107, 475-483.

Laplace, P., S., 1814, A philosophical Essay on Probabilities, reprint, Dover Publications, Inc., New York, 1951.

La Pointe, P. R., Huston, J. A., 1985, Characterization and interpretation of rock mass joint patterns, Spec. Pap. Geol. Soc. Am., 199, 1-37.

Lauback, S. E., and M. L. Jackson, 1990, Origin of

Leary, P.C., Li Y.-G, Aki, K., 1987, Observation and modeling of fault-zone fracture seismic anisotropy -I P, SV and SH travel times, Geophys. J. R. Astr. Soc., 91, 461-484.

Lefeuvre, F., Cliet, C. Nicoletis, L., 1989, Shear-wave birefringence measurement and detection in the Paris basin, 59th Ann. Int. SEG Meeting, Dallas, Expanded Abstracts, 2, 786-790.

Lewis, C., Davis., T. L., Vuillermoz, C., 1991, Three-dimensional multicomponent imaging of reservoir heterogeneity, Silo Field, Wyoming, Geophysics, 56, 2048-2056.

Li, Y.-G, Leary, P.C., Aki, K., 1990, Ray series modeling seismic wave travel times and amplitudes in three-dimensional heterogeneous anisotropic crystalline rock: borehole vertical seismic profiling seismograms from the Mojave Desert, California, J. geophys. Res., 95, 11225-11239.

Li, X.-Y, Mueller, M.C., Crampin, S., 1993, Case studies of shear-wave splitting in reflection surveys in South Texas, Can. J. expl. Geophys., 29, 189-215.

Liu, E., Crampin, S., Queen, J. H., Reizr, W. D., 1993a Velocity and attentuation anisotropy caused by microcracks and macrofractures in azimuthal reverse VSPs, Can. J. expl. Geophys., 29 177-188.

Liu, E., Crampin, S., Queen, J. H., 1991, Fracture detection using crosshole surveys and reverse vertical seismic profiles at the Conoco Borehole Test Facility, Oklahoma, Geophys. J. Int., 107, 449-463.

Lloyd, P., P. Tandom, N. Ngoc and H. D. Tjia, 2000, Identifying and evaluating producing horizons in fractured basement, AAPG Bulletin, vol. 84, no. 9, pp. 1456.

Lockner, D., N. Beeler, 1999, Premonitory slip and tidal triggering of earthquakes, Journal of Geophysical Research, B, Solid Earth and Planets, vol.104, no.9, pp.20,133-20, 151.

Lorenz, J. C., H. Farrel, C. Hanks, W. Rizer and M. Sonnenfeld, 1997, Characteristics of natural fracture in carbonate strata, in: I. Palaz and K. Marfurt eds, Carbonate Seismology, Geophysical Developments No. 6, chapter 8.

Loucks, R. A., Cole, M. Ver Hoeve, 1996, Paleotopography association, litho-facies architecture and reservoir quality of the upper James Lime reservoir (Pearsall Fm, Lower Cretacesous) in the Poplarville Field, Pearl River County, Mississippi, AAPG Gulf Coast Association of Geolog. Soc., San Antonio, TX., XLVI 235-248.

Lynn, H.B., Thomsen, L.A., 1986, Reflection shear-wave data along the principal axes of azimuthal anisotropy, 56th, Ann Int. SEG Meeting, Houston, Expanded Abstracts, 473-477.

Lynn H. B., Simon, K. M. and Bates, C.R. 1996, Correlation between P-wave AVOA and S-wave traveltime anisotropy in a naturally fractured gas reservoir, The Leading Edge, 15, 931-935.

Lynn, H.B., Thomsen, L.A., 1990, Reflection shear-wave data collected near the principal axes of azimuthal anisotropy, Geophysics, 55, 1147-156.

Lynn, H. B., Campagna, D., Simon, K. M., Beckham, W. E., 1999, Relationshiop of P-wave seismic attributes, azimuthal anisotropy and commercial gas pay in #D P-wave multiazimuth data, Rulison Field, Piceance Basin, Colorado, Geophysics, 64, 1293-1311.

Maertel, S., 1990, Formation of compound strike-slip fault zones, Mount Abbot quadrangle, California, Journal of Structural Geology, v. 12, no. 7, 869-882.

Maerten, F. and L. Maerten, 2001, Unfolding and restoring complex geological structures using linear elasticity theory, AGU Fall Meeting Program and Abstracts.

Maerten, Laurent, D. Pollard, and R. Karpuz, 1994, How to constrain 3-D fault continuity and linkage using reflection seismic data; a geomechanical approach, AAPG Bulletin, vol.84, no.9, 1311-1324.

Mallick, S., Craft, K. L., Meister, L. J., Chambers, R.E, 1998, Determination of the principle directions of azimuthal anisotropy from P-wave seismic data: Geophysics 63, 692-706.

Marfurt, K. J., R. L. Kirlin, S. L. Farmer, M. Bahorich, 1998, 3-D seismic attributes using a semblance-based coherency algorithm, Geophysics, vol.63, no.4, 1150-1165.

Martin, M.A., Davies, T.L., 1987, A new tool for evaluating fractured reservoirs, The Leading Edge, 6, 6, 22-28.

Mavko G., and Mukerji, T., 1998, A rock physics strategy for quantifying uncertainty in common hydrocarbon indicators, Geophysics, 63, 1997-2008.

Mavko G., Mukerji, T., Dvorkin, J., 1998, The rock physics handbook, Cambridge University Press.

McClay, K. R., 1995, 2D and 3D analogue modeling of extensional fault structures: templates for seismic interpretation: Petroleum Geoscience, v. 1 no. 2, 163-178.

Molotkov, L. A., Backulin, A. V., 1997, An effective model of a fractured medium with fractures modeled by the surfaces of discontinuity of displacements, Journal of Math. Sci., 86, 2735-2746.

Morley, C.K., R. Nelson, R. Patton and S. Munn, 1990, Transfer zones in the East African Rift system and their relevance to hydrocarbon exploration in rifts: AAPG Bulletin, v. 74, no.8, 1234-1253.

Mueller, B., Reinecker, J., Heidbach, O. and Fuchs, K., 2000, The 2000 release of the World Stress Map (available online at www.world-stress-map.org).

Mueller, M.C., 1991, Prediction of lateral variability in fracture intensity using multicomponent shear-wave surface seismic as a precursor to horizontal drilling in Austin Chalk, Geophys. J. Int., 107, 409-415.

Mukerji, T., Avseth, P., Mavko, G., Takahashi, I., Gonzales, E., 2001, Statistical rock physics: combining rock physics, information theory, and geostatistics to reduce uncertainty in seismic reservoir characterization, The Leading Edge, 20, No 3, 313-319.

Mukerji, T., 1995, Ph. D. dissertation, Stanford University.

Myers, R., A. Aydin, *in prep*., The evolution of faults formed by shearing across joint zones in sandstone, Rock Fracture Project, Department of Geological and Environmental Sciences, Stanford University.

Narr, W., 1990, Fracture density in the deep subsurface; techniques with application to Point Arguello oil field, American Association of Petroleum Geologists Bulletin, vol.75, no.8, pp.1300-1323.

Narr, and Suppe, 1991, Joint spacing in sedimentary rocks, Journal of Structural Geology, vol.13, no.9, pp.1037-1048.

Nelson, R. A., E. P. Moldovanyi, C. C. Matcek, I. Azpiritxaga and E. Bueno, 2002, Production characteristics of the fractured reservoirs of the La Paz field, Maracaibo basin, Venezuela. American Association of Petroleum Geologists, v. 84, no. 11, pp. 1791-1809.

Nelson, R.A., 1985, Geologic analysis of Naturally Fractured Reservoirs, Houston: Gulf Pub CO., Book Division, c1985.

Nicol, A., J. Watterson, J. J. Walsh and C. Childs, 1994, The shapes, major axis orientations and displacement patterns of fault surfaces, Journal of Structural Geology, v. 5, no. 5, 483-495.

Nilsen, K. T., B. C. Venderville, J. T. Johansen, 1995, Influence of regional tectonics on halokinesis in the Nordkapp Basin, Barents Sea, in M. P. A. Jackson, D. G. Roberts, and S. Snelson, eds., Salt tectonics: a global perspective AAPG Memoir 65, 413-436.

Nunn, J. A., Relaxation of continental lithosphere: an explanation for Late Cretaceous reactivation of the Sabine uplift of Luisiana-Texas, Tectonics, 9, 41-359.

Nur, A., 1971, Effects of stress on velocity anisotropy in rocks with cracks, J. Geophys. Res., 76, 2022-2034.

Nur, A., and G. Simons, 1969, Stress-induced velocity anisotropy in rocks: An experimental study, Journal of Geophysical Research, v. 74, 6667.

Peakock, S., Crampin, S., Booth, D. C., Fletcher, J. B., 1988 Shear-wave splitting in the Anza seismic gap, Southern California: temporal variations as possible precursors, Journal Geoph Rws., 93, 3339-3356.

Peel, F.J., C.J. Travis, and J.R. Hossack, 1995, Genetic structural provinces and salt tectonics of the Cenozoic offshore U.S. Gulf of Mexico: a preliminary analysis, in M. P. A. Jackson, D.G. Roberts, and S. Snelson, eds., Salt tectonics: a global perspective: AAPG Memoir 65, 153-175.

Perez, M.A, Grechka V., Michelena, R. J., 1999, Fracture detection in a carbonate reservoir using a variety of seismic methods, Geophysics, 64, 1266-1276.

Pollard, D., and A. Aydin, 1988, Progress in understanding jointing over the past century, Geological Society of America Bulletin, vol.100, no.8, 1181-1204.

Pollard, D. D., and P. Segall, 1987, Theoretical displacements and stresses near fractures in rock: with applications to faults, joints, veins, dikes, and solution surfaces, in Atkinson, B. K., Fracture Mechanics of Rock, Academic Press, 277-349.

Priest, S. D., Houston, J. A., 1976, Discontinuity spacing in rocks, Int. J. Rock Mech. Mining Sci Geomech. Abs., 13, 135-148.

Queen, J.H., Rizer, W.D., 1990, An integrated study of seismic anisotropy and the natural fracture system at the Conoco Borehole Test Facility, Kay County, Oklahoma, J. geophys. Res., 95, 11255-11273.

Renfro, H.B., D. Feray, R. Dott and A. Bennison, 1984, Geological highway map of Texas. American Association of Petroleum Geologists.

Reuss, A., 1929, Berechunung der fliessgrense von mischkristallen auf grund der plastizitatsbedinggung fur einkristalle, Zeitschrift fur Angewandte Mathematik and Mechanik, 9, 49-58.

Rives, T., Razack, M., Petit, J.-P., Rawnsley, K. D., 1992, Joint spacing: analogue and numerical simulations, Journal of Structural Geology, Vol 14, No 8/9, 925-937.

Roberts, G., Crampin, S., 1986, Shear-wave polarizations in a hot-dry-rock geothermal reservoir: anisotropic effects of fractures, Int. J., Rock Mech. Min. Sci., 23, 291-302.

Ross, S., 2001, A first course in probability theory, 6th edition, Prentice Hall.

Rouleau, A, Gale, J. E., 1985, Statistical characterization of the fracture system in the Stripa granite, Sweden, Int. J. Rock Mech. Mining Sci Geomech. Abs., 22, 353-367.

Rüger, A., 1995, P-wave reflection coefficients for transversely isotropic media with vertical and horizontal axis of symmetry, Expanded Abstracts, Society of Exploration Geophysicists, 65th Annual Meeting, 278-281.

Rüger, A., 1996, Variation of P-wave reflectivity with offset and azimuth in anisotropic media, Expanded Abstracts, Society of Exploration Geophysicists, 66th Annual Meeting, 1810-1813.

Ruger, A., 1998, Variation of P-wave reflectivity with offset and azimuth in anisotropic media, Geophysics, 63, 935-947.

Sava, D. C., Mukerji, T., Florez, J. M., Mavko, G., 2001, Rock physics analysis and fracture modeling of the San Andres reservoir, Yates field, 71th Ann. Int. SEG Meeting, San Antonio, TX, Expanded Abstracts, 1748-1751.

Sava, D. C., Florez, J. M., Mukerji, T., Mavko, G., 2002, Seismic fracture characterization using statistical rock physics: James Lime reservoir, Neuville field, 72nd Ann. Int. SEG Meeting, Salt Lake City, UT, Expanded Abstracts,1889-1892.

Savage, M.K., Shih, X.R., Meyer, R.P., Aster, R.C., 1989, Shear-wave anisotropy of active tectonic regions via automated S-wave polarization analysis, Tectonophysics, 165, 279-292.

Savage, M.K., Peppin, W. A., Vetter, U.R., 1990, Shear-wave anisotropy and stress direction in and near Long Valley Caldera, California, 1979-1988, J. Geohys. Res. 95, 11165-11177.

Schoenberg, M., 1980, Elastic behavior across linear-slip interfaces, 1980, J. Acoustic Society Am., 68, 1516-1521.

Schoenberg, M., 1983, Reflection of elastic waves from periodically stratified media with interfacial slip, Geophys. Prosp. 31, p. 265-292.

Schoenberg, M and Muir, F, 1989, A calculus for finely layered anisotropic media, Geophysics, 54, 581-589.

Schoenberg, M and Douma, J., 1988, Elastic wave propagation in media with parallel fractures and aligned cracks, Geophys. Prosp., 36, p. 571-590

Schoenberg, M and Sayers, C. 1995, Seismic anisotropy of fractured rock, *Geophysics*, 60, 204-211.

Segall, P., and D. Pollard, 1980, Mechanics of discontinuous faulting, Journal of Geophysical Research, v. 85, 4337-4350.

Segall, P., and D. Pollard, 1983, Nucleation and growth of strike slip faults in granite, Journal of Geophysical Research, v. 88, 555-568.

Selsing, 1981, Stress analysis on conjugate normal faults in unconsolidated Weichselian glacial sediments from Brorfelde, Denmar, Boreas, v. 10, no. 3, 275-279.

Sen, Z., Kazi, A., 1984, Discontinuity spacing and RQD estimates from finite length scanlines, Int. J. Rock Mech. Mining Sci. Geomech. Abs., 21, 203-212.

Shannon, C., 1948, A mathematical theory of communication: Bell System Technical Journal, 27, 379-423, 623-656.

Shen, F., Sierra, J., Burns, D. R., Toksoz, M. N., 2002, Azimuthal offset-dependent attributes applied to fracture detection in a carbonate reservoir, Geophysics, 67, 355-364.

Shih, X.R., Meyer R. P., 1990 Observations of shear-wave splitting from natural events:

Shuey, R. T., 1985, A simplification of the Zoeppritz equations, Geophys., 50, 609-614.

South Moat of Long Valley Caldera, California, June 29 to August 12, 1982, J. geophys. Res., 95, 11179-11195.

Shuck, E. L., 1991, Azimuthal anisotropy analysis from shear VSPs, Geophys. J. Int., 107, 639-647.

Slater, C., Crampin, S., Brodov, L..Y., Kuznetsove, V.M., 1993, Observations of anisotropic cusps in transversely isotropic clay, Can. J. Expl. Geophys, 29, 216-226.

Snow, D. T., 1968, Anisotropic permeability of fractured rocks. In: Hydrology and Flow through Porous Media (edited by De Wiest, R. J. M.)

Takahashi, I., Mavko, G., Mukerji, T., 1999, A strategy to select the optimal seismic attributes for reservoir property estimation: Application to information theory, Soc. Expl. Geophys., Expended Abstracts.

Takahashi, I., 2000, Ph.D. dissertation, Stanford University.

Tarantola, A., Vallete, B., 1982, Inverse problems = Quest for information: J. Geophys., 50, 150-170.

Tarantola, A., 1987, Inverse Problem Theory, Elsevier Science B. V.

Teng, L., 1998, Ph.D. dissertation, Stanford University.

Thomas, Andrew, Poly3D: a three-dimensional, polygonal element, displacement discontinuity boundary element computer program with applications to fractures, faults, and cavities in the Earth's crust. M Sc thesis. Stanford University.

Thomsen, L., 1986, Weak elastic anisotropy: Geophysics, 51, No. 10, 1954-1966.

Tsvankin, I., 1997, Reflection moveout and parameter estimation for horizontal transverse isotropy, Geophysics, 62, 614-629.

Vavrycuk, V. and Psencik, I., 1998, PP-wave reflection coefficients in weakly anisotropic elastic media, Geophysics, 63, 2129-2141.

Ver Wiebe, W., 1949, Oil fields in North America, Monograph, American Geological Institute, 249 pp.

Villaescusa , E, Brown, E. T., 1990, Characterizing joint spatial correlation using geostatistical methods. In: Rock Joints (edited by Barton, N. and Stephansson, O.), Balkema, Rotterdam, 115-122.

Wang, L., 1998, Modeling complex reservoir lithofacies, Ph D dissertation, Stanford University.

Watterson J., A. Nicol, J. J. Walsh and D. Meier, 1998, Strains at the intersections of synchronous conjugate normal faults: Journal of Structural Geology, v. 17 no. 6, 847-862.

Winterstein, D. F., Meadows, M.A., 1991a, Shear-wave polarization and subsurface stress directions at Lost Hills field, Geophysics, 56, 1331-1348.

Winterstein, D. F., Meadows, M.A., 1991b, Changes in shear-wave polarization azimuth with depth in Cymric and Railroad Gap oil fields, Geophysics, 56, 1349-1364.

Wiprut, D., and Zoback, M.D., 2000, Fault reactivation and fluid flow along a previously dormant normal fault in the northern North Sea. Geology. 28:7, 595-598.

Withjack, M.O., Q. Islam, and P. La Pointe, 1995, Normal faults and their hanging-wall deformation, an experimental study, AAPG Bulletin, v.79, no. 1, 1-18.

Wu, H., and D. Pollard, 1995, An experimental study of the relationship between joint spacing and layer thickness, Journal of Structural Geology, vol.17, no.6, pp.887-905.

Wu, H. and W. Narr, 2000, Skull creek outcrop study: How well can we predict subsurface fracture system? Stanford Rock Fracture Project, Workshop, v. 11, G-1.

Yardley, G.S., Crampin, S., 1993 Shear-wave anisotropy in the Austin Chalk, Texas, From multi-offset VSP data: case studies, Can. J. Expl. Geophys., 29, 163-176.

Young, S., 2000, Conjugate normal faults in layered sedimentary rocks, Stanford Rock Fracture Project, Vol. 11, A-1.

Zoback, M. L.; Zoback, M. D., 1980, State of stress in the conterminous United States, Journal of Geophysical Research. B, vol.85, no.11, 6113-6156.

Zoeppritz, K., 1919, Erdbebenwellen VIIIB, On the reflection and propagation of seismic waves. Gottinger Nachrichten, I, 66-84.